UNIVERSITY OF CALIFORNIA
Los Angeles

Topographic effects on mesoscale ocean circulation

A dissertation submitted in partial satisfaction
of the requirements for the degree
Doctor of Philosophy in Atmospheric and Oceanic Sciences

by

Aviv Solodoch

2020

Abstract of the Dissertation

Topographic effects on mesoscale ocean circulation

by

Aviv Solodoch
Doctor of Philosophy in Atmospheric and Oceanic Sciences
University of California, Los Angeles, 2020
Professor James C. McWilliams, Co-chair
Professor Andrew L. Stewart, Co-chair

The trajectories and stability of boundary currents, of mesoscale vortices, and of recirculations, are often largely imposed by ocean bottom topography. Here several related questions in the influence of topography on mesoscale ocean circulation are investigated, largely motivated by observed circulation features in the sub-polar North Atlantic ocean.

Observations show that boundary currents tend to become highly variable and shed material near sharp topographic variations, such as peninsula edges or corners of underwater capes. Baroclinic instability is understood to be one of the main causes of internal variability of large scale ocean circulation. Therefore the influence of horizontally curving topography on baroclinic instability is studied, under the hypothesis that the curvature may cause a higher tendency towards instability. That is done within a minimum complexity model, a two-layer quasi-geostrophic model, and compared with the classic rectilinear model. First necessary conditions for instability as well as growth rate bounds are derived. Growth rates are calculated analytically or numerically for several flow and topography profiles. The growth rate in uniform azimuthal flow is similar to that in uniform rectilinear azimuthal flow, but decreases with increasing depth-averaged flow component amplitude. That is recognized as a generalization of the so called "barotropic governor" effect. Instability growth rate is nonetheless higher with uniform azimuthal flow when isopycnal slope is similar to the topographic slope magnitude, a common scenario in the ocean.

Non-normal instability is studied as well, and is generally intensified with uniform azimuthal flow. Thus a complex picture emerges as to the influence of horizontal curvature on baroclinic instability.

The Deep Western Boundary Current (DWBC) carries water masses formed in deep convection sites southward, as part of the Atlantic Overturning Meridional Circulation (AMOC), a circulation pattern of climatic importance. Observations show that the DWBC "leaks" material at an anomalously high rate in its path along two underwater capes in the Newfoundland Basin. The leakiness, resulting in water masses dilution, and in AMOC alternative (interior) pathways southward, has not been studied extensively from a dynamical perspective before. A high-resolution realistic regional numerical model configuration and a particle advection model are developed for this purpose. The numerical results, as well as two datasets of ocean float trajectories, are analyzed to determine the dynamical causes of leakiness and its phenomenology. It is found that leakiness is concentrated in three "hotspots", in which topography turns and steepens. Mean Lagrangian velocity is offshore at these locations, showing that leakiness occurs by mean separation. The mean velocity does not have a substantial eddy-rectified component at the two northern hotspots, where most of the mean leakiness happens. Likewise, energetic analysis shows eddies do not locally force the mean offshore flow. Furthermore, potential vorticity is not diluted substantially by eddies along mean separating streamlines. These results are consistent with mean leakiness occurring by inertial separation. A scaling analysis also suggests that bathymetric conditions near the leakiness hotspots are supportive of inertial separation. Eddy processes also contribute substantially to leakiness, partially through chaotic advection.

In several North Atlantic basins semi-stationary anticyclonic vortices (ACs) have been repeatedly observed for decades, within areas with bowl-like topography. These basins play significant parts in AMOC transport and transformations, and previous evidence suggests these ACs contribute to these processes. Therefore the formation processes of ACs above topographic bowls is studied here using idealized free evolution simulations in one or two isopycnal layers. It is demonstrated that ACs readily form under different (bowl-like) topographies and initial condi-

tions. A non-dimensional nonlinearity parameter ($\epsilon \sim$ ratio of vorticity to bowl PV gradient), or a potential vorticity (PV) inhomogeneity (PVI) parameter, largely determine if a trapped AC is formed from random mesoscale-like initial conditions. Trapped ACs form and stay close to bowl-center for $\epsilon \lesssim 0.5$ (PVI ~ 1). For $\epsilon \gtrsim 1$ (PVI ~ 0) vortices freely cross the topography by mutual interactions. For intermediate ϵ or PVI values, trapped ACs can form at different bowl radii since the PV gradient is nullified by the presence of a slope current. Trapped ACs generally form by repeated mergers of ACs within the bowl, and have anomalously low PV. Tracer analysis shows that ACs which eventually merge into the trapped AC are sourced from within (outside) the bowl in low (high) energy cases. Two different cross-bowl propagation mechanisms are examined. Monopole beta drift as well as dipole self propagation can both contribute to cross-bowl AC material transport, but the latter appears faster in relevant cases. The vertical structure of the trapped AC is studied as well. It is shown that it is top (bottom) intensified for top (bottom) intensified domain-mean initial conditions. That is consistent with observational structure but in contrast with the common vertical structure in Taylor Caps and of the slope current in our simulations, which remain bottom-intensified in all cases. Scaling laws for vertical structures are suggested in several cases. The robustness of AC formation to topographic complexity is studied, as well as its long-term evolution, and the results are contrasted with topographic turbulence theories, which predict a slope current but not a bowl-trapped AC.

The dissertation of Aviv Solodoch is approved.

Jonathan Aurnou

Gang Chen

Andrew L. Stewart, Committee Co-chair

James C. McWilliams, Committee Co-chair

University of California, Los Angeles

2020

I dedicate this work to my family. To my loving parents, Hana and Israel Solodoch, who imparted in me curiosity and the confidence to follow it. To my brothers, Dror and Omer, for always being there. To my wife, Gali, for lovingly making every day happier. To my daughter, Lia, for making everything worthwhile.

Table of Contents

List of Figures

List of Tables

Acknowledgments

I would like to thank my Ph.D. advisors, Andrew L. Stewart and James C. McWilliams for countless invaluable lessons in the craft of conducting scientific research; for joint exploration of extremely interesting scientific projects; for their support during the doctoral journey; and for their encouragement of my observational research activities during my work with them. I thank Dr. Jeroen Molemaker and the UCLA Marine Operations team, for introducing me to observational oceanography, which I believe has greatly impacted my personal development as a Physical Oceanographer. I also thank my dissertation committee: Gang Chen and Jon Aurnou for their constructive advice and support.

I thank our collaborators in the project described in chapter 3 [*Solodoch et al.*, 2020a]: Jon Gula of the University of Western Brittany, and Lionel Renault of the University of Toulouse. Jon and Lionel provided the parent grid we used for the North Atlantic numerical model computation. Lionel has introduced me to the methodology of setting up a ROMS model configuration. Additionally, both have offered good advice and generously shared computational tools during the project.

I appreciated insightful discussions with Mickael D. Chekroun and with Yizhak Feliks, which informed the non-normal growth analysis of chapter 2. I thank Michael Rudko for suggesting to look into it in the first place. I also thank Dr. Chekroun for many helpful conversations on science, academia, and more throughout my time in UCLA, for being open and generous with his time, and for offering much needed critical advice at various times.

Daniel Dauhajre has very kindly offered technical advice regarding the ROMS model on many occasions, as well as scientific advice. Kaushik Srinivasan provided much appreciated encouragement in the last few years, and helped solve some unfathomable cluster problems. Sasha Shchepetkin has also contributed from his time and immense numerical expertise in the initial phases of learning the ins and outs of the ROMS model. I also thank all the Stewart and McWilliams

research groups members, which have offered valuable feedback on this work over the years.

The analysis of chapter 3 benefited from several observational datasets which were freely available or freely provided by several different institutions. I thank Dr. Amy Bower for providing the Export Pathways dataset, and Dr. Christian Mertens for providing the processed shipboard ADCP observations at 47 N, east of Flemish Cap. The sea surface height altimeters reprocessed data product was produced by Ssalto/Duacs and presently distributed by the Copernicus Marine and Environment Monitoring Service (CMEMS), http: //marine.copernicus.eu (previously distributed by AVISO). The Argo data were collected and made freely available by the International Argo Program and the national programs that contribute to it (http://www.argo.ucsd.edu, http://argo.jcommops.org). The Argo Program is part of the Global Ocean Observing System.

This work was partially supported by US National Science Foundation (NSF) grants: OCE-1538702, OCE-1355970, and OCE-1751386; NASA grant 80NSSC19K1192 OCE-1538702; and Office of Naval Research (ONR) grant number N00014-18-1-2599. I am grateful for the grants as well as for the computational resources which were partially provided through the NSF Extreme Science and Engineering Discovery Environment (XSEDE).

Chapter 2 is an adapted version of [*Solodoch et al.*, 2016]. The work in Chapter 3 is an adapted version of [*Solodoch et al.*, 2020a]. Finally, Chapter 4 is an adapted version of a recently submitted manuscript [*Solodoch et al.*, 2020b].

Aviv Solodoch

Los Angeles, California, USA
July 2020

Vita

Degrees

2006	B.Sc. Physics and Mathematics, Tel Aviv University, Tel Aviv, Israel
2010	M.Sc. Physics, Weizmann Institute of Science, Rehovot, Israel
2016	M.Sc. Atmospheric and Oceanic Sciences, UCLA

Academic Positions

2014–2020	Graduate Student Researcher Department of Atmospheric and Oceanic Sciences, UCLA
2016, 2017	Teaching Assistant (Physical Oceanography) Department of Atmospheric and Oceanic Sciences, UCLA

Academic Awards

2019	Jacob A. Bjerknes Memorial Award, UCLA: *For a persuasive analysis of how water in deep western boundary currents leaks into the oceanic interior*

Observational Research and Affiliation

2014-2020	UCLA Marine Operations member, UCLA
2015-2017	Volunteer Captain and instructor for UCLA undergraduate and graduate oceanography classes boat excursions
2017	Participation in the “LASER” observational campaign, northern Gulf of Mexico

2018 Participation in the "SPLASH" observational campaign, northern Gulf of Mexico

Academic Service

2018–2019 Manuscripts reviewer for the Journal of Fluid Mechanics

2019–2020 Undergraduate students advisor. Stewart research group, department of Atmospheric and Oceanic Sciences, UCLA

Partial List of Oral Presentations

2019 What makes the Deep Western Boundary Current "leak"? UCLA department of Atmospheric and Oceanic Sciences. Departmental seminar.

2019 Leakiness and separation of the Deep Western Boundary Current. Caltech, Pasadena, CA. Oceanography groups seminar.

2019 Observations of a density current in a sheared stratified ambient. Tel Aviv University, Tel Aviv, Israel. Department of Mechanical Engineering. Toledo group seminar.

2019 Leakiness and separation of the Deep Western Boundary Current in the transition from the subpolar to the subtropical gyre. Hebrew University of Jerusalem, Israel. Climate Atmosphere and Oceanography seminar.

2019 Emergence of long-lived ocean anticyclones in topographic depressions. 22nd AMS Conference on Atmospheric and Oceanic Fluid Dynamics. Portland, Maine.

2019 Leakiness of the Deep Western Boundary Current near Flemish Cap. GFD Days Conference. Sde Boker, Israel.

2018 Detailed observations of structure and erosion of a Mississippi-plume front in the Gulf of Mexico. CARTHE-II Fall 2017 All- Hands Meeting. RSMAS, Miami, FL.

Publications

Solodoch, A., Excitation of slow Kelvin waves in the equatorial atmosphere by Yanai wave-group-induced convection. *MSc. Thesis*. Faculty of physics, Weizmann Institute of Science, Israel.

Solodoch, A., Boos, W., Kuang, Z., & Tziperman, E. (2011), Excitation of intraseasonal variability in the equatorial atmosphere by Yanai wave groups via WISHE-induced convection. *J. Atm. Sc.* **68**. 210–225, doi: https://doi.org/10.1175/2010JAS3564.1.

Solodoch, A., Stewart, A L. (2016), & McWilliams, J C. Baroclinic instability of axially symmetric flow over sloping bathymetry. *J. Fluid. Mech.* **799**. 265–296, doi: https://doi.org/10.1017/jfm.2016.376.

Solodoch, A., Molemaker, J M., Srinivasan, K., Berta, M., Marie, L. & Jagannathan, A. (2020), Observations of Shoaling Density Current Regime Changes in Internal Wave Interactions. *J. Phys. Ocean.* **50** (6): 1733–1751, doi: https://doi.org/10.1175/JPO-D-19-0176.1.

Solodoch, A., McWilliams, J C., & Stewart, A L. (2020), Why Does the Deep Western Boundary Current "Leak" Around Flemish Cap? *J. Phys. Ocean.* **In press**. doi: https://doi.org/10.1175/JPO-D-19-0247.1.

Solodoch, A., Stewart, A L., & McWilliams, J C. (2020), Formation of anticyclones above topographic depressions. **Submitted**

CHAPTER 1

Introduction

1.1 Topographic control in mesoscale ocean circulation

The rotation of the earth imparts strong constraints on large scale ocean circulation. One of the implications in cases of relatively low density stratification is vertical rigidity. That is, large scale ocean circulation is largely confined to horizontal directions. Vertical velocity is much smaller, by a factor even larger than to be expected based on the aspect ratio of ocean basins alone [*McWilliams*, 2006]. For this reason, the topography of the ocean bottom (bathymetry) plays key roles in the organization of large-scale ocean circulation [*Salmon*, 1998]. Vertical rigidity, when it applies, is maintained by a preferential direction of circulation along topographic contours (isobaths), i.e., topographic steering of ocean currents [e.g., *LaCasce*, 2000; *Bower et al.*, 2002a; *Gille*, 2003; *Isachsen et al.*, 2003; *Talley*, 2011].

The aforementioned effects are particularly strong for mesoscale ocean circulation. Mesoscale refers to scales larger than the Rossby radius of deformation R_d[1], but considerably smaller than ocean basin scale ($\sim 10^3 - -10^4$ km). At scales $l > R_d$, the Coriolis force is of first order in the momentum equation, imparting the constraints of quasi-geostrophic flow and vertical rigidity. Since here the mesoscale is defined by size, it includes the finer features of mean basin scale circulation, i.e., boundary currents and some small inertial recirculation gyres [e.g., *Hogg and*

[1]Typically R_d =5–20 (20–100) km is subtropical (subpolar) areas [*Chelton et al.*, 1998].

Johns, 1995]. Mesoscale vortices (or eddies), swirling column-like flows, are ubiquitous ocean circulation features [*McWilliams*, 2008]. Indeed, large scale ocean variability (eddy kinetic energy) peaks in the mesoscale [*Khatri et al.*, 2018, show that is so at the ocean surface]. Mesoscale vortices are generally driven through instabilities of basin scale circulation, but in turn partially drive back the larger basin scale energetically through an inverse energy cascade.

The effects of rotation on large scale circulation can be qualitatively examined by the conservation of barotropic (depth-averaged) potential vorticity $q = (f + \zeta)/H$, where H is ocean depth, ζ is barotropic relative vorticity, $f = 2\Omega sin(\theta)$ is the Coriolis parameter, Ω is Earth's rotation rate, and θ is the latitude. Under approximate geostrophic balance (applicable for large scale ocean circulation), and in the absence of stratification[2], flow is constrained such that barotropic potential vorticity (q) is materially conserved [*McWilliams*, 2006]. In the mesoscale, H often varies much more rapidly in space than f does, hence inducing a stricter constraint. That is due to the mesoscale-like width of topographic features such as continental slopes, mid-ocean ridges, and seamounts [*Talley*, 2011, chapter 2]. Wind stress curl locally forces changes in q. However, the spatial scale of wind stress variation is similar to the basin scale [*Talley*, 2011, chapter 5], hence less directly forcing the mesoscale[3].

Topographic control is immediately apparent in the routes of boundary currents (of widths $\sim$ 100 km), which often quite strictly follow isobaths, and in deep cross-basin flows often restricted to fracture zones [e.g., *Bower et al.*, 2002a; *Talley*, 2011]. Propagation perpendicular to the bottom slope also generally reduces growth rates of linear instabilities [*Blumsack and Gierasch*, 1972; *Mechoso*, 1980], hence improving water retaining and allowing propagation over basin scale distances [4]. The topographic control often appears to break down where isobaths turn abruptly relative to the mesoscale. There boundary currents, or a component of their flow, often sepa-

[2] Stratification generally reduces the influence of H. In some cases the result can be approximated by conservation of a function f/F, where $F = F(H)$ is essentially a smoothed version of H [*Krupitsky et al.*, 1996; *Killworth and Hughes*, 2002].

[3] Note wind stress can have a damping effect on mesoscale vortices [*Renault et al.*, 2016a]

[4] Boundary currents are also predicted in flat rotating basins enclosed by vertical walls [e.g., *Stommel*, 1948]. However, boundary currents in earth's oceans often become unstable where the bottom slope steepens significantly [*Eden and Böning*, 2002; *Bracco and Pedlosky*, 2003; *Wolfe and Cenedese*, 2006; *Trodahl and Isachsen*, 2018]

rate from the boundary and continue to the interior temporarily as a free jet [e.g., *Lutjeharms and Van Ballegooyen*, 1988; *Bower et al.*, 2002b, 2009; *Holliday et al.*, 2009; *Molemaker et al.*, 2015; *Schoonover et al.*, 2017a].

While the effects of topography on mesoscale ocean circulation are readily observed, and well understood in many scenarios, many open questions remain, of practical and scientific importance. A general theory of mesoscale boundary current separation does not exist, often not even in particularly well-studied specific cases, such as Gulf Stream separation at Cape Hatteras [*Chassignet and Marshall*, 2008; *Schoonover et al.*, 2017b]. In comparison, boundary current instability is a more mature subject. However, important open questions remain there as well. For example, while moderate bottom slopes tend to reduce baroclinic instability relative to flat bottom cases, high slopes can cause higher instability in some (but not all) cases. Several competing theories were previously suggested for increased instability with high slopes [as summarized in *Isachsen*, 2011; *Trodahl and Isachsen*, 2018]. Additionally, application of linear instability theory to realistic cases where bathymetry and currents do not follow a simple geometry (e.g., approximate homogeneity along a horizontal axis) remains challenging. Practically, calculations are often done in a "local approximation", neglecting the horizontal in-homogeneity [*Tulloch et al.*, 2011].

This dissertation is comprised of three distinct studies in which topography plays a key role in determining mesoscale ocean circulation. The rest of this chapter gives background information to each project, and explains the connections between them. Section 1.2 is an introduction (relevant to chapters 2-3) to the physical oceanography of the Atlantic Meridional Overturning Circulation (AMOC), the leakiness of its deep southward-flowing boundary current, and their climatological effects. Section 1.3 introduces chapter 2, an idealized study of of boundary current instability motivated by the observed leakiness. Section 1.4 introduces chapter 3, analysis the boundary current leakiness in a realistic regional numerical model and in historical observational datasets. Chapter 4, introduced in section 1.5, is independent of the previous two studies. It deals with the spontaneous formation of anticyclonic eddies over topographic depressions. As the following chapters are reproductions of published (or submitted) papers, each has its own stand-alone

introduction section in its chapter. The following sections of the present chapter thus provide a more general, and somewhat less technical introduction for each of the following chapters, regarding their motivating scientific questions and the chosen analysis methods.

1.2 Leakiness of the Deep Western Boundary Current

The first two projects were motivated by observations of the breakdown of topographic control within the Deep Western Boundary Current (DWBC) in the North Atlantic. The DWBC is a boundary current transporting dense water southward. These water masses are formed in a few key locations at high latitudes in convective processes due to severe heat loss to the atmosphere [*Talley*, 2011; *Bullister et al.*, 2013]. Their southward transport is associated with a compensating northward transport of warm equatorial surface water. This large-scale overturning circulation is known as the Atlantic Meridional Overturning Circulation (AMOC)[5].

The AMOC is a circulation pattern of great climatic significance. Its northward transport near the surface is responsible for a substantial fraction (e.g., $\approx$ 15% at 40N) of the global atmosphere-ocean system meridional heat transport [*Johns et al.*, 2011; *Trenberth and Fasullo*, 2017]. The meridional heat transport is spatially complex, which (among other results) contributes to the advection of warm subtropical surface (mixed layer) waters mainly to the east rather than west subpolar North Atlantic ocean, and thus also to more moderate west European winters compared to the North American east coast [*Burkholder and Lozier*, 2014]. The deep convection centers and the AMOC bottom cell are responsible for capturing large amounts of atmospheric CO_2 [*Takahashi et al.*, 2009; *Khatiwala et al.*, 2013; *Gruber et al.*, 2019] into the abyssal ocean, and for storing them for periods as long as centuries [*Matsumoto*, 2007; *Gebbie and Huybers*, 2012], serving as a climate change buffer in regards to this greenhouse gas, as well as other anthropogenic gases [e.g, *Pickart et al.*, 1989; *Rhein et al.*, 2015].

[5] Sometimes this name is used for the zonally averaged (within the Atlantic) circulation.

The DWBC was previously considered a principle southward conduit for the intermediate and deep water masses formed in the subpolar North Atlantic. However, as DWBC observations have accumulated over recent decades, it became clearer that the deep (southward) AMOC branch is considerably more complicated [*Bower et al.*, 2011; *Lozier*, 2012]. Passive tracer observations (using dynamically passive anthropogenic gases and trace atomic bomb radioactive materials: e.g., CFCs, CFMs, and Tritium) have shown that significant dilution of these water masses occurs along the southward trajectory, and that the dilution is not uniformly distributed [*Rhein et al.*, 2002; *Gary et al.*, 2012; *Le Bras et al.*, 2017]. In deployments of floats (passively drifting at a preset depth) within the DWBC in the subpolar North Atlantic, most floats have been ejected out from the current within the Newfoundland Basin [*Lavender et al.*, 2000; *Fischer and Schott*, 2002; *Bower et al.*, 2009]. Only a small fraction has continuously followed the current beyond this region to subtropical latitudes. Thus this region has been implicated as a particularly "leaky" region of the DWBC.

Furthermore, a significant fraction of the leaked floats have continued southwards within the ocean interior (i.e., outside of the boundary current), in what came to be known as "interior pathways" (IP). The importance of IP is that they are a deep AMOC path southwards, alternative (and additional) to the DWBC. Given the significance of the AMOC to the climate system (as described above), it is also important to clarify the trajectories by which its water mass transport occurs. The delineation of IP, and study of their dynamical reasons, is an ongoing research topic [*Gary et al.*, 2011, 2012; *Lozier et al.*, 2013; *Mertens et al.*, 2014; *Pedlosky*, 2018; *Biló and Johns*, 2018]

However, less focus has previously been devoted to the understanding of the mechanisms causing the initial DWBC leakiness in the Nfl basin (which secondarily leads to IP). The first project described here (chapter 2, introduced in section 1.3 below) was conceived as a theoretical and idealized study into one such potential mechanism, namely, baroclinic instability. In the second project (chapter 3, introduced in section 1.4 below), I analyzed historical observations as well as a realistic regional numerical model (a configuration which I designed and set up), to analyze in detail the mechanism of DWBC leakiness.

1.3 Baroclinic instability on curved isobaths

Time-mean rotating and vertically-sheared (e.g., surface-intensified) flow is associated with sloping density surfaces (isopycnals). The sloping isopycnals in turn are associated with increase in [*Lorenz*, 1955, "available"] potential energy (APE). The APE reservoir of the large scale time-mean ocean circulation (which is strongly influenced by rotation) is thus about 1000 times larger than its kinetic energy, and it has been inferred by several means that the release of APE is the main energy sink of the large scale circulation [*Gill et al.*, 1974; *Smith*, 2007; *Ferrari and Wunsch*, 2009]. The process of APE release to eddy kinetic energy (EKE, manifesting in the ocean essentially as time-varying mesoscale circulation) is termed baroclinic instability (BCI).

Linear baroclinic instability theory is by now a classic topic in geophysical fluid dynamics [*Charney*, 1990; *Eady*, 1949; *Phillips*, 1951; *Pedlosky*, 1987]. In many cases the linear theory has quantitative explanatory power for the observed variability of mean ocean (and atmosphere) circulation patterns such as boundary currents [e.g., *Smith*, 1976; *Mysak and Schott*, 1977; *Sherwin et al.*, 2006; *Poulin et al.*, 2014].

Given the ubiquitous importance of BCI for large scale ocean circulation, it is plausible that the observed leakiness of the DWBC (section 1.2) is the result of enhanced BCI within the Newfoundland basin. The float observations of [*Bower et al.*, 2009] have shown that much of the leakiness is concentrated around the convex areas of underwater capes along trajectory of the DWBC in the Newfoundland basin. Therefore, we embarked on a study of the effect on BCI, of isobath and mean flow (horizontal) curvature. The study [*Solodoch et al.*, 2016] is reproduced in chapter 2. We have chosen an idealized mean flow configuration, rather than one specifically based on the DWBC, with the goal of understanding the aforementioned effects in a general setting. The investigation, by analytical and numerical linear instability calculations, derives instability criteria and growth rates in several idealized cases, and compares results of rectilinear vs curved isobaths and mean flow. Possible implications to DWBC leakiness are discussed.

1.4 DWBC leakiness in a realistic regional numerical model

Given ambiguity in the implications of the results of chapter 2 to DWBC leakiness, and given the great complexity of the Newfoundland circulation system, it was considered necessary to conduct a realistic numerical simulation of the region. The circulation includes, additionally to the DWBC, a northward going surface-intensified boundary current further offshore (the North Atlantic Current, NAC), and multiple recirculation gyres [*Lavender et al.*, 2005]. Variability (EKE) is quite heightened in the vicinity of the boundary currents. The bathymetry in the Newfoundland Basin DWBC path is also quite complex, as described above. Distinguishing various possible causes of leakiness is difficult in the face of these intricate patterns, without detailed datasets. Given that the DWBC is a bottom-intensified current, and given the relative remoteness of the region, observational data is sparse, as it is over most of the ocean. Therefore we concluded that a realistic numerical simulation was the best way forward in this case.

A regional configuration (hereafter GB_B) of ROMS [*Shchepetkin and McWilliams*, 2005], a primitive equations (PE) numerical ocean model was designed and run, spanning the Newfoundland Basin, and a large part of the surrounding North Atlantic Ocean. The model, its validation, and its analysis in regards to DWBC leakiness, are described in [*Solodoch et al.*, 2020a], and reproduced in chapter 3 here.

The analytical approximations made in the PE, hydrostatic balance and Boussinesq approximation, are an excellent approximation in the mesoscale [*McWilliams*, 2006]. The horizontal (2 km) and vertical resolution (50 layers) well resolved the mesoscale, and perhaps penetrated the submesoscale regime. An observations-based bahtymetric product, and an (observations-constrained) atmospheric reanalysis were used in the ROMS GB_B configuration. The latter was used in the determination of surface thermodynamic fluxes and wind stress. The implementation and the main numerical parameterizations used (e.g., vertical mixing operators) are described in detail in chapter 3.

The model was validated using freely available historic observations of the region. It compares well qualitatively and quantitatively with the main regional circulation patterns. Several biases do occur and are explored as well. Furthermore, we use the historical observations to validate the analysis of leakiness phenomenology in the model.

We investigate both the phenomenology of the leakiness and its dynamical mechanisms. The former are addressed based on the model results as well as the historical observational datasets. The numerical results are analyzed in both Lagrangian and Eulerian perspectives. The former is useful since leakiness is in many ways a Lagrangian phenomenon, as even the time-mean circulation is not homogeneous. A particle advection code was developed and used to create numerical "float" trajectories (starting) from the DWBC, based on GB_B model velocities. The numerical Lagrangian experiments were modeled after the oceanic float experiments that delineated the DWBC leakiness and interior pathways (section 1.2).

The dynamics are investigated within the model based on energy transformations, and potential vorticity budget. Additionally, the comparison of Eulerian and Lagrangian circulation metrics, allows drawing conclusions on the magnitude and local importance of eddy rectification. The analysis results are compared with several previously suggested causes of leakiness, including our own [*Solodoch et al.*, 2016]. The possibility that loss of topographic control occurs due to variations in the along isobath steepness and curvature, is considered as well. Finally, a simple and rough scaling relation is suggested to examine the latter possibility.

1.5 Formation of Anticyclones above topographic depressions

In several North-Atlantic basins and seas, a semi-stationary anticyclonic vortex has been observed repeatably for decades. That includes the Lofoten Basin Eddy [*Köhl*, 2007], the Rockall Trough Eddy [*Le Corre et al.*, 2019a], the Mann Eddy of the Newfoundland Basin [*Mann*, 1967], and

the Iceland Basin repeated AC observations [e.g., *Martin et al.*, 1998]. In each of these regions, the anticyclone occurs within bowl-like topographic depressions, with steep slopes in the basin periphery, and a relatively flat interior region. These basins are all of importance to AMOC transport and/or AMOC related water mass conversions.

Additionally to the topographic similarity between these basins, they all reside in the North Atlantic sub-polar region, where stratification is relatively weak and Coriolis force relatively strong, hence increasing the potential impact of topography on mesoscale circulation. Several previous investigations have attributed various formation and sustenance mechanism in each case above, involving various manifestations of topographic effects (chapter 4), based on regional numerical simulations or observations. We therefore conducted idealized simulations based on the common denominator in the different basins, i.e., bowl like topography and (although not exclusively in our simulations) weak stratification. The idealized modeling allows exploring parameter sensitivities of the emergent circulation patterns, to constrain the limits of validity of contributing mechanisms. The model solves the primitive equations with one or two isopycnal layers. The former allows investigation of depth-independent circulation, maximally sensitive to the topography. The latter allows coarse probing of depth-dependence effects.

We conduct a large array of experiments varying relevant bathymetric and circulation parameters. The emergence of a bowl-trapped anticyclone is studied to identify and quantify the mechanisms of formation and its controlling parameters. The robustness and long term evolution of the circulation is studied as well. The relation of emergent ACs to boundary currents in the model is examined as well using a vorticity budget. Depth dependence of the emergent anticyclone is probed using two-layer experiment. Possible implications of the results for the observed recurrent ocean ACs are discussed. Additionally, the results are contrasted with previous theories of topographic turbulence, where some differences are found.

CHAPTER 2

Baroclinic Instability Of Axially-Symmetric Flow Over Sloping Bathymetry

2.1 Introduction

Baroclinic instability is one of the main energy conversion processes to and from the mesoscale in the ocean [*McWilliams*, 2008]. The baroclinic source of energy, available potential energy due to tilting of isopycnals (constant density surfaces), is ubiquitous. Studies based on high-resolution altimetry [*Chelton et al.*, 2011] reveal that virtually all areas of the world's oceans are sources of mesoscale eddies, and therefore may be baroclinically unstable. A few of the many roles mesoscale eddies play in the ocean are: supporting the forward and inverse turbulent energy cascades, relaxing isopycnal slopes and thus restratifying the ocean, vertical transfer of momentum via the eddy form stress and transport, and ventilation and subdaction of tracers [*McWilliams*, 2008; *Dong et al.*, 2014].

Baroclinic eddy variability peaks in the ocean near strong persistent currents [*Chelton et al.*, 2011], such as large boundary currents (e.g., the Gulf Stream). The task of measuring and characterizing eddy generation mechanisms is more challenging for deep (sub-surface intensified) boundary currents, since they are much less amenable to remote sensing, and since even after decades of oceanographic expeditions, in situ measurements are quite sparse. A prominent example is the variability associated with the Deep Western Boundary Current (DWBC) in the Grand Banks (GB)

area, where eddy shedding and interior flow pathways are prevalent, as observational campaigns using deep Lagrangian floats have revealed [*Lavender et al.*, 2000, 2005; *Bower et al.*, 2009].

The data presented in *Bower et al.* [2009] suggest that the horizontally curving slopes around the GB and Flemish Cap (FC) are associated with increased eddy generation relative to less curved portions. The curvature, convex or concave, we refer to is of isobaths, horizontal lines of constant bottom depth. Thus "underwater capes" such as GBs and FC, are convex, while the area between them is concave. Arguably, the data also visually suggest greater eddy generation at convex sections of the continental slope than at concave sections. Their figure 1 suggests that nearly all floats cross the 4000 meter isobath off-shore after drifting south to FC (where the continental slope is convex), most of which do not return to the DWBC further downstream. The few floats that remain shoreward of the 4000 meter isobath, do not drift significantly further offshore until they reach the next convex segment, the GB. In the GB area more floats are shed from the continental slope and cross the 4000 meter isobath. *Lavender et al.* [2005] found similar loss of floats to the interior ocean at the vicinity of FC, as well as a maximum in eddy kinetic energy there. Since the floats are generally drifting with the (baroclinic) DWBC, these findings raise the possibility that the influence of coastal curvature on baroclinic instability could explain the localization of eddy generation around FC and GB. There are many dynamically similar examples of boundary currents leaking around convex continental slopes, such as the Mediterranean Overflow Water, which sheds Submesoscale-Coherent Vortices as it propagates around the Iberian peninsula [*McDowell and Rossby*, 1978; *McWilliams*, 1985; *Bower et al.*, 1997]. The California Undercurrent also sheds submesoscale eddies at convex bends, for example at the mouth of Monterey Bay [*Stegmann and Schwing*, 2007; *Molemaker et al.*, 2015].

To study the influence of horizontal curvature in a controlled setting, we employ a model of minimal complexity that admits baroclinic instability, a 2-layer quasi-geostrophic (QG) model, in an annular channel. This model is a geometric variant of the straight-channel 2-layer QG model presented in *Pedlosky* [1964]. The case of linear baroclinic instability in horizontally-uniform QG flow over a flat bottom was solved by *Phillips* [1951] with 2 vertical layers and by *Eady* [1949] with a

continuous vertical coordinate. *Blumsack and Gierasch* [1972] extended the Eady model to include a sloping bottom boundary. *Mechoso* [1980] similarly extended the Phillips model, and systematically investigated the influence of a sloping bottom boundary in both models. *Pedlosky* [1964] derived integral stability constraints for instability, for a more general family of straight channel flows over sloping bathymetry. Multiple investigators found that linear 2-layer baroclinic instability models compared well with observed variability in boundary currents over continental slopes in various regions, including the Denmark Straight Overflow [*Smith*, 1976], the Norwegian Current [*Mysak and Schott*, 1977], and the Färoe-Shetland flow [*Sherwin et al.*, 2006]. Phase speeds and wavelengths were within $\sim$ 30% of observed values, and eigenmode structures were qualitatively similar to those derived from observations. Other authors have attempted to incorporate this theory into eddy parameterizations over continental slopes [*Stipa*, 2004a; *Isachsen*, 2011].

Choboter and Swaters [2000] used a non-QG asymptotic derivation to analyze the baroclinic instability of a double-frontal dense water layer over sloping topography in an annulus. Their explicit solutions are for a relatively narrow (1.5 Rossby radii apart at the bottom) coupled front on the bottom of an otherwise stationary fluid, whereas we investigate wider and more horizontally-uniform 2-layer flows here. Since we model wider currents, we use the approximation that isopycnals do not intersect the bathymetry, consistent with the QG approximation. In addition, our focus here is deducing the influence of horizontal curvature on the instability, whereas *Choboter and Swaters* [2000] aimed to compare an existing theory for rectilinear bottom-trapped flow against laboratory experiments in a rotating tank.

A key measure of the effect of bathymetry on baroclinic instability is the ratio of the bathymetric slope to the mean isopycnal slope (hereafter δ, see also figure 2.1, and §2.2.4). *Blumsack and Gierasch* [1972] found that the wavelength of the most rapidly growing mode was lower (higher) for negative (positive) δ, compared to the wavelength at $\delta = 0$, and that the mean flow was stable to all disturbances for $\delta > 1$. *Mechoso* [1980] reported the same result for the analogous case in a 2-layer model. *Isachsen* [2011] used δ to characterize the topographic regime in both Eady model calculations and in nonlinear three-dimensional simulations. We similarly use δ throughout this

paper to quantify the influence of the topographic slope.

The outline of this paper is as follows. In §2.2 we present the model, and in §2.3 we derive integral theorems that constrain the growth rates and phase speeds of unstable waves. In §2.4 we apply the model to investigate instability of solid-body rotation over parabolic bathymetry, and establish a close analogy with straight channel uniform flow over linear bathymetry (supplemental section 2.8.2, hereafter uniform rectilinear flow). In §2.5 we similarly, and in more detail, investigate instability of uniform azimuthal flow in an annulus over linear bathymetry. In §2.6 we discuss the essential factors, independent of channel geometry, that make uniform rectilinear flow and solid body rotation similar and uniform azimuthal flow quite different. We briefly discuss a few other experiments in support of the generality of these factors and their influence on baroclinic instability. In §2.7 we discuss our results and their relevance to the stability of oceanic boundary currents.

2.2 Linear model of baroclinic growth in an annular channel

A schematic drawing of the domain and model is shown in figure 2.1. We model a horizontally-curved continental slope as an annular channel, in which the walls represent the shoreward and offshore extents of a baroclinic slope-trapped current. We model the mean current as a 2-layer axisymmetric azimuthal flow, a minimal discrete approximation to a continuous density stratification. We prescribe different geostrophic mean velocities in each layer, creating a vertical shear and thus allowing the possibility of baroclinic instability. The vertical axis is denoted by z, and the reference frame is assumed to revolve around that axis to imitate the earth's rotation (§2.2.1).

2.2.1 Quasi-geostrophic model equations in cylindrical coordinates

In this section we present the QG potential vorticity (PV) and energy equations for axially symmetric mean flow and bathymetry. Quasigeostrophy is an approximation to fluid flow in a rotating reference frame, which is often a good approximation for synoptic scale oceanic flows (oceanic mesoscale), i.e., with characteristic lengthscales comparable with the Rossby radius of deformation, defined below [*Pedlosky*, 1987]. The necessarily small parameter in the approximation is the Rossby number $\mathrm{Ro} = U/fX \ll 1$, where f is the Coriolis parameter, U the velocity scale and X the horizontal lengthscale. In these cases the Coriolis force approximately balances the pressure gradient, and to first order in Ro, the evolution of the flow field is given by the QG PV equations. The QG approximation also requires the bathymetry and isopycnals to exhibit small variations relative to their respective domain-wide averages. While these conditions are not necessarily satisfied over continental slopes, previous studies suggest that QG captures the essential features of large-scale flows over topographic steepnesses typical of the ocean's continental slopes [*Williams et al.*, 2010; *Stewart et al.*, 2011, 2014; *Poulin et al.*, 2014; *Stern et al.*, 2015].

We use the f-plane approximation [*Pedlosky*, 1987], in which the reference frame revolves around the vertical axis with the same rate everywhere in the domain, neglecting the effect of the Earth's curvature on the Coriolis acceleration. This isolates the effect of continental slope curvature, and thereby simplifies our analysis. This is partially justified by the fact that, dynamically, a topographic gradient induces a similar dynamical effect on rotating flow as does the latitudinal gradient of the rotation rate. This so-called topographic β effect is usually much larger than the planetary β effect in the local dynamics of slope-trapped currents.

We write the 2-layer QG PV equations [*Pedlosky*, 1964] in cylindrical coordinates,

$$\left[\frac{\partial}{\partial\tilde{t}} + \tilde{u}_{1r}\frac{\partial}{\partial\tilde{r}} + \frac{\tilde{u}_{1\phi}}{\tilde{r}}\frac{\partial}{\partial\tilde{\phi}}\right]\left[\tilde{\nabla}^2\tilde{\psi}_1 - \frac{1}{L_1^2}(\tilde{\psi}_1 - \tilde{\psi}_2)\right] = 0, \tag{2.1a}$$

$$\left[\frac{\partial}{\partial\tilde{t}} + \tilde{u}_{2r}\frac{\partial}{\partial\tilde{r}} + \frac{\tilde{u}_{2\phi}}{\tilde{r}}\frac{\partial}{\partial\tilde{\phi}}\right]\left[\tilde{\nabla}^2\tilde{\psi}_2 - \frac{1}{L_2^2}\left(\tilde{\psi}_2 - \tilde{\psi}_1 - \frac{g'}{f_0}\tilde{\eta}_b\right)\right] = 0. \tag{2.1b}$$

The upper and lower layer variables are denoted by the subscripts 1 and 2 respectively. Tildes

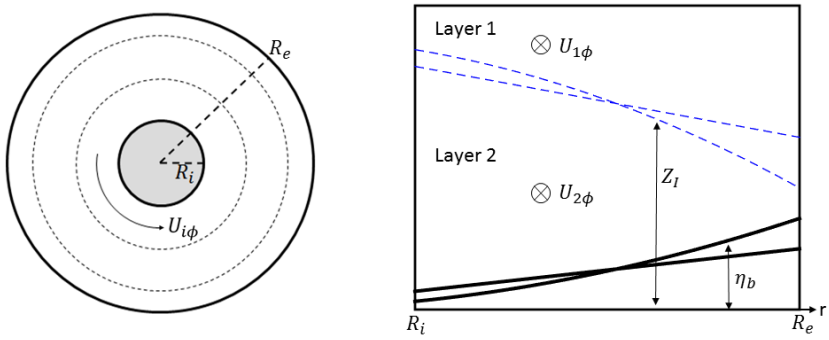

Figure 2.1: Schematic drawing of the domain boundaries, bathymetry and mean circulation. (left) Top-down view of the annular channel, with dashed lines representing isobaths or mean streamlines. (right) Along-slope view of the mean flow configuration. The dashed line represents the isopycnal profile $z = Z_I(r)$, the interface between the two fluid layers. Two particular bathymetry ($\eta_b(r)$) and isopycnal profile pairs are plotted here, linear and parabolic in r, corresponding to uniform azimuthal flow and solid body rotation, respectively. The isopycnal and bathymetric profiles for uniform rectilinear flow are identical to those of uniform azimuthal flow, i.e., linear in the cross-channel coordinate. A rigid lid is assumed, consistent with stratified quasi-geostrophy. The δ parameter, i.e., ratio of bathymetric to isopycnal slopes, is negative in both specific cases displayed here, although both signs are considered in this study.

are used since we will later nondimensionalize the equations and use variables without tildes. The annular channel interior and exterior radii are denoted by $\tilde{R}_i$ and $\tilde{R}_e$ respectively. The radial ($\tilde{r}$) and azimuthal ($\tilde{\phi}$) velocity components are related to the streamfunction $\tilde{\psi}_j$ by $\left(\tilde{u}_{jr},\, \tilde{u}_{j\phi}\right) = \left(-\tilde{r}^{-1}\partial\tilde{\psi}_j/\partial\tilde{\phi},\, \partial\tilde{\psi}_j/\partial\tilde{r}\right)$. Vorticity $\tilde{\zeta}_j$ is related to the streamfunction by $\tilde{\zeta}_j = \tilde{\nabla}^2\tilde{\psi}_j$. Other parameters include the gravitational acceleration g, the density ρ_j, the reduced gravity $g' = g\frac{\rho_2-\rho_1}{\rho_1}$, the average layer thicknesses H_j, the reference Coriolis parameter f_0, the Rossby radii of deformation $L_j = \sqrt{g'H_j}/f_0$, and the bottom elevation $\tilde{\eta}_b(\tilde{r})$. For boundary conditions, we require that there be no flow normal to the inner and outer walls, $\partial\tilde{\psi}_j/\partial\tilde{\phi} = 0\,|_{\tilde{r}=\tilde{R}_i,\tilde{R}_e}$.

To study the instability of currents flowing parallel to the bathymetric isobaths, we assume a

geostrophic, axially-symmetric, azimuthal mean flow $\tilde{U}_{j\phi}(\tilde{r}) = \partial\overline{\tilde{\psi}}_j/\partial\tilde{r}$. This is an exact steady solution of (2.1a)–(2.1b). We partition the streamfunction into mean and perturbation components, $\overline{\tilde{\psi}}_j$ and $\tilde{\psi}'_j$ respectively. Linearizing the QG PV equations (2.1a)–(2.1b) yields a linear system of equations for the perturbation streamfunctions,

$$\left[\frac{\partial}{\partial\tilde{t}} + \frac{\tilde{U}_{1\phi}}{\tilde{r}}\frac{\partial}{\partial\tilde{\phi}}\right]\left[\tilde{\nabla}^2\tilde{\psi}'_1 - \frac{1}{L_1^2}(\tilde{\psi}'_1 - \tilde{\psi}'_2)\right] - \frac{1}{\tilde{r}}\frac{\partial\tilde{\psi}'_1}{\partial\tilde{\phi}}\frac{\partial\tilde{Q}_1}{\partial\tilde{r}} = 0, \tag{2.2a}$$

$$\left[\frac{\partial}{\partial\tilde{t}} + \frac{\tilde{U}_{2\phi}}{\tilde{r}}\frac{\partial}{\partial\tilde{\phi}}\right]\left[\tilde{\nabla}^2\tilde{\psi}'_2 - \frac{1}{L_2^2}(\tilde{\psi}'_2 - \tilde{\psi}'_1)\right] - \frac{1}{\tilde{r}}\frac{\partial\tilde{\psi}'_2}{\partial\tilde{\phi}}\frac{\partial\tilde{Q}_2}{\partial\tilde{r}} = 0, \tag{2.2b}$$

$$\tilde{Q}_j = \tilde{\nabla}^2\overline{\tilde{\psi}}_j - \frac{1}{L_j^2}\left[(-1)^j\left(\overline{\tilde{\psi}}_2 - \overline{\tilde{\psi}}_1\right) - \Delta_{j2}\frac{g'}{f_0}\tilde{\eta}_b\right]. \tag{2.2c}$$

Here $\Delta_{j2} = 0, 1$ for $j = 1, 2$ respectively.

The model describes a concave (convex) continental slope is if $\tilde{\eta}_b(\tilde{r})$ is monotonically increasing (decreasing) with radius. A given convex (concave) along-slope flow can be transformed to the analogous concave (convex) along-slope flow by a radial reflection $P(\tilde{r} - \tilde{R}_i) \to P(\tilde{R}_e - \tilde{r})$, for any scalar radial property $P(\tilde{r} - \tilde{R}_i)$ of the mean state, such as bathymetry $\tilde{\eta}_b(r)$ or isopycnal profile $\tilde{Z}_I(\tilde{r})$.

The baroclinic growth rate in uniform rectilinear flow [*Mechoso*, 1980] peaks close to the wavenumber corresponding to the first baroclinic Rossby radius of deformation. Therefore we non-dimensionalize the equations by scaling $\tilde{r} \sim L$, where

$$L = \sqrt{\frac{g'H_1H_2}{f_0^2\,(H_1 + H_2)}}. \tag{2.3}$$

We denote the velocity scale (to be specified later) by U. The non-dimensional variables are defined by

$$t = (L/U)^{-1}\tilde{t}, \quad U_{j\phi} = U^{-1}\tilde{U}_{j\phi}, \quad \eta_b = (ULf_0/g')^{-1}\tilde{\eta}_b, \quad r = L^{-1}\tilde{r}. \tag{2.4}$$

For notational convenience we also define $F_j = L^2/L_j^2 = 1 - H_j/(H_1 + H_2)$, which measures the fraction of the total depth that is not occupied by layer j. Although F_1 and F_2 are not independent, we shall keep both parameters to preserve some symmetry in the presentation of the equations.

2.2.2 Method of solution

In what follows we drop the prime notation from the perturbation streamfunction for ease of presentation. The eigenvalue problem is derived by decomposing the perturbation streamfunction into normal azimuthal and temporal modes,

$$\psi_j = \mathrm{Re}\left\{\Psi_j(r)\exp(i(m\phi - \sigma t))\right\}. \tag{2.5}$$

The notation Re $\{\}$ indicates the real part of the expression in the curly braces, and $i \equiv \sqrt{-1}$. The azimuthal wavenumber is denoted as m, and σ is the nondimensional complex frequency (dimensional $\tilde{\sigma}$ scales like (U/L) by (2.4)). The real and imaginary parts of σ are the frequency and the growth rate, respectively. The no-normal flow boundary condition (stated above) simplifies to $\Psi_j|_{r=R_i,R_e} = 0$. Writing $\nabla_r^2 = (\frac{\partial}{\partial r} + \frac{1}{r})\frac{\partial}{\partial r}$, the linear vorticity equations (2.2a)–(2.2b) may be simplified as

$$\left[\frac{U_{1\phi}}{r}m - \sigma\right]\left[\nabla_r^2\Psi_1 - \frac{m^2}{r^2}\Psi_1 - F_1(\Psi_1 - \Psi_2)\right] - \frac{m}{r}\Psi_1\frac{\partial Q_1}{\partial r} = 0, \tag{2.6a}$$

$$\left[\frac{U_{2\phi}}{r}m - \sigma\right]\left[\nabla_r^2\Psi_2 - \frac{m^2}{r^2}\Psi_2 - F_2(\Psi_2 - \Psi_1)\right] - \frac{m}{r}\Psi_2\frac{\partial Q_2}{\partial r} = 0, \tag{2.6b}$$

$$\frac{\partial Q_j}{\partial r} = \frac{\partial}{\partial r}\left(\frac{\partial}{\partial r} + \frac{1}{r}\right)U_{j\phi} - F_j(-1)^j\left[\left(U_{2\phi} - U_{1\phi}\right) - \Delta_{j2}\frac{\partial \eta_b}{\partial r}\right]. \tag{2.6c}$$

In most cases presented below we solve the eigenproblem posed by (2.6a)–(2.6c) numerically. We discretize equations (2.6a)–(2.6b) using second-order centered finite differences and solve the resulting matrix eigenvalue problem using the "eig" function in Matlab, which uses the QZ algorithm [*Moler and Stewart*, 1973]. The grid resolution is $dr = 0.025$, giving 40 grid points per Rossby radii, thus resolving well the spatial scales normally associated with QG dynamics. Verification of the numerical setup including convergence tests and comparison with some analytic results are presented in supplemental section 2.8.1. The standard experiment parameters are: $F_1 = F_2 = 1/2$, $R_i = 3$, $R_e = 10$. The chosen channel width $(R_e - R_i)$ is motivated by the widths of deep western boundary currents, which are typically at least a few Rossby radii [*Xu et al.*, 2015; *Stommel and Arons*, 1972]. Similar bathymetric curvature radii (in the range of $3 - 10$ Rossby radii)

are found around the Grand Banks and Flemish Cap. Other parameter ranges and sensitivity tests are discussed in supplemental section 2.8.1.

2.2.3 Energy equation

To study the modes of energy conversion from the mean state to perturbations, we derive the volume-integrated energy equation. The general method is standard [*Pedlosky*, 1987]: multiplying equations (2.2a) and (2.2b) by $D_1\psi_1$ and $D_2\psi_2$ respectively, adding the two resulting equations together, integrating in the entire domain, and using several integrations by parts and the no-normal flow boundary conditions. We defined the relative layer thicknesses D_i, by $D_1 = F_2 = H_1/(H_1 + H_2)$ and $D_2 = F_1 = H_2/(H_1 + H_2)$. In addition, one line integral over the domain boundaries, $\sum_{j=1}^{2} D_j \oint \psi_j' \frac{\partial^2}{\partial t \partial n} \psi_j' ds$ (where n is the normal to the boundary), is required to vanish (McWilliams, 1977, specifically equation 13), for consistency with the analogous asymptotic expansion (in Rossby number) of the Primitive Equations energy balance. The derived energy equation in non-dimensional variables is

$$\frac{\partial}{\partial t} E = \frac{\partial}{\partial t} \left\{ \sum_{j=1}^{2} EKE_j + EPE \right\} = \sum_{j=1}^{2} RS_j + PEC, \tag{2.7a}$$

$$EKE_j = \frac{1}{2} D_j \iint \left(\nabla \psi_j\right)^2 r \, \mathrm{d}r \, \mathrm{d}\theta, \quad EPE = \frac{1}{2} D_1 D_2 \iint \left(\psi_1 - \psi_2\right)^2 r \, \mathrm{d}r \, \mathrm{d}\phi, \tag{2.7b}$$

$$RS_j = D_j \iint \left(r \frac{\partial}{\partial r} \frac{U_{j\phi}}{r} \right) \left(\frac{1}{r} \frac{\partial \psi_j}{\partial \phi} \right) \left(\frac{\partial \psi_j}{\partial r} \right) r \, \mathrm{d}r \, \mathrm{d}\phi \tag{2.7c}$$

$$PEC = D_1 D_2 \iint \left(U_{1\phi} - U_{2\phi}\right) \psi_1 \frac{1}{r} \frac{\partial \psi_2}{\partial \phi} \, r \, \mathrm{d}r \, \mathrm{d}\phi. \tag{2.7d}$$

The energy of perturbations to the mean flow (E) is a sum of the so-called eddy kinetic energy ($\sum EKE_j$) and eddy potential energy (EPE). Thus energy tendency $\partial_t E$ is balanced by the volume-integrated Reynolds Stresses work ($\sum RS_j$) and by Potential Energy Conversion (PEC), i.e., conversion rates from mean kinetic and mean potential energy, respectively [*Pedlosky*, 1987]. When the net perturbation energy tendency (i.e., left hand side of (2.7a)) is positive (i.e, perturbations

grow), we may define a purely baroclinic instability as one where the Reynolds stresses volume-integrated work is zero, as occurs in uniform rectilinear flow [*Pedlosky*, 1987]. We later show that when RS_j do not vanish, they in fact are negative, i.e., decrease the perturbation growth rate in all cases we study here.

Bathymetry does not enter the energy equation explicitly: it does contribute to energy exchange locally, but integrates to zero over the entire domain. The energy equation has zero energy tendency for an azimuthally constant perturbation, and therefore such perturbations are necessarily neutral. RS_j are identically zero when the radial strain,

$$S_r \equiv r\frac{\partial}{\partial r}\frac{U_{j\phi}}{r}, \tag{2.8}$$

is identically zero, which in an annular channel occurs everywhere only for flow in solid-body rotation. Therefore solid body rotation is the only annular flow that has zero Reynolds stresses volume-integrated work for any infinitesimal perturbation. If S_r is nonzero anywhere then there exist many particular $\psi(r,\phi)$ perturbation shapes that make RS_j nonzero.

2.2.4 Mean flow profiles

Throughout this paper we compare our results against the case of uniform flow in a straight channel over linear bathymetry [*Pedlosky*, 1964; *Mechoso*, 1980], which is described in supplemental section 2.8.2. We hereafter refer to this case as uniform rectilinear flow for short. In the annular channel, we investigate in detail two specific configurations of the bathymetry and the mean azimuthal flow. Since the mean flows we prescribe are geostrophic, the isopycnal profile $Z_I(r)$ is determined by the Margules relation [*Cushman-Roisin*, 1994]. In dimensional variables,

$$\tilde{U}_{1\phi} - \tilde{U}_{2\phi} = -\frac{g'}{f}\frac{\partial \tilde{Z}_I}{\partial \tilde{r}}. \tag{2.9}$$

The first case, solid body rotation, is motivated by the fact that both uniform rectilinear flow and solid-body rotation have zero strain rate, defined for solid body rotation by (2.8), and thus

it is a simple starting point from which to study the effect of horizontal curvature. We assume parabolic bathymetry to simplify the analysis, though we later briefly explore linear bathymetry too (see §2.6). Formally, we define our solid body rotation case as

$$U_{j\phi} = \Omega_j r, \quad Z_I \sim -(\Omega_1 - \Omega_2) r^2, \quad \eta_b = \frac{1}{2} p r^2, \tag{2.10}$$

where Ω_j are the constant angular velocities of the flow in each layer, and p is a quadratic coefficient for the bathymetry.

The second case is uniform azimuthal flow, where we assume constant mean azimuthal velocity everywhere. This is similar to uniform rectilinear flow in that the speed is uniform, and the isopycnals are linear in the cross-flow coordinate (r). It is different in that the velocity direction varies, i.e., speed is everywhere azimuthal but the azimuthal direction varies with the azimuthal angle ϕ. We take the bathymetry to be linear as well (as in the uniform rectilinear flow case), though we later briefly explore parabolic bathymetry as well (see §2.6). Formally, we define our uniform azimuthal flow case as

$$U_{j\phi} = \text{constants}, \quad Z_I \sim -(U_{1\phi} - U_{2\phi}) r, \quad \eta_b = br, \tag{2.11}$$

where $U_{1\phi}$ and $U_{2\phi}$ are the azimuthal velocities and b is the linear coefficient for the bathymetry.

We note that in uniform azimuthal velocity R_i cannot be chosen to approach $r = 0$, both because the azimuthal velocity must be zero in the $r \to 0$ limit, and because even before the actual limit, the centrifugal force becomes larger than the Coriolis force, in violation of the QG conditions. The balance between the two forces results in a local Rossby number, $\mathrm{Ro} = U/f\tilde{r} = U/(r\sqrt{g' H_1 H_2/(H_1 + H_2)})$. For example, taking $H_1 = H_2 \approx 500m$, $g' \approx 10^{-3} g$, and $U \approx 0.1 m/s$, we have $r > 1$ (and $R_i > 1$) as an approximate condition for $\mathrm{Ro} = o(1)$. Therefore our choice of $R_i = 3$ (§2.2.2) is also consistent with the QG approximation.

We define the mean vertical rotation rate shear and velocity shear for solid body rotation and for uniform azimuthal flow as follows: $\Omega_s = \Omega_1 - \Omega_2$, and $U_s = U_{1\phi} - U_{2\phi}$, respectively. Motivated by the fact that the baroclinic instability growth rate in uniform rectilinear flow varies linearly

in the vertical velocity shear [*Mechoso*, 1980], we choose the velocity scale $U = L\tilde{\Omega}_s$ for solid body rotation, and $U = \tilde{U}_s$ for uniform azimuthal flow. We assume everywhere that $U > 0$ (and hence $Z_I(r)$ is monotonously decreasing). This assumption is general since we explore both positive and negative δ and can then deduce corresponding results for $U < 0$ results by symmetry (see §2.5.3).

Similarly we define for solid body rotation and uniform azimuthal flow, the barotropic mean rotation rate and velocity as follows: $\Omega_{bt} = \frac{1}{2}(\Omega_1 + \Omega_2)$, and $U_{bt} = \frac{1}{2}(U_{1\phi} + U_{2\phi})$, respectively. In fact Ω_{bt} (or U_{bt}) is exactly the barotropic component only if mean layer thicknesses are equal, but for ease of notation we refer to it as the barotropic component in what follows.

2.3 Integral constraints on baroclinic growth

The classical theorem by *Rayleigh* [1880] on flow instability conditions was adapted by *Pedlosky* [1964] to the straight-channel rotating-baroclinic instability problem. It gives necessary (though not always sufficient) conditions for instability to occur, using only knowledge of the mean flow. Equivalently, the theorem provides a range of values for the physical parameters over which linear perturbations cannot grow. Here we adapt Pedlosky's derivation to the annular channel case, and use it to derive stability bounds for the profiles described in §2.2.4. The derivation and the results remain unchanged if $R_i \to 0$ and also if $R_e \to \infty$, and so are also applicable to other phenomena, e.g., geophysical vortices [*Olson*, 1991; *Paldor and Nof* , 1990; *Dewar and Killworth*, 1995; *Benilov*, 2005].

While qualitatively similar instability theorems have been derived in the literature for a variety of flows [*Pedlosky*, 1970], we were unable to find this derivation or result elsewhere for azimuthal flow (QG or not) over bathymetry with no further constraints (e.g. thin layers, flat bottom). We also derived bounds on the phase speed and on the growth rate (semi-circle theorem, *Pedlosky*

1964) for general annular 2-layer flow, but we defer their presentation to supplemental section 2.8.3.

2.3.1 Derivation of the Rayleigh theorem

Our starting point is the modal PV equations (2.6a)-(2.6b). We define the complex phase speed $c = \sigma/m$, and its real (c_r) and imaginary (c_i) parts. By (2.5), only unstable eigenmodes have a non-zero c_i, so for unstable eigenmodes we may divide the equation for the layer j by $m(U_{j\phi}/r - c)$.

$$\nabla_r^2 \Psi_1 - \frac{m^2}{r^2}\Psi_1 - F_1(\Psi_1 - \Psi_2) - \frac{1}{U_{1\phi} - cr}\Psi_1 \frac{\partial Q_1}{\partial r} = 0, \tag{2.12a}$$

$$\nabla_r^2 \Psi_2 - \frac{m^2}{r^2}\Psi_2 - F_2(\Psi_2 - \Psi_1) - \frac{1}{U_{2\phi} - cr}\Psi_2 \frac{\partial Q_2}{\partial r} = 0. \tag{2.12b}$$

We multiply the first and second of these last two equations by $D_1\Psi_1^*$ and $D_2\Psi_2^*$, respectively (where * denotes complex conjugate), and integrate with the volume element (rdr) between the domain boundaries R_i and R_e. The first (Laplacian) term can be simplified via integration by parts, making use of the boundary conditions $\Psi_j(R_i) = \Psi_j(R_e) = 0$. The result is

$$\int_{R_i}^{R_e} \left[\sum_{j=1}^{2} D_j \left| \frac{\partial}{\partial r}\Psi_j \right|^2 + \sum_{j=1}^{2} D_j \frac{m^2}{r^2} \left|\Psi_j\right|^2 + D_1 D_2 \left|\Psi_1 - \Psi_2\right|^2 \right] r \, \mathrm{d}r + \int_{R_i}^{R_e} \left[\sum_{j=1}^{2} \frac{D_j}{U_{j\phi} - cr} \frac{\partial Q_j}{\partial r} \left|\Psi_j\right|^2 \right] r \, \mathrm{d}r = 0. \tag{2.13}$$

The imaginary part of this expression is

$$c_i \int_{R_i}^{R_e} \sum_{j=1}^{2} \frac{D_j}{\left|U_{j\phi} - cr\right|^2} \frac{\partial Q_j}{\partial r} \left|\Psi_j\right|^2 r^2 \mathrm{d}r = 0. \tag{2.14}$$

For an unstable mode c_i is nonzero, and so the last integral must vanish. Therefore a necessary condition for instability (hereafter, the Rayleigh criterion) is that the mean PV gradient must be somewhere negative and somewhere positive in the domain interior.

Another necessary condition for instability can be found using the real part of (2.13). Substituting (2.14) into (2.13), eliminates ther terms proportional to c_r and c_i, leaving

$$\int_{R_i}^{R_e} \sum_{j=1}^{2} \frac{D_j}{\left|U_{j\phi} - cr\right|^2} \left|\Psi_j\right|^2 \left(U_{j\phi} \frac{\partial Q_j}{\partial r}\right) r \, \mathrm{d}r =$$
$$- \int_{R_i}^{R_e} \left[\sum_{j=1}^{2} D_j \left| \frac{\partial}{\partial r} \Psi_j \right|^2 + \sum_{j=1}^{2} D_j \frac{m^2}{r^2} \left|\Psi_j\right|^2 + D_1 D_2 \left|\Psi_1 - \Psi_2\right|^2 \right] r \, \mathrm{d}r < 0. \tag{2.15}$$

Therefore, another necessary instability condition (hereafter, the Fjortoft criterion) can be stated as: at least one of the products $U_{1\phi} \frac{\partial Q_1}{\partial r}$ and $U_{2\phi} \frac{\partial Q_2}{\partial r}$, must be negative inside at least part of the domain (R_i, R_e).

Both the first and second conditions as phrased here are the same as found in a straight-channel [*Pedlosky*, 1964]. These (straight channel) conditions are used frequently to identify unstable flow regimes in boundary currents, as well as other ocean and atmosphere flow regimes.

2.3.2 Stability bounds for solid-body rotation and uniform azimuthal flow

For solid body rotation, using the same notation as [*Mechoso*, 1980] the ratio between bathymetric slope and isopycnal slope is the bathymetric parameter $\delta = pr/\Omega_s r = p/\Omega_s$. Vorticity is constant and hence the PV gradients are simply

$$\frac{\partial Q_1}{\partial r} = -F_1 r, \quad \frac{\partial Q_2}{\partial r} = F_2 \left(1 - \delta\right) r. \tag{2.16}$$

By the Rayleigh criterion instability is possible only if the PV gradient changes sign, which is seen from (2.16) to occur only if $\delta < 1$, exactly as in uniform rectilinear flow.

For uniform azimuthal flow, in non-dimensional variables, $U_{1\phi} = U_{2\phi} + 1$. The bathymetric parameter is now $\delta = -b$, and from equation (2.6c),

$$\frac{\partial Q_1}{\partial r} = -\frac{1}{r^2}\left(U_{2\phi} + 1\right) - F_1, \quad \frac{\partial Q_2}{\partial r} = -\frac{1}{r^2} U_{2\phi} + F_2 \left(1 - \delta\right). \tag{2.17}$$

Using (2.17) in the instability criteria (§2.3.1), it follows that a necessary condition for instability is that, at least somewhere inside the domain,

$$\delta < \delta_0(r) \equiv 1 - \frac{1}{F_2}\frac{U_{2\phi}}{r^2}. \tag{2.18}$$

Equivalently, a sufficient condition for stability is $\delta > \max(\delta_0)$, similarly to the uniform rectilinear flow case which is stable for $\delta > 1$. Note that $\delta_0 = 1$ exactly if $U_{2\phi} = 0$, and $\delta_0 \approx 1$ if $\frac{1}{F_2}\frac{|U_{2\phi}(r)|}{r^2} = o(1)$. Unlike the case in uniform rectilinear flow, the stability threshold depends on the mean velocity magnitude, i.e., the cutoff bathymetric parameter, δ_0, increases (decreases) for negative (positive) $U_{2\phi}$. As evident from the Rayleigh criterion and from (2.17), the difference is due to the non-zero mean relative vorticity caused by curved streamlines.

We add that for $U_{2\phi} < -1 - F_1 R_i^2$, instability is not prohibited, irrespectively of the δ value, since a PV gradient sign change occurs within a single layer. However, since the mean flow becomes almost barotropic, that regime is less relevant to this study.

2.4 Stability of flows in solid-body rotation

In this section, we investigate baroclinic instability of flow in solid body rotation, and show that it bears strong dynamical similarity to baroclinic instability of uniform rectilinear flow. The isopycnal cross-flow profile for solid-body rotation is parabolic (§2.2.4), and we specifically choose to investigate the flow over a cross-flow profile similar to the isopycnal profile, namely a parabolic bathymetry profile. This simplifies the PV equations significantly, and allows for some analytical results which help with more general interpretation of the physical system. Linear bathymetry does not qualitatively change the results, as discussed in §2.6.

In the solid body rotation case, equations (2.6a)-(2.6b) are,

$$\left[\left(\Omega_{bt}+\frac{1}{2}\right)m-\sigma\right]\left[\nabla_r^2\Psi_1-\frac{m^2}{r^2}\Psi_1-F_1(\Psi_1-\Psi_2)\right]+mF_1\Psi_1=0, \tag{2.19a}$$

$$\left[\left(\Omega_{bt}-\frac{1}{2}\right)m-\sigma\right]\left[\nabla_r^2\Psi_2-\frac{m^2}{r^2}\Psi_2-F_2(\Psi_2-\Psi_1)\right]+mF_2\Psi_2\left[-1+\delta\right]=0. \tag{2.19b}$$

Since Ω_s does not appear explicitly, it follows from the scaling in section 2.2.4 that the dimensional growth rate and frequency depend linearly on the dimensional angular shear $\tilde{\Omega}_s$. In addition, the variables Ω_{bt} and σ appear only together, in the expression $(\Omega_{bt}m-\sigma)\equiv\sigma_0$. Solving (2.19) for σ_0 would correspond to a σ solution Doppler-shifted by $\Omega_{bt}m$. The only effect of the barotropic velocity is a real frequency Doppler-shift, with no influence on growth rate or stream-function structure. Therefore to derive the dispersion relation we may take $\Omega_{bt}=0$, and after deriving it, just Doppler-shift the frequency back by adding to it the term $\Omega_{bt}m$.

The terms in the left brackets may vanish only for neutral modes. In this section we are only interested in modal instability (non-normal growth is covered in §2.5.2) and hence assume that the terms in the left brackets do not vanish and rearrange (2.19) to obtain a pair of coupled Bessel equations,

$$\nabla_r^2\Psi_1-\frac{m^2}{r^2}\Psi_1+\alpha_1\Psi_1+F_1\Psi_2=0, \tag{2.20a}$$

$$\nabla_r^2\Psi_2-\frac{m^2}{r^2}\Psi_2+\alpha_2\Psi_2+F_2\Psi_1=0, \tag{2.20b}$$

$$\alpha_1=F_1\frac{\frac{1}{2}m+\sigma}{\frac{1}{2}m-\sigma},\qquad \alpha_2=F_2\frac{\left(\frac{1}{2}-\delta\right)m-\sigma}{\frac{1}{2}m+\sigma}. \tag{2.20c}$$

The solution can be found in terms of Bessel functions of the first kind J_m and of the second kind Y_m. A complete and orthogonal set of Bessel functions in the radial domain (R_i,R_e) can be found as the solution set of the Bessel equation in the same geometry with Dirichlet boundary conditions. This set is given by $P_m(\mu_i r)$,

$$P_m(\mu r)=J_m(\mu r)-\frac{J_m(\mu R_e)}{Y_m(\mu R_e)}Y_m(\mu r), \tag{2.21}$$

provided that μ_i are determined from

$$J_m(\mu_i R_i)Y_m(\mu_i R_e) - Y_m(\mu_i R_i)J_m(\mu_i R_e) = 0. \tag{2.22}$$

The general solution to (2.20) may be then expanded in the Fourier-Bessel series,

$$\Psi_j = \Sigma_{i=1}^{\infty} A_{j,i} P_m(\mu_i r). \tag{2.23}$$

The amplitudes $A_{j,i}$ are constants. Plugging the general solution (2.23) into (2.20), using the identity that a Bessel function of order m satisfies, $\nabla_r^2 P_m(\mu r) - \frac{m^2}{r^2} P_m(\mu r) = -\mu^2 P_m(\mu r)$, and exploiting the orthogonality of the P_m functions, one finds that the solution (2.23) is consistent, under the following condition on the coefficients of each Bessel function,

$$(\alpha_1 - \mu_i^2)A_{1,i} + F_1 A_{2,i} = 0, \tag{2.24a}$$

$$(\alpha_2 - \mu_i^2)A_{2,i} + F_2 A_{1,i} = 0. \tag{2.24b}$$

Requiring the determinant to disappear we find, after some algebra, the solid body rotation dispersion relation, relating the complex frequency σ to the radial wavenumber-like parameter μ_i,

$$\sigma_i = \Omega_{bt} + m\frac{\mu_i^2 (F_2 - F_1 - F_2\delta) - mF_1F_2\delta + \sqrt{D}}{2\mu_i^4 + 2\mu_i^2 (F_1 + F_2)}, \tag{2.25a}$$

$$\begin{aligned}\frac{D}{m^2} =& \mu_i^8 + (2F_2\delta)\,\mu_i^6 + \left(-4F_1F_2 + 2F_1F_2\delta + F_2^2\delta^2\right)\mu_i^4 \\ &+ \left(-4F_2^2F_1\delta + 2F_2^2F_1\delta^2\right)\mu_i^2 + F_1^2F_2^2\delta^2.\end{aligned} \tag{2.25b}$$

The main result of this section is that the solid body rotation dispersion relation (2.25) is isomorphic to the uniform rectilinear flow dispersion relation (2.31), showing that the dynamics are in some sense identical, although the geometries are different. The mapping between the dispersion relations is symbolic (and simple), with $(\Omega_{bt}, m, \mu) \rightarrow (V_{bt}, l, K)$. Here k, l, $K = \sqrt{k^2 + l^2}$, and V_{bt}, are the uniform rectilinear flow cross-stream, down-stream, total wavenumbers, and mean barotropic velocity, respectively (see supplemental section 2.8.2). Since the dispersion relations are analogous, the dependences of the growth rates and frequencies on the dimensionless parameters are similar, though not identical since the allowed μ_i are determined from (2.22),

while the allowed K are determined from an equation with harmonic functions instead of Bessel functions.

In figure 2.2 we display numerical dispersion curves (growth rates and phase speeds as a function of wavenumber m) for solid body rotation and for uniform rectilinear flow, setting $\delta = -0.2$ for the purpose of illustration. We normalize the azimuthal wavenumber by the mean radial coordinate $R = (R_1+R_2)/2$, $\hat{m} = m/R$ to provide an approximate analogue of the Cartesian wavenumber in uniform rectilinear flow. The uniform rectilinear flow and solid body rotation curves are very close to each other, and the main qualitative features are identical for both cases: (i) two eigenmodes exist in each case (for other δ values either 1 or 2 eigenmodes but no more exist per downstream wavenumber). (ii) The global maximum in growth rate occurs at a wavenumber slightly smaller than 1 (in dimensional variables $l \approx 1/L$). (iii) The phase speed has the opposite sign to δ. This is in fact true for all δ values and is explained by a resonance condition [*Pichevin*, 1998] with topographic Rossby waves (which propagate with shallow water to their right in the northern hemisphere). Panels (c) and (d) show a typical first (fastest growing) eigenmode streamfunction for solid body rotation. The streamfunction is centered in the channel, and no mean horizontal tilt (relative to the cross-stream direction) is present in the circulation cells. The second fastest growing eigenmodes (not shown) have two periods in the radial axis, rather than one as the first mode, and are generally similar to the first mode in that they have no horizontal tilt.

Figure 2.3b shows the solid body rotation growth rate as a function of both m and δ. Again, the growth rate values are almost identical to the uniform rectilinear flow case (figure 2.3a). We also confirmed numerically that (as in uniform rectilinear flow) there is no growth rate dependence on barotropic velocity. Thus we can summarize the solid body rotation case as follows: (i) The dispersion relation is isomorphic to the previously-derived uniform rectilinear flow dispersion relation, thus demonstrating that the dynamics are essentially identical. The growth rate is independent of the barotropic velocity and linearly dependent on the vertical shear. Thus, (ii) despite different geometries (affecting the boundary conditions) in solid body rotation and in uniform rectilinear flow, the growth rates are very similar (figure 2.3a and b). (iii) Both cases have van-

ishing strain rates and RS_j and are thus pure baroclinic instabilities.

2.5 Stability of uniform azimuthal flow

In this section we explore the stability of uniform azimuthal flow over bathymetry that varies linearly with radius, as defined in §2.2.4.

2.5.1 Normal modes

In figure 2.3, we plot growth rate (GR) as a function of normalized wavenumber $\hat{m}$ and of δ for uniform azimuthal flow (each panel for a different U_{bt} value), and for reference also the GR of the uniform rectilinear flow and solid body rotation cases. Note that at each point in $(\hat{m}, \delta)$ space there may be multiple unstable modes, so we have plotted the growth rate of the most unstable mode in each case. While for zero barotropic flow $U_{bt} = 0$ the growth rate is similar to uniform rectilinear flow, nonzero barotropic velocity results in very different $\mathrm{GR}(\hat{m}, \delta)$ dependence. In contrast, uniform rectilinear flow and solid body rotation have no barotropic velocity dependence. Additional local maxima in $\mathrm{GR}(\hat{m}, \delta)$ appear in uniform azimuthal flow for nonzero barotropic velocity.

The streamfunctions for several unstable uniform azimuthal flow modes are presented in figure 2.4. Two geometrical differences from uniform rectilinear flow and solid body rotation (see examples in figure 2.2) are evident: (a) While in solid body rotation streamfunctions are always centered in the channel, the streamfunctions in uniform azimuthal flow cases with nonzero U_{bt} are shifted off the center of the channel. (b) While in uniform rectilinear flow the streamfunction circulation cells axes are aligned with the radial direction, those in uniform azimuthal flow cases with nonzero U_{bt} are often tilted. Reynolds stress work varies linearly with the strain and the tilts

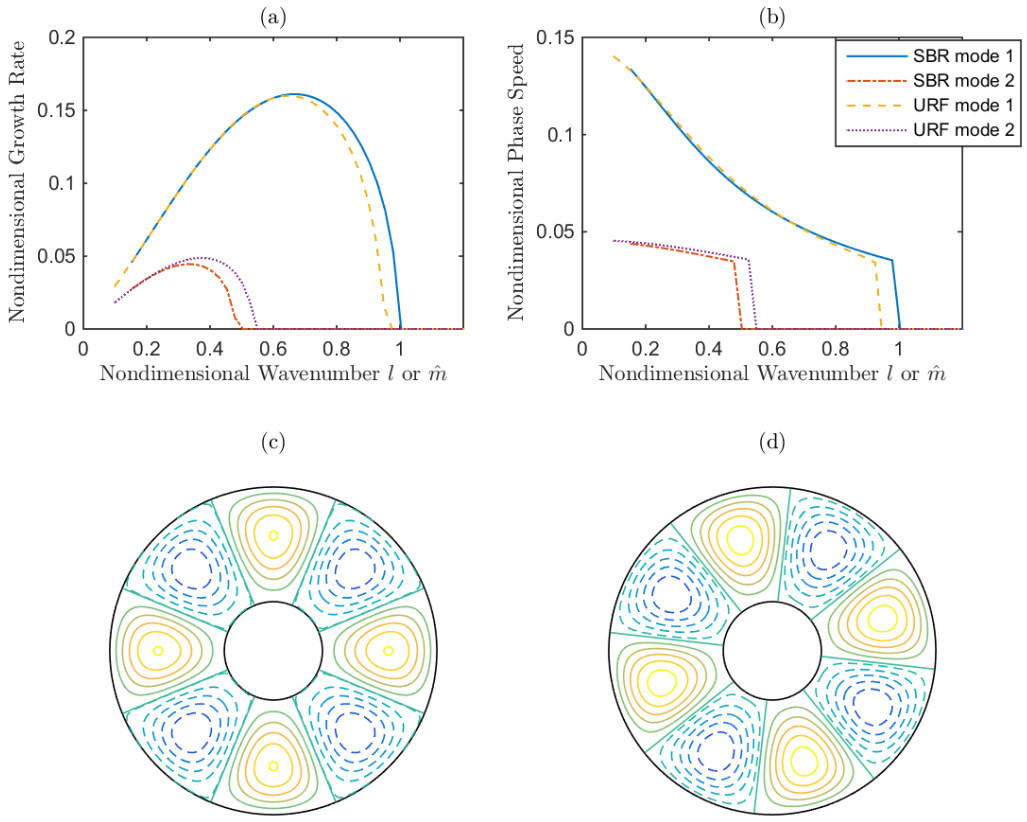

Figure 2.2: Properties of unstable modes for mean solid body rotation over parabolic bathymetry and for mean uniform rectilinear flow over linear bathymetry, with $\delta = -0.2$ in both cases. (a) Growth rate vs wavenumber and (b) phase velocity vs wavenumber (all dimensionless). In both cases two independent eigenmodes are found. The first (second) mode is presented with solid and dashed/dotted lines for solid body rotation (SBR) and uniform rectilinear flow (URF), respectively. The abscissa is downstream Cartesian wavenumber (nondimensional values). In solid body rotation the downstream wavenumber is defined as $l \approx \hat{m} = m/R$. Here m is the azimuthal wavenumber and R is the radius of the channel center. In panel (b) the (real) phase speed is approximately Doppler-corrected and normalized to Cartesian values (for comparison with uniform rectilinear flow) via $\hat{c}_r = c_r R - \Omega_{bt}$. (c,d) Upper and lower layer streamfunctions, respectively, for the first (fastest growing) eigenmode of solid body rotation with wavenumber $m = 4$ ($\hat{m} = 0.615$). The inner and outer circles mark the domain boundaries at $r = R_i$ and R_e, respectively. The lines intercepting the boundaries are the zero contours of the streamfunctions, while positive (negative) streamfunction contours are denoted by full (dashed) closed curves. The absolute value of contours is not given since eigenmode amplitudes are arbitrary unless specified by initial conditions.

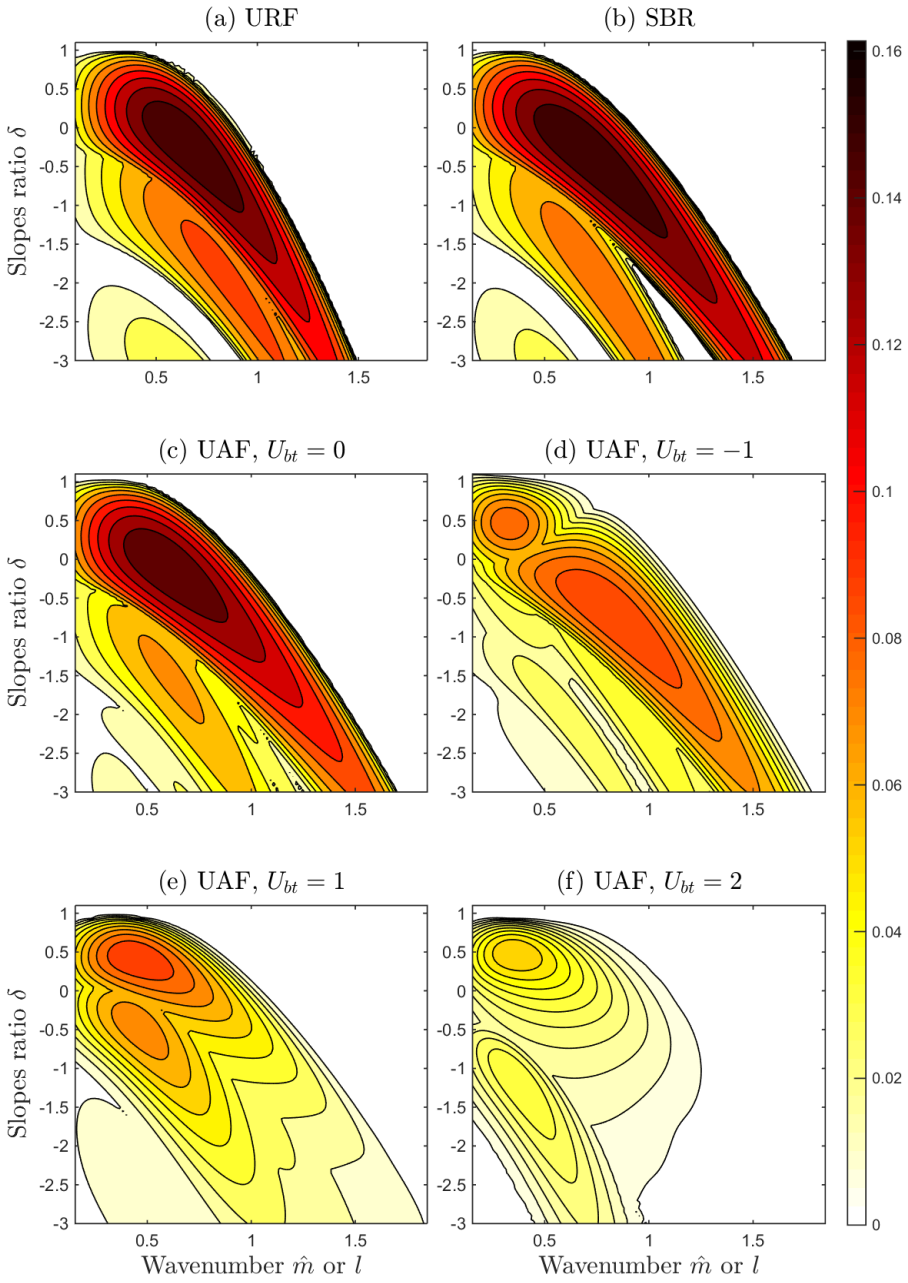

Figure 2.3: Linear growth rates as a function of along-flow wavenumber and the ratio of the bathymetric to isopycnal slopes. All values are non-dimensionalized as described in §2.2.1. Where more than one unstable modes exist, the highest growth rate is shown. (a) Mean uniform rectilinear flow (URF) over linear bathymetry, with wavenumber l. In all other panels the wavenumber is the normalized azimuthal wavenumber $\hat{m}$, defined in §2.4. (b) Mean solid body rotation (SBR) over parabolic bathymetry. (c–f) Mean uniform azimuthal flow (UAF) over linear bathymetry, with with the mean barotropic velocity equal to (c) $U_{bt} = 0$, (d) $U_{bt} = -1$, (e) $U_{bt} = 1$, and (f) $U_{bt} = 2$. In contrast to uniform azimuthal flow, the growth rates in the uniform rectilinear flow and solid body rotation cases do not depend on the barotropic velocity.

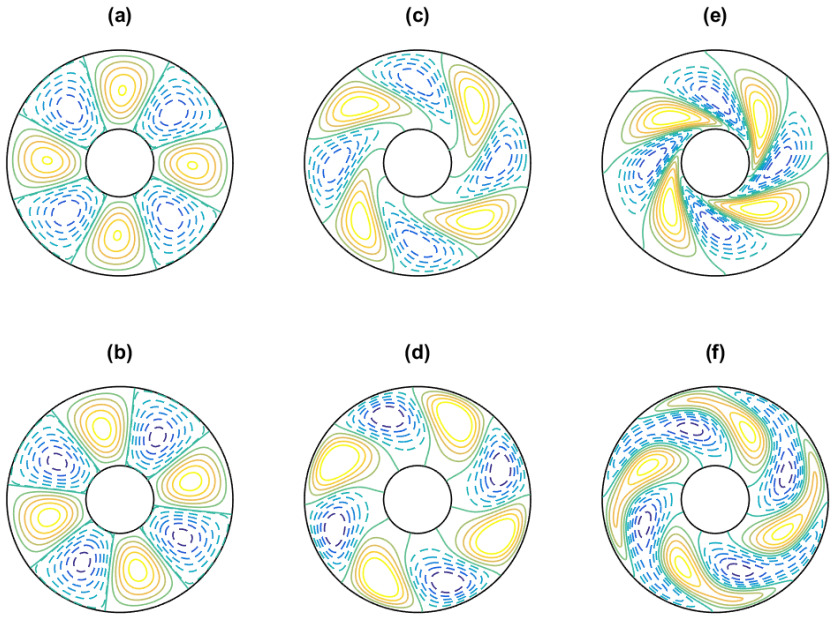

Figure 2.4: Mean uniform azimuthal flow, selected unstable eigenmodes. Upper (lower) layer streamfunctions are shown in the upper (lower) panels. The bathymetric slope parameter is $\delta = -0.2$, and the azimuthal wavenumber is $m = 4$. (a,b) $U_{bt} = 0$, fastest growing eigenmode. (c,d) $U_{bt} = -1$, fastest growing eigenmode. (e,f) $U_{bt} = -1$, third-fastest growing eigenmode. The inner and outer circles mark the domain boundaries at $r = R_i$ and R_e, respectively. The lines intercepting the boundaries are the zero contours of the streamfunctions, while positive (negative) streamfunction contours are denoted by full (dashed) closed curves. The absolute value of contours is not given since eigenmode amplitudes are arbitrary unless specified by initial conditions.

of the circulation axes, and vanishes when the tilt is zero [*Pedlosky*, 1987]. In polar coordinates,

$$RS_j \sim -(S_r)_j \left(\frac{\partial r}{\partial \phi}\right)_{\psi_j} . \tag{2.26}$$

The uniform azimuthal flow streamfunction for the first mode at $U_{bt} = 0$ (left panel) has zero or very small tilt, implying insignificant Reynolds stresses work. The center and right panels (for the first and third eigenmodes with $U_{bt} = -1$) show progressively higher positive tilts, implying higher negative RS_j, since by (2.8) strain rate is positive for constant negative velocity.

The local maxima in the panels (d)-(f) of figure 2.3 are due to changes in the number and character of growing eigenmodes with U_{bt} value. This can be seen in figure 2.5, where we plot several properties for all uniform azimuthal flow growing eigenmodes at $\delta = -0.2$ and $U_{bt} = 1$ (compare with solid body rotation and uniform rectilinear flow, figure 2.2). We find that up to four unstable eigenmodes can co-exist at a given wavenumber, whereas no more than two co-existed for uniform rectilinear flow and solid body rotation. While in uniform rectilinear flow the second mode has considerably lower growth rate than the first, in uniform azimuthal flow they have similar maximum values but still peak at different wavenumbers, thus explaining the multiple maxima observed in figure 2.3 panels (d)-(f). The growth rates of third- and fourth-most unstable modes are considerably smaller. In figure 2.5(c) we plot the eigenmodes' phase speeds, doppler-corrected and normalized via $\hat{c}_r = c_r R - U_{bt}$ to compare approximately with equivalent values in uniform rectilinear flow. While uniform rectilinear flow has waves propagating with shallow water to their right (prograde), in uniform azimuthal flow the second most rapidly growing mode is retrograde, and eigenmodes 3 and 4 have much smaller propagation speeds $\hat{c}_r$.

The middle panel of figure 2.5 shows the ratios of volume-integrated Reynolds stress work ($\Sigma_j RS_j$) to potential energy conversion (PEC), which are negative in all cases. In contrast, uniform rectilinear flow has zero RS_j values in all cases. Thus the uniform azimuthal flow unstable eigenmodes are largely baroclinic modes whose growth rates are somewhat diminished by Reynolds stresses work. The two extra eigenmodes that appear with non-zero barotropic velocity have much higher $\Sigma_j RS_j$ to PEC ratio magnitudes, consistent with their very low growth rates. These results are also consistent with the tilts of streamfunctions shown in figure 2.4, and are qualitatively similar

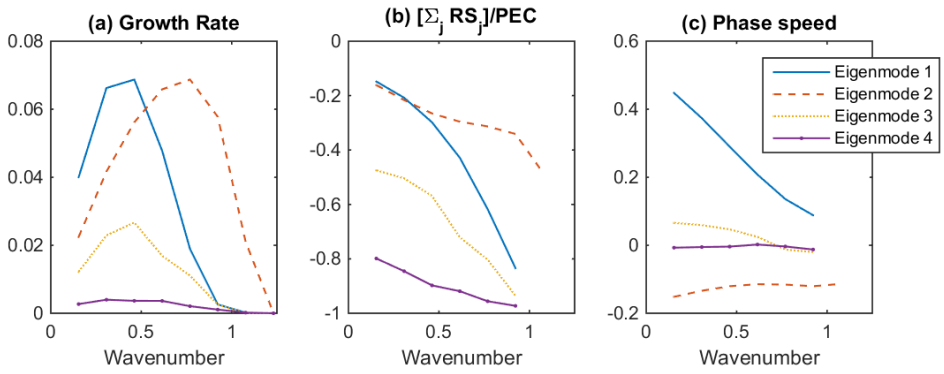

Figure 2.5: Mean uniform azimuthal flow with barotropic velocity $U_{bt} = 1$ and bathymetric to isopycnal slopes ratio $\delta = -0.2$. (a) Growth rate, (b) ratio of Reynolds stresses volume-integrated work to potential energy conversion, and (c) Doppler-corrected Cartesian phase speed vs normalized azimuthal wavenumber $\hat{m} = m/R$, for all growing eigenmodes. In panel (c) the (real) phase speed is Doppler-corrected and normalized to Cartesian values by $\hat{c}_r = c_r R - U_{bt}$, to facilitate comparison with the other mean flow cases (figure 2.2).

for other values of δ, m and U_{bt}. The general reduction in growth rate with $|U_{bt}|$ is thus partially attributed to increase in Reynolds stresses work.

In figure 2.6 (panels a and b) we plot the maximum growth rate over all unstable modes and over all wavenumbers as a function of U_{bt} and δ. Unless $\delta \sim 1$, the growth rate peaks at or close to $U_{bt} = 0$, and is close to peak growth rate for the uniform rectilinear flow case, while lower growth rates are found for non-zero U_{bt}. However, the uniform rectilinear flow instability has a cutoff at $\delta = 1$, whereas the uniform azimuthal flow cutoff depends on U_{bt} and can occur for δ larger than 1, as predicted by the instability criteria derived in §2.3.2. Therefore horizontal curvature decreases eigenmodes' growth rates when U_{bt} is non-zero, unless the isopycnals are approximately parallel to the bathymetry ($\delta \sim 1$) and $U_{bt} < 0$, in which case the curvature destabilizes the flow. Although we report above that Reynolds stresses work is partially responsible for reduction in growth rate (both relative to uniform rectilinear flow and between different uniform azimuthal flow modes), figure 2.6c demonstrates that reduction in potential energy conversion is responsible for a $\sim 2-4$ times larger fraction of the growth rate reduction, than is the $|\Sigma_j RS_j|$ increase.

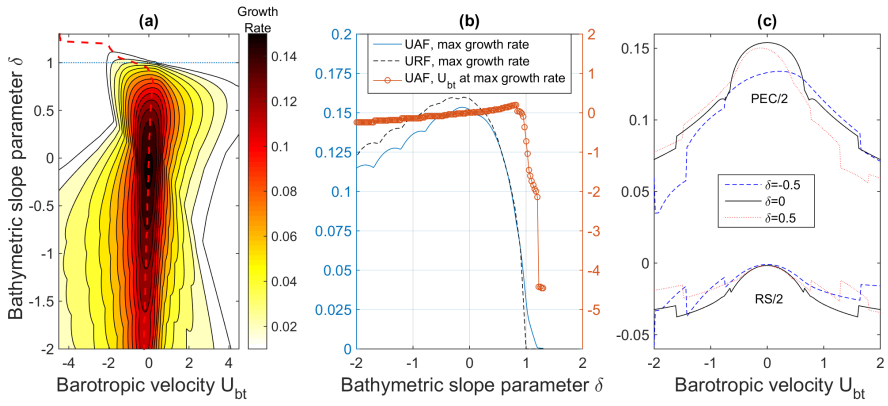

Figure 2.6: (a) Maximum growth rate (filled contours) in the uniform azimuthal flow (UAF) case as a function of the barotropic velocity, U_{bt}, and the ratio of the bathymetric to isopycnal slopes, δ. The dashed line marks the barotropic velocity corresponding to the largest growth rates at each δ. The dotted line marks $\delta = 1$, above which straight channel uniform flow is stable. (b) Maximum uniform azimuthal flow growth rate (full line) and the barotropic velocity at which it is achieved (full line with circles), as a function of δ. The dashed line is maximum growth rate for uniform rectilinear flow (URF). (c) (Half the value of) Potential Energy Conversion (PEC) and Reynolds stresses work ($RS = \Sigma_j RS_j$), for the fastest growing eigenmode, in three different δ values. Discontinuities (as a function of U_{bt}) are expected since $PEC - RS$ distribution changes with m, and since up to four different eigenmodes exist per m.

For an eigenmode, $GR = (PEC + \Sigma_j RS_j)/2$ and hence the changes in growth rate are proportional to changes in PEC and RS_j. Generally PEC decreases monotonously with $|U_{bt}|$, thus supporting the barotropic governor effect interpretation, given below.

Reduction in baroclinic growth rate in the presence of lateral barotropic shear is a somewhat general phenomenon, often called barotropic governor effect [*James and Gray*, 1986; *James*, 1987]. *James* [1987] attributes the effect to the horizontal shear of advection. To remain in phase in the cross-flow direction in the presence of advective shear, the unstable eigenmodes are tilted in the horizontal plane and have a reduced cross-flow extent. These circulation features make the unstable eigenmodes less ideally suited for extracting mean potential energy and hence their growth rates are smaller.

Though the usual barotropic governor effect interpretation is due to barotropic shear, we find that in curved flow geometry, it may be more general to refer to barotropic strain rather than shear. In uniform azimuthal flow, the eigenmodes are azimuthally traveling waves, with constant angular phase velocity [rad/s]. If they were to have no tilt, azimuthal advection would need to be radially constant. The azimuthally advecting quantity is the (mean) angular velocity, $\Omega_j(r) \equiv U_{j\phi}/r$, and its radial gradient is the strain rate (2.8). Thus the barotropic governor effect can generally occur in azimuthal flow with non-zero strain, i.e. flow not in solid-body rotation (§2.4). In accordance, we find (figure 2.4) that some uniform azimuthal flow eigenmodes have substantial horizontal tilts, often with much lower growth rates. Similar results were obtained in a primitive-equations 2-layer vortex instability model *Dewar and Killworth* [1995]. The authors found that Gaussian vortices with co-rotating lower layers had reduced PEC and growth rates relative to vortices with counter-rotating lower layers, and attributed the result to the barotropic governor effect.

2.5.2 Non-normal growth

While the above diagnosis focuses on perturbation growth by individual eigenmodes (aka normal modes), non-orthogonality of eigenmodes, which is a common occurrence in sheared flow, means that what is known as non-normal growth is also possible [*Trefethen et al.*, 1993; *Farrell and Ioannou*, 1996]. Linear evolution of two or more non-orthogonal eigenmodes, even if they are all neutral or decaying, can result in transient (non-normal) growth before the eventual decay of the disturbance. For parameter values where growing eigenmodes exist, they do dominate the linearized dynamics, at long enough times. But transient non-normal growth may dominate at shorter times, as well as for parameter ranges where no growing eigenmodes exist.

To calculate the non-normal growth, using the same numerical eigenvalue solver described above, we recast the PV equations (2.6) in the form: $M\Psi = \sigma B\Psi$, where M and B are differential operators, and $\Psi = (\Psi_1, \Psi_2)^T$ (T for transpose). We refer the reader to *Farrell and Ioannou* [1996] for details of the method. Assuming B is invertible we can rewrite the differential equation as $\sigma\Psi = L\Psi$, where $L = B^{-1}M$. And since $\Psi \sim \exp(-i\sigma t)$,

$$\partial_t \Psi = -iL\Psi. \tag{2.27}$$

So the propagator to time t is $\exp(-iLt)$. If we define $\hat{L} = N^{1/2}LN^{-1/2}$, where N is the energy norm operator [*Farrell and Ioannou*, 1996], then the maximal instantaneous growth-rate of disturbances is given by the eigenvalues (and eigenstates) of the operator $H = \frac{1}{2}i(\hat{L}^\dagger - \hat{L})$. The energy-norm operator in the annulus case is, prior to the performed discreziation of the differential operators and of r,

$$N = \frac{1}{2}\begin{pmatrix} rD_1 & 0 \\ 0 & rD_2 \end{pmatrix}\left(-\nabla_r^2 + \frac{m^2}{r^2}\right) + \frac{1}{2}D_1 D_2 \begin{pmatrix} 1 & -1 \\ -1 & 1 \end{pmatrix}. \tag{2.28}$$

In figure 2.7 the maximal instantaneous non-normal growth in energy norm is shown for uniform azimuthal flow and uniform rectilinear flow. Interestingly, the result is independent of δ,

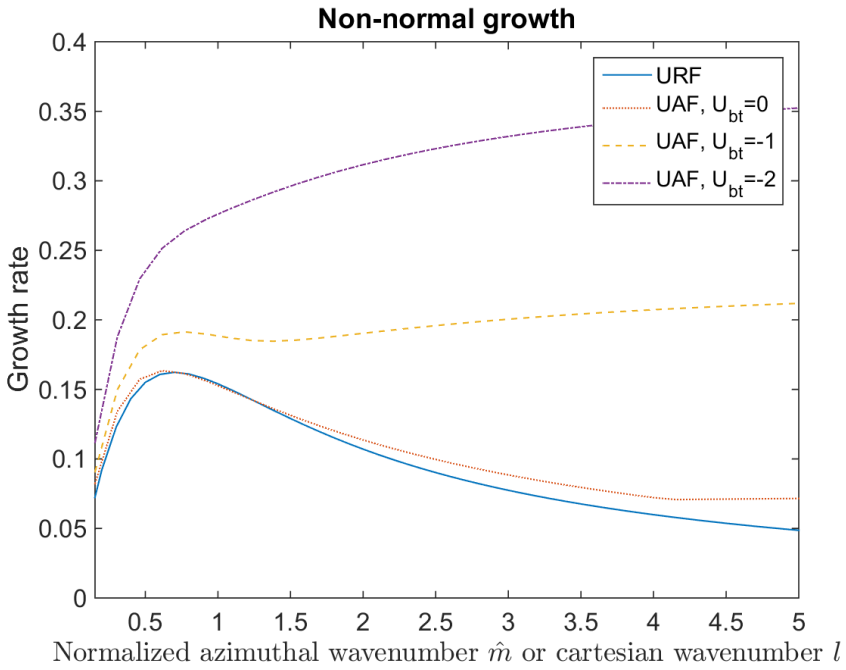

Figure 2.7: Maximal instantaneous (non-normal) growth rates. The blue curve corresponds to mean uniform rectilinear flow. The other curves correspond to mean uniform azimuthal flow with three different barotropic velocities U_{bt}. Linear bathymetry was used in all cases.

as the bathymetry does not appear in the energy equation (2.7). Bathymetry affects local energy conversion but not its domain integral. However, in finite time bathymetry certainly effects energy growth or decay since it affects the streamfunction evolution, and would likely render sub-optimal the fastest-growing non-normal perturbations calculated using (2.28). For $U_{bt} = 0$, uniform azimuthal flow growth is very similar to uniform rectilinear flow (which is independent of barotropic velocity), and both have non-normal growth just slightly higher than peak normal growth rate (compare with figure 2.6). However, non-normal growth occurs for a wider range of wavenumbers than the range in which unstable normal modes exist. The decay of the non-normal growth rate with wavenumber is slower in uniform azimuthal flow relative to uniform rectilinear flow. In addition, at nonzero U_{bt}, the uniform azimuthal flow growth rate is higher everywhere, and decays even slower with $\hat{m}$, or even (not shown) grows and oscillates in $\hat{m}$ before decaying again. Growth at very high wavenumbers is probably not physical, and would likely not appear if some form of scale-selective “eddy" viscosity were included.

2.5.3 Convex and concave cases

The convex to concave transformation (by reflection of $\eta_b(r)$ and $Z_I(r)$, as explained in §2.2.1), results for uniform azimuthal flow in $b \rightarrow -b$ and $U_{j\phi} \rightarrow -U_{j\phi}$. Therefore equations (2.6) are unaltered if in addition $\sigma \rightarrow -\sigma$. Also, if $\{\sigma, \Psi_j(r)\}$ are an eigenvalue-eigenfunction pair of equations (2.6) then so are their complex conjugates $\{\sigma^*, \Psi_j^*(r)\}$, as can be verified by taking the complex conjugate of (2.6). Combining the last two observations, if $\{\sigma, \Psi_j(r)\}$ is an eigenvalue-eigenfunction pair in a convex geometry, then $\{-\sigma^*, \Psi_j^*(r)\}$ is an eigenvalue-eigenfunction pair in a concave geometry, and vice-versa. Thus the growth rate and the real (physical) part of the streamfunction are unaltered, and the phase speed is reversed. The reversal of phase speed, along with reflection of $\eta_b(r)$ (shallow water at other side of the channel) results in the same phase speed direction relative to shallow water, and therefore the physical propagation direction is also unaltered.

Different eddy growth rate at convex versus concave sections is not accounted for in the linear uniform azimuthal flow model, contrasting with the pronounced instabilities observed around convex bends in the real ocean's continental slopes (see §2.1). Despite this symmetry of our QG model, there is still a potentially important difference between unstable modes growing over convex and concave bends in the continental slope. If the perturbation streamfunction is displaced off the center of the channel, say toward shallower water, then switching between concave and convex continental slopes will result in the streamfunction being displaced toward deep water instead. As noted in §2.5.1, the uniform azimuthal flow perturbation streamfunctions are indeed typically displaced from the center of the channel (see figure 2.4). The significance of this difference between structure of growing modes over convex and concave continental slopes cannot be determined from our linear instability analysis, and warrants further investigation using a nonlinear model.

2.6 Relation between baroclinic instability in straight and curved geometries

Although uniform azimuthal flow and uniform rectilinear flow share the same cross-stream isopycnal and bathymetric profiles, the properties of their unstable modes are quite different (§2.5). In contrast, we found strong similarity (§2.4) between the uniform rectilinear flow and solid body rotation cases, despite differing isopycnal and bathymetric profiles. Using insights from §2.4-2.5, we can reduce the parallel between uniform rectilinear flow and solid body rotation to three conditions:

1. Vanishing horizontal mean strain, resulting in zero Reynolds stresses work. From a dynamical perspective, the mean flow does not shear waves propagating in the direction of the mean flow.

   The following two factors stem from the Rayleigh criterion (§2.3).

2. Vanishing horizontal gradient of the mean vorticity. Under this condition the Rayleigh criterion depends only on the ratio of bathymetric to isopycnal slopes, δ.

3. Congruous cross-stream bathymetric and isopycnal profiles. This renders δ constant. The implication can be understood by considering a uniform rectilinear flow-like case of uniform channel flow (linear isopycnals) but over non-linear bathymetry. Then, using (2.9) and defining $\delta(x) = \frac{\partial \eta_b(x)}{\partial x} / \frac{\partial Z_I}{\partial x}$, the PV gradient (2.30) can be rewritten as

   $$\frac{\partial Q_j}{\partial x} = -F_j(-1)^j \left[1 - \Delta_{j2}\delta(x)\right]. \tag{2.29}$$

   By the Rayleigh criterion (§2.3) if $\delta(x) < 1$ anywhere, instability is not prohibited. Thus even if $\bar{\delta} > 1$ (the bar denoting a cross-stream average), but locally $\delta(x) < 1$ somewhere, then this uniform flow case may be unstable.

For annular flow, the vanishing of the strain rate occurs only for parabolic isopycnals (or equivalently, solid-body rotation), while zero horizontal gradient of vorticity occurs only for parabolic

or logarithmic isopycnals. Therefore the only annulus flow case in which conditions (i)–(iii) all occur together is parabolic isopycnals over parabolic bathymetry, which is our solid body rotation case (§2.4). Mean flow over any other bathymetry (such as linear bathymetry, as in §2.5) will necessary violate at least one of (i)–(iii). For uniform azimuthal flow, condition (iii) is satisfied, but the curvature results in non-zero strain rate and non-zero vorticity gradient. Superficially uniform azimuthal flow may appear to be the most similar to uniform rectilinear flow since both cases have isopycnals (linear bathymetry in the present treatment) in the cross-stream direction, but conditions (i)–(iii) identify solid body rotation as the true dynamical analogue of uniform rectilinear flow.

We have verified conditions (i)–(iii) using some additional numerical experiments, whose results are summarized in this paragraph, rather than plotted. The same numerical solver was used in all cases. We considered two cases in which only factor (iii) is violated: (*a*) Uniform straight channel flow (i.e., linear isopycnals) over parabolic bathymetry, and (*b*) solid body rotation (i.e., parabolic isopycnals) over linear bathymetry in an annular channel. Both have zero strain, and therefore were found to be similar to uniform rectilinear flow/solid body rotation in that the magnitudes of their growth rates are very similar, in that the Reynolds stresses work is zero, and in that the results are independent of the barotropic velocity. However, non-zero (though small) growth occurs for $\delta > 1$ in (a) because condition (iii) is violated. We also tested a third case, where only condition (i) is violated: (c) annular flow with logarithmic isopycnals and bathymetry. We found this case to be similar to our uniform azimuthal flow results, though with a more exaggerated dependence on the magnitude of the barotropic velocity $|U_{bt}|$. Unlike uniform azimuthal flow, the logarithmic profile used in case (c) has zero growth rate at $\delta > 1$ because the vorticity is zero.

2.7 Summary and Discussion

To study the effect of horizontal curvature in flow and bathymetry on baroclinic instability, we study several mean flow and bathymetry cases in an annulus and compare them with uniform mean flow over linear bathymetry in a straight channel (uniform rectilinear flow). We consider uniform rectilinear flow a reasonable though simple test case for deep western boundary currents since these tend to be quite broad relative to the Rossby radius [*Xu et al.*, 2015; *Stommel and Arons*, 1972]. Some further justification may be required for the use of a periodic annular channel in place of an open domain that is approximately an annular section. We expect that for time intervals short compared to the travel time of perturbations along the section, azimuthal edge effects will be small, as long as the wavelength is somewhat smaller than the section length.

We find solid body rotation (§2.4) to be very similar to uniform rectilinear flow, with an exact simple transformation between the dispersion relations of both cases. We trace the similarity in instability properties to the three commonalities between of the mean flows and bathymetries (§2.6): vanishing strain rate, vanishing vorticity, and constant ratio of bathymetric slope to isopycnal slope $\delta(r) \equiv \delta$. In contrast, the uniform azimuthal flow case (§2.5), which has (like uniform rectilinear flow) linear isopycnals (and bathymetry), has quite different stability properties from because it has non-vanishing strain rate and mean vorticity. While we began a preliminary exploration of more significantly sheared velocity profiles (i.e., jets and free shear layers), an adequate coverage of this topic requires at least a full additional paper. However, we would like to stress that the analysis in §2.6 is very general as it is based on the Rayleigh criterion (§2.3) and on the energy equation (§2.2.3), and that a few experiments with other simple profiles (§2.6) support the generality of these results.

Baroclinic instabilities in uniform azimuthal flow differ in several ways from uniform rectilinear flow and solid body rotation: (a) The eigenmodes depend on the mean barotropic velocity. The growth rate of unstable eigenmodes generally decreases with $|U_{bt}|$, unless $\delta \approx 1$. (b) Whereas

solid body rotation and uniform rectilinear flow are stable for $\delta \geq 1$, uniform azimuthal flow is (weakly) unstable for a small interval of δ greater than 1. That is due to non-zero mean flow vorticity. (c) Negative Reynolds stresses work manifest as part of the barotropic governor effect (BGE). Although BGE is usually attributed to barotropic shear, we find that in non-parallel flow the cause may be generalized to barotropic strain (even when cross-flow shear is zero, as in uniform azimuthal flow). (d) For non zero $|U_{bt}|$, more growing eigenmodes arise, with diverse growth rates, phase speeds, and barotropic to baroclinic energy conversion ratios. (e) Non-normal growth is generally faster and occurs over a larger wavenumber range. The growth rate becomes even larger with increased $|U_{bt}|$ magnitude.

The uniform azimuthal flow case has a small but non-zero growth rate for $\delta > 1$, due to the vorticity associated with curved streamlines, unlike the straight-channel case [*Mechoso*, 1980]. Deep western (and some surface) boundary currents often have isopycnal profiles similar to the bathymetric profile, i.e., $\delta(r) \approx 1$ [*Xu et al.*, 2015; *Stommel and Arons*, 1972; *Stipa*, 2004b; *Spall*, 2010]. Thus the increased instability of uniform azimuthal flow relative to uniform rectilinear flow in the $\delta(r) \approx 1$ regime is potentially relevant for the DWBC eddy-shedding observations that motivates this work. Assuming that the DWBC flow is faster in the deeper layer, and that the barotropic flow is in the same direction as the flow in the deeper layer, flow on a convex slope is described (in addition to $\delta \approx 1$) by $U_{bt} < 0$. Negative U_{bt} is indeed the range in which we find the instability is possible for $\delta > 1$ (figure 2.6, and §2.3.2). Note that by the symmetry described in §2.5.3, a concave section would have the same linear growth rates as the convex section described.

The result regarding instability of eigenmodes for $\delta \approx 1$ may also be relevant for parameterizations of eddies on sloping boundaries, still a little explored subject. *Isachsen* [2011] compares parameterizations based on the extended Eady model with eddy fluxes diagnosed in a Primitive Equation simulation over a straight continental slope. While the parametrization predicts zero flux at $\delta > 1$, the diagnosed eddy flux is very low but non-zero. This might be due to non-zero horizontal vorticity gradients in the flow, which in any case may be relevant to the equivalent parameterization problem on a horizontally curved slope. Non-normal growth, which we found has

larger maximal values in uniform azimuthal flow, may also play a role in eddy fluxes when $\delta > 1$, especially since maximal potential non-normal growth rate is independent of the bathymetry. Disturbances with large non-normal growth, even if they occur rarely, may produce non-zero eddy fluxes for any value of δ.

The curved streamlines and associated strain introduce more growing eigenmodes in uniform azimuthal flow, generally with diminished growth rates and negative Reynolds stresses work. These propagate in various directions and speeds, unlike the strictly topographic Rossby wave-like propagation direction (with shallow water to the right) in uniform rectilinear flow. The wavenumber of maximum growth rate thus changes, and in some cases more than one local maxima in wavenumber exist (for a fixed δ value). This raises questions about the validity for curved slopes of some continental slope eddy parameterizations [*Stipa*, 2004a; *Isachsen*, 2011], where diffusivity is determined by solely the global maximum in wavenumber (of the Eady model growth rate).

Perturbations over convex or concave continental slopes have the same perturbation growth rates in uniform azimuthal flow, but the streamfunction profiles are reflected relative to mid-channel on the shallow-deep water axis (§2.5.3). Uniform azimuthal flow eigenmodes are generally not centered at mid-channel (figure 2.4). If an eigenmode on a convex slope is centered offshore from mid-channel, the analogous eigenmodes on a concave plane would be displaced shoreward from mid-channel, and vice-versa. While in linear theory this has no direct implications for the growth rate, non-linear evolution, interaction with topography, and bottom boundary layers may result in implications we cannot determine here.

While non-normal peak instantaneous growth rate and the range of unstable wavenumbers are larger due to non-zero mean strain and mean vorticity gradient in uniform azimuthal flow, their importance relative to individual eigenmodes' growth remains unclear due to the transience of non-normal amplification. Differentiating between the two effects would probably require fully non-linear, time-evolution integrations. The domain would preferably be open rather than peri-

odic, to prevent confusion with down and upstream disturbance interaction occurring in finite time. In such a case and especially if the domain were to have changing curvature, it may be that the transience of non-normal growth would not be as large a limitation to actual growth. Non-orthogonality of growing eigenmodes may also influence their nonlinear evolution: their nonzero mutual projections may encourage nonlinear interactions between modes and accelerate the path to finite-amplitude effects.

While we have striven to choose relevant and similar flow profiles for comparison of straight and curved flow and bathymetry, we can imagine a different criterion for selection of the curved profile given a straight flow profile, viz., that the curved profile is the downstream-adjusted profile of the straight flow after meeting a curve in the continental slope. Assume that the upstream (straight flow) boundary current has linear isopycnals and linear bathyemtry, as in uniform rectilinear flow. Once the current traverses a horizontally curved slope section, assuming adjustment to solid-body rotation does not happen, then strain and relative vorticity are necessarily induced in the mean flow (§2.6). Hence Reynolds stresses will modulate and generally decrease the baroclinic instability growth rates, and the relative vorticity will modulate the range of unstable δ parameters. We find the same results in the uniform azimuthal flow case (§2.5), which can also be regarded as a study of these effects, when the linear isopycnals remain (cross-stream) approximately linear after meeting the bend in the slope. In §2.6 we find that a logarithmic isopycnal profile generally has similar results to uniform azimuthal flow, and we expect this to hold quite generally for other broad and relatively uniform flow profiles. Exactly how and how much the mean isopycnal structure actually adjusts to curvature is a question worthy of further investigation.

To summarize, the initial hypothesis is that horizontal curvature of bottom slopes increases baroclinic instability. We find that to the contrary, peak growth rates are mostly reduced in uniform azimuthal flow relative to uniform rectilinear flow. One exception is the $\delta >\sim 1$ regime. $\delta \sim 1$ is actually quite common in deep boundary currents [*Xu et al.*, 2015; *Stommel and Arons*, 1972], and despite the relatively smaller values of growth rates (relative to $\delta < 1$) the increased instability

in this regime thus appears relevant. We also find higher peak non-normal growth in uniform azimuthal flow relative to uniform rectilinear flow, but the relative effect of transient non-normal growth versus normal exponential growth is unclear and will remain so unless evaluated in a particular context. The actual profile a deep western boundary current adjusts to (from which baroclinic instability arises), may be different than linear, but it is conjectured above that the results may be quite similar in terms of the baroclinic instability. Exceptions to that may occur, if one takes into account the finite width of the slope and of the current.

2.8 Supplement

2.8.1 Numerical verification and sensitivity tests

Here we give results of numerical convergence tests, including comparison with some analytical results, to show the validity of the solver and of the numerical solutions. We also give results of sensitivity tests where we vary R_i, R_e, F_1, and F_2, showing that the general results presented in the main text still hold over a larger parameter range.

The numerical setup in a straight-channel was verified in the uniform rectilinear flow case to reproduce the known [*Mechoso*, 1980] analytical dispersion relation. We also verified the numerical solution of the solid body rotation case in a cylinder (annulus with $R_i = 0$) relative to the analytical dispersion relation (2.25). A cylinder (rather than annulus) is chosen because deriving the numerical value of growth rate from the dispersion relation requires first solving the nonlinear algebraic equation (2.22). That can be avoided since in a cylinder since the functions P_m are replaced then by Bessel functions of the first kind J_m, and thereby only (tabulated) Bessel zeros values are needed for the calculation. The results (figure 2.8a) show a very small relative error in the numerical result with the standard $dr = 0.025$, and decreasing super-exponentially with decreasing dr in the range shown, implying the numerical scheme is convergent.

Since the same solver was used for both solid body rotation and uniform azimuthal flow, the comparison described in the previous paragraph verifies partially the correct setup for uniform azimuthal flow too. We also present in figure 2.8b the difference in growth rates computed, relative to the result with a higher resolution, namely $dr = 0.003125$. The results suggest that growth rates of all four modes have probably converged to a very good approximation at the resolution used thorough the paper, i.e., $dr = 0.025$. While the specific plot is for $m = 2$, $\delta = -0.2$, and $U_{bt} = 1$, we find that the results are similar in other cases. The difference in the growth rates of the most unstable mode calculated with $dr = 0.025$ relative to that with $dr = 0.0125$ are generally $< 10^{-5}$ inside of the instability boundary.

Further verification for uniform azimuthal flow came from a test of convergence of the uniform azimuthal flow growth rates and frequencies to uniform rectilinear flow values, as the channel inner radius R_i is increased (with constant channel width $W = R_e - R_i$). That is since in the strict $R_i \to \infty$ limit, the mean state of uniform azimuthal flow converges to the mean state of uniform rectilinear flow. We verified that for large enough R_i the GR(m, b) functional form for any U_{bt} value indeed became arbitrarily close to the channel result (which is independent of U_{bt}) for large enough R_i values as far as was tested. The convergence test was deemed successful.

The standard experiment described has a radial extent $[R_i, R_e] = [3, 10]$. It is found that moderate increases to domain size (and hence also to current width) do not result in significant changes to the growth rates. For example a current with radial extent $[R_i, R_e] = [3, 15]$ has a similar GR$(\hat{m}, b)$ to the standard experiment considered (with the wavenumber normalized by average domain width, $\hat{m} = mR$). Increasing R_i while keeping channel width constant generally results in more uniform rectilinear flow-like results, as described in the previous paragraph. We find that convergence is slower for larger $|U_{bt}|$ cases, and so the differences described in the main text between annulus and channel instabilities remain qualitatively similar. Decreasing R_i down to a value of 1 (while either keeping $(R_e - R_i)$ constant, or keeping R_e constant) barely changes the growth rates of the fastest growing modes, though the pattern shifts to smaller m's. Note that, as derived in §2.2.4, $R_i \lesssim 1$ is not consistent with QG.

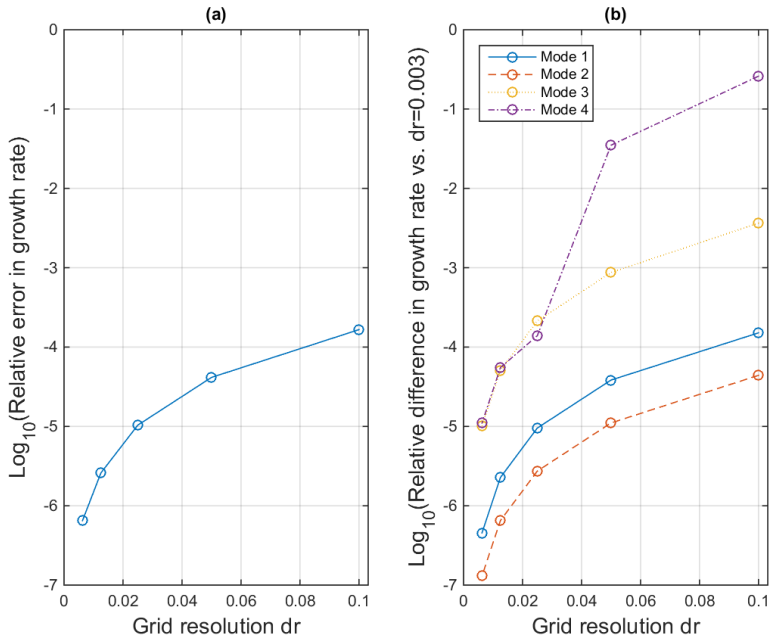

Figure 2.8: (a) Numerical convergence of growth rate for cylinder solid body rotation eigenmodes to that obtained from the analytical dispersion relation (2.25), for azimuthal wavenumber $m = 2$ and bathymetric slope parameter $\delta = 0$. The cylinder width was set by $R_1 = 0$ and $W = R_2 = 7$ to be equivalent to the annulus width taken in sections 2.4 and 2.5. The circles denote actual numerical values calculated, in which dr is decreased by factors of two. Note the logarithmic scale of the ordinate. (b) Numerical convergence of uniform azimuthal flow growth rates with various dr values to the value similarly calculated with a twice the highest resolution shown ($dr = 0.00625$), .i.e. with $dr = 0.003125$. Results for all four unstable eigenmodes shown. The presented results are for $m = 2$, $\delta = -0.2$, and $U_{bt} = 1$. The convergence was similarly tested for a large portion of the parameter space. The value actually used to generate all other results in this paper is $dr = 0.025$ (or $dx = 0.025$ in the channel case).

A layer thickness ratio of 1 ($F_1 = F_2 = 1/2$) was taken throughout the numerical experiments. Further experiments were done as sensitivity tests with non-equal layers in uniform azimuthal flow, and these show similar growth rate dependence on U_{bt} and m as in the standard experiments, with a few differences. The growth rate maximum is achieved at $F_j = 1/2$ and decreases as $|F_j - 1/2|$ increases. If a line of maximum instability (in m) per δ is fit (in figure 2.3), then its slope generally increases with H_1/H_2 (maximum $\delta < 0$ instability occurs at higher wavenumbers).

2.8.2 Straight channel equations

We use the uniform rectilinear flow instability case [*Pedlosky*, 1964; *Mechoso*, 1980] as a point of comparison for our investigations. Since it is not new, and to avoid confusing notation, we provide details in this supplemental subsection.

Generalizing uniform rectilinear flow by allowing non-uniform currents in a straight channel, we provide below the perturbation modal equations for mean geostrophic along-channel flow $\bar{V}_j = V_j(x)\hat{y}$, and bathymetry $\eta_b(x)$, which vary in the cross channel coordinate (x) only (and in each layer). The background and perturbation streamfunctions are again denoted by $\overline{\psi}_j$ and ψ_j respectively, and therefore $V_j(x) = \partial\overline{\psi}_j/\partial x$. Note that usually the straight channel is modeled with the x coordinate along the channel axis (in the downstream direction). We chose to take the x coordinate in the cross-stream direction for easy comparison with the annular channel, which naturally has the cross-stream coordinate (the radial coordinate r) as the first coordinate of a right-handed triplet.

Assuming an harmonic solution in x and in t, $\psi_j = \text{Re}\left\{\Psi_j(x)exp(i(ly - \sigma t))\right\}$ (where Re is the real part of the expression that follows, l is a real down-stream wavenumber, and σ is the complex frequency), we have the (nondimensional) quasi-geostrophic potential vorticity equations

[*Pedlosky*, 1964]:

$$[V_1 l - \sigma]\left[\frac{\partial^2}{\partial x^2}\Psi_1 - l^2\Psi_1 - F_1(\Psi_1 - \Psi_2)\right] - l\Psi_1\frac{\partial Q_1}{\partial x} = 0, \tag{2.30a}$$

$$[V_2 l - \sigma]\left[\frac{\partial^2}{\partial x^2}\Psi_2 - l^2\Psi_2 - F_2(\Psi_2 - \Psi_1)\right] - l\Psi_2\frac{\partial Q_2}{\partial x} = 0, \tag{2.30b}$$

$$\frac{\partial Q_j}{\partial x} = \frac{\partial^2}{\partial x^2}V_j - F_j\left[(-1)^j(V_2 - V_1) - \Delta_{j2}\frac{\partial \eta_b}{\partial x}\right]. \tag{2.30c}$$

For uniform rectilinear flow, $\frac{\partial \eta_b}{\partial x}$ and the V_j are constants. We state the equations in more general form for easy comparison with the general annulus case given in the equation set (2.6). The eigenvalue problem is defined by the PV equations together with no-normal flow boundary conditions. The channel boundaries are denoted by X_i and X_e, and since only their difference (channel width) is important, $X_i = 0$ is chosen. In the standard uniform rectilinear flow experiment, $X_e = 7$, $F_1 = F_2 = 1/2$, and $V_{bt} \equiv (V_1 + V_2)/2 = 0$. The last condition (zero barotropic velocity) is not limiting since the growth rates and eigenmodes are invariant with V_{bt}, which just Doppler-shifts the (real) frequency. The numerical solution is obtained in a similar way as for the annulus.

The eigenmodes streamfunctions are sums of harmonic functions and the nondimensional uniform rectilinear flow dispersion relation is

$$\sigma = V_{bt} + l\frac{K^2(F_2 - F_1 - F_2\delta) - lF_1F_2\delta + \sqrt{D}}{2K^4 + 2K^2(F_1 + F_2)}, \tag{2.31a}$$

$$\begin{aligned}\frac{D}{l^2} =& K^8 + (2F_2\delta)K^6 + \left(-4F_1F_2 + 2F_1F_2\delta + F_2^2\delta^2\right)K^4 \\ &+ \left(-4F_2^2F_1\delta + 2F_2^2F_1\delta^2\right)K^2 + F_1^2F_2^2\delta^2.\end{aligned} \tag{2.31b}$$

Here k, and $K = \sqrt{k^2 + l^2}$ are the cross-stream, and total wavenumbers, respectively. The nondimensionalization is similar to the uniform azimuthal flow case, and (in non-dimensional variables) $\delta = -\frac{\partial \eta_b}{\partial x}$.

2.8.3 Semicircle theorem

In this section we adapt the *Pedlosky* [1964] semi-circle theorem, which gives growth-rate bounds and the associated phase-speed bounds to the annular channel, and we extend it for the general case where the bathymetry is not flat. First, we make the transformation $\Psi_j = (U_{j\phi} - cr)b_j$ in equations (2.12a)-(2.12b), then multiply the first and the second equations by $D_1 b_1^*(U_{1\phi} - cr)$ and $D_2 b_2^*(U_{2\phi} - cr)$ respectively. Summing both equations and integrating the result with the volume element (rdr), results, after an integration by parts of the Laplacian terms, in

$$\begin{aligned}
&\sum_{n=1}^{2} \int_{R_i}^{R_e} (U_{j\phi} - cr)^2 P_j r dr \\
&= D_1 D_2 \frac{1}{2} \int_{R_i}^{R_e} (U_{1\phi} - U_{2\phi})^2 |b_1 - b_2|^2 r dr - D_1 \int_{R_i}^{R_e} (U_{2\phi} - cr) J_2 \frac{\partial \eta_b}{\partial r} r dr. \qquad (2.32)
\end{aligned}$$

Here we made use of the identity,

$$(U_{1\phi} - cr)(U_{2\phi} - cr) = -\frac{1}{2}\left[(U_{1\phi} - U_{2\phi})^2 - (U_{1\phi} - cr)^2 - (U_{2\phi} - cr)^2\right],$$

with the following definitions:

$$\begin{aligned}
P_j &= D_j \left[\left| \frac{\partial}{\partial r} b_j \right|^2 + \frac{m^2 - 1}{r^2} |b_j|^2 \right] + D_1 D_2 \frac{1}{2} |b_1 - b_2|^2 \\
J_j &= D_j |b_j|^2.
\end{aligned}$$

The real part of (2.32) is thus

$$\begin{aligned}
&\sum_{n=1}^{2} \int_{R_i}^{R_e} (U_{j\phi}^2 + c_r^2 r^2 - 2U_{j\phi} c_r r - c_i^2 r^2) P_j r dr \\
&= \frac{1}{2} D_1 D_2 \int_{R_i}^{R_e} (U_{1\phi} - U_{2\phi})^2 |b_1 - b_2|^2 r dr - D_1 \int_{R_i}^{R_e} (U_{2\phi} - c_r r) J_2 \frac{\partial \eta_b}{\partial r} r dr. \qquad (2.33)
\end{aligned}$$

If $c_i \neq 0$, from the imaginary part of (2.32) we have

$$\int_{R_i}^{R_e} \sum_{n=1}^{2} (U_{j\phi} - c_r r) P_j r^2 dr = -\frac{D_1}{2} \int_{R_i}^{R_e} J_2 \frac{\partial \eta_b}{\partial r} r^2 dr. \qquad (2.34)$$

Table 2.1: Summary of phase speed bounds

Condition	Phase speed bounds
$\eta_b \equiv 0$	$u_{min} \le c_r \le u_{max}$
$\left(\frac{\partial \eta_b}{\partial r}\right)_{max} < 0$	$u_{min} - \frac{D_1\left\|\left(\frac{\partial \eta_b}{\partial r}\right)_{min}\right\| R_e^2}{2R_i(m^2-1)} \le c_r \le u_{max}$
$\left(\frac{\partial \eta_b}{\partial r}\right)_{min} < 0$ and $\left(\frac{\partial \eta_b}{\partial r}\right)_{max} > 0$	$u_{min} - \frac{D_1\left\|\left(\frac{\partial \eta_b}{\partial r}\right)_{min}\right\| R_e^2}{2R_i(m^2-1)} \le c_r \le u_{max} + \frac{D_1\left(\frac{\partial \eta_b}{\partial r}\right)_{max} R_e^2}{2R_i(m^2-1)}$
$\left(\frac{\partial \eta_b}{\partial r}\right)_{min} > 0$	$u_{min} \le c_r \le u_{max} + \frac{D_1\left(\frac{\partial \eta_b}{\partial r}\right)_{max} R_e^2}{2R_i(m^2-1)}$

For $m > 1$, we can derive the following inequality between integrals of J_j and P_j:

$$\begin{aligned}\int_{R_i}^{R_e} P_j r^2 dr &= D_1 \int_{R_i}^{R_e} \left[\left[\left|\frac{\partial}{\partial r} b_j\right|^2 + \frac{m^2-1}{r^2}|b_j|^2\right] + D_1 D_2 \frac{1}{2}|b_1 - b_2|^2\right] r^2 dr \\ &\ge \frac{m^2-1}{R_e^2} D_j \int_{R_i}^{R_e} |b_j|^2 r^2 dr\,,\end{aligned}$$

from which follows a result we will refer to as the $J-P$ inequality:

$$\int_{R_i}^{R_e} J_j r^2 dr \le \frac{R_e^2}{m^2-1} \int_{R_i}^{R_e} P_j r^2 dr. \tag{2.35}$$

Pedlosky [1964] found a tighter J-P type inequality for the straight-channel case, using a spectral estimate, which we were unable to adapt to the annulus case. The next two subsections will derive phase speed and growth rate bounds respectively, based on the results so far derived in this section.

Bounds on phase speed Defining $u_j = U_{j\phi}/r$, equation (2.34) can then be written as

$$\int_{R_i}^{R_e} \sum_{n=1}^{2} (u_j - c_r) P_j r^3 dr = -\frac{D_1}{2} \int_{R_i}^{R_e} J_2 \frac{\partial \eta_b}{\partial r} r^2 dr. \tag{2.36}$$

Bounds on the phase speed can be found from the last equation, using the $J-P$ inequality, assuming that information about Information on η_b and u is available. The bounds are derived separately for 4 different types of η_b profiles, and are summarized in Table 2.1.

Growth rate bound We define $u_{\max} = \max_{j=1,2}\{\max_{R_i \le r \le R_e}[u_j(r)]\}$ and $u_{\min} = \min_{j=1,2}\{\min_{R_i \le r \le R_e}[u_j(r)]\}$, and use the following inequality:

$$0 \le \int_{R_i}^{R_e} \sum_{n=1}^{2} (u_j - u_{\min})(u_{\max} - u_j) P_j r^3 dr$$
$$= \int_{R_i}^{R_e} \sum_{n=1}^{2} \left[-u_j^2 + u_j(u_{\max} + u_{\min}) - u_{\min} u_{\max} \right] P_j r^3 dr. \qquad (2.37)$$

In a similar manner to the straight-channel case [*Pedlosky*, 1964], we take (2.37) + (2.33) $-(u_{\min} + u_{\max} - 2c_r)$(2.34), resulting in,

$$\sum_{n=1}^{2} \left[\left(c_r - \frac{u_{\min} + u_{\max}}{2} \right)^2 + c_i^2 - \left(\frac{u_{\max} - u_{\min}}{2} \right)^2 \right] \int_{R_i}^{R_e} P_j r^3 dr \le$$
$$- D_1 \int_{R_i}^{R_e} \left(\frac{u_{\max} + u_{\min}}{2} - u_2 \right) J_2 \frac{\partial \eta_b}{\partial r} r^2 dr. \qquad (2.38)$$

Now, using $\left| \frac{2_{max} + u_{min}}{2} - u_j \right| \le \frac{u_{max} - u_{min}}{2}$ together with the J-P inequality (assuming $m > 1$), we obtain the semi-circle inequality:

$$\left(c_r - \frac{u_{\min} + u_{\max}}{2} \right)^2 + c_i^2 \le \left(\frac{u_{\max} - u_{\min}}{2} \right)^2 + \frac{R_e^2 D_1 \left| \frac{\partial \eta_b}{\partial r} \right|_{\max}}{R_i (m^2 - 1)} \left(\frac{u_{\max} - u_{\min}}{2} \right). \qquad (2.39)$$

The first term on the left may be dropped as it is positive definite. In fact, by the phase speed bounds derived (in table 2.1), this term may attain a zero value in all cases.

A tighter bound may be derived by noting that

$$- D_1 \int_{R_i}^{R_e} \left(\frac{u_{\max} + u_{\min}}{2} - u_2 \right) J_2 \frac{\partial \eta_b}{\partial r} r^2 dr \le$$
$$- D_1 \min \left[0, \min \left[\left(\frac{u_{\max} + u_{\min}}{2} - u_2 \right) \frac{\partial \eta_b}{\partial r} \right] \right] \int_{R_i}^{R_e} J_2 r^2 dr \,,$$

from which follows

$$c_i^2 \le \left(\frac{u_{\max} - u_{\min}}{2} \right)^2 - \frac{R_e^2 D_1}{R_i (m^2 - 1)} \min \left[0, \min \left[\left(\frac{u_{\max} + u_{\min}}{2} - u_2 \right) \frac{\partial \eta_b}{\partial r} \right] \right]. \qquad (2.40)$$

CHAPTER 3

Why Does the Deep Western Boundary Current "Leak" Around Flemish Cap?

3.1 Introduction

The Atlantic Meridional Overturning Circulation (AMOC[1]) connects disparate water masses, depths, and geographical locations [*Buckley and Marshall*, 2016; *Lozier*, 2012], and plays major roles in the broader climate system [*Srokosz et al.*, 2012; *Bullister et al.*, 2013]. These include driving a significant fraction of the global atmosphere-ocean meridional heat flux, e.g., an estimated $\approx$ 15% at 40 °N [virtually all of the oceanic component, *Trenberth and Fasullo*, 2017, Fig. 3], and influencing the CO_2 sink in the North Atlantic [*Takahashi et al.*, 2009]. Despite its importance, the characterization of three-dimensional AMOC pathways remains incomplete, as does the understanding of their driving mechanisms [*Lozier*, 2012].

A significant portion of the deep (southward) AMOC branch occurs within the Deep Western Boundary Current (DWBC). The occurrence and role of the DWBC was predicted by *Stommel and Arons* [1959], albeit on the basis of assumptions now partially outdated [*Ferrari et al.*, 2016]. The DWBC has nonetheless been observed from the subpolar North Atlantic southward to the southern Atlantic, forming an intensified boundary current that carries North Atlantic Deep Water (NADW) along the western Atlantic continental slope [*Hogg and Johns*, 1995; *Talley*, 2011].

[1] A table of acronyms and terms commonly used in the text appears in supplemental subsection 3.6.1.

However, in recent decades it has become clearer that the DWBC is not the only southward transport branch of the AMOC. A series of float experiments [*Lavender et al.*, 2000; *Fischer and Schott*, 2002; *Bower et al.*, 2009] and tracer analyses [*Rhein et al.*, 2002; *Gary et al.*, 2012; *Le Bras et al.*, 2017] have identified significant loss ("leakiness") of material from the DWBC in the Newfoundland (Nfl) Basin. This leakiness was specifically targeted and quantified in the "Export Pathways" experiment [ExPath, *Bower et al.*, 2011]. The majority ($\approx$ 90%) of floats seeded upstream within the DWBC at Labrador Sea Water (LSW) depths[2] leaked to the interior within the Nfl basin. Much of the leakiness occurred between two large underwater capes (Fig. 3.1) in the DWBC's path: Flemish Cap (FC) and the Grand Banks of Newfoundland (GB).

Within the two-year lifespan of the floats, $\sim$ 20% of the floats that leaked out of the DWBC continued southward in the basin interior away from the boundary. Hence these additional pathways are referred to as interior pathways. These findings of DWBC leakiness and interior pathways represent a significant revision of the classical picture of deep southward AMOC transport being confined to the DWBC. Furthermore, Argo observations [*Biló and Johns*, 2018] and numerical simulations [*Gary et al.*, 2011, 2012; *Lozier et al.*, 2013] suggest that interior pathways continue south further than the 2-year ExPath observations demonstrate. *Gary et al.* [2012] shows that 75% of simulated floats initialized within the DWBC and traveling from 44 N to 30 N did so in the interior rather than within the DWBC.

Two contrasting views on the dynamical causes of interior pathways were examined hitherto: *Gary et al.* [2011] have shown that within realistic numerical models and in hydrography, interior pathways were largely collocated with Eulerian recirculation gyres, elevated eddy kinetic energy, and decreased potential vorticity gradients [see also *Lozier*, 1997], all qualitatively consistent with previous theory of eddy-driven gyres [*Rhines and Young*, 1982a]. Furthermore, in the eddy-resolving model examined in *Gary et al.* [2011], eddy fluxes explained a large fraction of the potential vorticity balance. In contrast, *Pedlosky* [2018] has shown, in the context of an idealized, steady, flat-basin model, that interior pathways are necessary somewhere in the domain to pro-

[2] LSW, formed mainly in Labrador Sea deep convection events, comprises the NADW upper component, typically $\approx$ 400 – 2000 m [*Yashayaev and Loder*, 2016; *Bullister et al.*, 2013]. The lower component is Overflow Water [*Talley*, 2011].

vide westward flow into the boundary current at all latitudes to its south; That is since inertial boundary currents need inflow from the east to avoid Rossby wave energy radiation away from the boundary

Previous studies have thus addressed the locations of DWBC leakiness, interior pathways trajectories, as well as interior pathways dynamics. In contrast, the mechanism underlying the leakiness itself remains unclear. In the following paragraphs, we review four hypotheses that have been posited in the literature.

1. DWBC-NAC interactions. The DWBC and the more energetic, surface-intensified North Atlantic Current (NAC, an extension of the Gulf Stream), pass quite close to each other in the GB-FC area. The currents come especially close together at the southern tip of the GB, and at the southeast corner of FC, where a large fraction of the floats leaked out of the DWBC. Therefore, interaction between these currents could plausibly cause material to leak from the DWBC [*Fischer and Schott*, 2002; *Lavender et al.*, 2005; *Bower et al.*, 2009, 2011]. The high eddy kinetic energy (EKE) values measured [e.g., *Carr and Rossby*, 2001] near the GB region and east of FC imply that the loss of floats from the DWBC may be eddy-driven. Additionally, the surface-intensification of EKE in the region suggests that the eddies result from instabilities of the surface-intensified NAC.

2. Inertial separation. Current systems throughout the Nfl region are strongly steered by topography, including the surface-intensified NAC and the DWBC [*Rossby*, 1996; *Kearns and Paldor*, 2000; *Fischer and Schott*, 2002; *Lavender et al.*, 2005]. Boundary currents approaching coastal bends may separate from the coast if they have sufficient inertia [*e.g. Ou and De Ruijter*, 1986; *Klinger*, 1994]. *Pickart and Huang* [1995] examined the inertial downstream adjustment of a DWBC-like current to changes in bathymetry in a steady, semigeostrophic, 1.5 layer model. They found that a substantial fraction of the current volume flux was lost to offshore or to a recirculating component, although these solutions lay outside the formal regime of applicability of the semigeostrophic model.

3. SCVs. Previous studies have found that material may leak from boundary currents via shedding of Submesoscale Coherent Vortices (SCVs) [*McWilliams*, 1985; *D'Asaro*, 1988; *Bower et al.*, 1997]. Bottom-reaching prograde boundary currents (propagating left of inshore in the northern hemisphere) can generally be expected to develop negative vorticity near the bottom boundary layer due to bottom drag [*Molemaker et al.*, 2015]. If the prograde boundary current then separates from the slope, e.g., at a bathymetric cape, the negative vorticity in the bottom boundary layer can cause a roll up into an anticyclonic SCV. Of the ExPath float data set, *Bower et al.* [2013] indeed found that three floats became trapped within anticyclonic SCVs formed at the southern tip of the GB.

4. Instabilities of the DWBC. Oceanic boundary currents may be unstable, and therefore intrinsically favor leakiness [*e.g. Cimoli et al.*, 2017]. Motivated by the observed leakiness around FC and GB, the effect of horizontal curvature of bathymetry (and streamlines) upon baroclinic instability was examined by *Solodoch et al.* [2016], in a 2-layer Quasi-Geostrophic model. They found that uniform parallel flow over curved bathymetry has similar baroclinic modal instability growth rates to the case of rectilinear bathymetry [i.e., the extended Phillips model, *Mechoso*, 1980], if the mean flow has a weak barotropic component. The growth rate generally diminishes with increasing mean barotropic flow, an example of the Barotropic Governor effect [*James*, 1987] in the presence of mean strain.

Based on Eulerian transport measurements at southeast FC and at southeast GB, *Mertens et al.* [2014, hereafter M14] estimated that out of $\approx$ 30 Sv of southward flowing NADW at southeast FC, 15 Sv are lost offshore before the southern tip of the GB. *Biló and Johns* [2018] analyzed interior pathways of LSW based on Argo data, and found that of the water leaked from the DWBC within the Nfl basin, 9.3 ± 3.5 Sv recirculates within the subpolar basin, while 3.2 ± 0.4 Sv continues eastward. These studies therefore show that DWBC leakiness has a significant (on the order of multiple Sverdrups) uncompensated component, *i.e.*, that there is a net loss of mass from the DWBC, rather than simply an exchange of mass with the ambient ocean. This defines a distinction between compensated and uncompensated leakiness, which we shall use in what follows.

In this paper we focus on DWBC leakiness in the Nfl basin, rather than on the interior pathways which follow leakiness. We combine a new regional model of the northwest Atlantic with historical observations to characterize the leakiness process in detail, and to investigate the mechanisms via which it occurs. In section 3.2 we describe the regional model, a particle advection code, and the observational datasets used in this study. In section 3.3 we diagnose the leakiness of the DWBC around FC, using both Lagrangian trajectories (section 3.3.1) and Eulerian-mean flow patterns (section 3.3.2). We then quantify the variability in the patterns of leakiness (section 3.3.3) and use budgets of PV (section 3.3.4) and energy (section 3.3.5) to investigate the relative roles of mean flows and variability in driving the leakiness. In section 3.4 we relate our results to the mechanism of leakiness (1-4) summarized in this section, and we put forward a hypothesis for the dependence of leakiness on the geometry of the continental slope. In section 3.5 we summarize our findings and conclude.

3.2 Methods

3.2.1 Numerical Model

We use the Regional Oceanic Modeling System (ROMS), which solves the Boussinesq primitive equations with a free surface [*Shchepetkin and McWilliams*, 2005]. ROMS is appealing for use in modeling areas of varying bathymetry, such as the path of the DWBC in the Nfl basin, due to the combination of terrain-following coordinates that allow fine resolution of the bottom boundary layer and accurate pressure gradient calculation [*Shchepetkin and McWilliams*, 2011] to minimize spurious along-slope flows. The specific ROMS branch we use is the Coastal and Regional Ocean Community (CROCO) branch [*Debreu et al.*, 2012].

We designed a North Atlantic domain ROMS configuration (hereafter GB_B), with the Nfl basin close to the domain center. The model domain is shown in Fig. 3.1, along with the barotropic

(depth-averaged) velocity magnitude averaged over model year 16. Several important topographic features discussed below are annotated in the figure. The domain extends to and beyond the Mid-Atlantic Ridge on the east, and to the Labrador and Irminger Seas on the north. The Gulf Stream enters from the western boundary, following its separation from Cape Hatteras within the parent grid (discussed below).

The GB_B horizontal resolution is approximately 2.5 km, which is small compared to the first baroclinic Rossby radius of deformation ($R_d \approx 10 - 20$ km) in the Nfl basin [*Chelton et al.*, 1998]. Therefore, the model configuration resolves the mesoscale, and possibly a portion of the submesoscale. Fifty (terrain-following) vertical levels are used. At mid-depths, the typical resolution is then $\approx$ 100 m in the deep ocean, and finer in shallower areas, e.g., the DWBC path along the continental slope. Top and bottom coordinate stretching (with stretching factors $\theta_s = 6$ and $\theta_b = 4$, respectively) further increases vertical resolution near the top and bottom boundaries. Vertical resolution is approximately 5 m near the surface. At continental slope to continental rise seabed depths (1000 $-$ 4000 m), vertical resolution near the bottom is $\approx$ 15 $-$ 50 m , respectively. The model bathymetry is derived from the 30 arc second-resolution Shuttle Radar Topography Mission global product, SRTM30_PLUS [*Becker et al.*, 2009], processed for use in ROMS as described by *Renault et al.* [2016b].

Boundary conditions at open boundary segments are prescribed using an offline nesting approach [*Mason et al.*, 2010]. Model variables at the open boundaries are relaxed to values from a coarser parent domain, using radiation-like boundary conditions. These are as described in *Marchesiello et al.* [2001], except for the barotropic momentum and surface elevation boundary conditions, which are described in *Mason et al.* [2010]. The parent (ROMS) solution is described in *Renault et al.* [2016b]. Its domain covers the entire North Atlantic ocean, with $\approx$ 5 km horizontal resolution in GB_B region, and 50 vertical levels as well. The parent configuration was spun-up for 14 years using climatological forcing, and subsequently solved for five additional years with time-dependent forcing, corresponding to calendar years 2000-2004. For boundary data used in the nesting procedure, in the first four GB_B years we use the last four parent solution years,

since they were conducted with time dependent forcing. For each following four-year GB_B period (years 5-8, 9-12,13-16), we recycle the same four years of boundary data from the parent solution. Thus inter-annual variability is statistically limited in the model (see discussion in supplemental section 3.6.3). To minimize shock-like numerical artifacts when the forcing cycle is restarted, the last 10 samples of the boundary data cycle (last 10 days of December 2004) are linearly interpolated toward its first sample (January 1st, 2001). Because radiation boundary conditions are generally not completely free of artifacts, such as boundary reflections, sponge layers are applied near the open boundaries, with a maximum viscosity of 300 m^2/s at the boundary, and a decrease as a cosine quarter cycle to zero over a distance of 25 km from the boundary. Air-sea fluxes are accounted for using bulk formulae [e.g., *Fairall et al.*, 1996], with the atmospheric state interpolated from 6-hour interspersed CFSR reanalysis data [*Saha et al.*, 2010].

Vertical sub-grid scale mixing is parameterized via the K-Profile Parameterization [*Large et al.*, 1994]. For the tracer advection scheme we initially used the split-rotated scheme "RSUP3", with the diffusive componenta aligned with the local neutral plane [*Lemarié et al.*, 2012]. However, we found severe numerical issues in our configuration (supplementary section 3.6.2). Therefore, we reverted to isopotential alignment of the diffusive part of RSUP3 [*Marchesiello et al.*, 2009]. We integrate the model for 16 ocean years, and save 2-day averages of output variables, on which all presented analysis are performed offline. Domain-integrated kinetic energy and Available Potential Energy [*Vallis*, 2017] are examined (not shown), to probe the degree to which the model has spun-up. Both quantities have pronounced seasonal cycles, with no clear interannual drift, i.e., the solution appears close to a statistical steady state. Further model validation is presented in supplemental sections 3.6.3-3.6.6. Given that statistics of domain integrated energy, water mass properties, and circulation pattern exhibit little variation after year 8 (supplemental section 3.6.3), the presented results (e.g., mean quantities) are based on model years 9-16, unless stated otherwise.

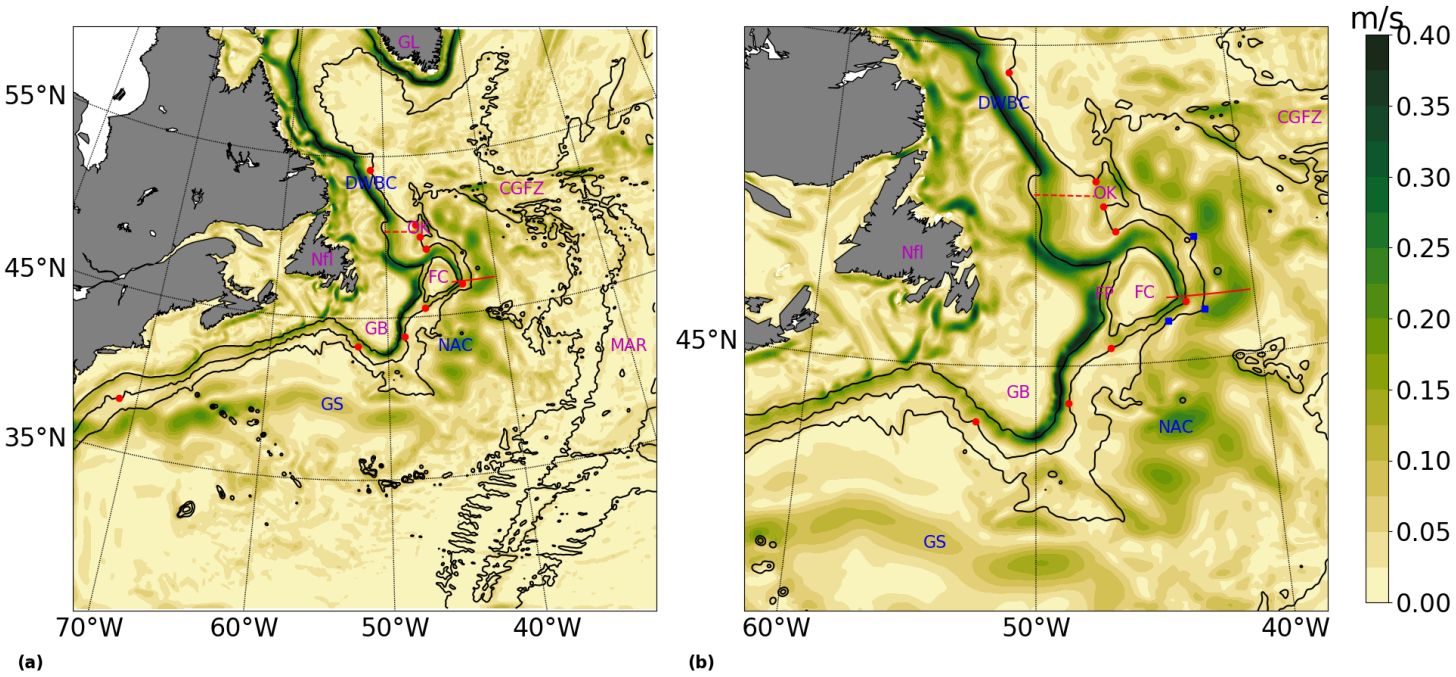

Figure 3.1: Model depth-averaged speed, averaged over years 9-16. Panel (a) shows the full domain of the numerical solution (section 3.2.1). Panel (b) focuses on the area implicated in leakiness in the DWBC (section 3.1). The 1, 3, and 4 km depth isobaths are marked with thin black lines. Geographic features marked in the figure: Newfoundland (Nfl), the Grand Banks of Newfoundland (GB), Flemish Cap (FC), Flemish Pass (FP, the $\approx$ 1150 m deep channel west of FC), Orphan Knoll (OK), the Mid-Atlantic-Ridge (MAR), the Charlie-Gibbs Fracture Zone (CGFZ), and Greenland (GL). Major currents: Gulf Stream (GS), its continuation as the North Atlantic Current (NAC), and the Deep Western Boundary Current (DWBC). The NAC extends northward, approximately along and meandering about the 4.2 km isobath, from the Gulf Stream termination about -45 E. The solid red line east of FC, around 47 N, marks the location of the vertical sections shown in Fig. 3.11. The dashed red line west of OK, around 50 N, marks the model particle deployment line (OKL, see text for details), also shown in Fig. 3.3. Red filled circles mark points of interest along the 3 km isobath, shown in Fig. 3.4. Blue filled squares on the 4 km isobath in panel b schematically mark the leakiness hotspots identified here and defined in the text: (from north to south) Northeast Corner (NEC), Southeast Corner (SEC), and Southern Face (SF).

3.2.2 Float datasets

Two observational datasets of subsurface Lagrangian floats are used here. One is "Export Pathways from the Subpolar North Atlantic Experiment" (ExPath) data set [*Furey and Bower*, 2009; *Bower et al.*, 2011]. In ExPath, RAFOS floats were seeded within the DWBC region west of Orphan Knoll (Fig. 3.1). These are isobaric (i.e., approximately depth-maintaining) floats that are tracked by acoustic sound sources and hence do not need to surface during their trajectory (unlike Argo floats, see below).

Relative to float datasets used in prior analyses of DWBC leakiness in Newfoundland [*Lavender et al.*, 2000; *Fischer and Schott*, 2002], the ExPath dataset has the advantages that the floats used are not profiling (eliminating contamination of velocity from surfacing), and that the floats were all seeded within the DWBC and just north of the leakiness area, whereas previous floats were seeded further upstream in the Labrador sea. In numerical simulations the isobaric nature of simulated ExPath-like floats did not appreciably change the interior pathways statistics compared with 3D simulated floats [*Bower et al.*, 2011].

Approximately equal fractions of floats were ballasted for 700 $dbar$, and for 1500 $dbar$ (1 $dbar \approx 1\ m$) depth. Each float drifted for two years before resurfacing. We analyze the trajectories of the fifty-five floats deemed usable in *Furey and Bower* [2009]. Floats positions are generally available with daily resolution. Exceptions include the positions of floats within Flemish Pass (the channel running between FC and GB), which was shielded from sound sources. Due to failure of sound sources during part of the experiment, position triangulation for some trajectories in the continental slope area south of FC were also not possible [*Furey and Bower*, 2009].

The second dataset consisted of a subset of Argo floats [*Riser et al.*, 2016]. Argo floats drift at a set "parking depth". After a typical period of 9 days, the float first descends to 2 km depth, and then ascends to the sea surface, while taking hydrographic measurements. At the surface the float transmits collected data via satellite communication. Then the float descends back to its parking

depth, restarting the cycle. We compiled a dataset of all Argo floats that have ever crossed the DWBC cross-section along which the ExPath floats were deployed. Specifically, the chosen area is west of Orphan Knoll, between latitudes 49.5 to 50.5 N, and longitudes 49.6 to 47.7 W. We find 67 floats that meet this criterion, with parking depths between $800-2000$ m, between the years 1998-2017. Specifically, the number of floats that have parking depths $(800, 1000, 1500, 2000)$ m, respectively, is $(3, 43, 18, 3)$. Unfortunately, not all floats in the assembled dataset have actual pressure readings stored from their drift periods, in which case we rely on the programmed parking depth. Despite this caveat, we find this dataset to be a useful complement to the ExPath observations.

3.2.3 Particle advection

The phenomenon in question, Lagrangian leakiness, is most directly addressed in a Lagrangian framework. For that purpose, and for comparison with the float observations, we seed and track passive particles in the velocity fields obtained from the numerical model described in section 3.2.1. We developed a Fortran code (named "TrajInt", for trajectory integration) that allows 3-dimensional (3D) integration of particle trajectories given their initial positions at a particular time. Particle advection experiments were performed offline, i.e., after running GB_B (section 3.2.1). The main features of the code are described here. The particles are passively advected by solving the advection ordinary differential equation $\partial_t \underline{x} = \underline{u}$, where $\underline{x} = \underline{x}(t)$ is the particle position at time t, and $\underline{u}$ is the ROMS velocity field interpolated to time t and position $\underline{x}$. The temporal interpolation is done using cubic splines, the spatial interpolation is tri-linear, and time stepping is done using the classical fourth-order Runge–Kutta method. The chosen advection time step is half an hour, which is 1/96 of the GB_B saved output rate (2-day averages). At characteristic speeds within the Nfl basin at mid-depth of up to 0.3 m/s, the maximal displacement within a TrajInt time step is $\approx$ 0.5 km, or one fifth of a grid cell side length. Therefore, the time step is likely sufficient to resolve the model output space and time scales. We confirmed this via sensitivity experiments in which trajectories were recomputed with refinement (repeated halving) of the time step size, and found that the differences in the trajectories were smaller than one

grid point for at least 10 model days after initialization, when the larger time step is $\lesssim$ one hour. This time period is comparable to the observed velocity auto-correlation time in sub-thermocline depths in the northwest North Atlantic [*Böning*, 1988; *Lumpkin et al.*, 2002], hence we consider the convergence satisfactory.

We conduct several particle advection experiments. Floats are initialized along a line (Figs. 3.1, 3.12) within the DWBC, west of Orphan Knoll (hereafter OKL), close to the seeding locations of ExPath floats [*Furey and Bower*, 2009], between the 1 and 2.8 km isobaths, and with an initial depth at least 300 m above the bottom. The specified line is chosen since it is located upstream of Flemish Cap, where much of the leakiness occurs, and for comparison with the ExPath dataset (section 3.2.2). The mean model velocity at the seeded depths along OKL is everywhere downstream (approximately southward) within the DWBC, except for a clockwise recirculation at Orphan Knoll.

Experiment 1 (Exp3d) employs a large number of deployments ($\approx 550,000$ particles) to get statistically robust estimates of leakiness metrics. We deploy up to 1000 particles at depths of 700 and 1500 m each, uniformly distributed along the entire OKL section, every 10 days between years 9 and 16. At each seeding date, particles were only seeded along the OKL in locations where the meridional component of the 2-day averaged velocity was directed southward.

These particles are advected for 200 days each. Because the velocity auto-correlation (integral) time scale in this region is generally between 5 and 10 days [*Böning*, 1988; *Lumpkin et al.*, 2002], seeding more often than 10 days would not likely have been effective in terms of relative contribution of additional effective degrees of freedom. Experiment 2 (Exp3dMean) uses the time mean (years 9-16) velocity field in place of the 2-day-averaged output velocity field. Its purpose is to delineate the mean offshore flow pathways and compare time-mean with variable leakiness. We deploy 1000 particles each at depths of 700 and 1500 m, uniformly distributed along the OKL section. Only floats that drift southward past Orphan Knoll are considered here to delineate the mean DWBC trajectory, and thus are used in the analysis of Exp3dMean.

3.3 Results

3.3.1 Lagrangian leakiness pathways

An estimated 73 – 84% of all ExPath floats were lost ("leaked") from the DWBC to the interior before circumnavigating FC (supplementary section 3.6.7), demonstrating its relative importance in DWBC leakiness within the Nfl basin. We therefore focus mostly on the FC area in this section. Fig. 3.2a shows the trajectories of the ExPath floats around the time that each float makes its first (offshore) crossing of the 4 km isobath at FC, which is approximately the offshore limit of the DWBC. This diagnostic parameter is useful as floats which crossed offshore around FC[3] do not appear to have reentered the DWBC [see individual trajectories in *Furey and Bower*, 2009]. While some do cross the 4 km isobath back near FC, these either recirculate immediately offshore again, or travel close to the same isobath upstream, apparently entrained in the NAC.

The distribution of trajectories leaving the DWBC around FC (Fig. 3.2a) suggests that leakiness of ExPath floats occurs in three main FC sub-regions ("leakiness hotspots"): at the northeast (NEC) and southeast (SEC) corners of FC, and in the south face (SF) just following SEC. Their approximate locations are marked in Fig. 3.1b. The concentration of ExPath floats leakiness near SEC was previously reported by *Bower et al.* [2011].

At the NEC and SEC, ExPath floats leave the DWBC via trajectories that are oriented almost directly offshore. In the SF area, the offshore velocity component is weaker relative to the along-shore component, but some of the floats abruptly turn back upstream (approximately north-eastward) midway through the SF. The hotspots are approximately collocated with local maxima in topographic changes: convex curvature at NEC and SEC, and a 2-3 fold increase in bottom steepness in the SF area (section 3.4). Fig. 3.2 also shows that as floats travel offshore, they tend to turn cyclonically, consistent with vortex stretching assuming conservation of potential vorticity of the

[3] Further downstream, around GB, several floats did come back into the DWBC [*Bower et al.*, 2009].

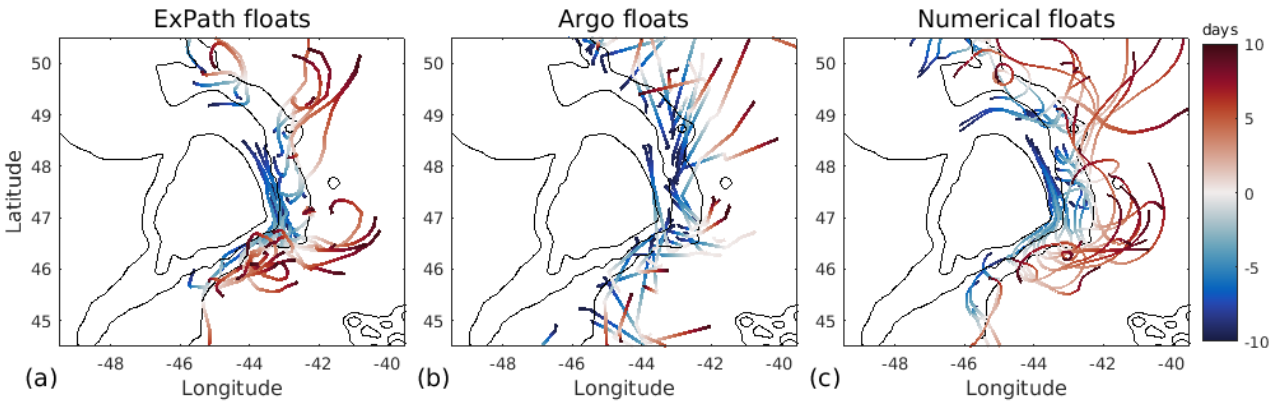

Figure 3.2: Comparison of observed and modeled float trajectories in the Flemish Cap (FC) region, centered on the time at which they crossed the 4 km isobath (section 3.3.1). Color of plotted trajectories corresponds to time (in days) relative to their first offshore crossing of the 4 km isobath. Leakage of floats out of the DWBC occurs preferentially in the convex bends of FC, and downstream from the second bend, in the region of steepening bathymetry. Physical floats are shown in panels (a) (ExPath floats) and (b) (Argo floats). These data sets are described in section 3.2.2. Panel (c) shows the trajectories of a random batch of 60 model particles from Exp3d (section 3.2.3). Temporal resolution of position data for ExPath floats, Argo floats, and the numerical particles, respectively, are 1 day, $\approx$ 9 days, and 2 hours. Continuous curves are used in all panels for visibility. The jagged appearance and deviations between day 0 position and the 4 km isobtah in panel b are due to the linear interpolation between 9 day-intervals of Argo position data.

layer below the pycnocline. The question of what sets the locations of the leakiness hotspots is discussed in Secs. 3.3.4-3.3.5 and 3.4.

We further examine Lagrangian pathways in observations, by performing a similar analysis (Fig. 3.2b) on Argo floats traveling south within the DWBC [4]. The subset of Argo floats is described in section 3.2.2. While the temporal resolution of Argo floats locations is an order of magnitude lower, the clustering of the Argo floats' crossings of the 4 km isobath is qualitatively similar to that of the ExPath floats.

Next we examine Lagrangian pathways of particles seeded within the numerical model (section 3.2.2), beginning with a small subset of the seeded particles for a qualitative visual comparison with the floats. Panel c of Fig. 3.2 is identical to panels a and b, but displaying the trajectories of a random batch of 60 model particles from Exp3d (section 3.2.3) — 30 from each seeding depth (700 and 1500 m). The leakiness hotspots and other related properties described above for the ExPath floats are largely reproduced in this case. These results are consistent in other random samples of the floats from Exp3d (not shown).

To examine leakiness within the full set of ($\sim$ 550,000) model particles, we first plot the distribution of the locations at which each particle in Exp3d first crossed from the DWBC to offshore of the 4 km isobath (Fig. 3.3a). We find the same clustering as suggested in Fig. 3.2, i.e., the offshore crossing density is highest at the NE corner, SE corner, and SF. The pattern appears qualitatively consistent with the ExPath observations (circles superimposed in the panel). For a quantitative comparison, we apply a two-sample Kolmogorov-Smirnov (KS) test. The two sample sets are the ExPath and Exp3d offshore crossing locations. We partition the 4 km isobath into consecutive 50 km long sections, and count (bin) the number of floats or particles crossing each section. The cumulative distribution function (CDF) of the ExPath floats (F_f) offshore crossings is then compared with the same CDF for the Exp3d particles (F_p). The KS test statistic, defined by $D = max_n|F_f(n) - F_p(n)|$, is then compared with the theoretical KS distribution. The result from

[4] Leakiness of profiling floats in this region was investigated by *Lavender et al.* [2000]; *Fischer and Schott* [2002] as well.

the comparison is that the two distributions are statistically indistinguishable (p value = 0.96). This indicates that the observed and modeled float trajectories are consistent with one another, to the extent that differences between them could be distinguished statistically.

Finally we calculate the Lagrangian-mean velocity, based again on the full number of Exp3d model particles. The Lagrangian mean velocity is defined for our purpose as the average velocity within a grid cell of all particles that have crossed it. Note that this is a conditional average, in that it includes solely particles that were released within the DWBC, and in that we apply a further restriction by including particles only before their first crossing of the 4.2 km isobath offshore. This differs from an Eulerian average because, for example, the velocities of parcels carried by intrusions into the DWBC from offshore will not directly contribute to the calculation. In Fig. 3.3 panels b and c, the Lagrangian mean velocity is displayed and decomposed into along and cross-bathymetry components (hereafter v_a and v_c, respectively [5]). Only statistically significant (supplementary section 3.6.8) v_a and v_c values are displayed. We similarly calculate average Lagrangian eddy kinetic energy, $EKE = \frac{1}{2}\overline{(\underline{v} - \overline{\underline{v}})^2}$, where $\underline{v}$ is the velocity of an individual particle sampled within a grid cell, and an overbar again denotes an average over all such samples within a single grid cell. In Fig. 3.3 only the results based on 1500 m-deep model particles are shown. The same diagnostics for the 700 m-deep model particles are quantitatively similar (supplementary section 3.6.9).

The along-bathymetry velocity component (Fig. 3.3b) exhibits a maximum along the path of the DWBC on the continental slope. The cross-bathymetry component (Fig. 3.3c) shows that offshore Lagrangian-mean velocities occur in patches stretching across the DWBC to its offshore edge ($\approx$ 4 km isobath) at the identified Lagrangian leakiness hotspots (NEC, SEC, and SF). The Lagrangian-mean velocity follows pathways from the DWBC core to NEC, SEC and SF, which is most easily seen via the Lagrangian-mean velocity vectors overlaid on Fig. 3.3d.

The EKE (Fig. 3.3d) is considerably lower (by roughly 50% percent) at leakiness hotspots NEC and

[5]The cross-bathymetry component v_c points toward deeper water, and the along-bathymetry component v_a is defined to point to the right of v_c, i.e., generally downstream for the DWBC.

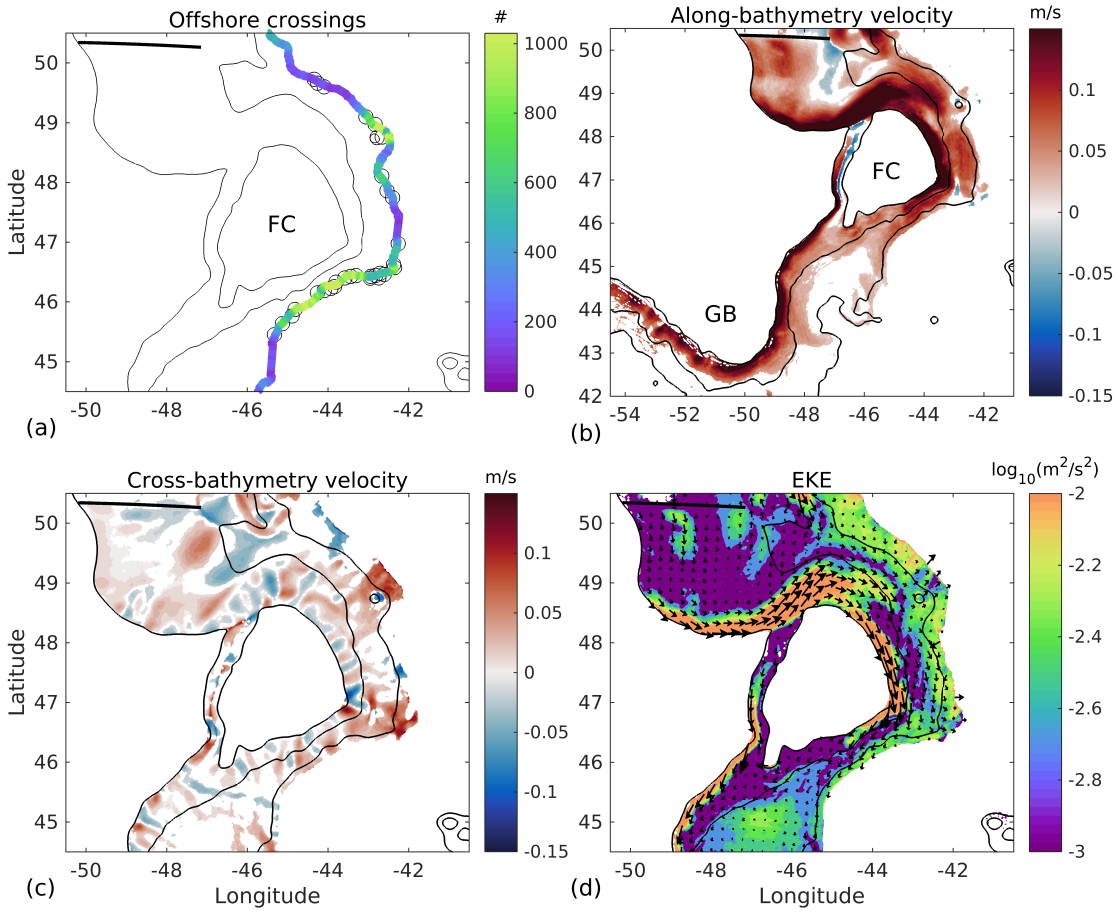

Figure 3.3: (a) Locations at which the ExPath floats (circles, both 700 and 1500 m depths) and 1500 m depth-initialized Exp3d particles (colors) first cross the 4 km isobath. The colors correspond to the number of model particles crossing the 4 km isobath at each model gridpoint along the isobath. The results for Exp3d particles initialized at 700 m depth for this and the next panel are very similar in pattern and magnitude to those shown here (supplementary section 3.6.9). (b) Lagrangian-mean along-bathymetry velocity component (positive ≈ downstream), (c) Lagrangian-mean cross-bathymetry velocity component (positive offshore), and (d) Lagrangian eddy kinetic energy (EKE) derived from the Exp3d particles initialized at 1500 m depth. Values as high as 0.04 m^2/s^2 occur in the saturated (orange) region near the 1 km isobath. In panels b-c, only statistically significant values are displayed, i.e., white patches are not associated with significant values. Lagrangian mean velocity vectors are superimposed in panel d. The 1, 3, and 4 km isobaths are marked with black contours in each panel. The deployment line (OKL) of model particles is marked by the thick black line. The bathymetric features of Flemish Cap and the Grand Banks of Newfoundland are marked by the letters FC and GB, respectively, in panels a-b.

SEC compared to adjacent patches along the same isobaths, suggesting that the cross-isobath Lagrangian transport at these hotspots is primarily due to an Eulerian-mean flow. In contrast, if the Lagrangian-mean offshore flow were an eddy-forced or eddy-rectified flow, one would expect it to be associated with elevated EKE values. That may be the case at SF, where EKE is indeed locally elevated (see subsections 3.3.3 and 3.3.5 as well).

In summary, the analysis presented in this section shows that in observations Lagrangian leakiness trajectories are clustered in a few key locations (NEC, SEC, SF). Additionally, the numerical model compares well with the observations, and using a much larger number of (numerical) particles demonstrates that these leakiness hotspots are associated with high Lagrangian mean offshore velocities, offshore deflections of the peak along-shore velocity (v_a) upstream, reductions in the magnitude of v_a, and (except at SF) low variability (EKE).

3.3.2 Eulerian characterization of leakiness

In section 3.3.1 we quantified the Lagrangian leakiness via the Lagrangian-mean offshore flow. The Lagrangian-mean flow may be locally represented as the sum of the Eulerian-mean flow, and the rectified eddy flow. In the present section we analyze the Eulerian-mean flow over the same time period (years 9–16), and thereby deduce the contribution of rectified eddy transport to the Lagrangian-mean offshore flow.

We begin by examining cumulative (Eulerian) offshore transport on the 3 km isobath (Fig. 3.4) [6], in comparison with the observational estimate of M14 (section 3.1). As in M14, we decompose the transport into densities greater or smaller than $\sigma_\theta = 27.68$ kg/m^3 (Fig. 3.4a), approximately the upper boundary of LSW. This partitioning is also useful because the bias in model isopycnal depths significantly decreases for $\sigma_\theta < 27.0$ kg/m^3 (supplemental section 3.6.3 and Fig. 11).

[6] The same calculation applied to the 4 km isobath yields very similar results (e.g., $\sim$ 15 Sv offshore flux at FC). The 3 km isobath is used here since it extends further north past Orphan Knoll.

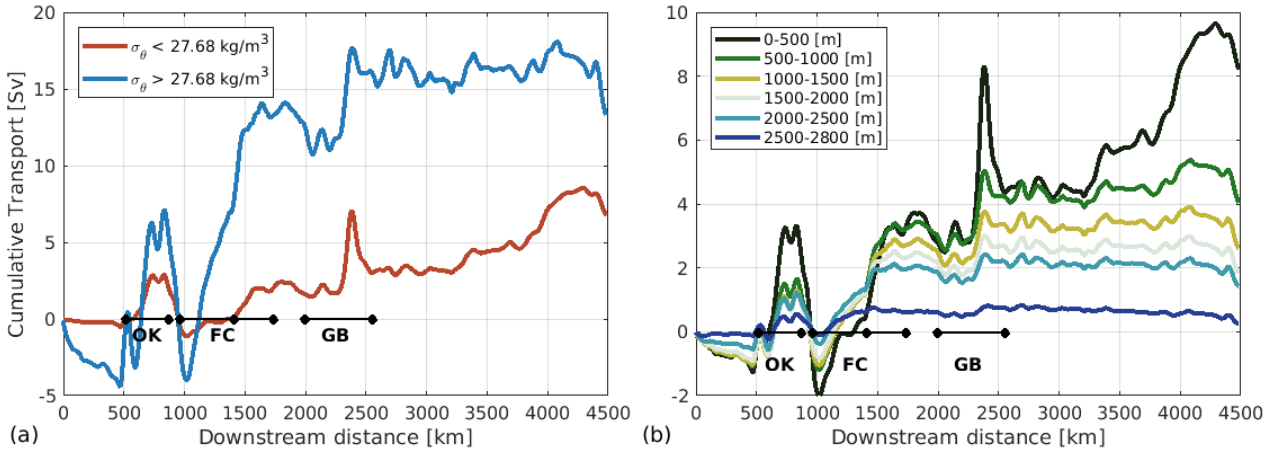

Figure 3.4: Cumulative offshore transport in (a) density layers and (b) depth layers, along the 3 km isobath, averaged over model years 9-16. Note that the deepest layer in panel b is thinner (300 m) than all other layers (500 m). Black circles correspond to the red circles marked on the 3 km isobath in Fig. 3.1, with the furthest upstream and downstream circles marking the section's beginning and end. Other circles mark points around FC and GB. The middle of the three circles labeled "FC" marks the SE corner (see section 3.3.1).

Although there is a substantial offshore transport (~4 Sv) at OK, it is compensated by shoreward flow immediately downstream, resulting in negligible net offshore transport around OK (Fig. 3.4a). In contrast, around FC there is an offshore transport of $13 - 16$ Sv, which is uncompensated in the $\sigma_\theta \geq 27.68$ kg/m^3 density range. The offshore transport rate (slope of the curve) greatly increases around the SE corner and downstream from it (around SF), where much of the Lagrangian leakiness is clustered. Additionally, $3 - 5$ Sv are lost around the southern tip of the GB. The cumulative loss from FC to GB is consistent with the M14 estimate, and our analysis further constrains (within the numerical model) the along-slope distribution of the offshore transport. Results for $\sigma_\theta \leq 27.68$ kg/m^3 show a similar pattern, with $\sim$ 3 Sv lost around FC, and $\sim$ 1 Sv lost around GB. An examination of the cumulative offshore transport in depth layers (Fig. 3.4b) reveals that the transport is largely depth independent down to 2.5 km depth (and slightly surface-intensified).

We now examine the Eulerian-mean circulation patterns around the DWBC leakiness hotspots.

Fig. 3.5 shows the Eulerian-mean velocity streamfunction on two representative isopycnal surfaces: $\sigma_1 = 32.43$ and $\sigma_2 = 37.014$ kg/m^3, averaged over years 9–16. The upper surface lies between depths of 800 and 1750 m in the DWBC (figure 3.5a), similar to ExPath floats and to the Lagrangian analysis in the previous section. It also corresponds to typical LSW depths [*Bullister et al.*, 2013; *Mertens et al.*, 2014]. The lower surface lies between depths of 1800 and 2700 m in the DWBC, corresponding to lower LSW or upper Overflow Water. These surfaces are hereafter referred to as LSW and lLSW for clarity. However, we do not suggest they correspond accurately to observed water mass properties (supplemental section 3.6.3). The streamfunction is calculated by an adaptation of a flood-fill algorithm (supplementary section 3.6.10). Closed streamlines with inner minima (maxima) are cyclonic (anticyclonic) recirculations, and streamfunction values are only meaningful up to an addition of a global constant.

Fig. 3.5 shows that the Lagrangian leakiness hotspots (NEC, SEC, SF; section 3.3.1) coincide with mean streamlines exiting the DWBC. This indicates that the leakiness is at least partially attributable to Eulerian-mean offshore flows at the NEC, SEC and SF hotspots. At NEC separating streamlines are apparent only in the deeper density surface ($\sigma_2 = 37.014$ kg/m^3) plotted, although they appear if more streamlines are plotted in the shallower density surface ($\sigma_1 = 32.43$ kg/m^3) as well. This is consistent with the larger offshore flux near SEC (figure 3.4).

Fig. 3.5 also reveals the existence of three closed cyclonic recirculations with radii of $O(100$ km) immediately offshore of the DWBC around FC. These recirculations stand between the DWBC and the NAC, complicating the potential NAC influence on DWBC leakiness (mechanism 1, section 3.1). Similar cyclonic recirculations around FC were reported in circulation estimates based on profiling floats [*Lavender et al.*, 2005], and in numerical simulations by *Xu et al.* [2015], which noted that the recirculations are consistent with the distribution of Tritium (see also Fig. 2a in *Biló and Johns* [2018], and Fig. 1a in *Getzlaff et al.* [2006]). The separating streamlines at NEC and SEC do not return to the DWBC, but rather turn (around the offshore recirculations) cyclonically east and northward post separation, and appear to join or travel adjacent to the NAC. The cyclonic turning of separated streamlines is visually similar to the cyclonic trajectories of the Lagrangian

particles after they have left the DWBC (Fig. 3.2). These circulation patterns (including separation and recirculation) are similar on both density surfaces shown in Fig. 3.5, which are separated by around 1 km vertically. Similar results are found when the streamfunction is computed for other, intermediate density surfaces, or for the depth-integrated flow (not shown).

We investigated the role of eddies transport by comparing the thickness-weighted averaged velocity streamfunction [*Young*, 2012] to the simple time-averaged velocity streamfunction discussed above in this subsection. The patterns (not shown) and speeds are nearly indistinguishable between the two different averages. The mean speed difference in the area shown in figure 3.5 is 0.002 m/s. The maximal difference ($\approx$ 0.01 m/s) occurs around the SF hotspots and in the confluence zone offshore of SF. This is consistent with the greater EKE diagnosed at SF relative to NEC or SEC from model particle motions (section 3.3.1). Thus, the eddy-rectified circulation is generally negligible in comparison with the mean Eulerian circulation on these isopycnals. This is consistent with the qualitative similarity between the Lagrangian-mean (section 3.3.1) and Eulerian-mean (figure 3.5) offshore flow velocity distributions. Furthermore, it suggests that the Eulerian-mean flow accounts for the offshore transport of Lagrangian particles at the leakiness hotspots.

3.3.3 Robustness of spatial patterns of separation

Diagnostics presented in the previous two subsections suggest that leakiness occurs, at least partially, as a spatially localized and temporally steady (time-mean) offshore flow pattern. In this section we examine the following question: how representative is the diagnosed time-mean circulation pattern of the time-varying circulation patterns? The answer permits dynamical interpretation of the mean circulation; for example, if the mean offshore flow is locally the result of infrequent but intense offshore flow events, while most of the time the velocity is inshore, the mean flow state itself would be atypical. Such a scenario may be consistent with rare but intense external events, e.g., NAC-derived eddies propagating inshore, causing the mean offshore flow.

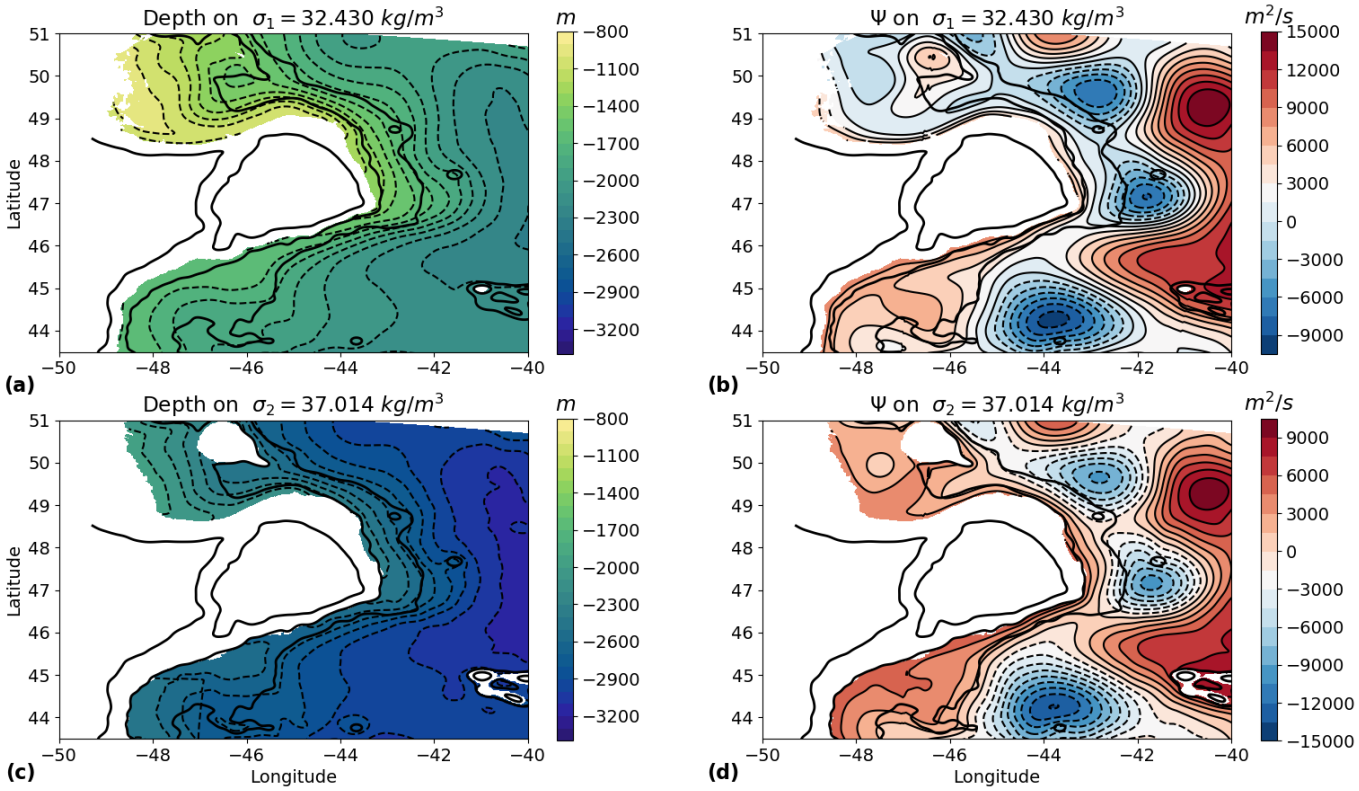

Figure 3.5: (a) Mean depth of the $\sigma_1 = 32.43\ kg/m^3$ (LSW) isopycnal in the vicinity of Flemish Cap. (b) Velocity streamfunction (section 3.3.2, and supplemental section 3.6.10) calculated over the same isopycnal layer as in (a). Panels (c–d) are identical to panels (a–b), but for the isopycnal layer $\sigma_2 = 37.014\ kg/m^3$ (lLSW). The 1, 3, and 4 km isobaths are shown in thick black contours. The depths of the isopycnal surfaces (a) and (b) in the displayed area, averaged between the 1 and 4 km isobaths, are 1450 m and 2420 m, respectively. Note that the depth of the upper surface (a) is as low as 800 m near the launch position of the Lagrangian particles (section 3.2.2)

.

We will see, however, that the mean circulation patterns are in fact statistically quite representative of instantaneous patterns.

In Fig. 3.6 we present statistics of the cross-bathymetry flow as a function of distance along the 4 km isobath. The velocity is averaged between depths of 700 m and 1500 m, but the findings are representative of velocity statistics in other layers between 500 m depth and the sea floor (not shown). Panel (a) shows the Eulerian mean, median, and mode of the cross-bathymetry flow, as well as the Exp3d Lagrangian mean cross-isobath velocity v_c. Here the mode was defined relative to 1 cm/s resolution binning of all samples. Panel (b) shows a histogram of the cross-isobath velocity at SEC, the location of which is marked in panel (a) and in Fig. 3.1b. In constructing the histogram, all time samples from locations up to two grid cells distant from the indicated point along the isobath were used. The error in estimation of the Eulerian mean, $std/\sqrt{N_e}$, is everywhere < 0.01 m/s, where std is the standard deviation over the $N = 1460$ time samples (years 9-16, 2 day intervals), and $N_e = N/(10/2)$ is the number of effective degrees of freedom, assuming an integral timescale of 10 days (section 3.2.3). Hence, the mean offshore velocity at NEC, SEC, and SF, is statistically significant ($p < 0.05$).

The Eulerian mean and median are very close to one other along this section, and particularly so at the mean leakiness hotspots (Fig. 3.6a). The mode fluctuates strongly, but generally follows the mean values well over length scales $\gtrapprox 50-100$ km. The mode is very close to the mean at the SEC and (slightly less so at) NEC. Fig. 3.6b shows that offshore flow is indeed the typical occurrence, and the distribution is quite symmetric around the mean. The distributions at NEC (not shown) and SEC are both center-heavy (an excess kurtosis magnitude of $|\kappa| \approx 0.25$), and symmetric (a skewness magnitude of $|\gamma| \leq 0.1$). At SF the distribution (not shown) remains center-heavy, although to a lesser degree: ($\kappa = 0.75$ and $\gamma = 0.5$). In summary, the Eulerian-mean offshore flow is statistically representative, i.e., typical values are close to the mean. In supplemental section 3.6.11 we present a cluster analysis that demonstrates that the spatial Eulerian pattern of mean separation (including separating streamlines) is statistically representative as well, in a similar sense to that described above.

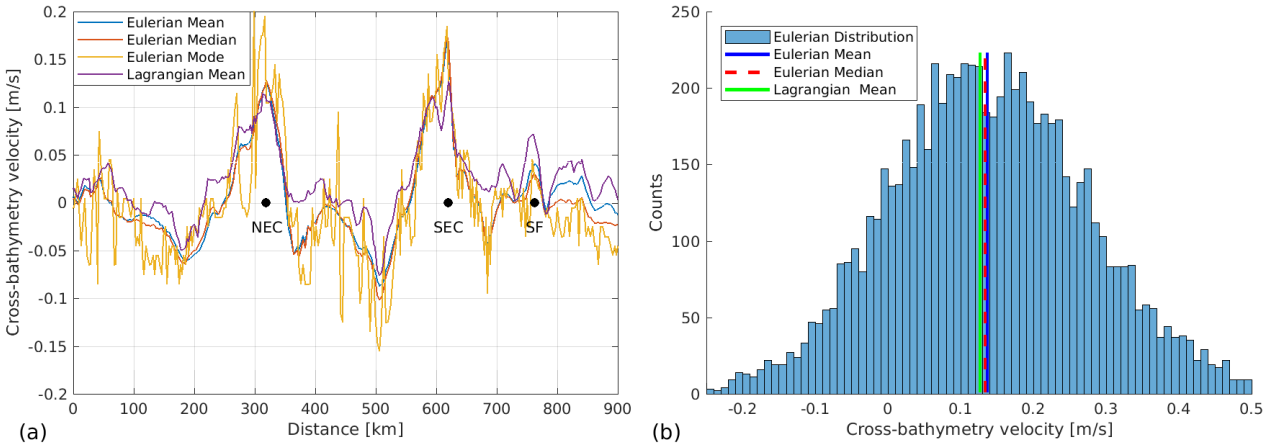

Figure 3.6: (a) Statistics of cross-bathymetry velocity component averaged between depths of 700 and 1500 m, as a function of distance along the 4 km isobath around Flemish Cap. The Northeast corner (NEC), Southeast Corner (SEC), and South-Face (SF) leakiness hotspots are labeled, and correspond to the locations marked by blue squares in Fig. 3.1b. The mean, median, and mode of the Eulerian velocity distribution at every location is shown, as well as the Lagrangian mean derived from Exp3d. The latter is averaged between the two particle populations (initialized at 700 and 1500 m depths). (b) Histogram of the Eulerian cross-bathymetry velocity at SEC (location marked in panel a), with vertical lines indicating the Eulerian mean, Eulerian median and Lagrangian mean cross-bathymetry velocities.

The Lagrangian and Eulerian means are very similar around most of FC, confirming that the eddy-induced rectified offshore flow is relatively low in this area (Figure 3.6a). Along eastern FC outside of the hotspots the Lagrangian-mean is generally slightly higher, increasing mean leakiness there (compare with Fig. 3.4). Another exception is that at SF the Eulerian mean only accounts for around 50% of the Lagrangian mean offshore velocity, suggesting that the remainder of the transport is due to the rectified eddy mean flow. This is consistent with the elevated Lagrangian-mean EKE at SF (section 3.3.1). However, the Lagrangian mean offshore flow is also generally weaker at SF than it is at NEC or SEC.

We emphasize that although Lagrangian and Eulerian mean velocities are almost identical at the leakiness hotspots, particularly NEC and SEC, time variability nonetheless has a non-negligible in-

fluence on the Lagrangian leakiness. In Exp3d, more than 90% of the particles are exported across the 4 km isobath before they can reach the GB (longitude $\approx -55\ E$). In contrast, in Exp3dMean, in which particles are advected by the time-mean velocity fields, only $\sim$ 59% (35%) of the particles initialized at a depth of 700 m (1500 m) are exported across the 4 km isobath before they can pass GB (longitude $\approx$ -55 E). Therefore flow variability contributes substantially to the leakiness. This contrasts with the high quantitative similarity demonstrated between Eulerian and Lagrangian mean offshore flow, and the relatively low magnitude of eddy-rectified offshore flow.

Although mean streamlines leave the DWBC offshore at the three identified leakiness hotspots, fewer particles in Exp3dMean reach those hotspots. This is to be expected given approximate planetary vorticty (f/h) conservation. Indeed, the DWBC at and upstream of the particle seeding locations [*Fischer et al.*, 2004; *Bower et al.*, 2011] is confined inshore of the 3 km isobath, but around FC (figure 3.11) and GB [*Schott et al.*, 2004] it extends to the 4 km isobath. With temporal variability (i.e., in Exp3d), particles cross f/h lines and populate the mean leakiness hotspots offshore of the 3 km isobath, where mean velocity can propel them further offshore. This may be a manifestation of the phenomenon known as chaotic advection [e.g., *Shepherd et al.*, 2000; *Rypina et al.*, 2010]. Chaotic advection [*Aref*, 1984] refers to complex Lagrangian trajectories which often result even from simple Eulerian fields by the kinematics of superimposed eddies and non-uniform mean circulation.

3.3.4 PV distribution and balance

Given the separation of the mean flow from the DWBC into the interior, one might ask: how does the mean flow cross the dynamical barrier presented by the cross-bathymetry potential vorticity (PV) gradient? To address this, we now examine the thickness-weighted-averaged (TWA) PV budget [*Smith*, 1999; *Young*, 2012]. The TWA of a variable a, and its deviation from TWA, are defined by $\hat{a} = \frac{\overline{ha}}{\overline{h}}$, and $a'' = a - \hat{a}$, respectively. Here an overbar denotes a time-average and $h = -\rho_0 \frac{\partial z}{\partial \rho}$ is the isopycnal "thickness density", where $\rho_0 = 1027.4$ kg/m^3 is a constant reference density.

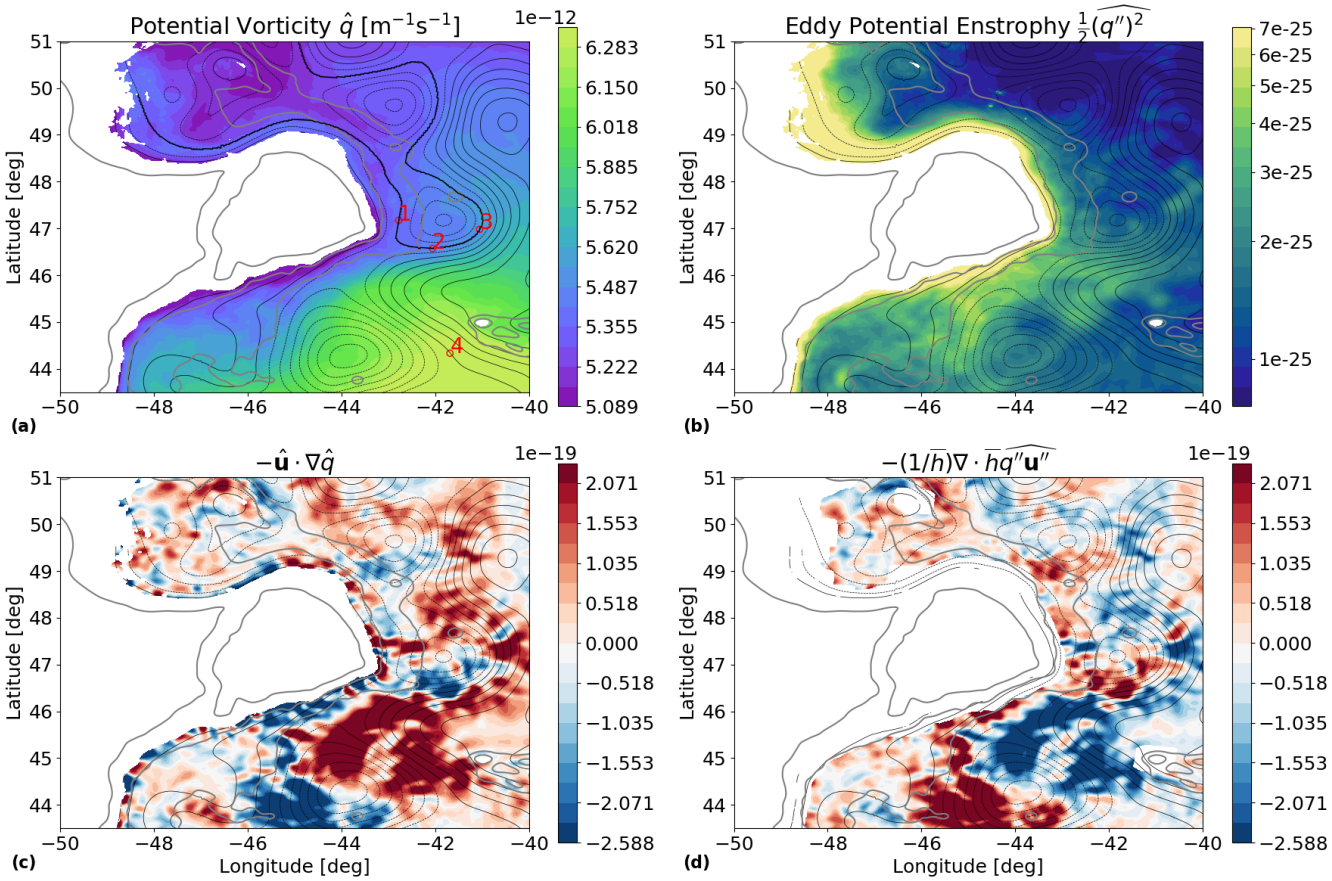

Figure 3.7: Time-mean (over years 9–16) model fields related to Potential Vorticity (q), on the $\sigma_1 = 32.43\ kg/m^3$ (LSW) isopycnal (see Fig. 3.5). Streamfunction contours are shown in thin black lines. (a) thickness-weighted average (TWA) Potential vorticity (PV). The thick black line marks a selected separating streamline. The TWA PV values at the numbered red circles [1,2,3,4] are $[5.36, 5.48, 5.55, 6.37] \times 10^{-12} m^{-1} s^{-1}$, respectively. (b) TWA eddy potential enstrophy. Terms in the TWA PV equation are shown in bottom panels: (c) the mean advection of mean PV, and (d) the eddy PV flux divergence term. Smoothing with a Gaussian filter of 5 km half-width (truncated at distance $=$ 20 km) was applied to the fields displayed in panels c and d. The 1, 3, and 4 km isobaths are shown in gray in all panels. The pattern correlation between the PV budget terms in panels (c) and (d) is $(-)0.85$.

All averages are performed on a selected isopycnal. The TWA PV ($\hat{q}$), and its balance, are then respectively defined by [*Smith*, 1999],

$$\hat{q} = \frac{f + \overline{v}_x - \overline{u}_y}{\overline{h}}, \tag{3.1a}$$

$$\frac{\partial \hat{q}}{\partial t} = -\hat{\mathbf{u}} \cdot \nabla \hat{q} - (1/\overline{h}) \nabla \cdot \overline{h} \widehat{q'' \mathbf{u}''} + nct = 0. \tag{3.1b}$$

From left to right, the terms in (3.1b) are time tendency, advection of the mean PV by the mean velocity, the eddy PV flux divergence, and all non-conservative terms (nct) lumped together. Fig. 3.7 shows the TWA PV, its budget, and the TWA eddy enstrophy, all calculated on $\sigma_1 = 32.43$ kg/m^3, which is the same (LSW) isopycnal as in the top panels of Fig. 3.5. The analysis was also repeated (not shown) on $\sigma_2 = 37.014$ kg/m^3 (as in the bottom panels of Fig. 3.5), and we find that the patterns described below are similar on this deeper isopycnal as well.

The PV (Fig. 3.7a) is generally lower near the western boundary, due to the low stratification imparted to LSW in its formation via deep convection [*Talley and McCartney*, 1982; *Rhein et al.*, 2002]. We observe that in addition to the large-scale offshore gradient, low-PV pockets extend away from the DWBC along the mean flow streamlines at the NEC, SEC, and SF areas, and into the adjacent recirculations. Thus, separation occurs across (up) the mean PV gradient, and mean PV dilution or modification by the eddy and *nct* terms is sufficiently weak that low PV contours protrude offshore. Panel (b) displays TWA potential eddy enstrophy, $Z = \frac{1}{2}\widehat{(q'')^2}$, which peaks inshore within the DWBC, and upstream of FC. Values are lower further offshore, including the areas offshore of the leakiness hotspots.

The conservative terms of the PV equation (3.1b) are displayed in Fig. 3.7(c–d). At the leakiness hotspots the offshore mean PV advection (panel c) results in a negative contribution to the local PV tendency, because PV increases along the path of the TWA flow. Elsewhere the pattern at the offshore edge of the DWBC is generally less coherent. The eddy PV flux divergence (panel d) approximately matches the pattern and amplitude of the mean PV advection term, but is opposite in sign (with pattern correlation $= -0.85$). Therefore, at separation streamlines, mean PV advection is upgradient and balanced by eddy PV flux convergence, with only a secondary role for

non-conservative processes [7]. The magnitudes of the conservative PV terms are generally largest just downstream of the leakiness hotspots and within the cyclonic recirculations. Because eddy PV flux divergence is order one in the PV budget, we gauge its influence on the mean PV distribution by evaluating the change in mean PV along a mean streamline. We specifically pick a streamline that separates from the DWBC (at SEC), marked in Fig. 3.7a. The PV values at three points along this streamline, and an additional point along a mean NAC streamline, are given in the caption. The total growth in mean PV along the DWBC streamline after its separation (occurring between points 1 to 2 in the plot) is $\approx$ 10% of the DWBC-NAC mean PV difference (between points 1 and 4). The maximal cumulative growth along the streamline, $\approx$ 20%, occurs at point 3.

To summarize, eddy PV flux divergence is a first order term in the PV budget, largely balancing the offshore PV advection. However, cumulative mean PV change along mean separating streamlines (which is dominated by eddy stirring), is relatively modest. In contrast, if leakiness occurred mainly via eddies derived from the NAC (mechanism 1, section 3.1), then along a separating streamline eddy stirring should result in significant ($O(1)$) changes in PV relative to the NAC-DWBC mean PV difference. Furthermore, under mechanism 1, we would expect that variability would either peak offshore at the eddy source (NAC) or be more homogeneous in between the NAC and DWBC. That does not appear to be the case, based on our diagnostics of the eddy potential enstrophy and the Lagrangian EKE (section 3.3.1).

3.3.5 Energy conversions

To more completely characterize the role of eddies in leakiness of the DWBC, we examine in this section the energy balance around FC. Given that the PV budget is primarily a balance between the inviscid (mean advection and eddy flux divergence) terms, we focus on the conversion terms between the mean and eddy energy reservoirs. We define the mean kinetic energy (MKE), mean

[7] Non-conservative terms are almost certainly even lower in magnitude than indicated by the pattern correlation result. That is because diagnostics are based on 2-day averaged output and higher frequency variability is unresolved, i.e., aliased.

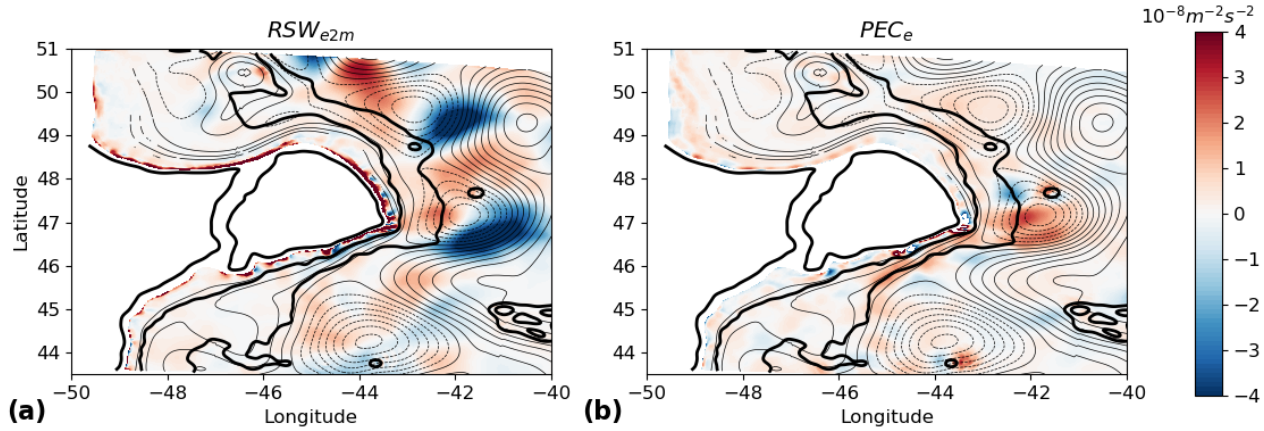

Figure 3.8: Model energy budget terms, averaged over years 9–16 on the $\sigma_1 = 32.43$ kg/m^3 (LSW) isopycnal (see Fig. 3.5). Panel (a) shows the Reynolds stress work by eddies on the mean flow, i.e., positive values correspond to local EKE conversion to MKE. Panel (b) shows the potential energy conversion to EKE. The 1, 3, and 4 km isobaths are shown in thick black contours in all panels. Streamfunction contours are shown in thin black lines.

potential energy (MPE), and eddy kinetic energy (EKE) as:

$$MKE = \frac{1}{2}\overline{u_i}^2, \quad MPE = \frac{1}{\rho_0}\overline{\rho} g z, \quad EKE = \frac{1}{2}\overline{u_i'^2}. \tag{3.2}$$

Here the time-mean (between model years 9-16) and deviation from the mean are denoted by the overbar and prime symbols, respectively. The MKE (eq. 3.3) and EKE (eq. 3.4) budgets are given by [*Harrison and Robinson*, 1978]:

$$\overline{u_i}\overline{\partial_t u_i} = RSW_{e2m} + PEC_m + T_m + nct_m, \tag{3.3}$$

$$\frac{1}{2}\overline{\partial_t u_i'^2} = RSW_{m2e} + PEC_e + \overline{w'b'} + T_e + nct_e, \tag{3.4}$$

Here we define

$$RSW_{e2m} = -\overline{u}_\lambda \partial_j \overline{u'_\lambda u'_j}, \quad PEC_m = \overline{w}\overline{b}, \tag{3.5}$$

$$RSW_{m2e} = -\overline{u'_\lambda u'_j}\partial_j \overline{u}_\lambda, \quad PEC_e = \overline{w'b'}, \tag{3.6}$$

where double indices imply summation. The left-side terms of equations (3.3)-(3.4) are the time tendency terms, which we find are negligible compared with all other terms in each equation. The

T symbols represent non-local transport and pressure work terms, whereas *nct* symbols denote non-conservative terms. The local energy conversion terms in both the MKE and EKE budgets are the Reynolds stress work terms (RSW), and potential energy conversion terms (PEC). In the MKE equation (3.3), RSW_{e2m} is the eddy-to-mean Reynolds stress work, which corresponds to conversion from EKE to MKE. The PEC_m term corresponds to conversion of potential energy to MKE. In the EKE equation (3.4), the RSW_{m2e} term is the mean to eddy Reynolds stress work, and PEC_e corresponds to conversion of potential energy to EKE. We calculate the local energy conversion terms in model (terrain-following) coordinates, and later sample them on the time-mean $\sigma_1 = 32.43\,\mathrm{kg/m^3}$ (LSW) isopycnal surface, for comparison with the previous diagnostics on the same surface. However, very similar conversion patterns are obtained at other LSW depths, and in a full depth integral (not shown). The results are also robust in that they vary little when alternative averaging periods are used in place of years 9–16, e.g., when averaging over individual years.

The EKE to MKE conversion term, RSW_{e2m}, is displayed in Fig. 3.8a. If the mean flow is driven by eddy fluxes, that should be reflected by positive values of Reynolds stress work by the eddies. Upstream of the leakiness hotspots, the mean flow is accelerated by positive RSW_{e2m}. However, RSW_{e2m} is low and close to a sign change at the leakiness hotspots, indicating that mean separation is not forced energetically by eddies. In particular, RSW_{e2m} becomes negative upstream of the SEC separating streamlines. The MPE to MKE conversion term, PEC_m (not shown), is positive at and following the mean separation areas, due to column stretching and downwelling which occurs in the offshore crossing of isobaths.

The conversion term of MPE into EKE (by slumping of sloping isopycnals, for example in the form of baroclinic instability) is shown in Fig. 3.8b[8]. This term is positive over most of the extent of the DWBC in the figure, including upstream of FC. At and downstream of separation points, as well as within the adjacent recirculating streamlines, PEC_e values are elevated. It is plausible that the separation of the mean flow from the continental slope contributes to the growth in PEC_e: a

[8]The RSW_{m2e} term (not shown) of the EKE equation is mostly similar in pattern and opposite in sign to RSW_{e2m} in the area.

parallel flow over sloping bathymetry exhibits lower linear growth rates compared to flows over a flat bottom or a free jet crossing isobaths [*Mechoso*, 1980; *Gula et al.*, 2014; *Solodoch et al.*, 2016].

We note that the release of MPE to EKE may locally contribute to the following conversion of EKE to MKE. Indeed, in most areas within the DWBC where RSW_{e2m} is positive, PEC_e is also positive. This path to MKE increase does not appear to facilitate the leakiness itself, but rather appears to be a consequence of the mean flow departing the continental slope, as noted above. However, positive PEC_e upstream of NEC may be sufficient to locally increase EKE, and so may contribute to the "diffusion" of particle trajectories across the DWBC and toward the leakiness hotspots (section 3.3.3).

3.4 Discussion

We now relate our results to the potential mechanisms of DWBC leakiness identified in section 3.1. We first argue that our results are consistent with inertial separation of the DWBC at FC, and we briefly review previous theoretical works on the conditions for inertial separation. Given that existing theories are not applicable to the DWBC, in section 3.4.2 we present a scaling argument for inertial separation. Finally, possible dependence of separation on model resolution and physics is briefly discussed (section 3.4.3).

3.4.1 Mechanism of DWBC leakiness

Taken together, the results presented in section 3.3 are consistent with inertial separation of the DWBC at FC (mechanism 2 in section 3.1). The evidence in support of this claim is as follows:

- The Lagrangian leakiness hotspots coincide with relatively sharp bathymetric variations,

namely convex turns and steepening of the continental slope (section 3.3.1).

- The offshore Lagrangian-mean flow coincides with the Eulerian-mean flow, which is a typical (rather than intermittent) offshore flow pattern at the leakiness hotspots.
- Mean DWBC PV contours are deformed in the offshore flow direction at leakiness hotspots NEC and SEC, indicating advection of PV from the continental slope into the open ocean by the separating mean flow. The PV exhibits relatively modest changes, mainly due to eddy stirring, along mean separating streamlines (section 3.3.4).
- Separating streamlines (Fig. 3.5) and floats leaving the DWBC (Fig. 3.2) tend to turn anticlockwise, consistent with potential vorticity conservation and thus vertical stretching.

The main hypothesis put forward in previous studies is that high NAC-generated EKE is responsible for DWBC leakiness (mechanism 1 in section 3.1), which may be expected based on the spatial proximity between the currents at separation areas. While rectified offshore eddy transport indeed accounts for $\approx$ 50% of the Lagrangian mean offshore velocity at SF, it is negligible at NEC and SEC. Eddying effects also play a significant role in shifting particles from the upper continental slope toward the leakiness hotspots at NEC and SEC via chaotic advection, as revealed in a comparison of Exp3d with Exp3dMean. However, the majority of the uncompensated, cumulative, leakiness occurs as an Eulerian time-mean offshore flow (Secs. 3.3.2–3.3.3). Additionally, the mean offshore flow does not appear to be directly forced by either internally or externally generated eddies (mechanisms 1 & 4 in section 3.1); baroclinic eddy production is relatively weak within the DWBC, and Reynolds Stress work by the eddies on the mean flow is negative close to the separation of mean streamlines (section 3.3.5). Finally, we do not directly address the possible role of SCV formation in DWBC leakiness [*Bower et al.*, 2013] here (mechanism 2 in section 3.1), a topic reserved for future study.

We note that the Nfl basin lies close to the latitude of zero wind stress curl. This marks the border between the subpolar and subtropical wind gyres in Sverdrup theory. Furthermore, the Sverdrup "streamfunction" predicts $10 - 20$ Sv leaving the western boundary near FC [*Talley*,

2011, Fig. S9.3], which is similar to the observed (uncompensated) leakiness of the DWBC (section 3.3.2). However, previous studies have demonstrated that Sverdrup-balance is significantly compromised in the subpolar gyre due to bottom pressure torque *Hughes and De Cuevas* [2001]; *Spence et al.* [2012] and eddy terms [*Gary et al.*, 2011]. In a high resolution (2 km) numerical model, *Le Corre et al.* [2019b] show that in the North Atlantic subpolar gyre, Sverdrup balance does not hold even to first order (including in the gyre interior). Rather, bottom pressure torque, nonlinearity, and other terms are dominant. Thus, it is not clear whether boundary current separation should be expected in the vicinity of the latitude of zero wind stress curl in the subpolar gyre.

The results of *Le Corre et al.* [2019b] further show that nonlinear terms, representing fluxes from the slope region, are a dominant positive (cyclonic) term in the interior vorticity balance of the simulated subpolar gyre. *Le Corre et al.* [2019b] show that this flux is high near FC and is mainly due to the mean rather than the eddying circulation. We interpret this result as supportive of locally determined mean inertial separation. Therefore, although large scale gyre constraints may play a role in DWBC separation, we focus on the local constraints and dynamics here and leave the role of the gyre-scale circulation in the FC separation as a topic for future study.

We likewise do not analyze here non-local energy transfer terms (pressure work, and eddy transport of EKE). These terms may be important in interactions between the DWBC and the NAC, but remain outside the scope of this work. This is related to the concept of boundary currents collision [*Cessi*, 1991; *Agra and Nof* , 1993], which occurs when two western boundary currents converge, and can substantially modify their latitude of separation. In the present case, however, the DWBC and NAC occupy distinct ranges of isobaths, and the NAC separates further north than the (partially separating) DWBC.

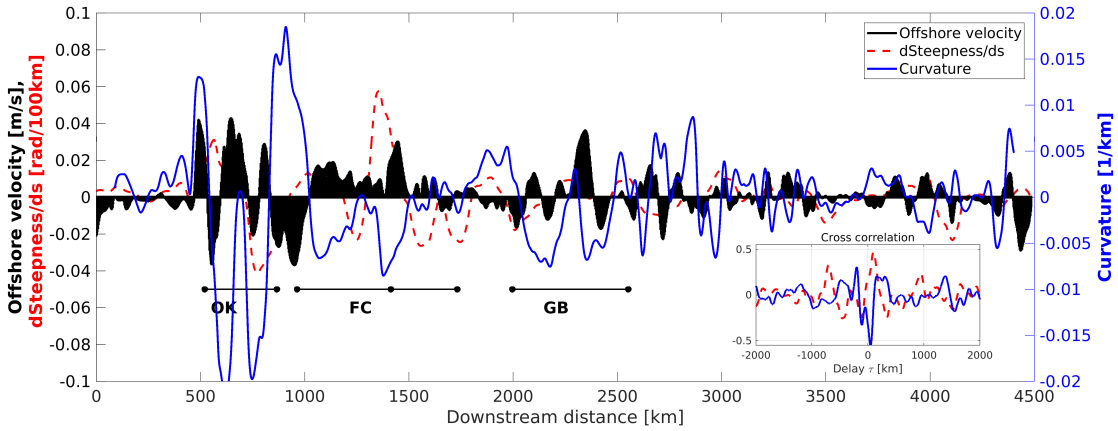

Figure 3.9: Offshore velocity averaged over depths greater than 500 m (black), as a function of distance along the 3 *km* isobath (compare with cumulative transport on the same curve shown in Fig. 3.4). Additional curves indicate the isobath curvature (blue) and along-isobath (downstream) gradient of bottom slope steepness (red). All plotted quantities have been smoothed via a running average with a box width of 100 km. Black full circles correspond to the locations of the red circles in Fig. 3.1, e.g., the black circle at the middle of the Flemish Cap (FC) line marks its southeast corner (SEC) (section 3.3.1). The inset shows cross-correlations along the same isobath between offshore velocity and bathymetric curvature (blue), and between offshore velocity and steepness gradient (red). Cross-correlation values and significance levels are also given in 3.6.12.

3.4.2 A scaling analysis of inertial separation

Given the evidence for inertial separation as the primary mechanism of DWBC leakiness (section 3.4.1), we now examine the distributions of offshore flow v_c and bathymetric changes. Fig. 3.9 shows that larger offshore values of v_c tend to be co-located with sharp increases in curvature and steepness (see Fig. 3.4 as well). Everywhere around FC $v_c > 0$, and it peaks around NEC and SEC. This occurs to a lesser degree around GB, where steepening and curvature are not as pronounced as around FC. Elsewhere, away from FC, v_c is either lower in magnitude or oscillates in sign along other bathymetric features. More quantitatively, we plot cross-correlation of offshore velocity with isobath curvature and steepening along the 3 km isobath in Fig. 3.9. The correlation between steepness gradient and offshore velocity reaches $r = 0.47$ at a downstream lag 73 km, while the correlation between curvature and offshore velocity reaches $r = -0.56$ at a downstream lag of 45 km (see supplemental section 3.6.12). These correlations are consistent with inertial separation initiated by sharp changes in the geometry of the continental slope. However, the correlations are at least partially due to meandering of the DWBC along the entire length of the isobath, rather than just the separation points around FC.

Inertial separation of currents flowing around capes or ridges was studied theoretically by *Pickart and Huang* [1995], *Ou and De Ruijter* [1986], *Klinger* [1994], and *Jiang* [1995] [9]. As reviewed in section 3.1, *Pickart and Huang* [1995] specifically studied a DWBC-like current traversing a ridge, and demonstrated that a significant flux is lost to offshore. However, these studies all made the semigeostrophic approximation, which is invalid when along-stream variations are of similar or shorter length scales than cross-stream variations. At FC, the radius of curvature at the SEC is around 10 km, and a few tens of km at the NEC. In comparison, the width of the DWBC (50−100 km) is considerably larger. Hence, at the convex corners, where much of the separation happens, the semigeostrophic approximation fails, and these models become inapplicable.

[9] Laboratory experiments related to the same parameter regimes as these theoretical works were conducted by, e.g., [*Whitehead and Miller*, 1979; *Bormans and Garrett*, 1989].

Furthermore, these works [except *Pickart and Huang*, 1995] all find separation happens within their respective models due to surface outcropping of a density surface bounding a surface current from below. The DWBC is not a surface current, but rather has significant deep and depth-independent components. Indeed leakiness and separation at FC are to a large degree depth-independent in our numerical model (e.g., figures 4, 5, and 10). Hence theories derived for separation via isopycnal outcropping in a buoyant boundary current are not applicable to the DWBC. Finally the cited works do not cover downstream changes in bottom slope, which the scaling analysis we employ (subsection 3.4.2) suggests is a significant factor at FC. In fact, most of the cited works assumed a flat bottom and vertical side walls.

Greenberg and Petrie [1988] presented a barotropic numerical model over a Nfl-like bathymetry, where the only prescribed current (by boundary conditions) is DWBC-like. The solution indeed displayed significant offshore transport around FC (their Fig. 3a), consistent with inertial separation. A caveat is that the eastern domain boundary was very close to FC.

In the absence of a closed-form theory of inertial separation relevant for the present case, we present a scaling analysis that seeks to determine a simple condition for cape separation of a prograde deep boundary current. The analysis first assumes that mean streamlines continuously curve around a convex corner, while conserving PV (as noted above, mean PV changes moderately along mean streamlines around FC in GB_B, including at separation). Then, a condition is derived under which offshore excursions or recirculations form. Because we do not explicitly solve for, or use constraints related to the global streamfunction, it is still conceivable that offshore excursions may be followed by meandering and reattachment downstream, rather than permanent separation. However, we are concerned with bathymetric turns of large angles ($\sim$ 90 degrees for SEC), which are likely more favorable for permanent separation. From a kinematic standpoint, larger bathymetric turn angles require larger inshore displacements to compensate for a set offshore detachment distance. A contributing factor in that regard is that for a prograde slope current, vorticity stretching upon offshore excursions may enhance separation, as discussed below.

We use the fact that vorticity can generally be decomposed into shear vorticity $\zeta_s = -\partial_n U$ and curvature vorticity, $\zeta_c = U/r_c$. Here t and n are the tangential and normal components of the "natural" coordinate system [*Holton*, 1973], where t is locally downstream, and n is to its left. The subscript n denotes differentiation in the n direction, U is the magnitude of the DWBC velocity, which is directed in the t direction, and r_c is the streamline radius of curvature, negative for clockwise turns as for, e.g., the DWBC around FC NEC or SEC. The expression for PV in isopycnal coordinates is then

$$PV = \frac{f + \zeta_c + \zeta_s}{h} = \frac{f + U/r_c - \partial_n U}{h}, \tag{3.7}$$

where h is the thickness (distance between two chosen density values), and f is the Coriolis parameter. The downstream change in PV along a mean streamline under the above assumptions is

$$d(PV) \sim df + d\zeta_c + d\zeta_s - \frac{f}{h} dh = 0.$$

The first term is the change in planetary vorticity, which is neglected over the scales relevant in the present analysis, i.e., $O(100\ \text{km})$. The last is the vorticity stretching term, which is linearized under the assumption that vertical excursions are a modest fraction of the total thickness for mesoscale motions.

At the turn itself, $d\zeta_c \approx \hat{U}/R_c$. Here $\hat{U}$ is a velocity scale, while R_c is the bathymetric radius of curvature. The scale of the downstream change in shear vorticity is written as $d\zeta_s \approx -\Delta U/W$, where W is the current width upstream, and ΔU is the downstream change in cross-current shear integrated in the positive n direction. Note that if width decreases (increases) downstream, then ΔU is an overestimate (underestimate). We assume that the change in current width will be a modest fraction, if the current does not partially separate. Therefore, we have a scaling equation relating cross-stream shear changes to bathymetric curvature and deepening (the latter related to steepening across the current):

$$\Delta U \approx \frac{W}{R_c}\hat{U} - \frac{fW}{h} dh. \tag{3.8}$$

At FC, the turn of the DWBC is clockwise, hence R_c is negative, especially at the leakiness hotspots NEC and SEC. Additionally, a steepening occurs at and prior to NEC, SEC, and SF. The deepening should be accompanied by vertical stretching ($dh > 0$), given that the current fills a significant part of the water column (Fig. 3.11). By (3.8) both clockwise curvature and vertical stretching each add to a drop in velocity per unit distance offshore (ΔU), tending to reduce current flux downstream along the isobaths. In the next two paragraphs we examine the contribution of each of these terms in turn.

It follows from equation (3.8) that if the radius of curvature R_c is similar in magnitude to or shorter than the current width W, then its contribution to ΔU is of the same magnitude as the mean current speed. At the outer rim of the current the added shear is then of sufficient magnitude to reverse its direction[10] , with speed comparable to $\hat{U}$. The associated large relative reduction in downstream flux in the steady circulation is a manifestation of inertial separation. As noted above, the radius of curvature at the SEC (NEC) is around (a few times) 10 km, while the width of the DWBC is $50 - 100$ km. Thus R_c is in fact significantly lower than W.

The stretching (2nd right-side) term in (3.8) has a similar effect in reducing downstream along-isobaths flux as does the curvature term, and is of a similar magnitude. The deepening of streamlines originating on, say, the $h = 3\ km$ isobath upstream of the SEC, is greater than $dh = 500\ m$, resulting in cumulative vorticity stretching as great as that from curvature vorticiy, $(\frac{R_c \cdot f \cdot dh}{h \cdot \hat{U}}) \sim 1$, assuming $\hat{U} = 0.15\ m/s$, and $R_c = 10\ km$. A similar but slighter steepening occurs around the NEC. Bathymetric steepening also limits streamline shoaling around bathymetric turns, which adds confidence to the scaling analysis since shoaling kinematiclly reduces streamline curvature.

Furthermore, if the (prograde) flow does "begin" to separate rather than turn around the cape, as a parcel travels offshore additional vortex stretching occurs. The increased vorticity may be expressed as increased cyclonic path curvature, steering the parcel further away from the up-

[10]Offshore of the downstream stagnation streamline, the present analysis cannot determine the circulation pattern, since offshore streamlines do not necessarily originate upstream. Rather than a reversal or recirculation, a split in the current may emerge for example. That does not affect the result inshore however.

stream isobath. That can result in a positive feedback, e.g., by creating more positive curvature vorticity (by vortex stretching), and further angular separation from the continental slope. Note that floats trajectories separating around FC do tend to turn cyclonically offshore (Fig. 3.2), as do mean separating streamlines (Fig. 3.5).

To summarize, the scaling analysis suggests that partial separation (loss of outer streamlines to offshore) of a prograde current is a plausible outcome where significant downstream bathymetric steepening occurs, and especially where it is accompanied by anticyclonic bathymetric turning. The dependence on curvature radius is particularly simple to express – an order one flux reduction may result for curvature radius $R_c < W$. Both conditions are met at the FC leakiness hotspots (section 3.3.1).

As an additional but still preliminary consistency check, we compare these conditions (downstream steepening and $R_c < W$) with the conditions at several locations of separation of other prograde currents: the western boundary current flowing around the southern tip of Greenland [*Holliday et al.*, 2009], the Mediterranean Overflow current propagating around the Iberian peninsula [*McDowell and Rossby*, 1978; *McWilliams*, 1985; *Bower et al.*, 1997] [11] , and the California Undercurrent at the mouth of Monterrey Bay [*Molemaker et al.*, 2015]. The width of these currents is $O(150, 50, 20)\ km$, respectively, while the capes they traverse have $R_c = O(10)\ km$. Furthermore, steepening occurs as well on the upstream side of these capes. It is difficult to determine the relative contribution of steepening to vorticity stretching without knowledge of trajectories or mean streamlines, but the relative contraction of cross-isobaths distance at these capes is a large fraction, as in the FC separation locations.

Several assumptions and idealizations were made in deriving this scaling that remain to be tested. a. The assumption of mean PV conservation along mean streamlines is only qualitatively motivated by the modest cumulative effect of eddy terms in the GB_B PV budget. b. If the current width decreases downstream (to a value W_2), then the magnitude of ΔU is overestimated in (3.8)

[11] Note that leakiness of the Mediterranean Overflow current is at least in some cases associated with SCV formation and interactions [*Bower et al.*, 1997].

by a factor $\sim W/W_2$. However, the magnitude of ΔU estimated from our scaling at FC is such that even, e.g., a factor of two width decrease is relatively minor[12]. c. If separation does occur, reattachment cannot be excluded within the analysis. It could only be suggested that lack of reattachment is likely for a prograde current separating from a large-angle bathymetric bend, due to cyclonic turning past separation resulting from additional vortex stretching. In light of these assumptions and simplifications, the analysis needs to be further refined and tested in dedicated and controlled (e.g., numerical) experiments.

3.4.3 Sensitivity to model circulation and resolution

The scaling analysis also suggests that inertial separation at a bathymetric turn should depend mostly on the local conditions: radius of curvature, bottom steepness changes, current width, and speed. Two implications may be that: (a) the leakiness at FC should be largely insensitive to external variations in the Nfl circulation pattern; (b) as long as numerical model resolution is fine enough that, e.g., bathymetric curvature radii are similar to or smaller than model DWBC width, separation should still occur to some degree.

The observed leakiness patterns are reproduced well in the FLAME model employed by *Bower et al.* [2011], which has a coarser resolution, $\approx 6.5\ km$, despite water mass biases (supplemental section 3.6.12) in the Nfl basin. Thus, the leakiness may not be strongly dependent on the detailed structure of the DWBC and surrounding currents, or on good resolution of baroclinic instabilities at the DWBC boundary (where the Rossby radius is $\approx 10\ km$). Indeed, with further decrease in model resolution, at least up to 0.5°, leakiness around FC and interior pathways still appear, but seem to gradually change and eventually severely deteriorate relative to observations [*Gary et al.*, 2011; *Spence et al.*, 2012].

[12] Additionally, even following separation at SEC (within GB_B) width decreases by only a small fraction locally (Fig. 3.5b and d).

3.5 Summary and Conclusions

3.5.1 Phenomenology

Using two observational float datasets and a realistic, high-resolution, numerical model, we demonstrate that within the Newfoundland (Nfl) Basin, the DWBC has a few well-defined geographical hotspots of maximal Lagrangian leakiness (Figs. 3.2-3.3). At the leakiness hotspots, local maxima of time-mean Lagrangian and Eulerian offshore velocities occur in the numerical model, while Lagrangian EKE is minimal (Figs. 3.3-3.6). These hotspots are further characterized by convex curvature and/or downstream steepening isobaths (Fig. 3.9). The localized, and time-mean nature of the leakiness, and its apparent correlation with bathymetric variations, suggests that it occurs largely via an inertial separation mechanism (mechanism 2 in section 3.1). This contrasts with previous hypotheses that suggested that the DWBC leakiness was due to interaction with NAC eddies (mechanism 1 in section 3.1).

The Eulerian mean circulation is examined within potential density layers, revealing that mean DWBC streamlines separate offshore at the identified Lagrangian leakiness hotspots (Fig. 3.5). Following separation, the streamlines revolve around deep cyclonic recirculations that reside between the DWBC and NAC. The Eulerian-mean and Lagrangian-mean DWBC velocities are very similar in the region. Consistently, the thickness-weighted average (TWA) flow is almost identical to the Eulerian-mean flow, which means that the rectified eddy mean flow is negligible. Cluster analysis (supplemental 3.6.11) supports these conclusions as well.

The mean offshore flow is associated with cumulative downstream reduction in DWBC mass flux (Fig. 3.4). Thus, we distinguish uncompensated leakiness from compensated leakiness: the former (latter) is associated with a net (zero) loss of material flux to offshore. The time-mean flow only contributes uncompensated leakiness, since no mean streamlines appear to join the DWBC from the interior (Fig. 3.5). The eddy component (with respect to the time-mean) can contribute

to uncompensated leakiness only via rectified eddy transport, which is found to be negligible compared to the Eulerian-mean circulation around most of FC. The eddies may contribute substantially to compensated leakiness, but this has not been examined in this study. The model DWBC volume flux decreases by 13-16 Sv around FC, within LSW and deeper waters. The reduction primarily takes place at the Lagrangian leakiness hotspots identified in this study. The result is generally consistent with observational estimates (M14) showing $\approx$ 15 Sv loss between FC and east GB.

3.5.2 Dynamics

The dynamics of separation are addressed from a (TWA) PV perspective (Fig. 3.7) as well as in terms of energetic transformations (Fig. 3.8). We find that mean separation deforms the PV contours offshore at the leakiness hotspots, which is consistent with inertial separation. Indeed, the cumulative change in mean PV along mean separating streamlines is modest ($\approx 10-20\%$) relative to the DWBC-NAC contrast. However, the mean PV advection is found to be balanced to first order by eddy PV flux divergence, indicating that eddies play a role in guiding the separated mean flow offshore. We therefore examined energy conversion processes in the region (Fig. 3.8). We find that the separation of mean DWBC streamlines is not directly forced by conversion of EKE to MKE (RSW_{e2m}). In fact RSW_{e2m} decreases and becomes negative prior to separation. This is consistent with the low magnitude of the eddy-rectified flow relative to the mean flow; as well as with cluster analysis (supplemental section 3.6.11), which shows that the separation of streamlines is statistically typical.

Outside of the separation areas, patches of positive PEC_e are collocated with positive RSW_{e2m}, which may be interpreted as a forcing of the mean flow by eddies spawned locally from baroclinic instability. This seems to occur in the recirculations, as well as in the DWBC itself (except at the separation areas). Rectified eddy mean flow is indeed towards offshore and significant at SF, but not elsewhere around FC. Our Lagrangian experiments using the time-mean model flow

field (Exp3dMean) highlights another role of eddies in DWBC leakiness: this experiment exhibits $\approx$ 50% less leakiness compared with Lagrangian experiments using the time dependent velocity (Exp3d). We attribute this difference to the eddies chaotically advecting Lagrangian particles from the upper continental slope toward the leakiness hotspots.

In contrast with previous hypotheses, our findings are in line with the main fraction of *mean uncompensated* leakiness occurring by inertial separation. Leakiness hotspots and mean streamline separation are localized at areas of convex and/or steepening bathymetry, where inertial separation may be expected. Furthermore, cumulative leakiness is demonstrated to be a persistent and typical occurrence, rather than eddying or intermittent. Along these mean separating streamlines, eddy PV flux divergence does not induce a dramatic change in mean PV, in support of inertial separation. The separation process is likely inviscid, since non-conservative terms have a small role in the TWA PV balance. Finally, past separation, Lagrangian trajectories as well as mean streamlines tend to turn cyclonically, which is consistent with vortex stretching in inertial motion into deeper water.

Previous theoretical frameworks determining conditions for inertial separation are not suitable for treating the DWBC conditions near FC. This is partially due their focus on buoyant rather than deep boundary currents. Additionally the semi-geostrophic approximation (made in these studies) is violated in areas of high curvature of the slope (section 3.4). Instead, a scaling analysis is presented (section 3.4.2) for the downstream evolution of a boundary current due to bathymetric variations. The result suggests that a steady and continuous DWBC flow around the convex corners of FC is unlikely. A significant reduction in flux (e.g., partial separation) is a plausible outcome, due to influence of bathymetric curvature and steepening. Several assumptions made in the scaling analysis cannot be validated in the present study, and they require detailed examination in dedicated numerical experiments.

3.5.3 Outlook

We note several caveats of the present investigation (also see supplemental section 3.6.3). (1) The numerical model configuration developed and presented here suffers from water mass biases that make detailed comparisons with observations delicate at times, although mean circulation features and their variability appear to agree favorably with observations (supplemental section 3.6.3). Similar water mass biases plague numerical models of the area, and have been partially resolved in some studies using relaxation of water properties toward climatology [e.g., *Tréguier et al.*, 2005; *Rattan et al.*, 2010], a method not without drawbacks for dynamical analysis. (2) Likewise, total model DWBC transport east of FC is anomalously high in comparison with observations (supplemental section 3.6.3). This may have an impact on the leakiness process. For example a faster current may be more likely to inertially separate. However, in supplemental section 3.6.6 we show that the model DWBC transport is in good agreement with observations elsewhere in several other locations in Newfoundland including along FC, and that the anomaly is likely related to the cyclonic recirculations east of FC rather than to the DWBC itself. (3) While the model output frequency of two days is likely sufficient to resolve mesoscale processes, it may not provide sufficient representation of the submesoscale. For that reason leakiness by SCV formation and escape (mechanism 3 in section 3.1) is not addressed. Indeed, *Bower et al.* [2013] found that several ExPath floats were trapped in SCVs at or near their leakage from the DWBC around the GB southern tip. (4) On a related note, while vertical resolution is at a relatively high present standard (section 3.2.1), it is not sufficient to resolve bottom boundary layer processes in deeper regions. (5) We note that the interpretation used here of binned and conditionally-sampled Lagrangian velocities as the Lagrangian mean velocity (section 3.3.1) is only approximately representative of true Lagrangian mean velocity. However, the low amplitude of rectified eddy flow as calculated independently of the defined Lagrangian mean (section 3.3.2), corroborates that the deviation of Lagrangian mean from the Eulerian mean flow is small.

The results of this study suggest that the leakiness and separation mechanism depend strongly on the bathymetric environment of the current. Therefore, future work should examine the cir-

culation in idealized scenarios where a DWBC-like current traverses a region of bathymetry resembling FC and GB. Within a simplified setting the dynamical mechanisms can be better isolated in experiments where factors such as bathymetry and the presence of a NAC-like countercurrent can be varied. Additionally, the geographical distribution of cumulative (uncompensated) leakiness was evaluated in our model, inspired by observational estimates [*Mertens et al.*, 2014; *Biló and Johns*, 2018]. While they are consistent in terms of total flux, the observational record is not yet extensive enough to test the model distribution in detail.

Comparison of model particle trajectories transported by time-averaged vs unaveraged currents (section 3.3.3) suggests that chaotic advection significantly increases the offshore leakiness of particles, including at the mean leakiness hotspots. We do not distinguish quantitatively the roles of pure eddy variability and of eddy interaction with spatial gradients in mean flow (i.e., chaotic advection). While several metrics were previously suggested to evaluate the relevance of chaotic advection in particular scenarios [e.g. *Shepherd et al.*, 2000; *Brett et al.*, 2019], it remains challenging to do so locally in a realistic flow such as examined here. Hence we do not attempt in the present study to determine quantitatively the enhancement of leakiness by chaotic advection.

This study has concentrated on the mechanisms of DWBC leakiness in the Nfl basin. Previous studies had a greater focus on characterization of the interior pathways that follow – from the subpolar to the subtropical region. It has also been shown previously that most leaked particles recirculate in the Nfl basin for years [*Bower et al.*, 2009; *Gary et al.*, 2011; *Lozier et al.*, 2013]. In this regard, the robustness of cyclonic mesoscale recirculations demonstrated in the present model also merits further study. Their relation to the larger scale interior pathways and recirculation is also of interest. Furthermore, it remains to be determined if and how diapycnal mixing and water mass transformations are associated with the leakiness process or with the long recirculation period water parcels spend within the Nfl basin.

3.6 Supplement

3.6.1 Terms and acronyms

Terms, acronyms, and symbols used often in the text are contained in table 3.6.1.

3.6.2 Tracer diffusion noise

For the GB_B ROMS solution (section 2a), split-rotated third-order upwind (RSUP3) tracer advection is used [*Marchesiello et al.*, 2009]. We initially used the RSUP3 version in which the diffusive component is rotated to align with isoneutral coordinates [*Lemarié et al.*, 2012], but found that severe grid-scale noise appeared at depth (especially near the bottom), including in vertical velocity, and was accompanied by temperature drift in the same locations. The problem appears to be accentuated by high spatial resolution, and does not appear or is greatly diminished in CROCO implementations of resolution twice coarser or more in our experience, e.g., the parent domain [*Renault et al.*, 2016b] used for the GB_B boundary conditions (section 2a). It is likely related to simplifying approximations made in the estimation of isoneutral-direction derivatives in the CROCO version we use (personal communication from Florian Lemarié). To circumvent the problem, we reverted to the isopotential-rotated RSUP3 version [*Marchesiello et al.*, 2009], and reinitialized the model solution. The noise and severe temperature drift did not occur in the isopotential configuration. Water mass biases that do appear in the final configuration are typical of numerical models in the subpolar region (appendix B); these biases have lower amplitude and a different spatial structure than encountered in the isoneutral noise case.

Table 3.1: Summary of acronyms, terms, and symbols commonly used in the text. The list is divided (by horizontal lines) into different subjects, from top to bottom: water masses; currents and circulation patterns; geographic and topographic features; observational and model names or terms; dynamical and technical terms and symbols. At the end of each row, the section number is given where the term is defined. Acronyms not used in the text are in parentheses. Note many of the geographical locations and currents are identified in Fig. 3.1 as well.

Acronym	Expansion and notes
(NADW)	North Atlantic Deep Water. Water masses advected southward in the deep AMOC branch. Sec. 3.1.
LSW	Labrador Sea Water. Upper component of NADW. Sec. 3.1.
lLSW	Lower Labrador Sea Water. Refers here to model isopycnal $\sigma_2 = 37.014\ kg/m^3$. Sec. 3.3.2.
(OW)	Overflow Waters. Lower component of NADW. Sec. 3.1.
AMOC	Atlantic Meridional Overturning Circulation. Sec. 3.1.
DWBC	Deep Western Boundary Current. Sec. 3.1.
(IP)	Interior Pathways. Equatorward routes of NADW to the subtropical region, but offshore of the DWBC. Sec. 3.1.
NAC	North Atlantic Current. Northward branch continuing from Gulf Stream north into Nfl. Sec. 3.1.
Nfl	Newfoundland (Basin). Sec. 3.1.
FC	Flemish Cap. Underwater cape within the route of the DWBC in Nfl. Sec. 3.1.
(FP)	Flemish Pass. Meridional channel between the continental shelf and FC. Sec. 3.2.2.
GB	The Grand Banks of Newfoundland. Underwater cape within the route of the DWBC in Nfl, downstream from FC. Sec. 3.1.
(OK)	Orphan Knoll. Underwater seamount north of FC, east of the continental slope. Sec. 3.1.

ExPath	Export Pathways. Float deployment campaign. Sec. 3.1.
ROMS	Regional Oceanic Modeling System. Numerical model in presented analysis. Sec. 3.2.1.
GB_B	Grand-Banks-B. Main ROMS solution designed for and used in presented analysis. Sec. 3.2.1.
OKL	Orphan Knoll Line. Deployment position of model particles, west of OK. Sec. 3.3.1.
NEC	North East Corner. Diagnosed "hotspot" of leakiness at NEC of FC. Sec. 3.3.1.
SEC	South East Corner. Diagnosed "hotspot" of leakiness at SEC of FC. Sec. 3.3.1.
SF	Southern Face. Diagnosed "hotspot" of leakiness at SF of FC. Sec. 3.3.1.
SCV	Submesoscale Coherent Vortex. Sec. 3.1.
MKE	Mean Kinetic Energy. Sec. 3.3.5.
EKE	Eddy Kinetic Energy. Sec. 3.3.5.
MPE	Mean Potential Energy. Sec. 3.3.5.
PV	Potential Vorticity. Sec. 3.3.4.
TWA	Thickness Weighted Average. Sec. 3.3.4.
Z	TWA Eddy Potential Enstrophy. Sec. 3.3.4.
v_c	Cross-bathymetry velocity component. Positive toward deeper water. Sec. 3.3.1.
v_a	Along-bathymetry velocity component. Positive to the right of v_c, i.e., generally downstream within the DWBC. Sec. 3.3.1.

3.6.3 Numerical model validation

In this section we describe model validation against observations and discuss possible caveats in model setup. We begin with examining sea surface height (SSH), because it determines surface geostrophic velocity. We compare model SSH to the measurements of Absolute Dynamic Topography from satellite altimetry. Model SSH is averaged over model years 9-16. The observational product we use is the DUACS L4 merged reprocessed product [*Pujol et al.*, 2016], with 1/4 degree grid resolution and product samples spaced 1-day apart, with data from 1993 to 2017. The Absolute Dynamic Topography to model SSH comparison is shown in panels (a)-(b) of Fig. 4.1. Some differences in mean SSH and EKE are to be expected due to differences in averaging periods. There is general agreement in SSH patterns and amplitudes of the main circulation features, including the mean paths of the Gulf Stream and the Labrador Current, and the standing meanders of the NAC, including the Mann eddy.

Geostrophic surface EKE= $\frac{1}{2}\mathbf{u_g}'^2$ is compared between the model and the altimetric observations over the same periods as for the mean SSH. The model geostrophic component of surface eddy velocity $\mathbf{u_g}'$ is calculated from eddy SSH [*Vallis*, 2017]. The observed eddy velocity is an available variable within the DUACS product. The model (observed) eddy component is defined as the instantaneous deviation from the time-mean SSH. Within the area shown in Fig. 4.1(c–d), the model EKE is higher on average by a factor of ≈ 5. Higher EKE is generally to be expected in the model because its grid resolution is about 10 times higher compared with the altimetric product grid resolution, and because R_d in this region is close to or lower than the altimetric product grid resolution. Low pass filtering of the model output shows that the unresolved scales likely account for the majority of the EKE difference (section 3.6.4, where effective resolution is taken into account). In addition, the spatial patterns of model and observed EKE are generally in good agreement. Both peak along the trajectories of the Gulf Stream and NAC. The model EKE also has a local peak of EKE along the 1 km isobath in the Labrador Sea and Nfl Basin. The peak is related to the Labrador Current, the inshore and upper ocean component of the western boundary current in the Subpolar North Atlantic, the deep component being the DWBC. The absence of Labrador

Current signature in the observed EKE is again likely due to the coarser resolution.

We compare the depth and cross-stream structure and amplitude of the DWBC east of FC at 47 N (Fig. 3.11) with the observations of M14 reproduced in panel b. The observational estimate was obtained by averaging over six individual vessel ADCP cross-DWBC sections, taken at various dates between April and August at six different years (M14). The ROMS data presented in panel (a) is an average over model years 9–16. However, model averages over single years are generally quite similar (e.g., for DWBC width variation). Considering the very different averaging details, the spatial patterns are visually similar between the model and observational estimates. Above the continental slope there is an intensified, quasi-barotropic DWBC core, while over the continental rise a bottom-intensified DWBC core is present. The northward flow to the east is related to the NAC and is similar in its structure between the model and observational estimates as well. The multiple surface-intensified cores present in the observational northward flow may be smeared out in the longer model time-average.

The maximal DWBC velocity magnitude is just under 0.3 m/s in both model and observational averages within both current cores, except within very limited regions in the observational estimate where the magnitude exceeds 0.3 m/s. The total width of the DWBC compares well with the observations. Here an operational definition of the current width is taken as the distance between the 0.05 m/s velocity contours near the bottom, west of the western (continental slope) core, and east of the eastern (continental rise) core. With this definition, the model (observed) width is 156 ± 13 (153) km. The model width error estimate quoted here is the standard deviation in annual-mean widths between years 9–16. We did not obtain the results for the individual (six) observational cruises on which Fig. 3.11b is based. However, based on Fig. 4 in M14, we estimate the observed width std at $O(50$ km), across the six cruises.

Despite the agreement with observations in patterns, widths, and maximal velocities along this section, the model flow is seen to be more barotropic than the observational estimate at the 47 N section, and therefore carries a higher total volume transport. In what follows, GB_B transport

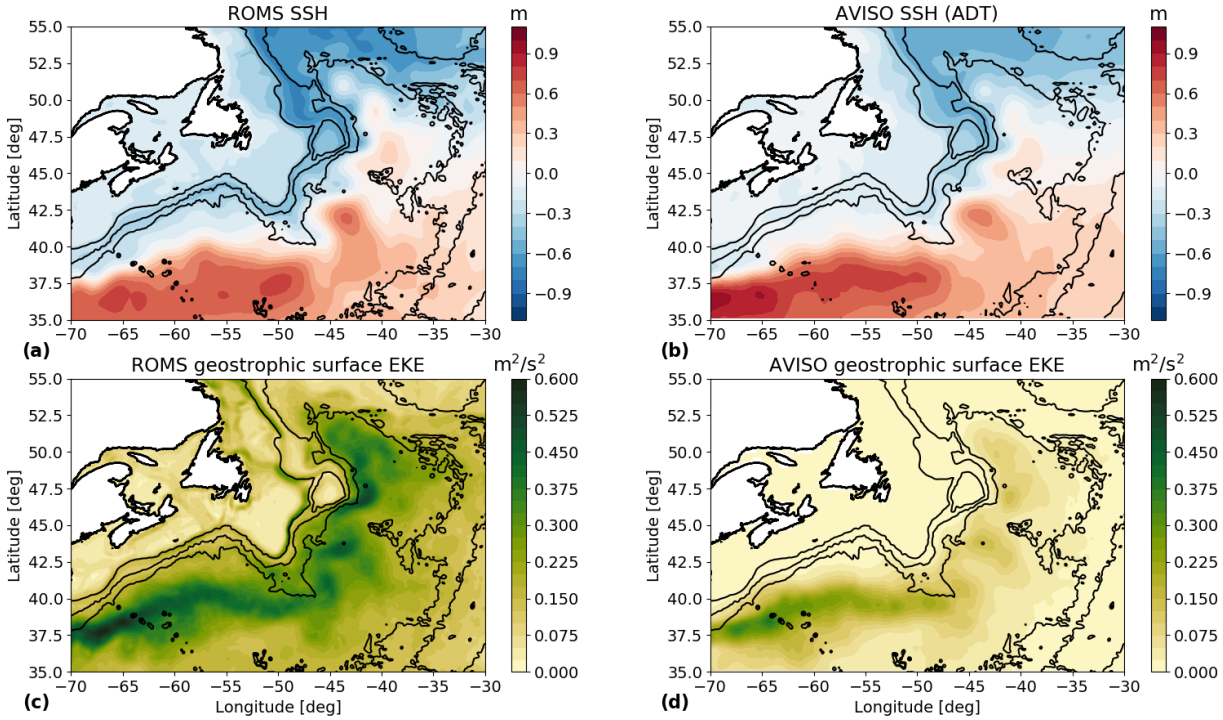

Figure 3.10: Comparison of mean sea surface height (SSH), and geostrophic surface eddy kinetic energy (EKE) in the ROMS simulation and in the DUACS L4 merged 1/4 degree product. The ROMS data is averaged between simulation years 9–16. The DUACS product is averaged between years 1993-2017. The specific mean SSH variable from DUACS is Absolute Dynamic Topography. ROMS (DUACS) SSH and EKE data are shown in panels a and c (b and d), respectively. Given the different definitions of Absolute Dynamic Topography and SSH, a spatially-average difference is expected. Therefore, a mean 0.4 m amplitude has been subtracted from the model SSH for plotting and comparison purposes. The 1, 3, and 4 km isobaths are marked with black contours.

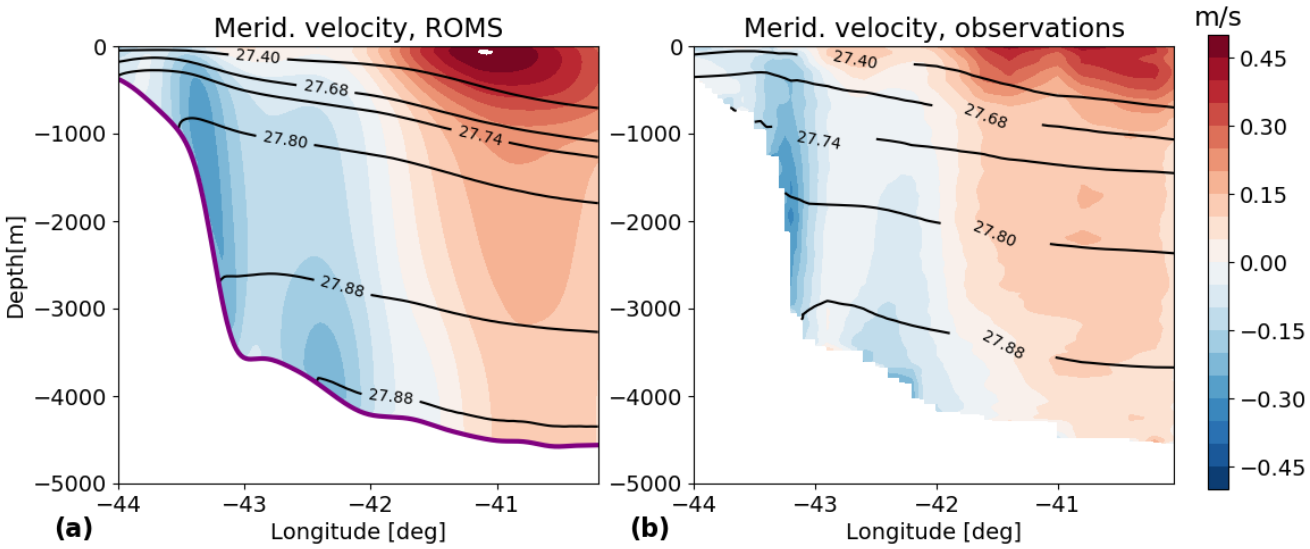

Figure 3.11: Vertical section of meridional (approximately along-slope) velocity east of Flemish Cap (FC) along 47 N, in (a) ROMS (year 16 average), and (b) 6-repeat ship ADCP observations after *Mertens et al.* [2014]. Section location is marked by the red line east of FC in Fig. 3.1.

uncertainties are calculated from interannual variations of annual mean flow, unless otherwise stated. Mean transport is calculated as the total southward transport west of 41 W of the averaged velocity across the section. Note that this straightforward Eulerian-mean transport definition is different than that of M14 (section 3.6.5). From the mean section of M14 observations, we calculate a depth-integrated transport estimate of 30.8 Sv. The DWBC transport in the model along this section is 58.5 ± 29.8 Sv, where the standard deviation is over all model (2-day) output samples, while interannual standard deviation in annual mean transports is 4.5 Sv. The difference between the model and observed transport sample-means is statistically significant (section 3.6.5). The model transport estimate, as well as the stronger barotropic tendency relative to the observations along the section, are similar to the results of the VIKING20 numerical model employed by M14, 60.3 ± 23.6 Sv. However, further validation deferred to section 3.6.6 shows that the (GB_B) model DWBC transport in other sections is very similar to observations, and a cause for this difference is suggested.

We also compared model Eulerian EKE with observations. *Fischer et al.* [2018a] have gridded veloc-

ity data from Argo floats [*Lebedev et al.*, 2007] at 1500 m depth around FC as well as further north. We use their Gaussian-interpolated product [*Fischer et al.*, 2018b], with grid-cell size (generally not equivalent to resolution) of 1/4 (1/2) degree latitude (longitude). Note figure 5b in [*Fischer et al.*, 2018a] is somewhat saturated in some areas around FC. We find that around east and south FC, within the DWBC and NAC, the model EKE is of similar magnitude or higher (by up to a factor ~ 3) than the *Fischer et al.* [2018a] gridded-EKE. As in the altimetric observations (see above) this is likely related to the coarser observational product not fully resolving smaller scale fluctuations. *Fischer et al.* [2018a] also provide EKE values at two moorings (K18 and B227) within the DWBC around FC. Mooring B227 is near the M14 section. We find that model EKE at these mooring locations is only $\sim 20\%$ higher than observed, and within the uncertainty range (the difference being equal to about one standard deviation of model EKE values).

The model suffers from a bias in the mid-depth density field. As seen in Fig. 3.11, the $\sigma_\theta = 27.8$ kg/m^3 isopycnal is $400 - 700$ m too deep in the model. The model density bias is mostly related to (not shown) a salinity bias. A salinity-related density bias, especially at mid-depth, is very common in Sub-Polar North Atlantic numerical models. See for example Figs. 3 and 6 in *Bower et al.* [2011] in comparison with Fig. 3.11; as well as Fig. 2 in *Handmann et al.* [2018]. This common problem was previously attributed [*Tréguier et al.*, 2005; *Rattan et al.*, 2010] largely to salt transport biases appearing in model boundary currents. Typically, nudging model salinity to climatological values is required, although not always sufficient, to reduce or eliminate the bias in present models. A disadvantage associated with a nudging procedure may be reduction in frontal features and sharpness of boundary currents in high resolution models, because the resolution of climatological datasets is generally coarser. We therefore did not apply such a nudging procedure. In our model the bias gradually appears during spin-up and appears to be fully developed by year 9, without further increase in the bias amplitude in the following years. It is difficult to determine with certainty to what degree our key results are affected by the water mass bias. We expect however, that the such effects should manifest mainly indirectly, through the effects on the mean circulation and on EKE. The good agreement of leakiness and recirculation patterns with other models, and with observations (here, and in section 3.3.1), is encouraging in this regard, as is the

comparison with EKE observations (above). It appears however, that DWBC flow east of Flemish Cap has a stronger barotropic component that observations suggest. The implications of this possible bias are discussed in section 3.5.3.

There are additional caveats concerning the temporal extent of the surface and horizontal boundary fields used to determine the model boundary conditions. These fields only have a 4-year length, corresponding to a 2001-2005 atmospheric state, and are recycled after the first four model years (section 3.2.1). Since the domain (open) boundaries are very far (over 500 km) from the analyzed area, the transient effects of the recycling method are likely very limited. Indeed, we do not observe any significant changes at the 4 year period (e.g., in mean kinetic or potential energy), other than the seasonal cycle similar to that observed in other years. Furthermore, the analysis presented in section 3.3.3 confirms that rare events are not important for either the mean or eddy components of offshore flow. However, years 2001-2005 cover only negative to moderate North Atlantic Oscillation index values, and therefore the model boundary forcing is likely not representative of the full range of DWBC variability. Interannual and decadal variability in atmospheric forcing, including that due to the North Atlantic Oscillation, influences the depth of deep convection in the Labrador Sea, and hence the variability in LSW thermohaline properties [*Yashayaev and Loder*, 2016] as well as DWBC transport [*Zantopp et al.*, 2017].

Finally, we qualitatively compare in Fig. 3.12 pathways of (3D) Lagrangian floats in the model (Exp3d, section 3.2.3) to the (isobaric) ExPath floats [*Bower et al.*, 2011]. At each deployment depth (700 and 1500 m), a batch of 30 particles are randomly selected and their trajectories extended to a 2 year duration. The full trajectories of these floats and ExPath floats are displayed in Fig. 3.12. The transport patterns are generally similar to those sampled by the ExPath floats: the majority of particles were caught in recirculations within the Newfoundland Basin. A smaller fraction traveled south in the interior of the ocean. Some particles crossed the Mid Atlantic Ridge eastward at the Charlie-Gibbs Fracture Zone. Only a few particles traveled within the DWBC continuously past the GB, although more model particles did so compared with ExPath floats. This likely due to fewer model particles traveling through Flemish Pass, which we speculate happens either due

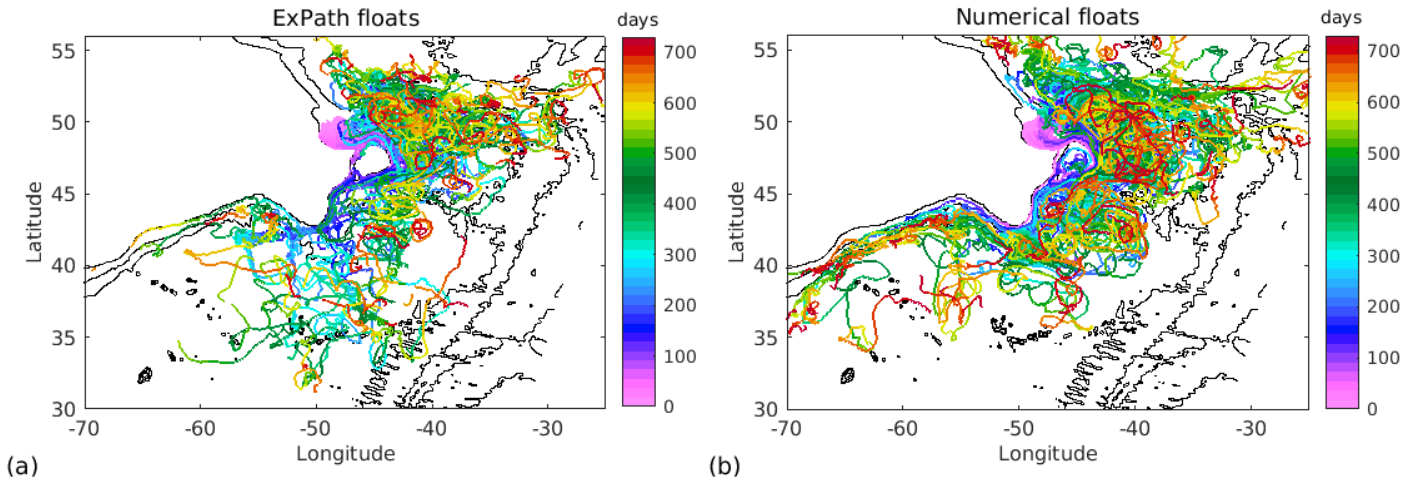

Figure 3.12: (a) Two-year trajectories of ExPath floats (note some of the floats had shorter life times). (b) Two-year trajectories of random batch of 60 3D model particles, divided equally between particles initiated at 700 and 1500 m depths. In both panels only a few floats cross the FC-GB region south and westward remaining within the DWBC. The rest leak into the interior, with the majority recirculating within the Nfl basin. A smaller but substantial fraction of leaked floats travel south within interior pathways away from the continental slope. Other apparent pathways are an eastward crossing of the Mid Atlantic Ridge at the Charlie-Gibbs Fracture Zone, and (with a higher number within model particles than ExPath floats) northward propagation to the Labrador Sea. The 1, 3, and 4 km isobaths are marked with black contours.

to model velocity output frequency not being high enough, or due to watermass biases. A second bias appears in the model in that more particles appear to cross north to the subpolar area compared to the number for ExPath floats. Some of these differences from the ExPath floats manifest similarly in the 3d float trajectories of *Bower et al.* [2011, their Fig. 7a].

3.6.4 EKE comparison with altimetry and degradation with resolution

The model surface geostrophic EKE (appendix B) is about five times larger than the altimetric estimates based on the DUACS L4 merged reprocessed product [*Pujol et al.*, 2016], in a region around

FC (figure 4.1(c-d)). Lower altimetric EKE is to be expected, since the model (GB_B) horizontal grid resolution is about 10 times higher than that of the altimetric product. In addition, the objective mapping technique applied in constructing the altimetric product is associated with coarser scales than its grid resolution. Indeed it is well documented that the altimetric product is biased low in EKE [*Pujol et al.*, 2016]. The unresolved scales contribute much of the difference in energy. For example, while the locations of elevated EKE are generally in agreement between the panels, the altimetric product shows no elevated values near the Labrador Current, which has width close to the product resolution. These issues are likely exacerbated since the Rossby radius of deformation in the region is close to or lower than the altimetric product resolution. Additionally, it is possible that model EKE is biased high due to not including current-atmosphere feedback parameterization [*Renault et al.*, 2016a,b, 2019].

To roughly gauge the effect of coarser resolution sampling on the model EKE, we applied a spatial Gaussian low pass filter (LPF) to GB_B SSH fields in calculation of (low-passed) EKE. Two different LPFs were tested separately. A 1/4 degree standard-deviation (std) LPF approximately represents a 25 km grid resolution. The 1/4 degree LPF applied to the model fields results in only a 40% EKE reduction within the same region. However, the effective spatial and temporal resolutions of the altimetric product are generally lower than its grid resolution and sample intervals, respectively. These depend on the details of the objective mapping method applied to the multiple-satellite data set (see appendix B in *Pujol et al.* [2016]). The enforced DUACS-L4 data correlation scales of observations to derived fields are $\geq$ 100km and $\geq$ 15 $days$ at the latitudes considered in figure 4.1. In addition the observation covariance matrix is constructed on a 1 degree grid. Thus, to account for the objective mapping effective resolution in a rough approximation, we thus exchange the 1/4 degree LPF for a 100 km std LPF. According to *Soufflet et al.* [2016], effective numerical model resolution is about 5 $\times$ the grid resolution. Therefore effective numerical (GB_B) model resolution is $\approx$ 12.5 km, and hence the 100 km st LPF is a reasonable method of comparison with the altimetric product. The resulting GB_B model spatially averaged LPF EKE (not shown) is within a few percent of the spatially-averaged altimetric observations within the region, demonstrating that the discrepancy in amplitude of the unfiltered model EKE compared with altimetry, is largely due

to lower effective altimetric product resolution.

3.6.5 Statistical comparison of model and observed DWBC transports

The model mean DWBC transport at the 47 N section east of Flemish Cap (FC) , 58.5 ± 29.8 Sv, is considerably higher than the observational value [*Mertens et al.*, 2014], 30.7 ± 7.4 Sv, an average of six summer-time LADCP ship-sections, from different years. Additionally the observations were taken in summertime, and Ma-August model mean transport is even 5.5 Sv higher. Here we defined the Eulerian mean transport as the sum over all southward transport cells west of 41 W, of the time-mean Eulerian velocity section. Note that M14 used a different definition, obtaining 37.47 ± 7.4 Sv. The model transport standard deviation is based on transport estimates over all (2-day) output samples from years 9-16, a total of 1460 samples. The time samples may be taken as approximately independent, since on the continental slope, variability over time scale of a few days is high [*Mertens et al.*, 2014], likely due to topographic Rossby waves. A more conservative approach, where the number of effective degrees of freedom is halved (analogous to a 4-day integral scale) leads to only a 3rd significant digit change in the p value we quote below. Since six observations are likely not enough to estimate variability well, we make the assumption that the variance of the distributions from which the model and observed samples were taken are equal, leading to equation 5.9 for the test statistic z in *Wilks* [2011],

$$z = \frac{\overline{x_1} - \overline{x_2}}{\sqrt{\frac{1}{n_1} + \frac{1}{n_2}} \sqrt{\frac{(n_1-1)s_1^2 + (n_2-1)s_2^2}{n_1+n_2-2}}}. \tag{3.9}$$

Here x_i is the transport mean, n_i is the number of degrees of freedom, and s_i is the standard deviation, within set i, i.e., the ROMS or observational [*Mertens et al.*, 2014] data. The test statistic value is then $z = 2.27$, leading to significance $p = 0.0231$ for a two-sided test. Therefore, the null hypothesis that the true means are equal is rejected. The high model transport is similar to the results of the VIKING20 numerical model employed by M14, 60.3 ± 23.6 Sv. However, in the next subsection we show that the model DWBC transport is in excellent agreement with observations in other locations, and suggest a reason for the reason for gross model disagreement with the

M14 observations.

3.6.6 Additional model DWBC transport validation

Here we show evidence that within the GB_B simulation, the high DWBC transport relative to observations at the *Mertens et al.* [2014] (M14) section is partially the result of southward flow on the western flank of the southern cyclonic recirculation to the east of the DWBC (figure 3.5). The cyclonic recirculations around FC have been reported previously based on observations and other numerical models as well (section 3b). The GB_B DWBC top to bottom transport east of FC but further north from the M14 section, between the two recirculation cells residing east of FC, is 33.2 ± 3.5 Sv, a value much closer to the M14 observations. Note that this and the following uncertainty values correspond to interannual standard deviation in annual mean transports, rather than variance of 2-day average values as for the (29.8 Sv) model value given previously. It is possible that model details such as bathymetric smoothing may influence the exact position of the model FC recirculations, and hence the apparent DWBC transport one derives without accounting for recirculation. The northward velocity magnitude further east of Flemish Cap in the model is generally higher as well than in the mean M14 section, which is together with the strong southward anomally nearer to FC, is consistent with the idea of a stronger recirculation locally in the model.

Indeed, further upstream, around 53 N, the model (ROMS) top to bottom DWBC transport is 36.5 ± 2.2 Sv, much closer to the M14 (47 N) observations. *Zantopp et al.* [2017] present and analyze 17-years (1997-2014) of data from an array of moorings maintained across the DWBC at 53 N. They measure the DWBC transport at this latitude at 30.2 ± 6.6 Sv, beneath 400 m depth. This depth approximately corresponds to the upper boundary of LSW at this location. At the same depths the (GB_B) model DWBC transports 26.8 ± 1.8 Sv. Due to water mass bias in our model, the ρ_θ surfaces are considerably less flat than the observations at this depth and location, and hence we calculate the transport under the $\rho_\theta = 27.4$ kg/m^3 surface, which has mean depth close to

400 m in the model at this location. The model result is then 29.3 ± 2.1 Sv, quite close to the observations. Additionally, model velocity within Flemish Pass agrees favorably in pattern (not shown) as well as in total DWBC southward transport (8.4 ± 0.7 Sv) with observations-based estimates ($6.3 - 9.8$ Sv) [*Hill and Folkard*, 1973; *Greenberg and Petrie*, 1988; *Petrie and Buckley*, 1996]. Note the Flemish Pass transport is substantial relative to the ≈ 30 and ≈ 15 Sv encircling eastern FP, and remaining downstream of FC, respectively (section 3b).

3.6.7 Loss of ExPath floats around Flemish Cap

The number of ExPath floats that have left the DWBC around FC (section 3a) is estimated from reviewing individual trajectories and their time dependence (not shown). Despite some trajectory gaps (section 2a), it appears relatively clear that 33 of the 55 floats with usable trajectories (Sec. 2b) have left the DWBC around FC (see also *Bower et al.* [2009], figure 2b). Here the 45 N latitude is used as the boundary between south FC and the GB. Changing the limit by up to almost 0.5 degree to the north and more to the south, does not change these numbers. Five additional floats have likely left the DWBC at either south FC or east GB, which remains uncertain since their trajectories are less complete in their loss region. Ten floats have crossed south through Flemish Pass rather than travel around FC (see also *Bower et al.* [2011])[13]. Therefore $73 - 84$% of all floats that traveled around FC (i.e., excluding floats traveling through Flemish Cap), were lost ("leaked") from the DWBC to the interior before circumventing this topographic feature.

3.6.8 Statistical significance of Lagrangian velocity average

Statistical significance of Lagrangian mean quantities (section 3a) in each grid cell was determined approximately by the condition that $|\overline{v_c}| > 2S(v_c)$. Here an overbar denotes the simple mean estimator, a sample average, while $S(\cdot)$ denotes an estimator of the error of the sample av-

[13] Flemish Pass has a 1100 m deep sill, and all floats crossing it were of the 700 dbar ballast type.

erage. Two error estimators were tested. The first was $S_e = STD/N_e$. Here STD stands for the standard deviation of all v_c measurements, N_e is the effective number of degrees of freedom. In our estimate for N_e we account for consecutive population of a grid cell by the same particle. We do not account for co-population of a grid cell by particles from different OKL releases. This type of event is likely rare, since auto-correlation time in this area [*Böning*, 1988; *Lumpkin et al.*, 2002], 5-10 days, is no longer than intervals between releases (10 days), and due to the fine grid resolution. The approximation $N_e = N/n$ was made separately for each grid cell, where N is the number of samples used to calculate $|\overline{v_c}|$, and $n = Adx/|\overline{v_c}dt|$ is the average number of TrajInt time samples (with time step dt) required for a particle to leave a grid cell (of length dx). The factor $A = 0.25$ approximately accounts for the two-dimensional geometry, assuming entry directions into cells are random. The second error estimator is based on the standard deviation (STD_{MA}) of annual v_c averages over $N_Y = 8$ years (model years 9-16) $S_M = STD_{MA}/N_Y$. Both methods yielded similar results, and hence the second, simpler method is used to define statistically significant values in figure 3.3.

3.6.9 Additional Lagrangian mean diagnostics for model particles

To complement figure 3.3, where the Lagrangian-mean quantities were shown for particles initialized over 1500 m depth, we display the same diagnostics for particles initialized over 700 m depth in figure 3.13 below. The results are very similar to 1500 m particles results. One difference is the transport of 700 m particles through Flemish Pass (the $\approx$ 1100 m deep channel west of Flemish Cap, FC in the figure). A second difference is that 700 m particles have statistically significant velocity further downstream than 1500 m initialized particles, including west of Grand Banks. For this reason, the displayed area in figure 3.13b is larger than in figure 3.3.

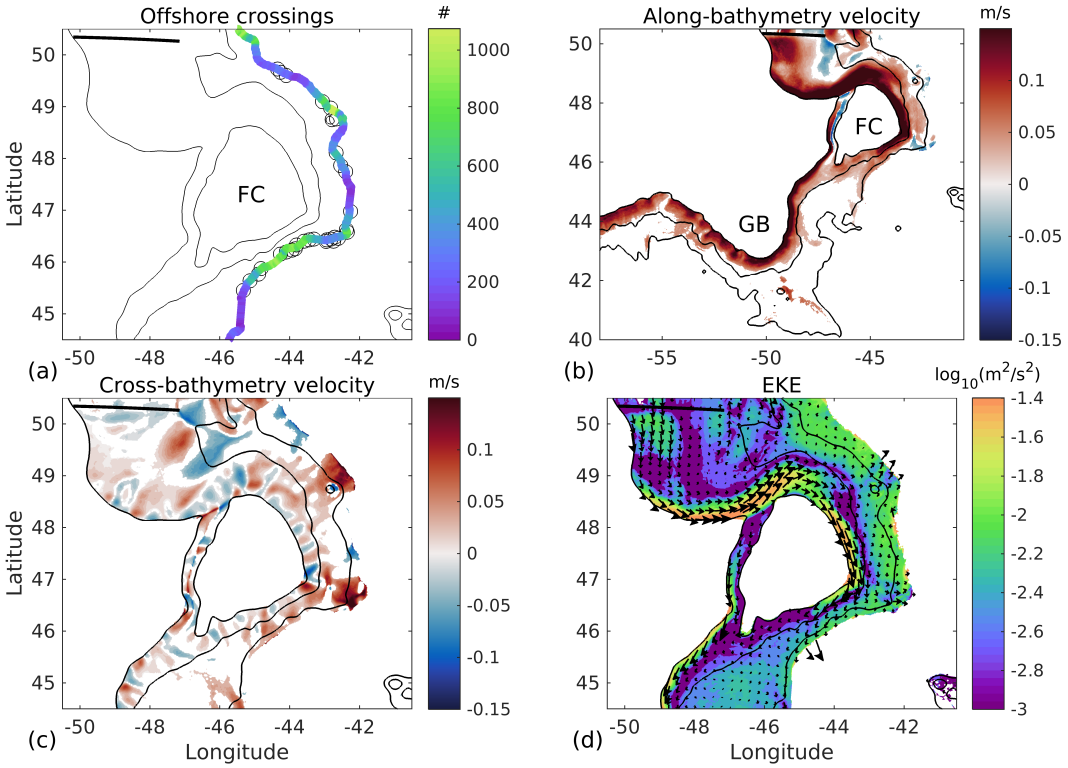

Figure 3.13: The figure is identical to figure 3.3, except that model particles initialized at 700 m depth (rather than 1500 m) are used here, and that a larger area is displayed in panel b. (a) Locations at which the ExPath floats (circles, both 700 and 1500 m depths) and 700 m depth-initialized Exp3d particles (colors) first cross the 4 km isobath. The colors correspond to the number of model particles crossing the 4 km isobath at each model gridpoint along the isobath. (b) Lagrangian-mean along-bathymetry velocity component (positive ≈ downstream), (c) Lagrangian-mean cross-bathymetry velocity component (positive offshore), and (d) Lagrangian eddy kinetic energy (EKE) derived from the Exp3d particles initialized at 1500 m depth (see section 3c for definitions). In panels b-c, only statistically significant values are displayed, i.e., white patches are not associated with significant values. Lagrangian mean velocity vectors are superimposed in panel d. The 1, 3, and 4 km isobaths are marked with black contours in each panel. The deployment line (OKL) of model particles is marked by the thick black line. The bathymetric features of Flemish Cap and the Grand Banks of Newfoundland are marked by the letters FC and GB, respectively, in panels a-b.

3.6.10 Streamfunction calculation by a flood-fill algorithm

Given that large scale flow averaged on isopycnal surfaces is largely geostrophic, it should also be approximately non-divergent. Hence the isopycnal velocity may be used to derive the streamfunction (ψ) locally to a good approximation [14], by simple integration of the relation

$$d\psi = vdx - udy. \tag{3.10}$$

To that end, an integration path need be chosen. One simple choice is interleaving integration along lines of constant model coordinate (x and y, approximately zonal or meridional, respectively, in our configuration), where a full line is continuously integrated until the region boundary, followed by integration of the next row in the opposite direction. A disadvantage of the interleaving integration approach is that errors accumulate over very different paths for adjacent pixels in different rows (when interleaving is between rows), hence making the streamfunction less smooth in the interleaving direction. To avoid this pitfall, we adapt a queue (i.e., first-in first-out) flood-fill algorithm [*Pavlidis*, 2012] to create multiple integration paths, growing outside in a dendritic-like fashion from a chosen initial seed point. A pseudo-algorithm follows. An added advantage is that taking into account "islands" and complex boundaries is accomplished simply by the definition of the mask array (see below).

Derivation of a streamfunction by direct integration of velocity is strictly correct only for a non-divergent velocity distribution. However, the divergent component of the mean flow on potential isopycnal surfaces is relatively small in our results. That is confirmed, by testing that the streamfunction describes the mean circulation to a good approximation (not shown). The mesoscale or larger patterns are confirmed qualitatively by plotting superimposed model velocity fields and the derived approximate ψ. The local velocity field defined by ψ is confirmed on the grid scale by deriving the velocity from $(u_1, v_1) = (-\partial y, \partial x)\psi$, and comparing it with the original (u, v) field. The maximal difference is orders of magnitude smaller than the actual velocity everywhere. That

[14] Note the only approximation in (3.10) is that the full isopycnal velocity is used rather than its the rotational component.

may not be the case using an interleaving integration method, for the velocity component perpendicular to the interleaving direction, as mentioned above. The pseudo-algorithm follows:
0. Initialize a streamfunction array (ψ), and a mask array (M). Set $M = 0$ in masked areas (e.g., land areas, boundary pixels, and other points where the isopycnal surface does not occur), and $M = 1$ elsewhere.
1. Choose an initial grid cell i, which has $M(i) = 1$. Set $\psi(i) = 0$, and $M(i) = 0$. Add pixel i to queue.
2. While queue is not empty,
3. Remove the first pixel (p_1) in queue.
4. For each pixel p which is adjacent to the removed pixel p_1, and for which $M(p) = 1$,
5. Calculate $\psi(p)$ by integrating (3.10) from p_1 to p. Set $M(p) = 0$.
6. Add pixel p to end of queue.

3.6.11 Cluster analysis of the horizontal circulation pattern variability

Here we examine the statistics of the horizontal circulation pattern. We are specifically interested in the typicality of streamline separation from the DWBC, and of the cyclonic recirculations. To achieve this, we perform a cluster analysis of velocity distribution on potential density surfaces. The clustering method used is a single-layer competitive neural network method [*Dreyfus*, 2005], as implemented in the MATLAB function "competlayer" [*Beale et al.*, 2019]. The algorithm finds a predefined number N_c of clusters (velocity distributions) that best represent the data in the metric used. Each cluster represents the "best" match to the instantaneous velocity in a Euclidean metric, for a significant number of model time samples.

A qualitative description of the clustering algorithm follows. For a thorough description see *Dreyfus* [2005], and the "competlayer" function description in *Beale et al.* [2019]. Each (2-day mean) GB_B velocity (3-dimensional) output time sample is interpolated onto a chosen (isopycnal) surface S_σ to form a two-dimensional distribution of horizontal velocity, $\underline{V}(t, x_1, x_2)$, which consti-

tutes an input sample for the cluster analysis. The cluster distributions $\underline{V}_n(x_1, x_2)$ are initialized randomly. In the main part of the algorithm, velocity samples $\underline{V}(t, x_1, x_2)$ are randomly drawn from a chosen input set, here all output samples from years 9-16. After each random draw, it is determined which cluster is closest, in a Euclidean metric, to the drawn sample. The closest ("winning") cluster is then adjusted to better represent the sample. At the end of the process, each sample is associated with exactly one cluster. Each cluster is then a velocity distribution which is approximately equally likely in terms of the number of samples closest to it within the input set.

Figure 3.14 shows results for circulation on $\sigma_1 = 32.43\ kg\ m^{-3}$ using eight clusters. The velocity distribution of each cluster is presented in terms of a streamfunction, for easy comparison with the time-mean circulation pattern. Note that each cluster represents typical circulation conditions during approximately an equal (1/8) fraction of time samples. It is evident that (1) the cyclonic circulations previously identified in the time-mean circulation around FC are present in some form in each of the clusters; (2) the main difference between clusters is the offshore location of the recirculation present east of the southeast FC corner, and (for a smaller fraction of time) its possible coalescence with the recirculation at the northeast corner; (3) the offshore separation of DWBC streamlines occurs in most of the clusters as well (although this is not clear in all panels due to the number of contours used). The clustering is qualitatively insensitive to the prescribed number of clusters (between 4 and 36 clusters were attempted, not shown), i.e., essentially no new patterns emerge with an increase in the number of clusters. Rather, clusters look much like combinations of patterns already present in Fig. 3.14. Therefore, the separation of DWBC streamlines around FC is not just a mean flow pattern (section 3.3.2), but also as a typical flow pattern.

The described results and the main qualitative features identified, are very robust to to changes in the values of the free parameters of the clustering method. Some of the parameter ranges which were tested are: a. choosing up to 36 clusters or as few as 4.; b. variations in the algorithm itself, including using "self-organizing maps" [*Dreyfus*, 2005]. c. The number of training "epochs".

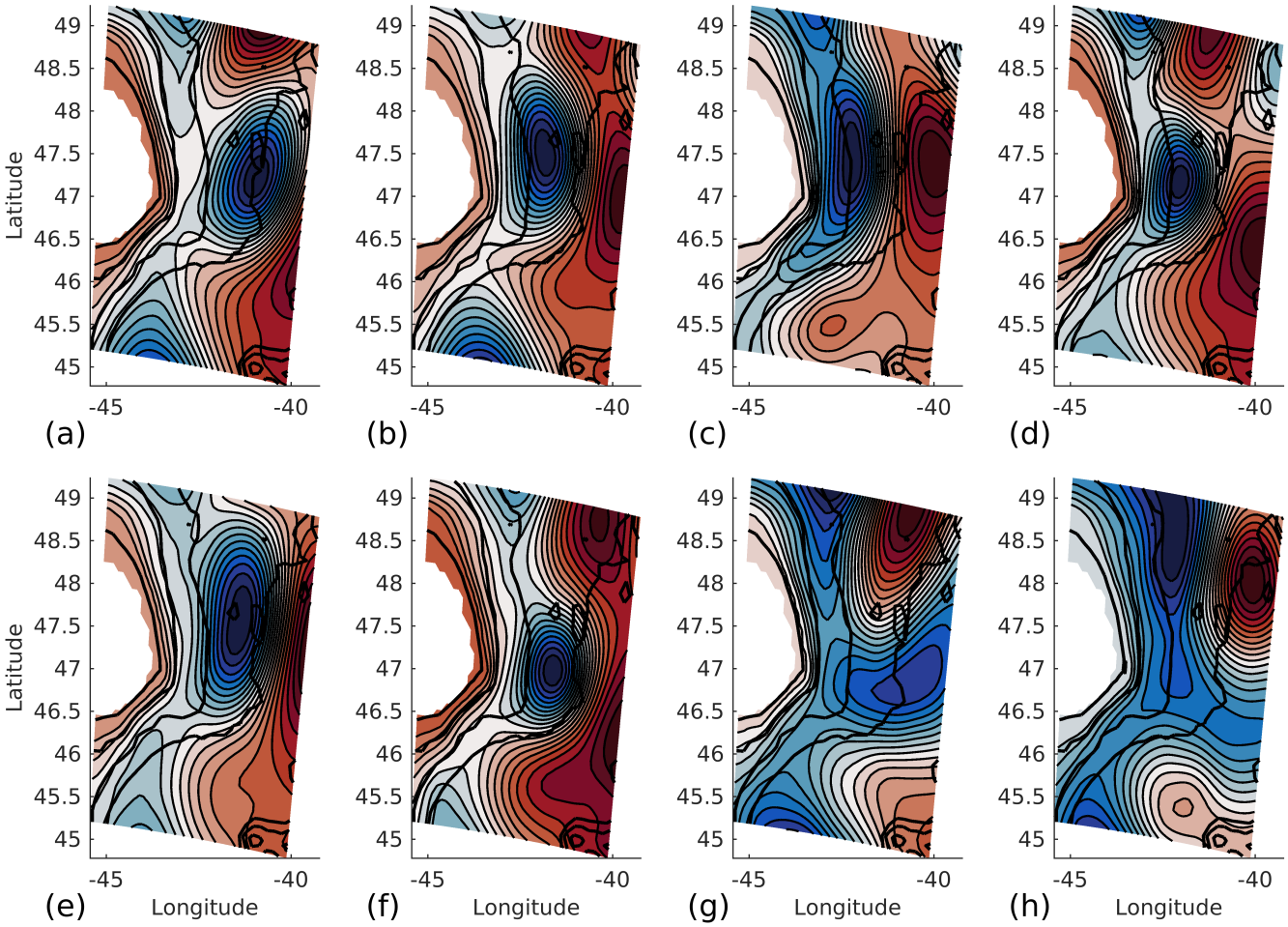

Figure 3.14: Clustering of the isopycnal circulation around Flemish Cap using a single layer competitive neural network. The clustered variable is velocity along the $\sigma_1 = 32.43\ kg/m^3$ surface between model years 10 and 16. Each panel displays the velocity distribution of a single cluster. Streamfunctions (colors and thin lines) are used rather than, e.g., arrow plots, for effective visualization. The $\{1, 3, 4, 4.5\}\ km$ isobaths are shown in thick black contours. The fraction of time each cluster "occurs" is approximately equal.

In each epoch each sample is drawn exactly once (and used to calculate and update the winning cluster), in random order. d. Changing the neural network learning rate parameters: Kohonen weight and conscience bias. Trials were conducted with the weights in the ranges $0.001 - 0.05$, and $0.0001 - 0.01$, whereas their default values in "competlayer" are 0.01 and 0.001, respectively. The results are also representative of other mid-depth or deep isopycnal layers as well, including $\sigma_2 = 37.014\ kg/m^3$ which was examined in the time mean above, as well as depth layers, e.g., $500 - 1000$ or $2000 - 2500\ m$ depth. Enlarging the horizontal area over which the analysis is done also does not change the main results. The clustering area of the results presented in figure 3.14 was chosen to maximize visibility of the patterns while still capturing most of the area of interest.

3.6.12 Correlations between offshore velocity and bathymetric variation

We present correlations between offshore velocity and variables related to bathymetric variation along the 3 km isobath. Offshore velocity is averaged over depths greater than 500 m. The bathymetric variables examined are curvature, steepness, and steepening. The latter is defined as the change in steepness with along-isobath distance. Offshore velocity and the former two bathymetric variables are displayed in Fig. 3.9. The correlation data is summarized in Table 3.6.12.

Table 3.2: Correlations (denoted "Corr." within the table) between offshore velocity and bathymetric variability along the 3 km isobath (Fig. 3.9). For each bathymetric variable, the correlation at zero lag, as well as the correlation of maximal magnitude (and its distance lag) are presented. Lag coefficients are positive (negative) if local peaks of offshore velocity tend to occur downstream (~southward) of the bathymetric variable local peaks. A curvature versus offshore velocity cross-correlation distance of $d_{ccor} = \int r(s)ds \approx 40\ km$ is obtained, where $r(s)$ is the respective cross-correlation function at lag distance s, and the integral is performed over the entire isobath section displayed in Fig. 3.9. The correlation $\pm 2\sigma$ (i.e., $p = 0.05$) confidence intervals are obtained using a Fisher z transform [*Wilks*, 2011] with number of degrees of freedom (n_{dof}) equal to section length divided by d_{ccor}, i.e., $n_{dof} = 100$.

Bathymetric variable	Corr. at lag= 0	2σ range	Lag at max |Corr.|	Corr. at max |Corr.|	2σ range
Isobath curvature	-0.34	$[-0.50, -0.15]$	$45\ km$	-0.56	$[-0.68, -0.41)$
Isobath steepening	0.22	$[0.02, 0.40]$	$73\ km$	0.47	$[0.3, 0.61]$
Isobath steepness	0.18	$[-0.02, 0.36]$	$-100\ km$	0.31	$[0.12, 0.48]$

CHAPTER 4

Formation Of Anticyclones Above Topographic Depressions

4.1 Introduction

In several ocean basins, long-lived and semi-stationary mesoscale anticyclones (ACs) appear above topographic bowls[1]. Examples are the Mann Eddy [*Mann*, 1967], Lofoten Basin Eddy [e.g., *Ivanov and Korablev*, 1995; *Köhl*, 2007; *Søiland et al.*, 2016], and the Rockall Trough Eddy [*Le Corre et al.*, 2019a]. The eddies have a clear climatological signature in sea-surface-height, as seen from satellite altimetry (figure 4.1). The first two have been repeatedly sampled in hydrographic surveys since their first discoveries. In the elongated bowl-like Iceland Basin long-lived ACs also appear to be common [*Martin et al.*, 1998; *Wade and Heywood*, 2001; *Read and Pollard*, 2001; *Zhao et al.*, 2018].

The aforementioned ACs all occur in high latitude North Atlantic[2] seas or basins, where stratification is relatively weak, and the Coriolis parameter (f) is relatively high. This results in a larger tendency for currents to respond to seabed depth (H) variations [*Salmon*, 1998] and follow ambient potential vorticity (f/H) contours [*Isachsen et al.*, 2003]. The latter are often well-approximated by H contours due to the limited relative f variation in in higher latitudes compared with relative H variation across basins [*Nøst and Isachsen*, 2003]. Thus the effect of topographic depressions may be enhanced in these areas and play a role in the formation of the ob-

[1] We loosely define a bowl as a topographic depression which has a central relatively flat region of similar width or wider than the outer slope region.

[2] The North Atlantic is by far the most-sampled of the oceans, and hence a statistical bias may be present.

served ACs.

Significant thermohaline fluxes and transformations occur in these basins, processes of climatic significance as part of the Atlantic Meridional Overturning Circulation (AMOC). *Tulloch and Marshall* [2012] suggested that the Mann eddy affects the trajectory and strength of the North Atlantic Current in the Newfoundland basin [cf. *Meinen*, 2001], as well AMOC variability, in two ocean general circulation models. The Lofoten Basin Eddy attains anomalously large wintertime mixed layer depths [*Yu et al.*, 2017]. It encompasses a large reservoir of heat, absorbing warm eddies shed from poleward flowing boundary currents [*Raj et al.*, 2015; *Søiland et al.*, 2016]. *Richards and Straneo* [2015] presented evidence for water mass transformation within a Lofoten Basin eddy. Likewise, *Zhao et al.* [2018] suggested that the long-lived anticyclones of the Iceland Basin are susceptible to air-sea interaction and water mass transformation due to isopycnal doming.

Several different mechanisms have previously been suggested to sustain these eddies. *Köhl* [2007] presented evidence that the Lofoten Eddy is maintained by repeated mergers with ACs, which are shed from the Norwegian Atlantic Current and descend into the Lofoten Basin due to planetary and topographic beta drift [see *Carnevale et al.*, 1991]. *Le Corre et al.* [2019a] showed that the Rockall Trough Eddy is similarly replenished by ACs, resulting from frictional vorticity generation at the adjacent topographic slope. *Zhao et al.* [2018] showed that Iceland Basin ACs are likely formed locally through mixed baroclinic-barotropic instability of the adjacent slope current. *Rossby* [1996] suggested that the Mann eddy is spawned from ACs released from the anticyclonic side of the adjacent North Atlantic Current.

In contrast, several theoretical and numerical studies have shown that in the absence of large scale external flow, mesoscale variability trends to produce rectified prograde[3] mean flows. That is, cyclonic (anticyclonic) circulation develops over topographic depressions (bumps), consistently with vorticity stretching (compression). This is predicted by "enstrophy-minimization" theory [*Bretherton and Haidvogel*, 1976][4], as well as statistical mechanics theories of topographic

[3]The same propagation direction as that of coastal Kelvin waves and topographic Rossby waves.
[4]Based on the tendency of enstrophy to dissipate faster than energy in 2d turbulence.

turbulence [starting with *Salmon et al.*, 1976]. This tendency is commonly known as the "Neptune" effect [e.g., *Merryfield et al.*, 2001]. With an imposed large scale impinging flow, dynamical seamount circulation theories also predict development of a prograde mean circulation [*Hogg*, 1973; *Huppert and Bryan*, 1976], as indeed had been observed in the ocean[5] [*Hogg*, 1973; *Owens and Hogg*, 1980; *Richardson*, 1981; *Freeland*, 1994; *White and Mohn*, 2004]. Alternative mechanisms must therefore explain the presence of long-lived ACs in topographic "bowls".

Although separate formation mechanisms were previously suggested for each of the above-mentioned semi-stationary oceanic ACs, there is not presently a unified dynamical understanding of AC formation and longevity above bowl-like topographic depressions. With the aim of achieving such an understanding, in this study we pose an idealized topographic-turbulence problem. Specifically, we conduct numerical simulations of the free evolution of mesoscale eddies randomly initialized over topographic depressions. We restrict our attention to the layered primitive equations, in one or two density layers, allowing wide sweeps of parameter space.

A description of the numerical experiments configurations is given in section 4.2. In section 4.3 we show that ACs form consistently over isolated topographic bowls in a very wide set of circumstances in single-layer experiments, and characterize the range of dynamical regimes that emerge in our simulations. In section 4.4 we investigate the degree of cross-topography exchange involved in AC formation, and its dynamical mechanisms. In section 4.5 we show that bowl ACs form from barotropic as well as baroclinic initial conditions in 2-layer experiments, and investigate the dependence of its final vertical structure on the initial conditions. A discussion and comparison with previous results is presented in section 4.6. A summary and conclusions are given in section 4.7.

[5] Such circulations can also result from tidal rectification [e.g., *Beckmann and Haidvogel*, 1997].

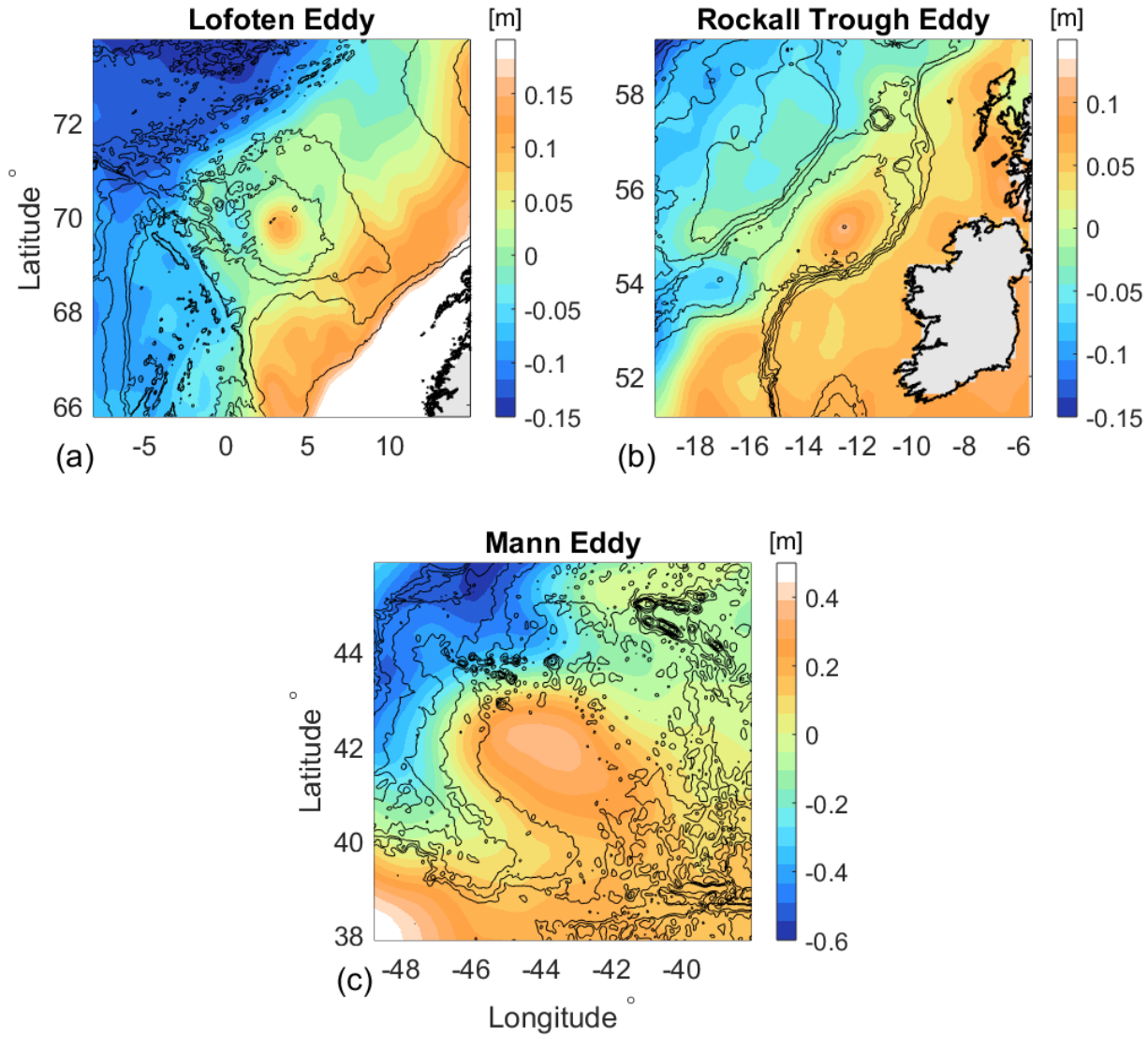

Figure 4.1: Observations of anticyclonic long time-mean motions within topographic depressions in the ocean. Observed mean Sea Surface Height (SSH, in color, between 1993-2018) is shown at three ocean basins with bowl-like bathymetry and semi-permanent anticyclones within the bowls: (a) Lofoten Basin; (b) Rockall Trough; (c) Newfoundland Basin. The climatological (time-mean) locations of long-lived semi-stationary anticyclonic vortices (section 4.1) are identified by local maxima in SSH within the bowls in each panel. Daily SSH data ("Absolute Dynamics Topography") was obtained from the SEALEVEL_GLO_PHY_L4_REP_OBSERVATIONS_008_047 product distributed by Copernicus (https://marine.copernicus.eu/). A (dynamically irrelevant) constant value is subtracted from each panel for visual clarity. Colormaps in panels (a) and (c) are saturated at high (low) values in areas far from the relevant anticyclone. Bathymetry is shown in thin black contours denoting, in (a) [-3200,-3000:1000:-1000], (b) [-3000:500:-1000], (c) [-5000:500:-2000] m depth. Land is in gray: Norway and Ireland, in panels (a) and (b), respectively.

4.2 Methods

4.2.1 Layered Primitive Equations model

We conduct our simulations using the layered primitive equations model AWSIM [*Stewart and Dellar*, 2016][6]. The model equations [e.g., for two-layers it is given by equation 5.6 in *McWilliams*, 2006] represent the simplest setting for studying topographic turbulence with finite amplitude topography and finite amplitude circulation effects. A primitive equation model is preferred over a quasi-geostrophic model because some of the observed ACs (section 4.1) have a high Rossby number ($\zeta = O(f)$) and reside in areas with $O(1)$ changes in H [*Søiland et al.*, 2016; *Yu et al.*, 2017; *Le Corre et al.*, 2019a].

The main model equations and its numerical scheme are described more fully in *Stewart and Dellar* [2016]. Here we summarize salient aspects of the model. The dynamical equations are discretized via finite differences on an Arakawa C grid. The spatial discretization of the momentum and thickness equations [*Stewart and Dellar*, 2016] is essentially identical to *Arakawa and Lamb* [1981] for the present experiments. Time stepping scheme follows the third-order Adams-Bashforth scheme [*Durran*, 1991]. The model conserves total energy and layer-wise potential enstrophy and mass to machine precision in the absence of explicit dissipation [*Stewart and Dellar*, 2016]. A rigid upper lid condition is applied for computational efficiency, and surface pressure is diagnosed at each time step by numerical solution of the associated elliptic equation using a multi-grid method. Grid-scale accumulation of energy and enstrophy is controlled using a hyperviscous operator in the momentum equation [*Griffies and Hallberg*, 2000].

The model can also evolve a passive tracer using an advection-diffusion equation, which was implemented in several of the experiments we conducted. We used the flux-limited tracer advection scheme of *Kurganov and Tadmor* [2000], which allows us to integrate the tracer equation without

[6]The AWSIM model code used in this study can be obtained from `https://github.com/andystew7583/AWSIM`.

any explicit diffusion operator in the tracer advection equation.

4.2.2 Main experiments

We conduct most of our experiments using an isolated topographic bowl, with the following topographic depth (H) structure:

$$H = H_0 + \frac{H_b}{2}\left[1 - \tanh\left(\frac{r - R_b}{W_b}\right)\right]. \tag{4.1}$$

Here H_0 is depth far outside of the bowl, H_b is bowl depth relative to H_0, R_b is bowl radius, and r is distance from bowl center. We call W_b the bowl half-width, since most of the topographic variation (76%) occurs over a distance $\pm W_b$ from slope center, and since the slope decreases appreciably at larger distances. We are interested mostly in small W_b/R_b values, which prescribe relatively flat bowl interiors (section 4.1). For example, with $W_b/R_b = 1/6$, the slope magnitude at $r = R_b - W_b$ is already an order of magnitude smaller compared with at $r = R_b$. Examples of several H profiles with different parameter choices used in our experiments are shown in figure 4.2. Experiments with more complex topography are discussed in section 4.6.

The initial velocity field is prescribed randomly such that dominant length scales are smaller than bowl size (e.g., its radius). Initial conditions for velocity are defined by a velocity streamfunction ψ, i.e., $v = \partial_x \psi$, $u = -\partial_y \psi$. The streamfunction is defined by its discrete Fourier transform,

$$\hat{\psi}_{k,l} = N^{-1} K^{-1} e^{-((K-K_0)/dK)^2} e^{i\theta_k}. \tag{4.2}$$

Here $K = \sqrt{k^2 + l^2}$ is the magnitude of the wavenumber vector $k\hat{\boldsymbol{x}} + l\hat{\boldsymbol{y}}$, where $\hat{\boldsymbol{x}}$ and $\hat{\boldsymbol{y}}$ are unit vectors in the x and y directions, respectively. The dependence of the eddy energy on wavelength is set by K_0, the wavenumber at which the spectral power peaks, and $dK = K_0/8$, the exponential width of the spectral power maximum. The phase θ_k of each Fourier component (k, l) is randomly generated from a uniform $[0, 2\pi]$ distribution. The factor N is a normalization constant that is selected to make domain-averaged kinetic energy density equal to a prescribed value E. An example of the resulting initial conditions is shown in figure 4.2a.

Table 4.1 lists our main single-layer experiments. We divide the experiments into batches according to the values of the geometric parameters H_0, H_b, R_b, W_b, and $\lambda_0 = 2\pi/K_0$. In each batch we fix these parameters and vary the initial kinetic energy density E. Each experiment is then referred to via the naming convention B_nE_m, where n is the batch number (left column of the corresponding row in table 4.1), and m is the experiment number within that batch. We set m equal to 1, 2, 3,... to denote the experiments with 1st, 2nd, 3rd,... lowest initial kinetic energies within each batch.

The values of H_0 used are typical of deep seas ($\sim$ 2 km) or abyssal ocean depths ($\sim$ 4 km). The values $H_b = 0.1$–0.5, $R_b = 150$–300, and $W_b = 50$–100 km, are loosely based on values relevant for the Mann eddy basin, although the latter is significantly more complicated than a symmetric bowl shape. The selected kinetic energy density values span (and surpass a factor of $\sim$ 2) the range of typical ocean velocities, i.e., velocity scales of cm/s to several m/s. We set the Coriolis parameter to a value of $f = 10^{-4}\ s^{-1}$ in all cases.

Unless otherwise specified, we conduct our experiments in square domain with a side length of 1000 km. We use periodic boundary conditions to facilitate comparison with topographic turbulence theories. We conducted several experiments with wall boundary conditions or with periodic domains multiple times larger, but we found no appreciable differences in the resulting bowl circulation. The horizontal resolution (dx) used is uniform and is either $\approx$ 2 or 1 km, corresponding to 512^2 or 1024^2 grid cells, respectively. The latter was used only in batch 1. In all cases $dx \leq \lambda_0/46$. We re-ran various experiments from several different batches with the grid spacing decreased by a factor of 2-4 to check the resolution sensitivity, but these experiments exhibited little quantitative and qualitative differences. Biharmonic momentum dissipation with constant coefficient $A_4 = 0.01dx^3U_{CFL}$ was used, where $U_0 = 1.5\ \max|\boldsymbol{u}(\underline{x}, t = 0)|$ is a velocity scale. Re-running several experiments with Smagorinsky-like [*Griffies and Hallberg*, 2000] biharmonic dissipation operator instead resulted in negligible quantitative differences. We also verified that kinetic energy does not accumulate at the grid scale over time — a sign of insufficient grid-scale dissipation. Model output was saved in 5-day (1-day) averages in batches 1-5 (6-9), except where

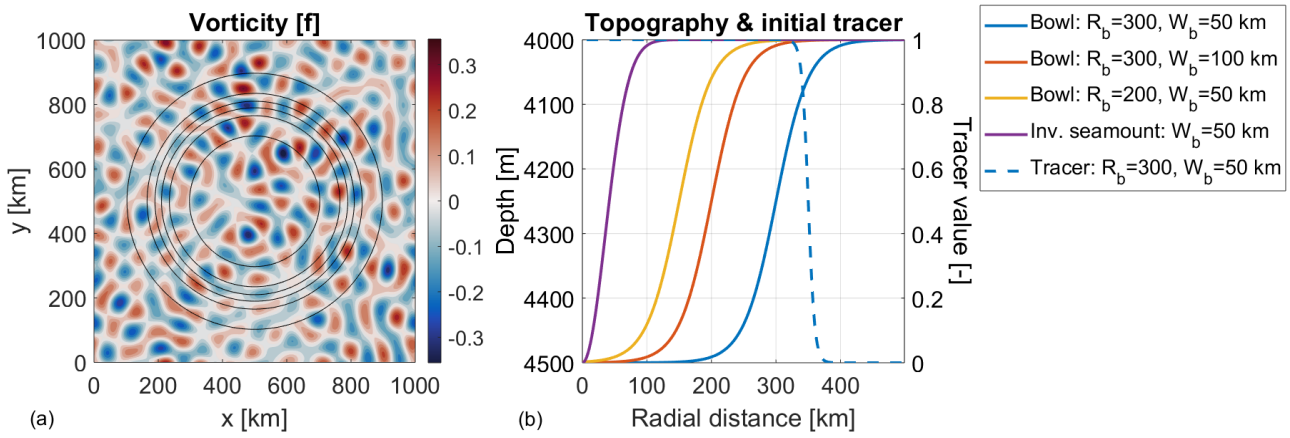

Figure 4.2: Initial conditions and examples of the experimental bathymetry. (a) Example of randomly generated vorticity initial conditions (in units of the Coriolis parameter f), with mean kinetic energy $E = 0.01\ m^2/s^2$ and dominant wavelength $\lambda_0 = 90\ km$. Black contours show the $(4010, 4100, 4200, 4300, 4400, 4490)\ [m]$ isobaths, for topographic parameters $R_b = 300$, $W_b = 50$, $H = 4$, $H_b = 0.5\ km$ (section 4.2.2). This domain geometry is typical of experiments described in sections 4.3-4.5. In panel (b) solid curves (left axis values) show several examples of radial topographic "bowl" profiles used in our experiments. We define a "bowl" loosely as a depression with a slope region of width ($\sim 2W_b$) that is narrow relative to mid-slope radius (R_b). Bowl-like topographies are typical of the locations in which persistent ACs occur in the ocean (section 4.1). The right axis shows initial conditions for the passive tracer (equation 4.3), which was included in experiment batches 2, 3, and 6 (see table 4.1).

noted otherwise.

A tracer field (section 4.2.1) is implemented in all experiments of batches 2, 3, and 6. We set the tracer initial condition $c(x, y, t = 0) = c_0(r)$, where r is distance from bowl center, as follows:

$$c_0(r) = \left[1 - \tanh\left(\frac{r - R_b - W_b}{W_c}\right)\right]/2. \tag{4.3}$$

This prescription is advantageous in estimating total cross-slope material transport (see section 4.4). The parameter W_c is set to a value of 10 km to minimize the width of the transition in the tracer concentration without introducing numerical artifacts in the calculation.

Table 4.1: Summary of our main single-layer experiments. Each experiment is later referred to by a name of form: B_nE_m, where n is the batch number (left column of appropriate row in the table), and m is the experiment number within the same batch. Parameters pertaining to the topography and initial conditions are given in each column. An experiment number m of 1, 2, 3,... corresponds to the 1st, 2nd, 3rd,... lowest initial kinetic energy experiment within each batch. Experiment energies for each batch are given in supplementary table 4.2. In all cases except in batch 9, the energies were 0.001,0.005,0.01,0.02,0.05,0.1,0.2,0.5,1,2 m^2/s^2, except that the last 3 values were not included in all batches and that the last value was in some cases replaced by the value 5 m^2/s^2. Therefore, e.g., experiment B_1E_5 (for which diagnostics are shown in figures 4.3-4.4) refers to the fifth lowest initial energy (0.05 m^2/s^2) among the experiments in the first row ($n = 1$).

Batch #	Bowl radius R_b $[km]$	External depth H_0 $[km]$	Depth change H_b $[km]$	Bowl half-width W_b $[km]$	IC: dominant wavelength λ_0 $[km]$
1	300	4	0.5	50	45
2	300	4	0.5	50	90
3	300	4	0.1	50	90
4	300	4	0.5	100	90
5	150	4	0.5	50	90
6	300	4	0.5	50	180
7	300	2	0.5	50	180
8	300	2	0.2	50	180
9	200	2	0.5	50	180

4.2.3 Coherent monopole and dipole experiments

To investigate dynamics of isolated vortices in the bowl geometry, we also conducted several experiments with a different circulation initialization scheme (results reported in section 4.4). Instead of random and domain-filling disturbances, either a single coherent anticyclone (monopole) or an AC-cyclone pair (dipole) was initialized outside of the bowl. The topographic parameters used were $H_0 = 4$, $R_b = 300$, $W_b = 50$, and $H_b = 0.5\ km$. A domain length of 1500–2000 km was used, with little difference between the two, and with 1024^2 grid cells. All other parameters were identical to those described above. The prescription of a single vortex (centered at initial location $\underline{x}_0$) was by a Gaussian streamfunction with length scale r_0 $[m^{-1}]$:

$$\psi(\underline{x}) \sim \exp\left(\frac{-(\underline{x} - \underline{x}_0)^2}{2r_0^2}\right) \tag{4.4}$$

A dipole was created by superposing two eddies of the form (4.4) with opposing signs.

4.2.4 Eddy Detection

To track the central AC we use an algorithm based on an Okubo-Weiss parameter (OWP) threshold. The OWP is defined by $\text{OWP} = s^2 - \zeta^2$, where s is horizontal strain ($s^2 = (u_x - v_y)^2 + (u_y + v_x)^2$), and $\zeta = v_x - u_y$ is the vorticity within an isopycnal layer. Eddies are characterized by negative OWP values, i.e., vorticity dominating over strain. Within a single time sample and isopycnal layer, a grid cell (with index i) is identified as a vortex-core candidate if the OWP in that cell satisfies $\text{OWP}_i < -a\ \text{STD}_{\text{OWP}}$, where STD_{OWP} is the spatial standard deviation of OWP for the same time sample and isopycnal layer, and a is a constant factor. Drawing on previous studies [*Pasquero et al.*, 2001; *Isern-Fontanet et al.*, 2006; *Volkov et al.*, 2015], we set $a = 0.2$.

A connected region of model grid cells is identified as containing a vortex "core" if each cell was identified as a candidate, if ζ is singly-signed in the connected region, and if the total area A is larger than an imposed minimum πr_{min}^2. We choose $r_{\text{min}} = 10$ km, equivalent to 5 grid

cells for the lowest resolution experiments reported here. The detected eddy radius is defined as $r_e = \sqrt{A/\pi}$, where A is the detected (connected) area size. The detected eddy vorticity is defined as the spatially average vorticity within the detected area. In simulations that develop a bowl-trapped AC, we found that the AC could be tracked accurately by searching for the strongest AC within the bowl at any given time.

4.3 Emergence of barotropic bowl-trapped anticyclones

We begin by describing the results of a representative single 1-layer experiment in some detail, in subsection 4.3.1. In subsection 4.3.2 we consider the results of all standard 1-layer experiments (section 4.2.2 and table 4.1) and identify nondimensional parameters that approximately constrain the properties of the bowl-trapped AC. In subsection 4.3.3 we investigate the long-time fate and stability of the emergent bowl AC. In subsection 4.3.4, we present a vorticity budget for the evolution of the trapped AC and of the bowl slope current.

4.3.1 Emergent circulation over a bowl — case study

In this subsection we describe the results of a experiment B_1E_5 (table 4.1), as an illustrative example of bowl AC formation and properties in our experiments. The results of free evolution from the random initial conditions (section 4.2) are graphically summarized in figures 4.3,4.4, and a movie (supplementary file SA1.avi, described in supplementary section 4.8.4).

Two main circulation patterns emerge within the bowl. One is a cyclonic slope-current, i.e., propagating with shallower water to its right (cyclonic in the present case). It is associated with positive vorticity in the inner slope region and somewhat interior to it, and azimuthal velocity peak at mid-slope. The second emergent circulation pattern is a central (bowl-trapped) AC. The AC is

apparent by its negative vorticity around the bowl center (figure 4.3), and by its negative (retrograde) azimuthal velocity, peaking at a radius of about 60 km (figure 4.4a). Multiple (mainly cyclonic) eddies survive outside of the bowl (panel d), although in time they tend to merge into a smaller number (supplementary movie SA1.avi).

The emergence and intensification of the trapped AC is related to repeated merging of ACs (figure 4.3). Down-slope migration of ACs contributes to these mergers. In contrast, cyclones are cleared from the center of the bowl, leaving a diffuse cyclonic layer over most of the bowl interior, up to the center of the slope (figure 4.3d). A consequence of this redistribution of cyclonic and AC vorticity is that potential vorticity (PV) becomes segregated, with low PV material forming the center AC (figure 4.4b). Material transport and vortex cross-slope propagation are further investigated in subsection 4.4.

The emergence of a prograde slope current is to be expected based on topographic turbulence theories posed by previous studies (section 4.1), whereas the emergence of a central AC is not. This is underlined by the late-time streamfunction-PV relation (figure 4.4); this relation is multivalued, contrary to the predictions of topographic turbulence theories [*e.g. Bretherton and Haidvogel*, 1976]. This point and further comparison with topographic turbulence theories are discussed in section 4.6. However, the evolution time scales of the slope current and of the AC are similar (figure 4.4a), which motivates a discussion of the relation between vorticity fluxes contributing to the AC and to the slope current formation (section 4.3.4). The anticyclone is stable and long lived, in the sense that it is little-changed in form or amplitude from its formation, around day 150, until the end of the present experiment, at day 500. The same applies to the slope current. AC longevity is further investigated in subsection 4.3.3.

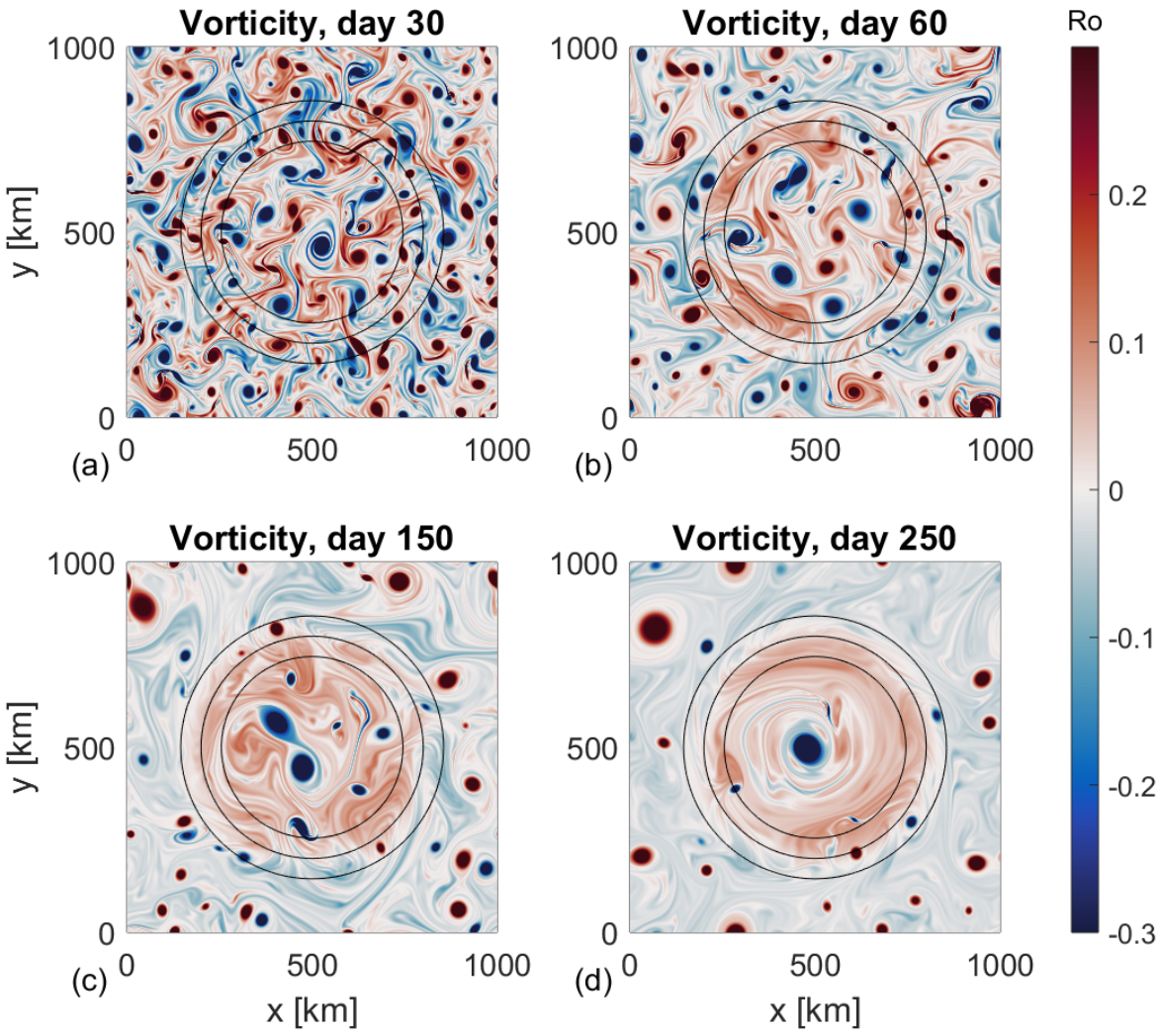

Figure 4.3: Evolution over time and formation of a bowl-trapped anticyclone in experiment B_1E_5 (table 4.1). The instantaneous vorticity distribution is shown at times indicated above each panel. Anticyclones aggregate within the bowl and repeatedly merge with each other, forming a long-lived AC confined to the central portion of the bowl. A cyclonic slope current also emerges, centered on the topographic slope, as seen by the broad regions of positive and negative vorticity inside and outside of the bowl, respectively. Note that the colormap is saturated to make the spatial features clearer. The 99th percentile vorticity magnitude is $0.78f$ and $0.42f$ in panels a and d, respectively.

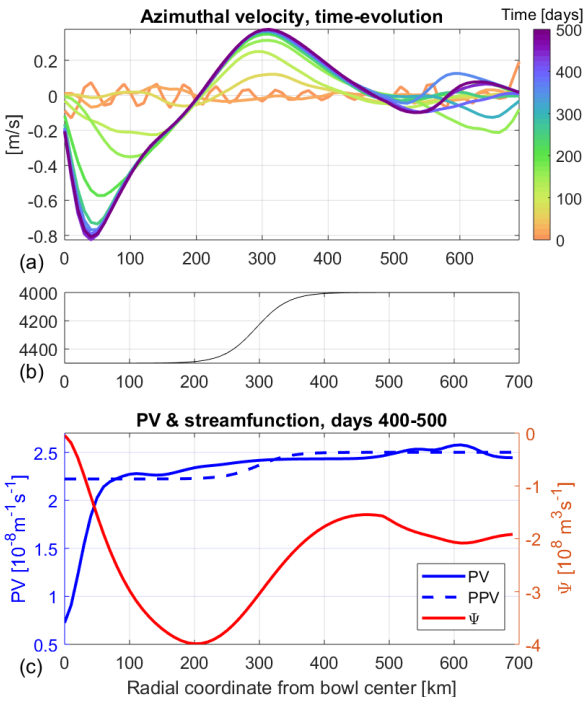

Figure 4.4: Evolution and late time properties of the bowl-trapped anticyclone and of the slope-current in experiment B_1E_5 (table 4.1, figure 4.3). Displayed variables are averaged azimuthally in radial bins from the center of the bowl. (a) Azimuthal velocity evolution, in 50-day time-averages centered around days 25:50:500. The initial conditions are also shown for comparison, and times are indicated by line colors. (b) Bathymetric profile $H(r)$. (c) Late-time (days 400–500) time- and azimuthal-mean potential vorticity PV $= (f + \zeta)/H$, "Planetary" Potential Vorticity PPV $= f/H$, and transport streamfunction Ψ.

4.3.2 Regime diagram

Non-linearity parameter. In this subsection we consider the conditions for bowl-trapped anticyclone formation across our entire array of experiments (table 4.1). We find that the formation or absence of a trapped AC is largely predicted by the value of a nonlinearity parameter. The parameter (ϵ) is defined by a vorticity magnitude V/L relative to fH_b/H_0, the value of topographically induced vorticity due to hypothetical crossing of the bowl slope:

$$\epsilon \equiv \frac{VH_0}{fH_bL}. \tag{4.5}$$

Here $V = \sqrt{2E}$ is the velocity scale, and L is an eddy length scale. The late-time radii of eddies (within and outside of the bowl) are of order 50 km in all cases, despite starting from different initial length scales. That is partially since topography limits the progression of the inverse cascade. Hence we set $L = 50$ km. The choice is preferable to using the final AC radius r_e since L (like V) is a "coarse-grained" parameter. However, we find that both choices result in similar ϵ values.

In figure 4.5a we plot the distance (D) of the AC from the center of the bowl (section 4.2.4), averaged over the last 100 days of each experiment. This shows that trapped ACs form within the bowl in all instances with small enough ϵ, i.e., $\epsilon \lesssim 0.5$, and in most cases with $\epsilon = 0.5 - 1$. However, advection is necessary to the formation, i.e., no mean anticyclonic flow emerges inside the bowl in the limit $\epsilon \to 0$, and neither does the slope current. In supplemental section 4.8.3 we verify this using a linear simulation. This is also consistent with the bowl vorticity budget (section 4.3.4).

Significant variation in D occur in the range $\epsilon = 0.5 - 1$, as discussed in (ii) below. At higher values of $\epsilon \gtrsim 1$ there is a transition to a regime with no bowl-trapped AC. In this regime, coherent eddies of both polarities freely move across the topography, their motions dominated by eddy-eddy interactions. Thus ϵ may be interpreted as determining the dominance of eddy-eddy vs eddy-topography effects. However, the cross-over does not occur sharply at a single ϵ

value across different experiment batches, as there is substantial scatter in the diagnostics due to inter-experiment variations in the random initialization. Note that the slope current, predicted by topographic turbulence theories (section 4.1), persists in all cases.

Finally, we quantify the bowl-trapped AC strength, i.e., integrated vorticity in its core, $\Gamma \approx \zeta_0 \pi r_e^2$, were r_e is the diagnosed AC radius (section 4.2.4). We pose a scaling for the core-averaged vorticity: $\zeta_0 \sim V_e/r_e$. Anticipating that V_e should scale with initial kinetic energy (E), we then pose $\Gamma = a\sqrt{E}\pi r_e$. We diagnose the value of the coefficient a in all experiments where a bowl trapped AC occurs. The result (mean ± standard deviation) is $a = -3 \pm 1$ across three orders of magnitude of E. Thus the AC is anomalously strong relative to scaling with domain-mean kinetic energy value, i.e., $|a|$ is ≥ 1. That is consistent with the accumulation of anomalously low PV within the AC through repeated mergers (section 4.3.1).

Background PV homogenization For $\epsilon \sim 0.5 - 1$, the trapped AC typically drifts azimuthally around the bowl center, at a radius which tends to increase with ϵ. These states can occur even with AC close to the slope peak ($r = R_b$). We find that these AC states near the topographic slope occur in cases where "background" PV is homogenized within the bowl. "Background" here refers to the area outside of (excluding) the trapped AC, as defined by a PV inhomogeneity parameter below. The topographic beta-drift tendency, including in the cross-slope direction [*Carnevale et al.*, 1991], is negated due to the homogenization of background PV. An example is shown in figure 4.6.

In the quasigeostrophic (QG) approximation, vortices within jets with homogenized PV propagate with the local-mean (eddy PV-weighted) velocity [*Marcus*, 1990]. We show in supplemental section 4.8.2 that in Shallow Water Equations (SWE) there is an additional along-topography drift, not present in the QG approximation. This additional drift is related to topographic stretching of relative vorticity, and does not vanish with homogenized background PV. In the experiment B_6E_7 shown in figure 4.6, the AC drifts with propagation speed ~0.82 m/s. Calculation of the vortex

propagation speed formula (4.22) in supplemental section 4.8.2 gives in this case a theoretical drift speed of 0.9–1 m/s, of which 0.24–0.34 are due to the additional SWE term (relative vorticity stretching), and the remainder is due to vortex advection by the mean velocity. The $10-20\%$ deviation is potentially due to vortex effects on the slope current which advects it, since the vortex is of significant magnitude and since rigid-lid barotropic vortices have long-range velocity tails [*McWilliams*, 2006].

The vortex in B_6E_7 is long-lived despite residing in a region of azimuthal-mean strain induced by the slope current. It was found by *Marcus* [1990] that a vortex can be stable within a large scale mean current $v(r)$ (flowing in the azimuthal direction, and varying in the radial direction) when its vorticity ζ has the same sign as the large-scale current strain, i.e., $S_r = r\partial_r(v/r)$, and if σ/ζ is of $O(1)$ or smaller. Indeed in the present case (Exp7) the mean radial strain is about (-0.04) $[f]$ in the radial position of the AC, while AC vorticity $\approx -0.5f$, fulfilling both the sign and magnitude requirements of *Marcus* [1990]. This implies that bowl-trapped ACs should be able to reside (while moving azimuthally) at any bowl radial position D within the homogenized area at which the mean strain sufficiently small. Indeed repeating experiments with identical parameters but different random initial phases (θ_k, section 4.2.2) generates trapped ACs that reside stably at different radii from the bowl center. Thus multiple "steady" states (or limit cycles, to be precise) are available. This explains the general tendency for larger D values at $\sim 0.5-1$ (compared with smaller ϵ), as well as the substantial scatter in D at fixed ϵ (figure 4.5a).

Therefore, we now quantify background PV homogenization across our suite of experiments by defining a background PV inhomogeneity parameter,

$$PVI = \frac{\text{PV IQR}}{\text{PPV IQR}}. \tag{4.6}$$

Here PV IQR is the PV inter-quartile range (IQR, the difference between 75th and 25th percentiles) within the bowl ($r < R_b$), excluding the trapped AC core, and PPV IQR is the IQR of the "planetary PV", PPV $= f/H$, in the same area. For partially or fully homogenized background PV cases, PVI < 1. Complete homogenization results in PVI $= 0$. We plot PVI against ϵ and against D, in figure 4.5 panels b and c, respectively. As expected, we find that PVI decreases as ϵ increases,

and in most cases approaches zero for $\epsilon \gtrsim 1$. Much of the scatter in D occurs when $PVI \leq 0.2$. As discussed above, PV homogenization results in a multiplicity of possible "steady states" (limit cycles) that produces the scatter in the ϵ–D and PVI–D relations, visible in figure 4.5.

4.3.3 Long-term evolution

Here we explore the long term evolution of bowl-trapped ACs in our experiments. This is motivated by the persistence of ocean ACs over depressions (section 4.1), and also in comparison with topographic turbulence theories (section 4.6). In all experiments in which a bowl AC formed (deduced by its persistence for $\gtrsim$ 100 days), it lasted for the rest of the experiment duration, with little qualitative or quantitative change. We also extended the duration of multiple experiments to several thousand days after AC formation, with similar results.

To further diagnose long term evolution of the bowl-trapped AC and its dynamical causes, we re-ran experiment B_1E_3 (hereby B_1E_3L) for 5000 days, with daily-mean outputs including online momentum equation diagnostics. The spatial resolution was ~2 km, twice as coarse as experiment B_1E_3. Although the trapped AC core circulation at, e.g., day 500 is 25% higher in the higher-resolution experiment, the end states are qualitatively similar and well resolved in each simulation. Thus the coarser simulation diagnostics are informative about the late time evolution of the trapped AC.

The evolution of the B_1E_3L AC between days 500 and 5000 is illustrated in figure 4.7. The AC central (peak) vorticity decays over time, by ~50%. However, the integrated core circulation, as diagnosed by eddy detection (section 4.2.4), does not decay by more than $\approx$ 5%. This percentage is the relative size of long-term circulation oscillations; smaller trends are impossible to distinguish due to these oscillations. The lack of appreciable circulation decay is not inconsistent with the peak vorticity decay, as the AC becomes wider with time (figure 4.7 panels a-b).

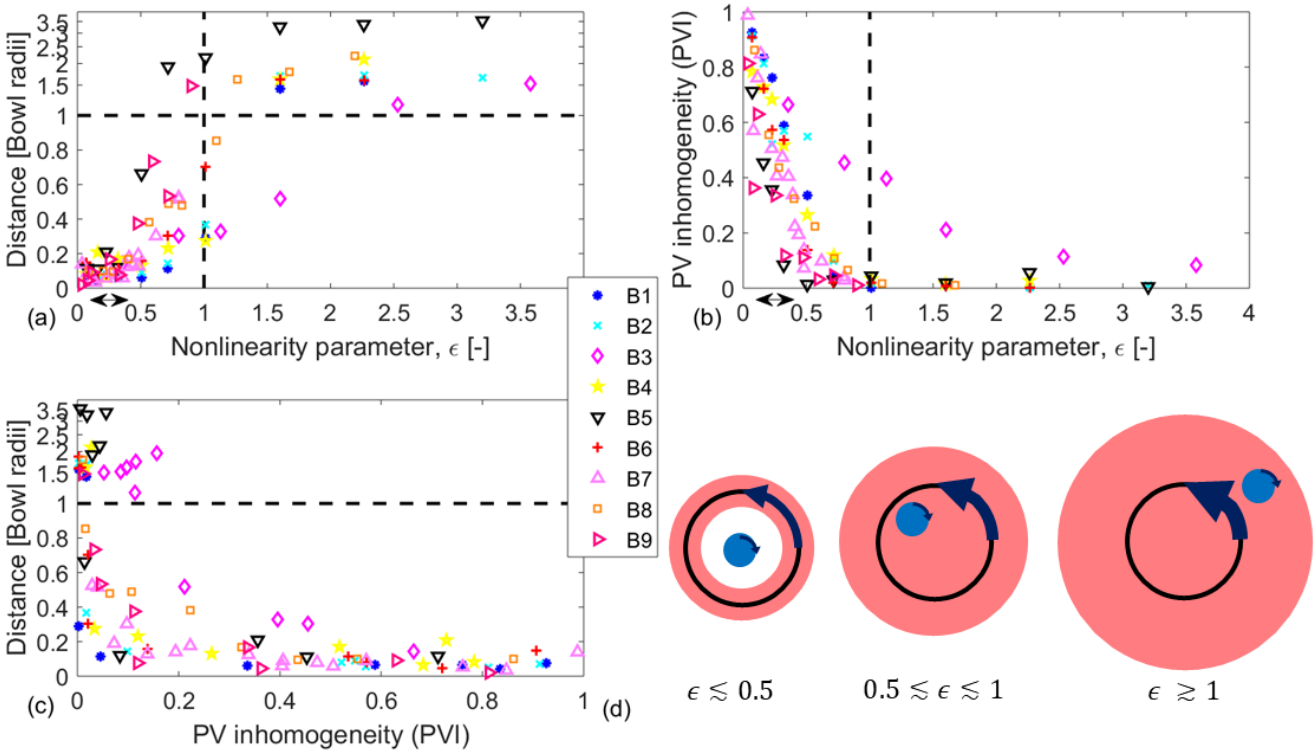

Figure 4.5: Regime diagrams for bowl-trapped anticyclone (AC) formation (section 4.3.2). (a) Mean normalized radial position (r/R_b) of the emergent anticyclone within the bowl for each free evolution experiment, versus the nonlinearity parameter $\epsilon \equiv VH/fH_bL$. The radial position r is normalized by bowl radius R_b. Bowl-trapped ACs correspond to $r/R_b < 1$. Values $r/R_b > 1$ are indicative of eddies (including ACs) moving freely across the bathymetry. (b) Position versus the PV inhomogeneity parameter (PVI, equation 4.6). (c) PVI vs ϵ. Each different colored marker represents a separate batch of experiments. Within each batch all parameters are kept identical except for the initialization energy E (section 4.2.2). The r/R_b-axis scale is linear (logarithmic) for values below (above) 1. The dashed lines at $\epsilon = 1$ and at $r/R_b = 1$ serve as visual aids. In panels (a–b), the double-arrow shows the range of ϵ values estimated to be relevant for the Mann, Lofoten, and Rockall Trough eddies. (d) A schematic illustration of the three regimes described in panels a–c. Note that the states shown are typical but not unique for each regime. For low ϵ, a trapped AC emerges close to bowl center. For intermediate ϵ values, a bowl-trapped AC typically emerges, but can occur at some finite bowl-radius, since the intensified slope current (illustrated in red) causes partial or complete PV homogenization within the bowl (outside of the AC). For high ϵ, the eddies are free to move across the slope and are not trapped within the bowl.

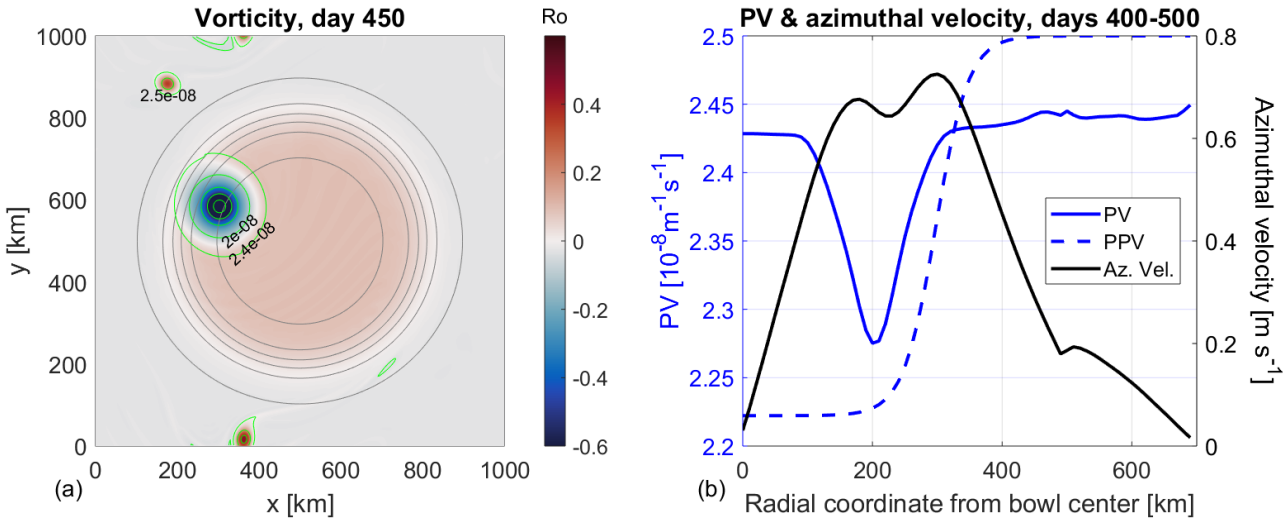

Figure 4.6: Potential vorticity (PV) homogenization in an experiment (B_6E_7, table 4.1) with intermediate nonlinearity parameter value $\epsilon = 1.01$. (a) Vorticity ($\zeta\ [f]$) distribution (in colors) at day 450. PV contours are shown in green, with contours plotted at $[0.5 : 0.5 : 2.5] \times 10^{-8} m^{-1} s^{-1}$. The $2.4 \times 10^{-8} m^{-1} s^{-1}$ contour is also marked; this contour separates the low-PV trapped AC from its higher-PV surroundings. Depth contours are shown in gray, at values of [4010,4100:100:4400,4490] m. (b) Radial profiles of potential vorticity (PV $= (f + \zeta)/H$), planetary PV (PPV $= f/H$), and azimuthal velocity averaged over days 300–500 (solid lines). PV is homogenized on the slope region, thus eliminating the vortex cross-slope beta-drift. The anticyclone is advected counter-clockwise (at constant bowl radius) by the cyclonic slope current. Vortex self-advection in the presence of bathymetry (supplemental section 4.8.2) also contributes to the cyclonic drift.

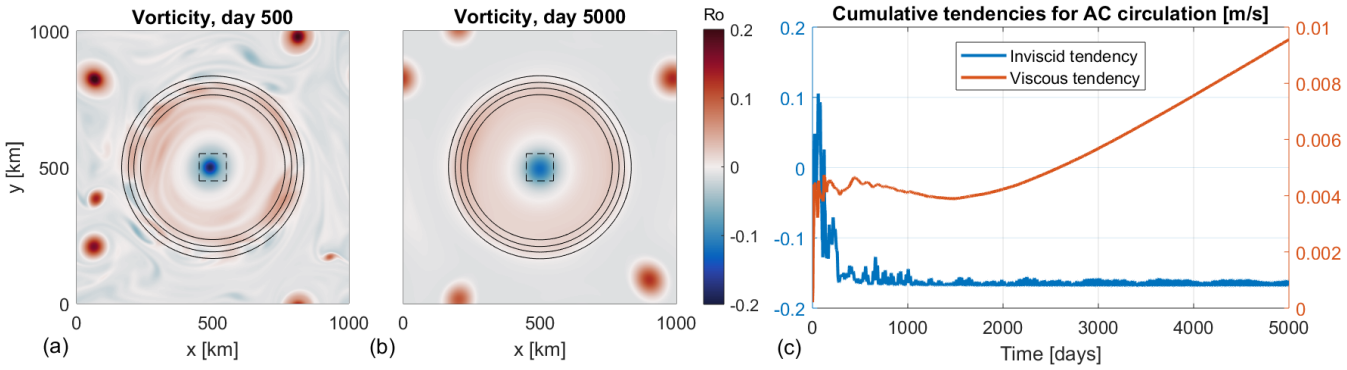

Figure 4.7: Long-time evolution of bowl-trapped anticyclone. Panels (a) and (b) show the instantaneous vorticity distribution at days 500 and 5000, respectively, for experiment B_1E_3L. Topographic contours (4100,4200,4300,4400 m depth) are shown in solid lines. The dashed square line in panels a–b shows the line along which circulation tendencies are calculated in panel c. Panel c: time-*cumulative* inviscid (blue) and viscous (red) circulation tendencies inside the bowl (just outside the anticyclone peak velocity radius, along the dashed lines of panels a–b). The cumulative tendencies are normalized by the perimeter of the dashed square such that they have dimensions of mean velocity, i.e., m/s.

We also diagnose the AC circulation evolution in an Eulerian frame. We calculate the circulation tendency at each time step due to each term in the momentum equation. We perform this analysis around the perimeter of a 50 km $\times$ 50 km square in the center of the bowl, which encloses the AC core. The perimeter is aligned with grid axes, to avoid introducing discretization errors. As expected, the AC is initially spun-up by the inviscid terms (figure 4.7c). Similar to the Lagrangian analysis of the eddy core discussed above, this Eulerian analysis shows no clear decay in AC circulation after its formation. Circulation oscillations are of order 2%. The viscous term cause a slight $\approx$ 2% decay in circulation between days 500 and 5000. We found that doubling the size of the perimeter used for this calculation did not qualitatively change the result. Therefore the AC does not decay directly by inviscid terms in a symmetric bowl, within at least a scale of thousands of days. The implications of these results are discussed in section 4.6.

4.3.4 Spin-up of the anticyclone and slope current: a vorticity budget

Here we show that the spin-up of the bowl anticyclone necessarily implies a tendency for cyclonic vorticity accumulation between the anticyclone and the topographic slope. We further suggest a scaling relation for determining the relative circulation magnitudes of the bowl anticyclone and of the slope current *a priori*.

We first derive an equation for the circulation tendency along an isobath by integrating the vorticity equation within the area bounded by that isobath:

$$\partial_t C(r,t) = \partial_t \int_0^{2\pi} \int_0^{r} \zeta \, \mathrm{d}A = -I(r,t) + \mathcal{F}\,, \tag{4.7a}$$

$$I(r,t) = \int_{\phi=0}^{2\pi} \zeta'(r,\phi) u'(r,\phi) r \mathrm{d}\phi. \tag{4.7b}$$

Here r denotes the distance from bowl center is denoted by r, u denotes the radial velocity, $\mathcal{F}$ denotes viscous terms, and primes denote deviations from an azimuthal average. In section 4.3.3 we showed that the primary contribution to circulation tendency is $I(r,t)$, i.e., cross-bathymetry eddy vorticity flux. Thus we hereafter neglect the viscous terms in (4.7a).

To address AC and slope current circulations, we define r_{AC} as the radial position of maximal magnitude in retrograde (anticyclonic) final-state azimuthal-mean velocity within the bowl. Likewise, we choose r_{SC} as the radial position of maximal magnitude in prograde (cyclonic) final-state azimuthal-mean velocity over the topographic slope. In our simulations the latter occurs around the position of maximal topographic slope, $r = R_b$. The equations for $C_{AC} \equiv C(r_{AC})$ and for

$C_{SC} \equiv C(r_{SC})$ then follow from (4.7a)-(4.7b):

$$\partial_t C_{AC} = -I(r_{AC}), \tag{4.8a}$$

$$\partial_t C_{SC} = -I(r_{SC}), \tag{4.8b}$$

$$\partial_t M_s \equiv \partial_t \int_0^{2\pi} \int_{r_{AC}}^{r_{SC}} \zeta \, dA = I(r_{AC}) - I(r_{SC}). \tag{4.8c}$$

Between the radii of maximal AC and slope current velocities ($r_{AC} < r < r_{SC}$) the late-time vorticity is positive (figures 4.3 and 4.7), principally due to the slope current. The trapped AC in our experiments typically has only a weak[7] "shield" of positive vorticity surrounding it [*McWilliams*, 2006]. The quantity M_s measures the slope current strength removing the AC integrated vorticity (by the Stokes theorem, equation 4.7a), and thus is a preferred slope current metric compared with C_{SC}. Therefore equation 4.8c shows that the slope current evolution ($\partial_t M_s$) has positive contributions from two flux integrals, i.e., at the slope region ($-I(r_{SC})$) and in the bowl interior ($I(r_{AC})$). Since C_{AC} decreases over time (as the anticyclone forms), we diagnose $I(r_{AC}) > 0$ for the $\epsilon \lesssim 1$ experiments of section 4.34.3.2. Likewise, since C_{SC} increases over time (as the cyclonic slope flow forms), we diagnose $I(r_{SC}) < 0$. We conclude that the spin-up of the retrograde bowl anticyclone is necessarily associated with an eddy vorticity flux of equivalent magnitude at r_{AC} driving the slope current. That is in addition to spin-up due to contributions of eddy-fluxes at the slope region (r_{SC}).

In figure 4.8a we compare the time evolution of the circulations C_{AC} and C_{SC} in experiment B_1E_5 (compare with figure 4.4a). These are equivalent to the two cumulative eddy-flux tendencies forcing the slope current strength metric M_s. First, in panel (a) it is seen that both eddy fluxes have similar evolutionary time scales. Second, the exterior (r_{SC}) fluxes are larger in magnitude (see below). These qualitative observations occur across all the experiments (table 4.1). The role of eddy fluxes as a function of position ($I(r)$, equation 4.7b) is examined in panel b. This panel shows cumulative change in circulation over days 150-250 ($\approx \int_{t_1}^{t_2} I(r,t)dt$), selected because $|C_{AC}|$

[7] In the reference experiment B_1E_5 for example, the AC shield has an integrated vorticity just 20% the magnitude of the integrated negative vorticity AC interior.

gains most of its amplitude during this time, as a function of r. It is seen that the locations r_{AC} and r_{SC} are indeed associated with approximately the largest cumulative eddy fluxes. Over this period the eddy vorticity fluxes at r_{AC} and at r_{SC} have similar sized contributions to the slope current metric M_s.

Figure 4.8a shows that the magnitude of the late-time bowl AC circulation is around 1/3 of that of the slope current. Therefore, by the above analysis inner bowl fluxes ($I(r_{AC})$) supply approximately 1/4 of the cyclonic vorticity that accumulates on the inner bowl slope (M_s). The remainder is contributed by slope-region fluxes ($I(r_{SC})$). We suggest that the larger contribution from external fluxes ($I(r_{SC})$) relative to internal fluxes ($I(r_{AC})$) is largely a geometrical effect, due to larger area outside of the bowl. If this is the case then the slope current circulation should equal the anticyclone circulation, scaled by the appropriate area from which external fluxes are sourced: $C_{SC,\text{theory}} \approx -C_{AC}D^2/\pi r_{SC}^2$ (figure 4.8, dashed line). Here $D = 1000$ km is the domain length. Indeed, in the figure C_{SC} and $C_{SC,\text{theory}}$ agree to within 3% at later times. In other experiments (table 4.1), the agreement is typically within ~20%.

4.4 Cross-slope motion and PV segregation

Our findings in §4.3 suggest that material transport is fundamental to the formation of the bowl central anticyclonic circulation. Indeed, the AC grows in our experiments through eddy mergers, and nonlinearity appears to be necessary (section 4.3.1 and supplemental section 4.8.3). Furthermore, PV (a materially conserved quantity) is anomalously low within the emergent AC (sections 4.3.1-4.3.2). Here we address the following questions: Are all ACs that participate in central AC formation initiated within the bowl at $t = 0$, or do some enter from outside of the bowl? If the latter, what are the mechanisms via which they transition from outside to inside the bowl?

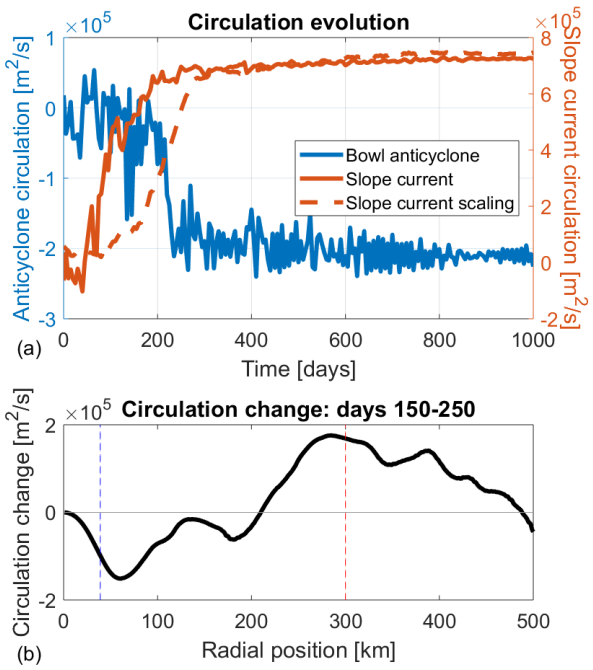

Figure 4.8: Evolution of the circulation in experiment B_1E_5. (a) Circulation time series at bowl radii corresponding to the bowl anticyclone ($C_{AC} = C(r_{AC})$, in blue) and to the slope jet ($C_{SC} = C(r_{SC})$, the red solid line). In this experiment we diagnosed $r_{AC} = 39$ km. The reader is referred to equations (4.7a)–(4.8b) for the definitions of C_{AC} and C_{SC}. The dashed red line is a theoretical prediction for the slope current circulation based on the anticyclone circulation alone ($C_{SC,\text{theory}}$, see text). Compare with figure 4.4a. (b) Cumulative circulation change, due to eddy vorticity fluxes (dissipation is negligible), during the period of AC formation (from t_1=150 to t_2=250 days) as a function of radial position , *i.e.*, $C(r,t_2) - C(r,t_1) \approx -\int_{t_1}^{t_2} I(r,t)dt$. See equations 4.7a–4.7b. In panel b, the radii of the AC and slope current time series of panel a are marked with blue and red vertical lines, respectively.

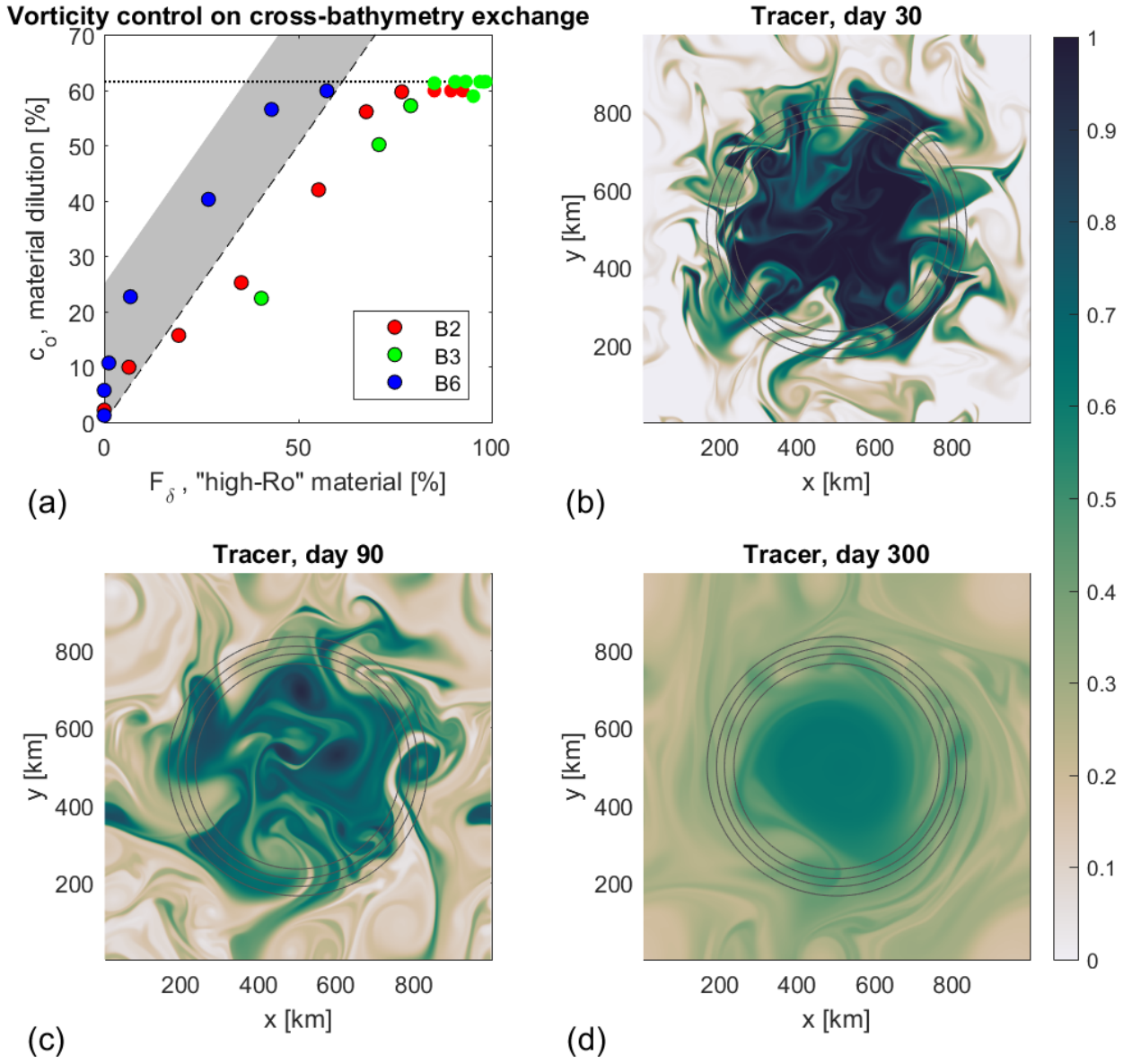

Figure 4.9: Contribution of anticyclones originating outside the bowl to the bowl-trapped anticyclone. (a) Anticyclone material fraction originating from outside of bowl (c_o), versus F_δ: the percent of initial material with $\delta = H\zeta/fh \geq 1$, i.e., anomalously high Rossby (Ro) number. The fraction c_o is estimated by the late-time tracer concentration c averaged between $r = 0$ and $r = R_b/2$, since initially $c = 1$ (0) inside (outside) of the slope region, with a transition region on the slope. Experiments in which a trapped anticyclone forms are shown by a black edge to the marker. The horizontal (dotted) line shows the maximal dilution possible in case of homogeneous final state. Different experiment batches (table 4.1) are denoted by different colors (legend). The diagonal (solid) line shows a hypothetical $c_o = \delta$ relation. The amount of bowl anticyclone material in the final state originating from outside the bowl is quite close to the fraction of material

Cross-bowl material transport First, we examine the amount of cross-bowl material transport which occurs in the process of AC evolution using passive tracer deployments. The tracer is initialized (section 4.2.2) with a radial tanh profile, with values close to 1 (0) inside (outside) of the bowl. Therefore a final average value $c = c_b < 1$ within the bowl center (diagnosed at $r \leq R_b/2$), implies that the fraction of material in the same area which originated outside the bowl is $c_o = (1 - c_b)$.

An anticyclone can maintain its coherence while crossing the slope into the bowl only if its vorticity (ζ) is high enough to avoid destruction by vortex stretching. The latter occurs if $\delta = H_0\zeta/fH_B \leq 1$. We test this in figure 4.9, which shows that the amount of bowl anticyclone material in the final state originating from outside the bowl is approximately proportional to F_δ, the fraction of material with $\delta \geq 1$ at $t = 0$. For small enough F_δ virtually no material is exchanged across the slope, and the AC forms only from material originally present within the bowl. At higher F_δ values, a substantial fraction of the late-time material in the AC originates outside the bowl.

The interpretation of the late-time tracer concentration is complicated by the initial $O(50km)$ wide tracer transition area on the bowl slope, where $0 \leq c \leq 1$. Due to this transition region, in a hypothetical end state in which no material is exchanged across $r = R_b + 2W_b$ (at the 98th depth percentile) and all material in $r < R_b + 2W_b$ is well mixed, the bowl tracer concentration would be $c \approx 0.75$. Hence we estimate the maximal possible bias from the tracer transition region via an added dilution of 25%, shown by the gray area in figure 4.9. Another complication is that in a finite domain only a finite maximal dilution can occur; this is also marked in figure 4.9.

In cases with small F_δ, the anticyclonic vortex growth still occurs by via repeated vortex mergers, but only emerges from AC eddies that are already in the bowl at $t = 0$. We observe (not shown) that anomalously high-PV material (*i.e.* cyclones) initially inside the bowl ultimately transit to the slope region, either as part of the cyclonic slope current, or as a coherent cyclonic eddy embedded within the slope current. Stability of cyclonic eddies within the inner part of the slope current

(where mean strain $\sigma > 0$) is generally consistent with the results of *Marcus* [1990].

In cases where F_δ is large enough, cross-slope motion may be induced by at least two processes in the present experiments: 1. Monopole vortex (topographic) beta drift [*Carnevale et al.*, 1991]; 2. Dipole propagation. Rather than attempting to determine the fraction of monopole and dipole (or multipole) interactions contributing to the AC formation in our turbulent experiments, we concentrate on a more tractable task. We present results from topographic bowl experiments initialized with a single monopole or dipole (section 4.2.3), and compare the cross-topography propagation speed of each. For brevity, in each case a single illustrative experiment is presented, along with formula for propagation speeds in the general case.

Monopole topographic beta-drift *McWilliams and Flierl* [1979] found that barotropic QG vortices on a beta plane (with constant β) drift merdionally (equivalently, cross-slope on a topographic β plane) with speed $\sim \beta r_0^2$, where r_0 is the vortex radius (or, more generally, the pressure e-folding scale). It is not clear to what extent these results should hold for a finite-width and curved bottom slope. In this case we define a cross-slope vortex (monopole) propagation speed ($v_{m,1}$) predicted from the local topographic beta value, $\beta(\mathbf{x}) = -(f/H)|\nabla H(\mathbf{x})|$:

$$v_{m,1}(\mathbf{x}, l) = \beta(\mathbf{x}) r_0^2. \tag{4.9}$$

However, vortex beta drift is driven by a secondary vorticity field which is set up by the vortex as it advects material a finite distance across f/H contours.Therefore, it may be that the relevant β value for vortex drift is to be evaluated in a region around the vortex rather than at its center. Thus we also test a second hypothetical speed,

$$v_{m,2}(\mathbf{x}, l) =< \beta(\mathbf{x}) > r_0^2, \tag{4.10}$$

where <> marks an average over the area defined by $r_0 \leq r_v \leq 2r_0$, with r_v = distance from vortex center.

Expressions $v_{m,1}$ and $v_{m,2}$ are compared with the diagnosed vortex down-slope propagation speed,

$v_{m,e}$ for a vortex of radius $r_0 = 45$ km initialized outside the bowl in figure 4.10a. Indeed, the approximate non-local generalization of the beta drift term, $v_{m,2}$, compares quite well with the diagnosed speed up until the vortex arrives at the middle of the slope. In comparison, $v_{m,1}$ is considerably lower outside the bowl.After the vortex reaches the middle of the slope region, both of the above formulae fail to reproduce it subsequent propagation speed. The vortex acquires a weak dipole component as it propagates across the slope [*McWilliams and Flierl*, 1979], which survives into the flat interior region. The companion is largely responsible for the deviation between the theoretical predictions and the diagnosed propagation speed, as are the presence of a slope current and topographic Rossby waves induced by the passage of the vortex.

Dipole propagation Dipoles propagate perpendicular to their eddy-separation axis. Topography causes an asymmetry in their dynamics such that propagation in the down-slope direction often results in the anticyclone shedding into the depression while the cyclone is repelled outside [*Carnevale et al.*, 1988].

The trajectory of the anticyclone from a representative dipole experiment (see section 4.2.3) is shown in figure 4.10b. Here the initial mean vorticity in each vortex is 0.25 f, and the dipole orientation was chosen such that the dipole propagates directly towards the bowl. The dipole propagates towards the bowl until the cyclone is shed upon arrival at the bowl slope [*Carnevale et al.*, 1988] between days 15-20, after which the anticyclone continues downslope and the cyclone is eventually ejected upslope. It is seen that away from the bowl rim, the dipole travels considerably faster than the monopole in panel a. For example at 1.5 bowl radii away ($r = 1.5R_b$) from its center (with present slope half-width parameter $W_b \approx R_b/6$) the dipole is an order of magnitude faster than the monopole. The dipole is initialized at a greater distance than the anticyclone to illustrate this difference further.

The dipole speed can be predicted based on a theoretical model of point vortices [*McWilliams*, 2006; *Kloosterziel et al.*, 1993]. The point model predicts a dipole speed $v_d = \frac{C}{2\pi d}$, where C is the

strength (peak circulation) of each vortex, and d the pair separation distance. The value of v_d is estimated based on diagnosis of these parameters from the dipole experiment. Its value generally agrees well in order of magnitude with the diagnosed anticyclone down-slope drift speed before the cyclone is shed. The dipole begins somewhat slower than v_d and overshoots its value slightly. This may be explained by that the initialized state is comprised of two superposed monopole vorticity fields, and hence some initial adjustment occurs. The adjustment process results in a smaller d, which explains the faster velocity at later times.

In summary, in this subsection it is shown that a bowl trapped anticyclone can form either locally from material initial present within the bowl, or also by sourcing material from outside the bowl. The percentage of externally sourced material depends largely on F_δ, the fraction of the initial anticyclonic vorticity outside the bowl that exceeds the topographically-imposed vorticity change. Anticyclones that enter the bowl can do so via either monopolar or dipolar propagation. It is shown that dipole cross-slope propagation can be considerably faster than monopole topographic beta drift former under certain conditions. For the monopole case, due to the non-uniform bottom slope, an approximate generalization the constant-slope formula is suggested, and reasonably matches the diagnosed speed.

4.5 Two-layer experiments

In this section we report the results of our 2-layer experiments — the minimal configuration that permits baroclinity. We examine whether a bowl AC forms in baroclinic conditions, and diagnose its vertical structure as a function of system parameters. The very long lived ACs observed in the ocean above depressions (section 4.1) are surface intensified (note their velocity maximum commonly occurs at depths of $\sim 500\ m$), but a non-negligible barotropic component is observed as well [*Mann*, 1967; *Willis and Fu*, 2008; *Köhl*, 2007; *Fer et al.*, 2018; *Bosse et al.*, 2019; *Le Corre et al.*, 2019a]. In our idealized barotropic experiments AC formation depends strongly on topographic

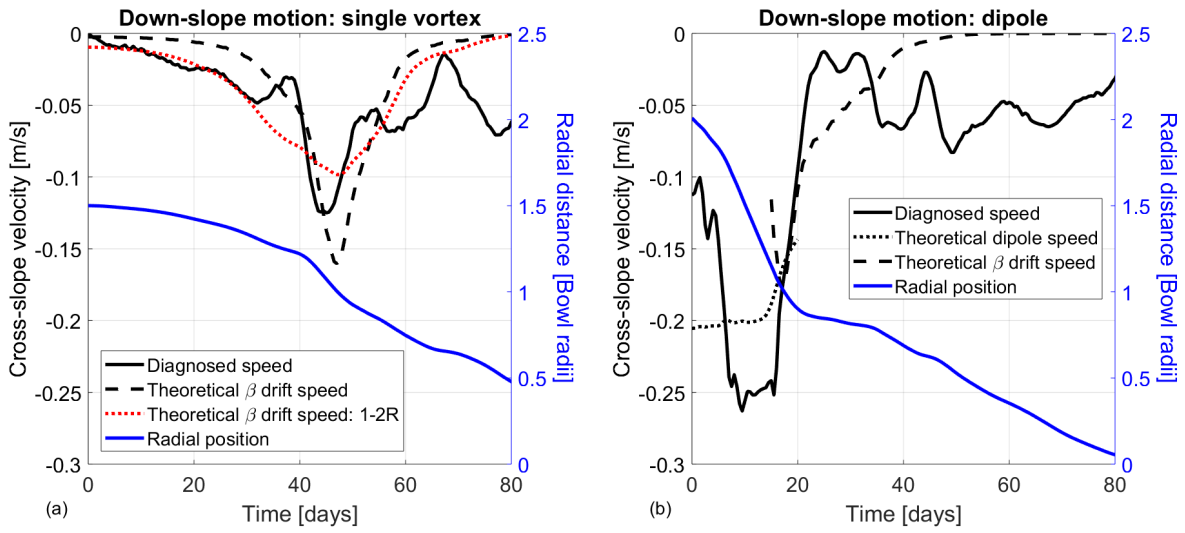

Figure 4.10: Coherent vortex propagation experiments. (a) A monopole vortex experiment. Diagnosed vortex down-slope velocity (solid black line) is compared with theoretical vortex down-slope beta-drift velocity (dashed line). The radial position from bowl center is shown in blue (right-side axis). (b) As panel (a), but for a dipole experiment. The theoretical dipole speed is shown by the dashed-dotted line. The initial conditions for the dipole are: mean vorticity within each dipole vortex of magnitude $0.25\ f$; vortex radii $d = 45$ km; vortex separation $= 2.6d$.

effects, and it is unclear whether this should favor a surface-intensified trapped AC structure.

Several batches of experiments were conducted. Stratification parameters were varied between batches, and the initial vertical structure was varied within each batch. For brevity we report mainly on a reference batch (hereafter B_{BC1}, BC standing for "baroclinic") of experiments with $\lambda_0 = 90$ km, upper layer rest thickness $H_1 = 1000$ m, and topographic parameters $R_b = 300$, $W_b = 50$, $H = 2$, and $H_b = 0.5$ km. The reduced gravity is set to $g' = 10^{-2}\ m/s^2$, resulting in a baroclinic Rossby deformation radius of $L_d = \sqrt{g'H_{eq}}/f = 22$ km [*McWilliams*, 2006]. Here the equivalent depth $H_{eq} = H_1H_2/H$ is used, with $H_2 = H - H_1$. These parameters are loosely motivated by the Mann Eddy basin (see also section 4.2.2). The Rossby deformation radius in the top (bottom) layer is $R_{d,1} = \sqrt{g'H_1}/f = 27$ ($R_{d,2} = \sqrt{g'H_2}/f = 38$) km.

The initial kinetic energy densities of the top and bottom layers (E_1 and E_2 $[m^2/s^2]$, respec-

tively) were varied between the B_{BC1} batch experiments, taking the following relative values: $(E_1, E_2)/E_0 = (0,1), (0.25,1), (0.5,1), (0.75,1), (1,1), (1,0.75), (1,0.5), (1,0.25), (1,0)$. These experiments were repeated with for two different kinetic energy densities in the dominant layer: $E_0 = 0.01$ or $E_0 = 0.1\ m^2/s^2$. In each experiment, the random initial phases θ_k were generated independently in each layer.

We find that a bowl-trapped AC forms in all B_{BC1} experiments. A specific example of the evolution is shown in figure 4.11, from the B_{BC1} experiment with $E_2 = 0$ and $E_1 = 0.1\ m^2/s^2$. By day 30 the circulation has largely barotropized as is generally expected for circulation features larger than the deformation radius [*Salmon*, 1998]. By day 250 a single coherent AC is formed near the bowl center. It is top intensified but has a substantial barotropic component. Topographic Rossby waves (TRW), straining of eddies on the slope, and the emergent slope current all appear to be bottom-intensified.

More generally, we find that the trapped AC tends to be top (bottom) intensified for top (bottom) intensified (random) initial conditions. Vertical structure results are presented in figure 4.12, in terms of a surface intensification metric: $S \equiv \log(v_1/v_2)$, where v_i is a velocity magnitude in layer i. Initial v_i is defined as the RMS velocity value in the layer. Final v_i is defined as azimuthal-mean azimuthal velocity at the radius of peak eddy velocity (for the AC), or at mid-slope (for the slope current). In contrast to the AC, the slope current is consistently bottom-intensified, with a similar value of final S value in all B_{BC1} experiments. Following these diagnosed trends, we suggest simple scaling rules for top intensification of the AC and slope current.

Scaling for the slope current vertical structure. We assume that the slope current is induced by TRW rectification [*Brink*, 1986; *Beckmann and Haidvogel*, 1997]. Hence, the slope current vertical structure may be expected to be similar to that of the waves. The upper layer QG PV equation for TRW is[8]

$$\partial_t \left(\nabla^2 \psi_1 - R_{d,1}^{-2} \psi_1 + R_{d,1}^{-2} \psi_2 \right) = 0. \tag{4.11}$$

[8]Here we linearize around the initial state of approximate zero mean flow along isobaths.

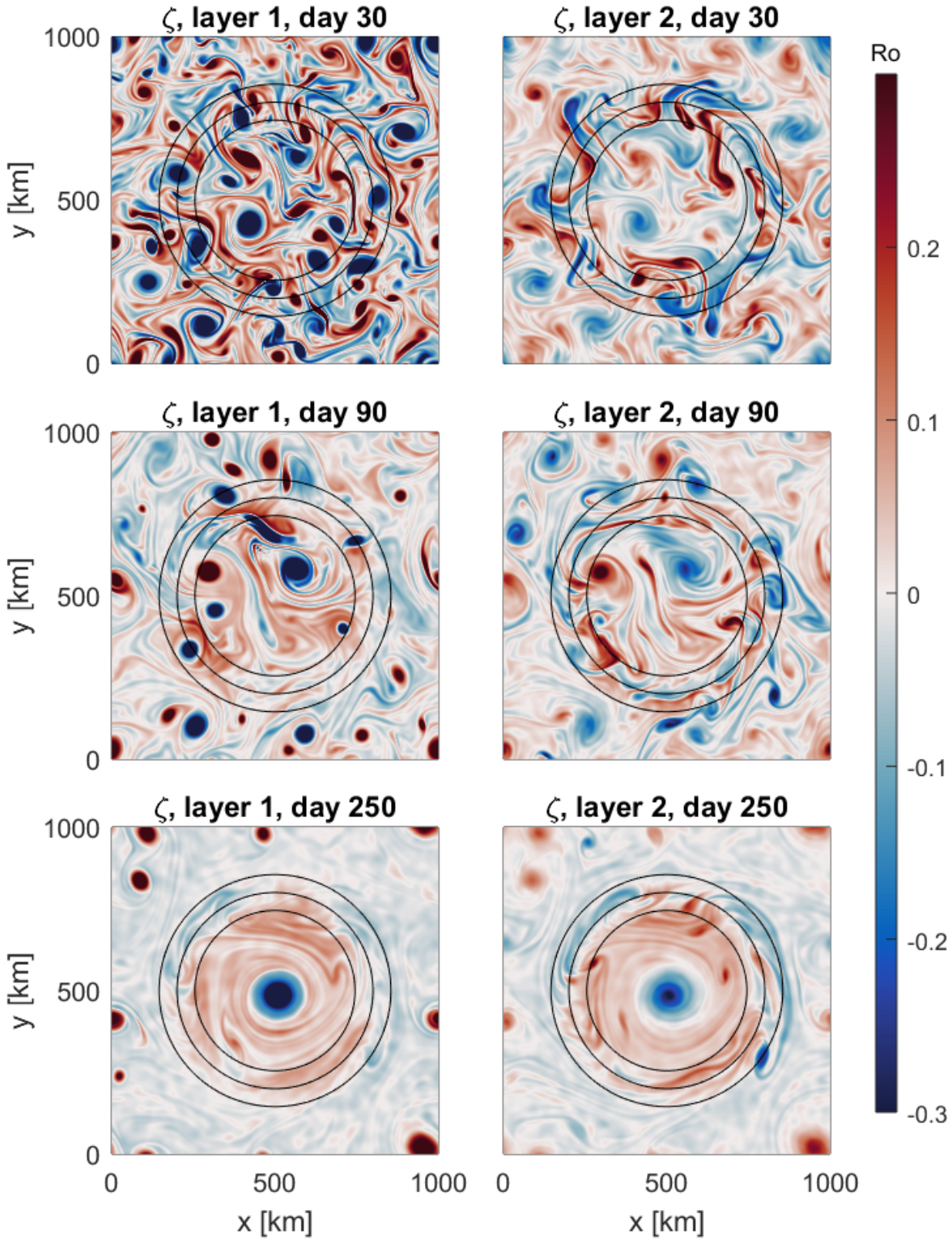

Figure 4.11: Vorticity (ζ) snapshots in a 2-layer experiment, with initial (at day 0) zero kinetic energy at lower layer. Layer number (1=top, 2=bottom) and number of days since initialization are indicated in each panel.

Here upper and lower layer quantities are denoted by $i = 1$ and $i = 2$ subscripts, respectively. For any wave mode (with nonzero frequency) the expression within the parentheses need be identically zero. Therefore,

$$\psi_2 = (1 - R_{d,1}^2 \nabla^2)\psi_1. \tag{4.12}$$

Over an isolated topographic feature TRW generally vary with scales similar to the topographic variation length scale, which we take as the bowl half-width W_b (section 4.2.2). Hence $\nabla^2 \sim -W_b^{-2}$, resulting in

$$\psi_1 \sim \frac{1}{1 + (R_{d,1}/W_b)^2}\psi_2. \tag{4.13}$$

The relation is similar to a Taylor Cap height over seamounts with continuous stratification [*Hogg*, 1973]. Statistical turbulence theories [*Salmon et al.*, 1976] predict functionally-similar, although not identical, relations.

Scaling for the anticyclone final vertical structure is suggested for the cases in which one layer is initially at rest ($S_i = 0$ or 1). Suppose conditions are initially surface intensified, i.e., $\psi_2(t = 0) = 0$ and $S_i = 1$. Then initially the lower layer evolution is likely approximately described by the linearized QG equation,

$$\partial_t \left(\nabla^2\psi_2 - R_{d,2}^{-2}\psi_2\right) = -\partial_t R_{d,2}^{-2}\psi_1 - J(\psi_2, h). \tag{4.14}$$

With random initial conditions we may assume $\psi_1(t = 0) \approx 0$ at the bowl center. We also assume that the topographic term will be initially negligible since $\psi_2(t = 0) = 0$ and since the topography is weak at bowl center. Therefore, in this case the AC amplitude in the lower layer follows from

$$\left(\nabla^2\psi_2 - R_{d,2}^{-2}\psi_2\right) = -R_{d,2}^{-2}\psi_1. \tag{4.15}$$

Assuming that horizontal structure is dictated by the energy-dominant layer, a scale estimate results by setting $\nabla^2 \sim -r_1^{-2}$, where r_i the AC core radius in layer i. The eddy core radii r_i are diagnosed in each case (section 4.2.4), and is typically 35–60 km in these simulations. Therefore

$$\psi_1 = \left[1 + (R_{d,2}/r_1)^2\right]\psi_2. \tag{4.16}$$

For a case with $S_i = 0$, the late-time scaling resulting from similar reasoning is

$$\psi_1 = \frac{1}{1 + (R_{d,1}/r_2)^2}\psi_2. \tag{4.17}$$

The top intensification scaling for the slope current and for the AC are examined against the B_{BC1} numerical experiments results in figure 4.12. The scaling laws predict the right sign of $\log(S_f)$, i.e., top or bottom intensification. The slope-current prediction (equation 4.13) is indeed very close to the numerical final state S_f, for all examined S_i values. The AC S scaling relations, (4.16) and (4.17)), are of the right ($\log(S)$) sign, and of the right (S) order of magnitude (within 7-40%) in all applicable cases (i.e., $S_i = 0, 1$).

The scalings (4.13)-(4.17) all share a dependency of the form R_i/L, where L is the relevant circulation feature length scale. Hence we conducted additional experiment batches varying the Rossby radii $R_{d,i}$ (e.g., by changing stratification). Cases with much higher Rossby radii of order $100-150$ km were attempted. The length scales r_i were < 90 km in all cases. We find that trapped anticyclones still form in cases with $S_i < 1$, and in some cases with $S_i = 1$ [9]. The trend predicted by the scaling relations is correct in these cases, i.e., top or bottom intensification is more acute relative to B_{BC1}, by as much as on order of magnitude. The scaling relations also predict the right S order of magnitude in each applicable case. The scatter in S is however relatively larger than in B_{BC1}, and we do not attempt a further systematic exploration.

4.6 Discussion - complex topography and topographic turbulence theories

All numerical experiments discussed above involved an isolated and functionally simple topographic feature. Real ocean topography is characterized by multiple scales and roughness. Hence, experiments with non-isolated topography were conducted as well. Complex topographic shapes were created using a similar random formula to (4.2) (e.g., figure 4.13). Cyclonic (anticyclonic) circulations emerge on the slopes of the topographic depressions (bumps), i.e., slope currents, consistent with previous results [e.g., *Bretherton and Haidvogel*, 1976]. However, embedded within the interiors of these large scale circulations, we find that coherent ACs (cyclones) with anoma-

[9] Time-scales to (partial) cross-layer coupling grow with R_i/l magnitude, and with S_i magnitude, which makes simulation more demanding and complicates analysis of the results.

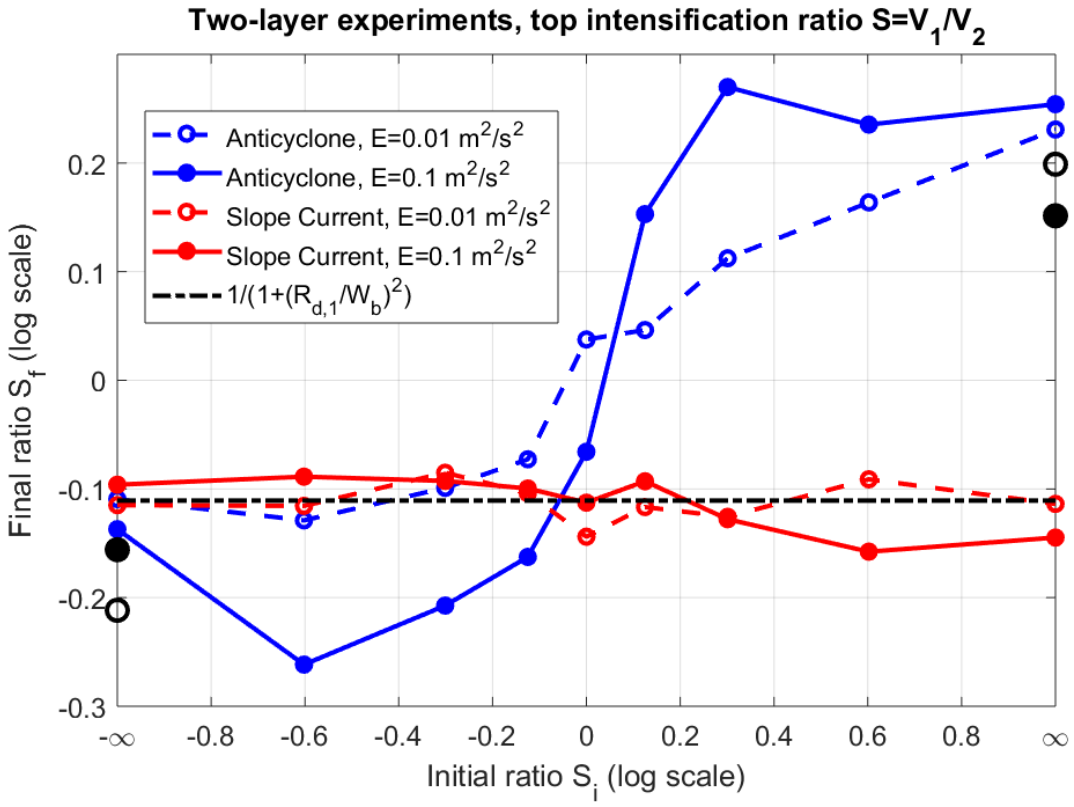

Figure 4.12: Vertical structure of the bowl-trapped anticyclone and of the slope current in two-layer experiments. A surface-intensification metric, $S = v_1/v_2$, is shown for the initial conditions (S_i, x-axis) vs. the final state (S_f, y axis). Here v_1 (v_2) is the velocity magnitude in the top (bottom) layer. Initial magnitudes are the prescribed RMS random velocities. Final velocities are defined as azimuthal-mean azimuthal velocity, either in the core of the slope current or at the radius of the anticyclone's maximum azimuthal velocity. The results are shown in log-scale. That is, e.g., $\log(S) = -\infty, 0, \infty$ for cases with $v_1 = 0$, $v_1 = v_2$, and $v_2 = 0$, respectively. The vertical structure of topographic Rossby waves (dashed-dotted line) closely predicts the slope current structure regardless of the initial conditions. Scaling estimates for the final anticyclone vertical structure in the limits $\log(S_i) = -\infty$ and $\log(S_i) = \infty$ (equations 4.16 and 4.17, respectively) are shown by isolated black circle symbols. Dashed lines and empty circles (solid lines and filled circles) denote cases with $E_0 = 0.01$ (0.1) m^2/s^2.

lously low (high) PV appear at the center of some or all topographic depressions (bumps) in each experiment. The trapped coherent eddies emerge as long as λ_0 is small enough (e.g., a factor of ≈ 5 was sufficient) relative to the analogous typical topographic wavelength (λ_t). This condition, as well as numerical resolution, may explain the lack of previous reports on these vortices in similar numerical simulations. Results from one of our random topography experiments are shown in figure 4.13.

We also conducted experiments with isolated topographic features lacking a significant central flat region of size larger than an eddy size, not shown here in the interest of space. We find that trapped (ACs) cyclones can emerge over the slope regions of such (inverted) seamount shapes, and propagate with the slope current at a constant radius. This occurs when partial homogenization of the PV field is achieved, i.e., the cause is similar to the $0.5 \lesssim \epsilon \lesssim 1$ regime of section 4.3.2, and may explain similar observations in the experiments of *Carnevale et al.* [1991].

As summarized in section 4.1, topographic turbulence theories broadly predict that (anti)cyclonic circulation should form over (bumps) depressions. These predictions have been verified in previous idealized numerical simulations [*Bretherton and Haidvogel*, 1976; *Salmon et al.*, 1976; *Merryfield*, 1998; *Majda and Wang*, 2006; *Venaille*, 2012] and in the present study. However, these theories do not predict a circulation of opposite polarity in the interior of closed topographic contours, *i.e.* they do not predict the formation of the bowl-trapped AC in our experiments.

A fundamental feature of these topographic turbulence theories is the prediction of a single-valued (i.e., monotonic) streamfunction (ψ) to PV (q) relation [*Bouchet and Venaille*, 2012]. To the contrary, we find the relation is multiple-valued in our simulations (e.g., figure 4.4b). It is clear that the multiple-valued $\psi - q$ relation is due to the cross-over from the bowl AC to the slope jet. Hence the theories cited above cannot predict these two features together. Earlier numerical random topography simulations [*Bretherton and Haidvogel*, 1976] did exhibit differing, quasi-linear, $\psi - q$ relations over different subdomains. However, we find a qualitatively different, multi-valued $\psi - q$ relation within a single isolated and smooth topographic feature. A deviation from single-

valued $\psi - q$ relations in idealized simulations was also previously reported by *Vallis and Maltrud* [1993], associated with alternating jets parallel to steep topography.

A possible explanation for the disagreement of our results with topographic turbulence theories is that the AC (unlike the slope current) is a transient feature, and hence should not be predicted by equilibrium theories. However as shown in section 4.3.3, the bowl AC does not decay by a measurable amount over a time scale of at least $\sim$ 10 years. In barotropic numerical simulations of a closed basin with a "continental slope" close to the basin edges and a flat bottom in the center, the spin up of a center anticyclone was previously reported [*Cummins and Holloway*, 1994; *Shchepetkin*, 1995]. In the case of *Cummins and Holloway* [1994], the center anticyclone decayed over a time scale equivalent to $\sim$ 100 years. *Cummins and Holloway* [1994] argued that the decay occurred inviscidly. We note, however, that the AC evolution and the slope-current evolution are not completely independent, as the results of section 4.3.4 show. Finally, it is possible that this local coupling is not captured in the discussed topographic turbulence theories since they impose conservation laws only in an integrated sense, or with a mean-field approximation [*Bouchet and Venaille*, 2012; *Venaille*, 2012].

4.7 Summary and conclusions

In several North-Atlantic basins, long-lived and semi-stationary mesoscale anticyclonic vortices (ACs) have been observed repeatedly. These basins are characterized by bowl-like topography, i.e., slopes surrounding a much less steep central area. The ACs reoccur over periods of years to decades, and have a significant signature on mean regional properties (e.g., SSH, figure 4.1). Previous work suggested different dynamical mechanisms for AC formation and persistence in each of these cases.

Motivated by these observations, we conduct idealized numerical experiments of flow evolution

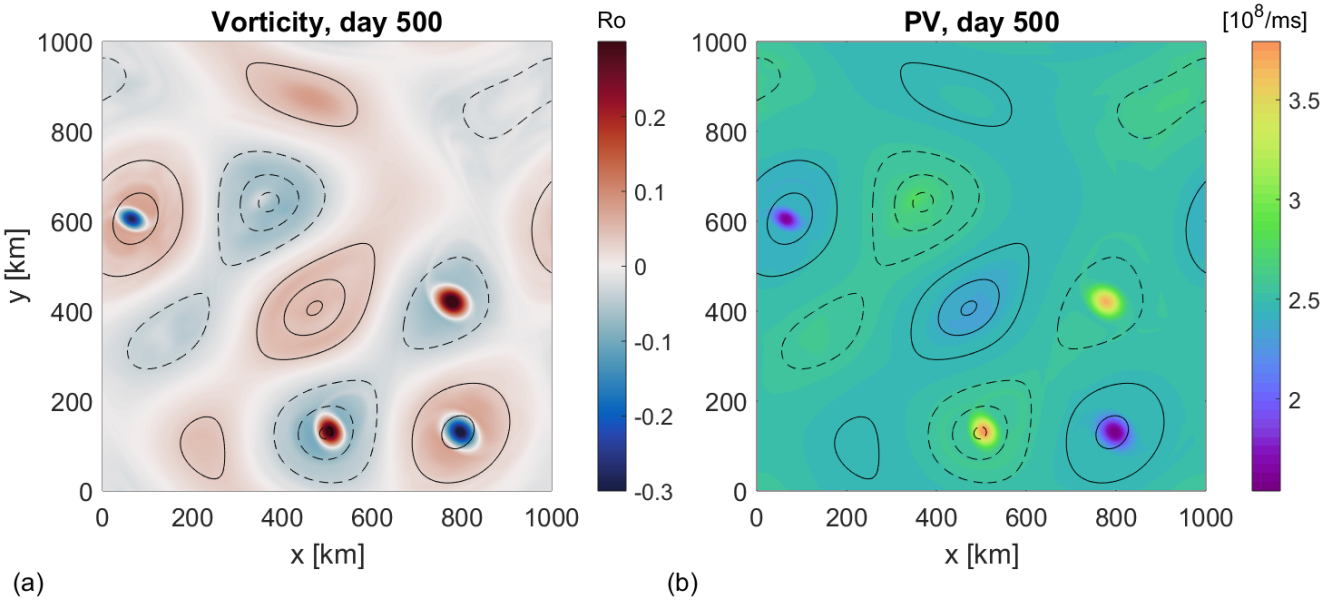

Figure 4.13: Coherent vortices emerging within topographic anomalies in an experiment with random topography. (a) Vorticity and (b) potential vorticity (PV) after 500 days of free evolution in a basin with complex topography. Dashed (solid) lines are elevated topographical areas (depressions) of height 200, 400, and 490 m above (below) a mean 4 km depth. Vorticity and PV are clearly influenced by the topography. Where relatively strong bottom slopes occur, the vorticity is positive at depressions and vice-versa. This is associated with development of slope currents, and is consistent with topographic turbulence theories (section 4.1). However, anticyclones (cyclones) tend to develop within centers of depressions (bumps), and are associated with anomalously negative (positive) PV. These central vortices are not predicted by topographic turbulence theories. Experiment parameters: $\lambda_0 = 45$, $\lambda_t = 400$ km, $E = 0.02\ m^2/s^2$, $\epsilon \approx 0.3$.

over bowl-like topography to determine if and how a trapped ACs evolve in a minimal complexity model. Primitive equation simulations with one or two isopycnal layers are conducted. Although many processes are neglected, the lighter computational burden facilitates multiple experiments, sweeping wide parameter ranges.

We find that a bowl-trapped AC does emerge spontaneously from random initial conditions under a wide range of circumstances. Typically this occurs through repeated mergers of ACs within the bowl interior, and the resulting trapped AC is characterized by anomalously low PV. Another general result, consistent with previous theory and simulations (the "Neptune" effect, section 4.1), is the emergence of a prograde slope current, corresponding to cyclonic circulation around a bowl.

To determine the robustness and parameter dependence of these phenomena, we conduct a large array of single-layer experiments. The initial kinetic energy and dominant initial circulation wavelength, as well as topographic shape parameters, are varied. A nonlinearity parameter (ϵ) is identified as largely determining the formation of a trapped AC in these experiments. This parameter is the ratio of vorticity scale to topographic vorticity stretching, and describes the relative effects of eddy-eddy interactions to topographic effects. The AC typically forms for $\epsilon \lesssim 1$, although it does not form for $\epsilon = 0$ (i.e., with advection terms neglected, as shown in supplemental section 4.8.3). In the first regime, $\epsilon \lesssim 0.5$, the AC is confined relatively close to the bowl center. In the second regime, $0.5 \lesssim \epsilon \lesssim 1$, trapped ACs typically still occur, but may revolve around bowl-center at different distances $r \leq R_b$, depending on initial conditions. In the third regime, $\epsilon \gtrsim 1$, eddy-eddy interactions dominate, and vortices freely cross topographic contours.

To explain the varying radial positions of the bowl-trapped ACs, we introduced a second nondimensional parameter, PVI, a metric of PV inhomogeneity (excluding the trapped AC PV signature). At small ϵ the radial PV gradient is dominated by the topography, and PVI ≈ 1. However, PVI generally decreases with increasing ϵ values, and in most cases satisfies PVI $\ll 1$ for $\epsilon \gtrsim 0.5$. The outcome is consistent with PV stirring and mixing by incoherent eddies, viewing the La-

grangian conservation of PV as approximately analogous to a passive tracer. A similar outcome was also predicted by *Rhines and Young* [1982b] within closed mean ocean gyre streamlines, at depths such that non-conservative process are negligible, under the assumption that eddy fluxes cause a mean down-gradient PV diffusion. The erosion of background PV gradient in the bowl eliminates the topographic beta drift, which otherwise tends to push ACs toward the center of the bowl. Hence, for $0.5 \lesssim \epsilon \lesssim 1$, the AC can occupy any radial position within the region of homogenized PV, and be passively advected cyclonically by the slope current. We show that a relatively smaller contribution to the cyclonic drift of the AC occurs through a nonlinear eddy-topography SWE effect, which is not eliminated despite the homogenization of background PV.

While it is clear that AC mergers contribute to the trapped AC formation, it is not *a priori* clear whether these ACs should originate from inside or outside of the bowl. We show that the origins of the ACs that contribute to the bowl-trapped AC is set by a parameter F_δ (section 4.4), which quantifies the fraction of the initial anticyclones that are outside of the bowl and are sufficiently strong to cross the topographic PV gradient. We show through tracer analysis that for weak vortices, *i.e.* small F_δ, there is negligible exchange of material across the topography. The relative exchange and amount of final "dilution" of the inner bowl material, grows approximately linearly with F_δ.

Motivated by the role of anticyclones migrating into the bowl in forming the trapped AC, we isolated and examined two different mechanisms of cross-bowl transport: eddy (topographic) beta drift [*Carnevale et al.*, 1991], and dipole interactions [*Carnevale et al.*, 1988; *Kloosterziel et al.*, 1993]. The former was previously suggested to be important in the case of the Lofoten AC [*Köhl*, 2007]. Using experiments with initial conditions of a single (monopole) AC, or of a close pair of opposite-signed eddies (dipole), we show that both mechanisms can allow anticyclones to enter the bowl. However, and dipole propagation is typically more efficient for reasonable parameter values, especially at larger distances from the bowl slope. We proposed an approximate generalization of previous theoretical monopole beta-drift to account for the variable topographic slope.

Two-layer experiments support the one-layer results on AC formation. We focus on the characterization of vertical structure of the emergent trapped AC, as well as of the slope current. We find that the emergent slope current is bottom intensified in all cases, to a degree determined by stratification conditions, similar to a Taylor Cap [*Hogg*, 1973]. In contrast, the emergent trapped-AC is bottom-intensified (surface-intensified) if domain-mean initial conditions are bottom-intensified (surface-intensified). The vertical structures of the observed ocean ACs (see section 4.1) are surface-intensified, with maximal velocities within the upper 1 km of the water column, and velocities decaying toward smaller but finite values near the sea floor. Thus an interpretation of our two-layer experimental findings is that the general tendency for ocean mesoscale eddies to be surface-intensified leads to surface-intensified trapped ACs such as the Mann and Lofoten eddies.

We find that, in the single layer experiments, the spin-up times of the bowl AC and the slope current are similar. Therefore, we examine the relation between vorticity and circulation evolution equations of both the AC and the slope current (section 4.3.4). This relation shows that the vorticity fluxes driving the formation of the bowl AC also contribute to the spin-up of the slope current. Furthermore, although the slope current is accelerated by a second source of vorticity fluxes as well (from outside the bowl), the final bowl AC strength is a good predictor of the slope current strength. These relations suggest that the vorticity fluxes inside and outside of the bowl are both mediated by similar mechanisms.

In section 4.6 we contrasted our results with topographic turbulence theories. These theories predict the emergence of a prograde slope current, but not a bowl-trapped AC. We find that depression-trapped ACs also occur in simulations with complex topographies, similar to experiments previously used to test topographic turbulence theories. We suggest an emergence criteria (for trapped ACs over depressions) in such simulations, based on the relative length scales of topography and circulation. The lack of bowl-trapped ACs in topographic turbulence theories is discussed. The aforementioned theories only predict strictly steady states. It is possible that the trapped AC is a transient state. However trapped ACs in our bowl simulations are stable over

time scales of at least dozens of years. Additionally, it is unclear if local vorticity fluxes, which couple the slope current and AC formation tendencies (section 4.6), are captured by mean-field approximations in such theories.

The numerical model used here is much too simple to directly apply to the discussed ocean observations of long-lived semi-steady ACs (section 4.1). One of the potentially important factors which are not included are more complicated stratification conditions [*Bashmachnikov et al.*, 2017]. The low stratification conditions, high f, and low planetary β values in the sub-polar areas make this limitation less severe than in other areas. Indeed, *Isachsen et al.* [2003] found that a barotropic model explains over 50% of seasonal gyre variability in the Nordic Seas (including the Lofoten basin). As mentioned above, each of the observed quasi-stationary vortices has a significant barotropic component (section 4.5).

Another limitation is that the neglect of external circulation patterns (e.g., boundary currents and eddy fluxes), and of atmospheric forcing. This limitation is very partially addressed here in the random topography experiments, as different topographic bowls (or bumps) and their emergent circulations, are not isolated from each other. The influence of regional circulation features and perpetual external variability or forcing need to be studied within intermediate complexity models or realistic regional numerical simulations.

Different formation mechanisms were previously suggested and diagnosed for observed semi-stationary ocean ACs (section 4.1). The present results suggest that whatever the source and exact location (cf. section 4.4) of low PV material in a topographic bowl region is, it is likely to lead to bowl-trapped AC formation. A rough estimate of the nonlinearity parameter value in the discussed oceanic basins (section 4.1) based on bathymetry and observed eddy strengths, gives $\epsilon < 1$, which in our idealized experiments predicts AC formation and topographic trapping. The vertical structure of the formed AC, also in rough agreement with observations, is a reflection of the domain (regionally) averaged vertical structure. As discussed above, in our model, trapped AC formation is related to prograde slope current formation tendency. The tendency for vorticity

Table 4.2: Initial kinetic energies for experiments in each batch defined in table 4.1.

Batch #	IC: average energy density [m^2/s^2]
1	0.001,0.005,0.01,0.02,0.05,0.1,0.2,0.5,1
2	0.001,0.005,0.01,0.02,0.05,0.1,0.2,0.5,1,2
3	0.001,0.005,0.01,0.02,0.05,0.1,0.2,0.5,1,2
4	0.001,0.005,0.01,0.02,0.05,0.1,0.2,0.5,1,5
5	0.001,0.005,0.01,0.02,0.05,0.1,0.2,0.5
6	0.001,0.005,0.01,0.02,0.05,0.1,0.2,0.5
7	0.001,0.005,0.01,0.02,0.05,0.1,0.2,0.5,1,5
8	0.001,0.005,0.01,0.02,0.05,0.1,0.2,0.5
9	0.001,0.005,0.01,0.05,0.1,0.2,0.3,0.4,0.6

segregation by eddy fluxes may in principle be tested within more realistic numerical models of the North Atlantic basins.

4.8 Supplement

4.8.1 List of initial kinetic energies in experiment batches

In this subsection the initial kinetic energies for all experiments described in section 4.2.2 are provided, within table 4.2. Other parameters of these experiments were provided in table 4.1 in the same section .

4.8.2 Vortex propagation in homogenized ambient PV over a slope in SWE

Here the motion of an isolated vortex over a slope is examined. Use Reynolds decomposition for any variable, $b = \overline{b} + b'$, the primed terms denoting vortex-induced deviations. PV is denoted by $q = \overline{q} + q'$. A special characteristic examined here is that $\overline{q}$ is constant, i.e., ambient or mean PV is homogenized (as occurs for $0.5 \lesssim \epsilon \lesssim 1$ in our experiments, section 4.3.2). Define the PV-weighted vortex center:

$$X = \frac{1}{Q}\int\int q' x dA, \tag{4.18a}$$

$$Y = \frac{1}{Q}\int\int q' y dA, \tag{4.18b}$$

$$Q = \int\int q' dA. \tag{4.18c}$$

Now,

$$\partial_t X = \frac{1}{Q}\int\int x\partial_t q' dA - \frac{X}{Q}\int\int \partial_t q' dA. \tag{4.19}$$

The first integral may be expanded as follows:

$$\begin{aligned}
&\int\int x\partial_t q' dA = -\int\int x\mathbf{u}\cdot\nabla q' dA \\
&= -\int\int \nabla\cdot(x\mathbf{u}q')\,dA + \int\int uq' dA + \int\int xq'\nabla\cdot\mathbf{u}\,dA \\
&= \int\int uq' dA - \int\int \frac{xq'}{H}\mathbf{u}\cdot\nabla H dA.
\end{aligned}$$

Here and below boundary terms are assumed to vanish. The velocity divergence term in the last integral was expanded as follows (using that $\nabla\cdot(\mathbf{u}H) = 0$ in SWE):

$$\nabla\cdot\mathbf{u} = \nabla\cdot\left(\frac{\mathbf{u}H}{H}\right) = \frac{1}{H}\nabla\cdot(\mathbf{u}H) - \frac{1}{H}\mathbf{u}\cdot\nabla H = -\frac{1}{H}\mathbf{u}\cdot\nabla H.$$

Similarly, the second integral in (4.19) may be expanded as follows:

$$\begin{aligned}\int\int \partial_t q' dA &= -\int\int \mathbf{u}\cdot\nabla q' dA \\ &= -\int\int \nabla\left(\mathbf{u}q'\right) dA + \int\int q'\nabla\cdot\mathbf{u}\, dA \\ &= -\int\int \frac{q'}{H}\mathbf{u}\cdot\nabla H dA.\end{aligned}$$

Using these expansions within (4.19), and defining $x' \equiv x - X$, we finally have

$$\partial_t X = \frac{1}{Q}\int\int u q' dA - \frac{1}{Q}\int\int \frac{x'q'}{H}\mathbf{u}\cdot\nabla H dA. \tag{4.20}$$

Similarly,

$$\partial_t Y = \frac{1}{Q}\int\int v q' dA - \frac{1}{Q}\int\int \frac{y'q'}{H}\mathbf{u}\cdot\nabla H dA. \tag{4.21}$$

The second term in each of the last two equations corresponds to vortex self-propagation, which does not occur in QG approximation (since $\nabla\cdot\mathbf{u} = 0$). It operates by differential self-advection and accompanying relative vorticity stretching over a bottom slope, rather than by planetary vorticity stretching as in topographic beta drift. The latter does not occur here despite of the bottom slope since mean PV is homogenized.

Finally, if the mean flow is along isobaths (say, along the x direction) and if the vortex has an axis of symmetry perpendicular to isobaths, i.e., (v') q' and u' are (anti)symmetric in x', then these symmetries vanish a few of the terms which appeared above, resulting in:

$$\partial_t X = \frac{1}{Q}\int\int \overline{u} q' dA - \frac{1}{Q}\int\int \frac{x'q'}{H} v'\partial_y H dA, \tag{4.22}$$

$$\partial_t Y = 0. \tag{4.23}$$

For an anticyclone the second integral results in a prograde contribution to vortex propagation, i.e., with shallower water to the right. That is, if $\partial_y H < 0$ then $\partial_t X < 0$, since $q' < 0$, $Q < 0$, and $x'v' < 0$.

4.8.3 Free linear evolution in a numerical model

To show explicitly that nonlinear effects are critical to the formation of the trapped anticyclone, we conduct a numerical experiment where the nonlinear (advection) terms are not included in the model equations. Since this option was not readily available in the model of *Stewart and Dellar* [2016], we conducted the linear experiment using the Back of Envelope Ocean Model [BEOM, *St-Laurent*, 2018], a primitive equation layered isopycnal model. Firstly, we ran BEOM in a fully nonlinear configuration identical to experiment B_7E_5, except that BEOM has a free surface rather than rigid upper lid. The BEOM experiment has very similar results to B_7E_5, including a trapped bowl AC and a cyclonic slope current. We conducted a second BEOM experiment identical to the previous, but without the advective terms in the momentum equation. Results are shown in figure 4.14. The circulation appears, as expected, composed of topographic Rossby waves. No tendency towards AC formation occurred over 1000 days. Indeed, linear dynamics cannot change azimuthal mean azimuthal velocity. That may be seen directly from equation 4.8a, as the right hand side vanishes under linear dynamics.

4.8.4 Supplementary animation description

An animation of vorticity evolution in the reference (single-layer) experiment B_1E_5 is presented in supplementary file SA1.avi. The reference experiment parameters are described in section 4.2.2. The results and evolution within this experiment are described in detail in section 4.3.1, as well as in subsequent subsections of section 4.3. Figures 4.3, 4.4, and 4.8 also show results of this experiment.

The animation shows daily-mean vorticity distribution, at 5-day intervals between days 0-1000 from initialization. Vorticity ζ is shown normalized by the (constant) Coriolis parameter f. Topographic contours are superimposed, at depths of 4010, 4100, 4200, 4300, 4400, and 4900 m. The minimal (maximal) depths in the domain are 4000 (4500) m, as described in section 4.2.2.

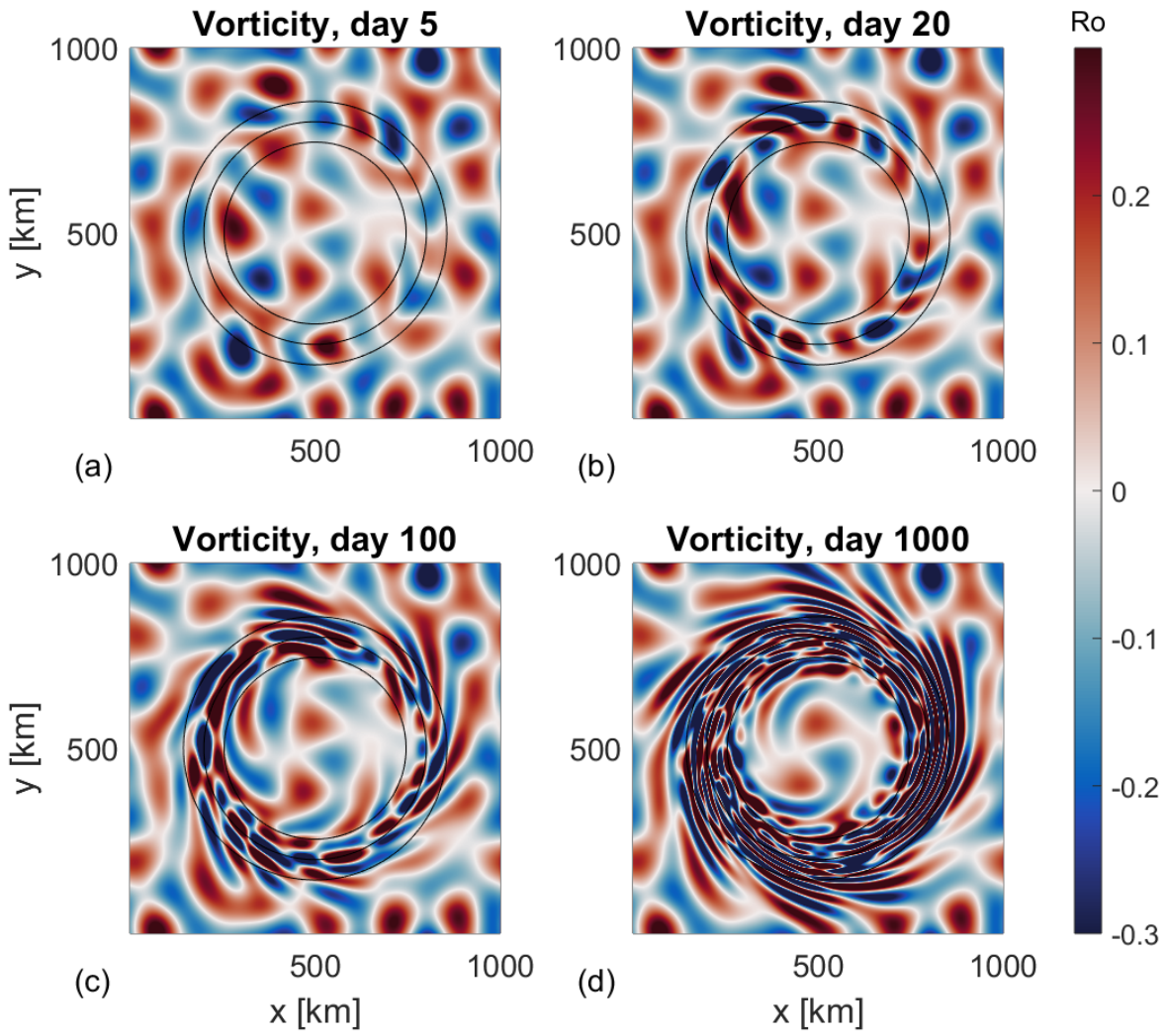

Figure 4.14: B1

Linear evolution experiment using BEOM [*St-Laurent*, 2018], with the same topographical parameters and initial conditions as in experiment B_7E_5. Instantaneous vorticity distribution is shown at times indicated above each panel. Neither a trapped anticyclone nor a slope current evolve. Motions due to linear topographic Rossby waves are apparent.

CHAPTER 5

Summary and Outlook

The following sections (5.1-5.3) provide high level summaries for chapters 2-4, respectively. Each of these chapters, as reproductions of published or submitted papers, contains a full length summary and conclusions section. Here a stand-alone, shorter, and less technical, summary of each chapter is provided. Additionally prospects for for future research based on these results are also discussed, and mostly do not overlap the outlook given in each chapter's summary section.

5.1 Baroclinic instability on curved isobaths

Observations and models of deep ocean boundary currents show that they exhibit complex variability, instabilities and eddy shedding, particularly over continental slopes that curve horizontally, for example around coastal peninsulas. The present investigation [chapter 3 here, *Solodoch et al.*, 2016] was motivated by such observations of the Deep Western Boundary Current (DWBC; studied in detail in chapter 3, and summarized in section 5.2 here). One ubiquitous cause of such variability is baroclinic instability (BCI), the release of ("available") potential energy stored by geostrophic vertically sheared currents. Here, the modulation of BCI by horizontal curvature of topography is investigated, in light of the observations of increased eddy shedding and variability from boundary currents near underwater capes. To generate as direct as possible comparison with classical instability of uniform rectilinear flow, an equivalent angular flow problem is iden-

tified and solved in several cases, concentrating especially on uniform azimuthal velocity and on solid-body rotation. The classical 2-layer quasi-geostrophic BCI problem [*Phillips*, 1951] over sloping bottom topography [*Mechoso*, 1980], is extended to the case of azimuthal flow in an annular channel. The linear instability problem, an eigenvalue problem, is addressed analytically and numerically.

We first analytically derive instability criteria and upper limits on growth rates for the present problem, generalizing classical results for the rectilinear problem [*Pedlosky*, 1964, 1987]. Growth rates for particular flow profiles are solved for either analytically or numerically. A criterion for time scale up to which BCI results in annular geometry is relevant to more general curved but open flow geometry is discussed.

It is found that solid-body rotation BCI is analytically analogous to the rectilinear uniform flow BCI instability. That is due to several reasons, which are identified, including that the strain rate and the vorticity gradient vanish in both cases. In case of uniform azimuthal flow, BCI can be quantitatively similar (in terms of, e.g., growth rates) to rectilinear uniform flow BCI. The similarity occurs in case of a vanishing depth-averaged (barotropic) mean flow. In the more general case of nonzero barotropic (uniform azimuthal) flow, BCI growth rate is suppressed. This suppression is identified as a generalization of the so called "barotropic governor effect" [*James*, 1987] whereby barotropic horizontal shear (strain in the present and more general, curvilinear, case) reduces BCI growth rate.

An exception to the relative reduction in growth rate occurs when the ratio of the bathymetric to isopycnal slopes (δ) is close to (positive) one, in which case the instability is enhanced. This value ($\delta \approx 1$) is in fact often observed in the ocean, as it is an empirical observation that often isopycnal slopes of boundary currents are parallel to the bathymetry [*Stommel and Arons*, 1972; *Stipa*, 2004b; *Spall*, 2010; *Xu et al.*, 2015; *Trodahl and Isachsen*, 2018]. This $\delta \approx 1$ regime is potentially relevant for the DWBC eddy-shedding observations that motivate this work

Additionally, it is found that with mean horizontal strain (as in, e.g., uniform azimuthal flow) a nonzero barotropic flow component results in increased growth rates of so called non-normal instability. That is transient but possibly explosive growth, which may bridge the gap to non-linear effects despite its finite growth time in linear theory. Given the sharp bathymetric changes in some areas at which DWBC leakiness has been identified, it is possible that the (finite-time) non-normal instability results are more relevant than modal instability (although the latter grows exponentially). Modal linear instability can provide predictions when the medium changes on length scales considerably longer than mesoscale (or at least a Rossby deformation radius), but not necessarily otherwise.

5.2 DWBC leakiness in a realistic regional numerical model

The Atlantic Meridional Overturning Circulation (AMOC) is an oceanic circulation pattern straddling the meridional extent of the Atlantic Ocean, communicating water mass transformations in sub-polar and polar regions across it, as well as with the other oceans. As such, it is of great climatic significance [*Lozier*, 2012]. Its important effects on climate include heat and greenhouse gas uptake from the atmosphere, heat transport and heat redistribution (section 1.2). The AMOC three dimensional circulation patterns and its variability are quite complex, and a subject of intense international observational efforts [e.g., *Bower et al.*, 2002a; *Lavender et al.*, 2005; *Bower et al.*, 2009; *Cunningham et al.*, 2007; *Bryden et al.*, 2009; *Meinen et al.*, 2013; *Lozier et al.*, 2017].

Decades of North Atlantic observations have shown that the the deep AMOC limb is comprised of both the Deep Western Boundary Current (DWBC) and of a second (more recently delineated) component: interior pathways. The latter are fed by the exchange and loss of material ("leakiness") from the DWBC in the Newfoundland Basin. Understanding the cause of leakiness and its phenomenology are necessary to better understand AMOC patterns, and to determine the relation of leakiness to other climate variability patterns. Therefore, we conducted the research

described in chapter 3 [*Solodoch et al.*, 2016], to investigate the cause of DWBC leakiness and its characteristics in detail.

The statistics and dynamics of the DWBC leakiness in the Newfoundland Basin are explored using an oceanic numerical circulation model in a high-resolution regional configuration designed for the present purpose. Additionally, two ocean float data sets and other observational data are used in the investigation. One of these data sets was originally a key indicator of DWBC leakiness [*Bower et al.*, 2009]. A direct comparison of model data with floats is made by advecting passive "particles" based on model velocities. The vast number of numerical particles ($\approx 550,000$) in comparison with available and relevant deployed ocean floats (~ 100) allows a detailed characterization of DWBC leakiness.

The float leakiness around Flemish Cap is found to be concentrated in several areas ("hotspots") that are collocated with bathymetric curvature and steepening. The leakiness of the model particles is consistent with presence and location of float leakiness hotspots. The large number of the latter allows systematic statistical analysis of the leakiness pattern. These reveal that Lagrangian mean velocity is offshore at these hotspots, while Lagrangian variability is minimal locally, which is an indication that leakiness by a non-eddying process is at work.

Model results are also analyzed from an Eulerian perspective. Time-mean Eulerian DWBC streamlines separate to the interior at the same leakiness hotspots identified in the Lagrangian analysis. Furthermore, eddy-rectified flow is negligible relative to the Eulerian mean flow, except at the southern face of Flemish Cap, where a smaller percentage of particle loss (leakiness) occurs. The Eulerian and Lagrangian results taken together show that leakiness occurs mainly due to Eulerian-mean cross-isobath flow at the identified hot spot locations.

Eddies[1] do play significant, if subtle, roles in the leakiness process. It is inferred, by comparison with particle advection experiments using the time-mean circulation, that eddies are conducive

[1] In this paragraph the term "eddy" relates to time-variability, not necessarily in the form of a coherent vortex.

to ≈ 50% of the Lagrangian leakiness. Eddy stirring allows DWBC parcels to cross the mean potential vorticity (PV) gradient to the offshore side of the DWBC and continental slope, where the time-mean offshore flow at leakiness hotspots finally transports these particles out of the current. This coupled eddy-mean flow process is identified as a manifestation of chaotic advection [*Shepherd et al.*, 2000; *Waugh et al.*, 2006].

The dynamics of mean leakiness of the DWBC is further investigated by model energy and PV budgets. The results confirm that eddy to mean flow energy conversion is not efficient near the leakiness hotspots, and that even downstream of mean streamlines separation (from the DWBC), eddy stirring imposes a modest change to mean PV. It is suggested that the evidence on mean flow leakiness and separation is consistent with a mechanism of inertial separation of the DWBC due to bathymetric changes, namely abrupt isobaths steepnening and turning near the deduced leakiness hotspots. Finally, a scaling relation for the ability of a boundary current to follow bathymetric changes is suggested, which is consistent with DWBC separation by inertial separation at the leakiness hotspots. The results are contrasted with previous suggested mechanisms for DWBC leakiness.

Possible implications of the investigation are discussed in regards to both modeling requirements, phenomenon robustness to varying climatic conditions, and relation to other circulation features (section 3.5). Additional prospects for future research are discussed here.

- The leakiness is characterized in this work by two components, compensated and uncompensated. The former (latter) results in null (nonzero) exchange of mass across the current. Here we quantify the cumulative value of the latter component, which compares well with observational estimates [*Mertens et al.*, 2014], and provides more detail (within the model). A similar quantification of compensated leakiness would be a useful calculation as well, in providing the amount of downstream dilution of DWBC water masses.
- It is indirectly inferred that mean-eddy coupling causes ≈ 50% of model leakiness. A more direct demonstration and quantification is perhaps possible. For example, in (preliminary)

particle advection experiments using only eddy velocity, considerably less leakiness occurs relative to full velocity experiments. The difference is also considerably larger that the leakiness due to mean flow advection alone. I presently understand this mean-eddy coupling as a kinematic process, and expect that studying its details, as well as disentangling it from the demonstrated dynamical processes of separation, would be informative from theoretical as well as observational perspectives.

- The process of leakiness by formation of anticyclonic submesoscale coherent vortices [*McWilliams*, 1985; *Bower et al.*, 1997] has previously been suggested to be relevant for the DWBC [*Bower et al.*, 2013] leakiness around the Grand Banks area, based on several observations with floats. Recently, SCVs with similar thermohaline properties where detected in the same area from Argo floats profiles by *McCoy et al.* [2020]. Leakiness by SCV shedding was not investigated in the published manuscript *Solodoch et al.* [2020a], which focused on the upstream Flemish Cap area. However, in a preliminary analysis bottom boundary layer vorticity (ζ) smaller than $(-f)$[2] are diagnosed in the model (GB_B, presented here) around the southern face of Flemish Cap and around the eastern and southern areas of the Grand Banks. That ($\zeta < -f$) is generally a necessary condition for inertial instability, previously found to result in SCV formation post separation in the California Undercurrent [*Molemaker et al.*, 2015]. Furthermore, SCVs have been diagnosed using an eddy tracking code [*Le Vu et al.*, 2018] with our GB_B configuration in similar location to the *Bower et al.* [2013] observations. That was done on model year 17 (not reported upon in *Solodoch et al.* [2020a]), which was run with 1/4 daily output in order to better resolve SCV motions. A quantitative measure of SCV role in the model leakiness, may be deduced by further analysis of these calculations.

[2] f denotes the Coriolis parameter

5.3 Formation of Anticyclones above topographic depressions

Long-lived anticyclonic eddies (ACs) have been repeatedly observed over several North-Atlantic basins characterized by bowl-like topographic depressions. Significant thermohaline fluxes and thermohaline transformations occur in these basins, processes of climatic significance as part of the Atlantic Meridional Overturning Circulation (AMOC). The possible relations of these trapped ACs with AMOC processes are discussed in section 4.1.

Motivated by these previous findings, we conduct numerical experiments of circulation over topographic bowls in simplified settings. We find, in experiments with 1 or 2 isopycnal layers, that a bowl-trapped AC is an emergent circulation pattern under a wide range of parameters. The trapped AC, often formed by repeated mergers of ACs over the bowl interior, is characterized by anomalously low PV.

It is demonstrated that the trapped-AC material may be sourced from both inside and outside of the bowl. The (former) latter occurs for (low) high scales of initial vorticity relative to topographic vorticity stretching. Two PV segregation mechanisms that can contribute to the AC formation in the latter case are examined, namely monopole vortex propagation by topographic beta-drift [*McWilliams and Flierl*, 1979; *Carnevale et al.*, 1991], and dipole self-propagation [*Carnevale et al.*, 1988]. We compare the down-slope propagation velocities of each mechanism in the present scenario. While previous studies of the Lofoten Basin Eddy have given consideration to topographic (and planetary) beta-drift [*Köhl*, 2007], we show that dipole propagation can be considerably faster with reasonable parameter choices.

A nonlinearity parameter (ϵ) is suggested to largely control the trapped AC formation or lack thereof. The former occurs under a low $\epsilon \lesssim 1$, although advection is necessary for formation. Under moderate values ($0.5 \lesssim \epsilon \lesssim 1$), partial PV homogenization allows the AC to travel finite distances within the bowl, rather than remain close to its center. Under higher $\epsilon \gtrsim 1$, eddies

freely cross the topography. A regime diagram is thus suggested to account for results from a large set of 1-layer experiments in terms of either ϵ or of a PV (in-)homogenization parameter.

Observed topography-trapped ACs in the ocean are top-intensified. That is in contrast to other topographically-induced circulation patterns, such as Taylor Caps above seamounts [e.g., *Hogg*, 1973; *Owens and Hogg*, 1980], and previously reported emergent circulation patterns in topographic turbulence theory and experiments [e.g., *Salmon et al.*, 1976; *Merryfield*, 1998; *Venaille*, 2012]. These latter circulation patterns are generally prograde (cyclonic over a topographic depression) and bottom-intensified. The latter characteristic occurs since density stratification provides partial "shielding" of top layers from topography-induced vortex-stretching. Model two-layer experiments reported here reproduce the bottom-intensification of an emergent prograde slope current. The emergent trapped AC vertical structure is found to depend on initial conditions, i.e., domain-mean vertical energy partition. The trapped AC is top (bottom) intensified for top (bottom) intensified domain-mean initial conditions. Mean top-intensified energy is the general rule in large scale ocean circulation, hence the results appear consistent with trapped AC observations. Simple physically-based scaling laws are suggested for slope current as well as trapped-AC top-intensification measures.

Finally, the results are compared with topographic turbulence theories [*Salmon et al.*, 1976; *Bretherton and Haidvogel*, 1976; *Majda and Wang*, 2006; *Venaille*, 2012], which predict the emergence of the prograde slope current, but do not predict a trapped AC. A vorticity budget suggests these features are nonetheless dynamically related. Possible reasons for the difference and implications are discussed.

One of the main limitations of the investigation is that the experiments are unforced, i.e., free evolution within a closed system is studied. In the ocean on the other hand, boundary currents, propagating waves and eddies entering the region, and air-ocean interaction, can all affect the regional circulation and trapped AC. For that reason, a suite of forced-dissipative experiments (not reported in [*Solodoch et al.*, 2020b]) were conducted as well. Random forcing was prescribed,

with length and time scales roughly relevant for mesoscale disturbances. Dissipation (additional to hyper-viscosity) was provided by linear bottom friction. The main qualitative result was that in many cases a coherent and trapped AC formed, as it did in the free evolution experiments. In those cases, the trapped AC occasionally did collapse due to the random forcing, but reformed again repeatedly, such that on average the inner bowl circulation was anticyclonic. The forced-dissipative experiments were not studied exhaustively, but results suggested that a trapped AC formed in cases that the random forcing auto-correlation time scale was longer than an advective time scale. The interpretation of this preliminary result is that if advective time scale [3] is short enough relative to the time over which the forcing pattern changes, than vortices can cross the topography and merge within the bowl in sufficient numbers to maintain a trapped AC. While the forced-dissipative experiments are quite idealized as well, they provide a demonstration that a trapped AC forms in the present setting, in non-equilibrium conditions as well.

The results of the idealized investigation suggest that common underlining mechanisms may be responsible for the various observed trapped oceanic ACs, although the mechanisms may manifest differently in each case. For example, it is found that the AC may be formed from either locally or remotely-sourced vortices (depending on the nonlinearity parameter, section 4.4). An investigation of the dynamics of the Mann Eddy based on observations and on a realistic regional numerical model (the same model developed in [*Solodoch et al.*, 2020a]) is underway as well. The Mann Eddy is the least studied of the discussed oceanic long-lived ACs, despite its potential effects on the AMOC. *Mann* [1967] suggested (based on tracer properties) that mid-depth convection happens within the eddy, changing the water mass propagating within the North Atlantic Current (NAC) as part of the AMOC[4]. The proximity to a (locally) retrograde current (the NAC), also distinguishes the Mann Eddy from the other observed ACs. Therefore, examination of the presently identified mechanisms for the Mann Eddy would be informative regarding the wider applicability of the idealized simulations as well.

[3] Generally inversely proportional to forcing amplitude, but dependent on other parametres, including the forcing time scale

[4] Additional climatic influences of the Mann Eddy were mentioned in chapter 4.

5.4 Outlook

As discussed in chapter 1, topographic effects on mesoscale circulation is a common theme of chapters 2-4. Without much repetition of the above summaries, it is noteworthy that within each chapter it is found that topographic control can manifest in opposite circulation tendencies. In chapter 2 it is found that for boundary currents above a sloping topography, downstream variation in isobath direction (curvature) can be either stabilizing or destabilizing in regards to baroclinic instability, depending on the details of the topography and mean flow. In chapter 3 it is deduced that downstream topographic variations do contribute to Deep Western Boundary Current leakiness and variability, through inertial separation. However, it is the presence of the bottom slope itself that guides the path of the DWBC. Furthermore, persistent recirculation gyres occur offshore of the topographic variation locations, and their existence is likely related to the leakiness and topographic separation of the DWBC. Thus a second time-mean circulation pattern is possibly supported by the topographic variation causing leakiness from the first. Finally, in chapter 4 we show that opposing circulation patterns emerge in the relatively flat interior of topographic bowls (a trapped anticyclone), and on their slope region away from the center (a cyclonic slope current). Furthermore, it is shown that the vorticity fluxes responsible for forming these two circulation patterns are in fact related to each other. It is apparent that topographic effects, even limited to purely mesoscale variety, are immensely varied and rich, and that even a single such mechanism can lead to contrasting and even opposite circulation patterns depending on local conditions.

References

Agra, C., and D. Nof (1993), Collision and separation of boundary currents, *Deep Sea Research Part I: Oceanographic Research Papers*, *40*(11-12), 2259–2282.

Arakawa, A., and V. R. Lamb (1981), A potential enstrophy and energy conserving scheme for the shallow water equations, *Monthly Weather Review*, *109*(1), 18–36.

Aref, H. (1984), Stirring by chaotic advection, *J. Fluid Mech.*, *143*, 1–21.

Bashmachnikov, I., M. Sokolovskiy, T. Belonenko, D. Volkov, P. Isachsen, and X. Carton (2017), On the vertical structure and stability of the Lofoten vortex in the Norwegian Sea, *Deep Sea Research Part I: Oceanographic Research Papers*, *128*, 1–27.

Beale, M. H., M. T. Hagan, and H. B. Demuth (2019), Neural network toolbox user's guide, *The MathWorks Inc*.

Becker, J., D. Sandwell, W. Smith, J. Braud, B. Binder, J. Depner, D. Fabre, J. Factor, S. Ingalls, S. Kim, et al. (2009), Global bathymetry and elevation data at 30 arc seconds resolution: SRTM30_PLUS, *Marine Geodesy*, *32*(4), 355–371.

Beckmann, A., and D. Haidvogel (1997), A numerical simulation of flow at fieberling guyot, *Journal of Geophysical Research: Oceans*, *102*(C3), 5595–5613.

Benilov, E. S. (2005), On the stability of oceanic vortices: A solution to the problem?, *Dynam. of Atmos. and Oceans*, *40*(3), 133–149.

Biló, T. C., and W. Johns (2018), Interior pathways of Labrador Sea Water in the North Atlantic from the Argo perspective, *Geophys. Res. Lett.*

Blumsack, S. L., and P. J. Gierasch (1972), Mars: The effects of topography on baroclinic instability, *J. Atmos. Sci.*, *29*(6), 1081–1089.

Böning, C. W. (1988), Characteristics of particle dispersion in the North Atlantic: An alternative interpretation of SOFAR float results, *Deep Sea Res. Part I. Ocean. Res. Papers*, *35*(8), 1379–1385.

Bormans, M., and C. Garrett (1989), A simple criterion for gyre formation by the surface outflow from a strait, with application to the alboran sea, *Journal of Geophysical Research: Oceans*, *94*(C9), 12,637–12,644.

Bosse, A., I. Fer, J. M. Lilly, and H. Søiland (2019), Dynamical controls on the longevity of a non-linear vortex: The case of the lofoten basin eddy, *Scientific reports*, *9*(1), 1–13.

Bouchet, F., and A. Venaille (2012), Statistical mechanics of two-dimensional and geophysical flows, *Physics reports*, *515*(5), 227–295.

Bower, A., S. Lozier, and S. Gary (2011), Export of Labrador Sea water from the subpolar North Atlantic: a Lagrangian perspective, *Deep Sea Res. Part II: Topical Studies in Ocean.*, *58*(17-18), 1798–1818.

Bower, A. S., L. Armi, and I. Ambar (1997), Lagrangian observations of Meddy formation during a Mediterranean Undercurrent seeding Experiment, *J. Phys. Oceanogr.*, *27*(12), 2545–2575.

Bower, A. S., B. Le Cann, T. Rossby, W. Zenk, J. Gould, K. Speer, P. Richardson, M. D. Prater, and H.-M. Zhang (2002a), Directly measured mid-depth circulation in the northeastern North Atlantic Ocean, *Nature*, *419*(6907), 603–607.

Bower, A. S., N. Serra, and I. Ambar (2002b), Structure of the Mediterranean Undercurrent and Mediterranean Water spreading around the southwestern Iberian Peninsula, *J. Geophys. Res. C. Oceans*, *107*(C10), 25–1.

Bower, A. S., M. S. Lozier, S. F. Gary, and C. W. Böning (2009), Interior pathways of the North Atlantic meridional overturning circulation, *Nature*, *459*(7244), 243–247.

Bower, A. S., R. M. Hendry, D. E. Amrhein, and J. M. Lilly (2013), Direct observations of formation and propagation of subpolar eddies into the Subtropical North Atlantic, *Deep Sea Res. Part II: Topical Studies in Ocean.*, *85*, 15–41.

Bracco, A., and J. Pedlosky (2003), Vortex generation by topography in locally unstable baroclinic flows, *Journal of physical oceanography*, *33*(1), 207–219.

Bretherton, F. P., and D. B. Haidvogel (1976), Two-dimensional turbulence above topography, *J. Fluid Mech.*, *78*(1), 129–154.

Brett, G. J., L. Pratt, I. Rypina, and P. Wang (2019), Competition between chaotic advection and diffusion: stirring and mixing in a 3-d eddy model., *Nonlinear Processes in Geophysics*, *26*(2).

Brink, K. (1986), Topographic drag due to barotropic flow over the continental shelf and slope, *Journal of physical oceanography*, *16*(12), 2150–2158.

Bryden, H., A. Mujahid, S. Cunningham, and T. Kanzow (2009), Adjustment of the basin-scale circulation at 26 degrees n to variations in gulf stream, deep western boundary current and ekman transports as observed by the rapid array, *Ocean Science*, *5*(4), 421–433.

Buckley, M. W., and J. Marshall (2016), Observations, inferences, and mechanisms of the Atlantic Meridional Overturning Circulation: A review, *Rev. Geophys.*, *54*(1), 5–63.

Bullister, J. L., M. Rhein, and C. Mauritzen (2013), Deepwater formation, in *International Geophysics*, vol. 103, pp. 227–253, Elsevier.

Burkholder, K. C., and M. S. Lozier (2014), Tracing the pathways of the upper limb of the North Atlantic Meridional Overturning Circulation, *Geophysical Research Letters*, *41*(12), 4254–4260.

Carnevale, G., R. Kloosterziel, and G. Van Heijst (1991), Propagation of barotropic vortices over topography in a rotating tank, *J. Fluid Mech.*, *233*, 119–139.

Carnevale, G. F., G. K. Vallis, R. Purini, and M. Briscolini (1988), Propagation of barotropic modons over topography, *Geophysical & Astrophysical Fluid Dynamics*, *41*(1-2), 45–101.

Carr, M.-E., and H. T. Rossby (2001), Pathways of the North Atlantic Current from surface drifters and subsurface floats, *J. Geophys. Res: Oceans*, *106*(C3), 4405–4419.

Cessi, P. (1991), Laminar separation of colliding western boundary currents, *Journal of marine research*, *49*(4), 697–717.

Charney, J. G. (1990), The dynamics of long waves in a baroclinic westerly current, in *The Atmosphere—A Challenge*, pp. 223–250, Springer.

Chassignet, E. P., and D. P. Marshall (2008), Gulf stream separation in numerical ocean models, *Geophysical Monograph Series*, *177*.

Chelton, D. B., R. A. Deszoeke, M. G. Schlax, K. El Naggar, and N. Siwertz (1998), Geographical variability of the first baroclinic Rossby radius of deformation, *J. Phys. Oceanogr*, *28*(3), 433–460.

Chelton, D. B., M. G. Schlax, and R. M. Samelson (2011), Global observations of nonlinear mesoscale eddies, *Prog. Oceanogr.*, *91*(2), 167–216.

Choboter, P. F., and G. E. Swaters (2000), On the baroclinic instability of axisymmetric rotating gravity currents with bottom slope, *J. of Fluid Mech.*, *408*, 149–177.

Cimoli, L., A. Stegner, and G. Roullet (2017), Meanders and eddy formation by a buoyant coastal current flowing over a sloping topography, *Ocean Sci.*, *13*(6), 905–923.

Cummins, P. F., and G. Holloway (1994), On eddy–topographic stress representation, *Journal of physical oceanography*, *24*(3), 700–706.

Cunningham, S. A., T. Kanzow, D. Rayner, M. O. Baringer, W. E. Johns, J. Marotzke, H. R. Longworth, E. M. Grant, J. J.-M. Hirschi, L. M. Beal, et al. (2007), Temporal variability of the atlantic meridional overturning circulation at 26.5 n, *science*, *317*(5840), 935–938.

Cushman-Roisin, B. (1994), *Introduction to geophysical fluid dynamics*, Prentice Hall.

D'Asaro, E. A. (1988), Generation of submesoscale vortices: A new mechanism, *J. Geophys. Res: Oceans*, *93*(C6), 6685–6693.

Debreu, L., P. Marchesiello, P. Penven, and G. Cambon (2012), Two-way nesting in split-explicit ocean models: algorithms, implementation and validation, *Ocean Modelling*, *49*, 1–21.

Dewar, W. K., and P. D. Killworth (1995), On the stability of oceanic rings, *J. of Phys. Oceanogr.*, *25*(6), 1467–1487.

Dong, C., J. C. McWilliams, Y. Liu, and D. Chen (2014), Global heat and salt transports by eddy movement, *Nat. Commun.*, *5*.

Dreyfus, G. (2005), *Neural networks: methodology and applications*, Springer Science & Business Media.

Durran, D. R. (1991), The third-order Adams-Bashforth method: An attractive alternative to leapfrog time differencing, *Mon. Weather Rev.*, *119*(3), 702–720.

Eady, E. T. (1949), Long waves and cyclone waves, *Tellus A*, *1*(3).

Eden, C., and C. Böning (2002), Sources of eddy kinetic energy in the Labrador Sea, *Journal of Physical Oceanography*, *32*(12), 3346–3363.

Fairall, C. W., E. F. Bradley, D. P. Rogers, J. B. Edson, and G. S. Young (1996), Bulk parameterization of air-sea fluxes for tropical ocean-global atmosphere coupled-ocean atmosphere response experiment, *J. Geophys. Res: Oceans*, *101*(C2), 3747–3764.

Farrell, B. F., and P. J. Ioannou (1996), Generalized stability theory. part i: Autonomous operators, *J. Atmos. Sci.*, *53*(14), 2025–2040.

Fer, I., A. Bosse, B. Ferron, and P. Bouruet-Aubertot (2018), The dissipation of kinetic energy in the lofoten basin eddy, *Journal of Physical Oceanography*, *48*(6), 1299–1316.

Ferrari, R., and C. Wunsch (2009), Ocean circulation kinetic energy: Reservoirs, sources, and sinks, *Annual Review of Fluid Mechanics*, *41*.

Ferrari, R., A. Mashayek, T. J. McDougall, M. Nikurashin, and J.-M. Campin (2016), Turning ocean mixing upside down, *J. Phys. Oceanogr*, *46*(7), 2239–2261.

Fischer, J., and F. A. Schott (2002), Labrador Sea Water tracked by profiling floats–From the boundary current into the open North Atlantic, *J. Phys. Oceanogr*, *32*(2), 573–584.

Fischer, J., F. A. Schott, and M. Dengler (2004), Boundary circulation at the exit of the Labrador Sea, *Journal of Physical Oceanography*, *34*(7), 1548–1570.

Fischer, J., J. Karstensen, M. Oltmanns, and S. Schmidtko (2018a), Mean circulation and EKE distribution in the Labrador Sea Water level of the subpolar North Atlantic, *Ocean Science*, *14*(5), 1167–1183.

Fischer, J., J. Karstensen, M. Oltmanns, and S. Schmidtko (2018b), Gaussian Interpolated (GI) gridded mean 10-day Argo float drift velocities and Eddy Kinetic Energy, PANGAEA, https://doi.org/10.1594/PANGAEA.894947.

Freeland, H. (1994), Ocean circulation at and near cobb seamount, *Deep Sea Research Part I: Oceanographic Research Papers*, *41*(11-12), 1715–1732.

Furey, H., and A. Bower (2009), Export pathways from the subpolar North Atlantic: DLD2 RAFOS Float Data Report July 2003–November 2008, *Tech. rep.*, WHOI Tech. Report WHOI-2009-06.

Gary, S. F., M. S. Lozier, C. W. Böning, and A. Biastoch (2011), Deciphering the pathways for the deep limb of the meridional overturning circulation, *Deep Sea Res. Part II: Topical Studies in Ocean.*, *58*(17-18), 1781–1797.

Gary, S. F., M. S. Lozier, A. Biastoch, and C. W. Böning (2012), Reconciling tracer and float observations of the export pathways of Labrador sea water, *Geophys. Res. Lett.*, *39*(24).

Gebbie, G., and P. Huybers (2012), The mean age of ocean waters inferred from radiocarbon observations: Sensitivity to surface sources and accounting for mixing histories, *Journal of Physical Oceanography*, *42*(2), 291–305.

Getzlaff, K., C. W. Böning, and J. Dengg (2006), Lagrangian perspectives of deep water export from the subpolar North Atlantic, *Geophys. Res. Lett.*, *33*(21).

Gill, A., J. Green, and A. Simmons (1974), Energy partition in the large-scale ocean circulation and the production of mid-ocean eddies, in *Deep sea research and oceanographic abstracts*, vol. 21, pp. 499–528, Elsevier.

Gille, S. T. (2003), Float observations of the southern ocean. part i: Estimating mean fields, bottom velocities, and topographic steering, *Journal of Physical Oceanography*, *33*(6), 1167–1181.

Greenberg, D. A., and B. D. Petrie (1988), The mean barotropic circulation on the Newfoundland shelf and slope, *J. Geophys. Res: Oceans*, *93*(C12), 15,541–15,550.

Griffies, S. M., and R. W. Hallberg (2000), Biharmonic friction with a Smagorinsky-like viscosity for use in large-scale eddy-permitting ocean models, *Monthly Weather Review*, *128*(8), 2935–2946.

Gruber, N., D. Clement, B. R. Carter, R. A. Feely, S. Van Heuven, M. Hoppema, M. Ishii, R. M. Key, A. Kozyr, S. K. Lauvset, et al. (2019), The oceanic sink for anthropogenic co2 from 1994 to 2007, *Science*, *363*(6432), 1193–1199.

Gula, J., V. Zeitlin, T. von Larcher, and P. Williams (2014), Instabilities of shallow-water flows with vertical shear in the rotating annulus, *Modelling Atmospheric and Oceanic flows: insights from laboratory experiments and numerical simulations, Amer. Geophys. Union, edited by T. von Larcher and P. Williams*, *15*.

Handmann, P., J. Fischer, M. Visbeck, J. Karstensen, A. Biastoch, C. Böning, and L. Patara (2018), The Deep Western Boundary Current in the Labrador Sea from observations and a high-resolution model, *J. Geophys. Res: Oceans*, *123*(4), 2829–2850.

Harrison, D., and A. Robinson (1978), Energy analysis of open regions of turbulent flows—mean eddy energetics of a numerical ocean circulation experiment, *Dyn. of Atmos. Oceans*, *2*(2), 185–211.

Hill, P. G. W. J. J. W. R., H. W., and A. R. Folkard (1973), A note on the Labrador and Atlantic currents to the east of Newfoundland Grand Bank, *ICNAF Res. Doc.*, *116*(3082).

Hogg, N. G. (1973), On the stratified taylor column, *Journal of Fluid Mechanics*, *58*(3), 517–537.

Hogg, N. G., and W. E. Johns (1995), Western boundary currents, *Rev. Geophys.*, *33*(S2), 1311–1334.

Holliday, N., S. Bacon, J. Allen, and E. McDonagh (2009), Circulation and transport in the western boundary currents at Cape Farewell, Greenland, *J. Phys. Oceanogr*, *39*(8), 1854–1870.

Holton, J. R. (1973), An introduction to dynamic meteorology, *American Journal of Physics*, *41*(5), 752–754.

Hughes, C. W., and B. A. De Cuevas (2001), Why western boundary currents in realistic oceans are inviscid: A link between form stress and bottom pressure torques, *Journal of Physical Oceanography*, *31*(10), 2871–2885.

Huppert, H. E., and K. Bryan (1976), Topographically generated eddies, in *Deep Sea Research and Oceanographic Abstracts*, vol. 23, pp. 655–679, Elsevier.

Isachsen, P. E. (2011), Baroclinic instability and eddy tracer transport across sloping bottom topography: How well does a modified Eady model do in primitive equation simulations?, *Ocean Modell.*, *39*(1), 183–199.

Isachsen, P. E., J. LaCasce, C. Mauritzen, and S. Häkkinen (2003), Wind-driven variability of the large-scale recirculating flow in the Nordic Seas and Arctic Ocean, *Journal of Physical Oceanography*, *33*(12), 2534–2550.

Isern-Fontanet, J., E. García-Ladona, and J. Font (2006), Vortices of the Mediterranean Sea: An altimetric perspective, *Journal of physical oceanography*, *36*(1), 87–103.

Ivanov, Y., and A. Korablev (1995), Formation and regeneration of the pycnocline lens in the norwegian sea, *Russian Meteorology and Hydrology*, (9), 62–69.

James, I. N. (1987), Suppression of baroclinic instability in horizontally sheared flows, *J. Atmos. Sci.*, *44*(24), 3710–3720.

James, I. N., and L. J. Gray (1986), Concerning the effect of surface drag on the circulation of a baroclinic planetary atmosphere, *Q. J. Roy. Meteorol. Soc.*, *112*(474), 1231–1250.

Jiang, X. (1995), Flow separation in the coastal ocean, Master's thesis, University of Victoria, British Columbia.

Johns, W. E., M. O. Baringer, L. Beal, S. Cunningham, T. Kanzow, H. L. Bryden, J. Hirschi, J. Marotzke, C. Meinen, B. Shaw, et al. (2011), Continuous, array-based estimates of Atlantic Ocean heat transport at 26.5 N, *Journal of Climate*, *24*(10), 2429–2449.

Kearns, E. J., and N. Paldor (2000), Why are the meanders of the North Atlantic Current stable and stationary?, *Geophys. Res. Lett.*, *27*(7), 1029–1032.

Khatiwala, S. P., T. Tanhua, S. E. Mikaloff Fletcher, M. Gerber, S. C. Doney, H. D. Graven, N. Gruber, G. McKinley, A. Murata, A. Ríos, et al. (2013), Global ocean storage of anthropogenic carbon, *Biogeosciences*, *10*(4), 2169–2191.

Khatri, H., J. Sukhatme, A. Kumar, and M. K. Verma (2018), Surface ocean enstrophy, kinetic energy fluxes, and spectra from satellite altimetry, *Journal of Geophysical Research: Oceans*, *123*(5), 3875–3892.

Killworth, P. D., and C. W. Hughes (2002), The antarctic circumpolar current as a free equivalent-barotropic jet, *Journal of marine research*, *60*(1), 19–45.

Klinger, B. A. (1994), Inviscid current separation from rounded capes, *J. Phys. Oceanogr*, *24*(8), 1805–1811.

Kloosterziel, R., G. Carnevale, and D. Phillippe (1993), Propagation of barotropic dipoles over topography in a rotating tank, *Dynamics of atmospheres and oceans*, *19*(1-4), 65–100.

Köhl, A. (2007), Generation and stability of a quasi-permanent vortex in the lofoten basin, *J. Phys. Oceanogr*, *37*(11), 2637–2651.

Krupitsky, A., V. M. Kamenkovich, N. Naik, and M. A. Cane (1996), A linear equivalent barotropic model of the antarctic circumpolar current with realistic coastlines and bottom topography, *Journal of physical oceanography*, *26*(9), 1803–1824.

Kurganov, A., and E. Tadmor (2000), New high-resolution central schemes for nonlinear conservation laws and convection–diffusion equations, *Journal of Computational Physics*, *160*(1), 241–282.

LaCasce, J. (2000), Floats and f/h, *Journal of Marine Research*, *58*(1), 61–95.

Large, W. G., J. C. McWilliams, and S. C. Doney (1994), Oceanic vertical mixing: A review and a model with a nonlocal boundary layer parameterization, *Rev. Geophys.*, *32*(4), 363–403.

Lavender, K. L., R. E. Davis, and W. B. Owens (2000), Mid-depth recirculation observed in the interior Labrador and Irminger seas by direct velocity measurements, *Nature*, *407*(6800), 66–69.

Lavender, K. L., W. B. Owens, and R. E. Davis (2005), The mid-depth circulation of the subpolar North Atlantic Ocean as measured by subsurface floats, *Deep Sea Res. Part I*, *52*(5), 767–785.

Le Bras, I. A., I. Yashayaev, and J. M. Toole (2017), Tracking Labrador Sea Water property signals along the Deep Western Boundary Current, *J. Geophys. Res: Oceans*, *122*(7), 5348–5366.

Le Corre, M., J. Gulaa, A. Smilenovab, and L. Houpertd (2019a), On the dynamics of a deep quasi-permanent anticylonic eddy in the rockall trough, *Association Français de Mécanique, Brest, France, https://cfm2019. sciencesconf. org/245538/document*, p. 12.

Le Corre, M., J. Gula, and A. M. Treguier (2019b), Barotropic vorticity balance of the north atlantic subpolar gyre in an eddy-resolving model, *Ocean Science, https://doi.org/10.5194/os-2019-114*.

Le Vu, B., A. Stegner, and T. Arsouze (2018), Angular momentum eddy detection and tracking algorithm (ameda) and its application to coastal eddy formation, *Journal of Atmospheric and Oceanic Technology*, *35*(4), 739–762.

Lebedev, K. V., H. Yoshinari, N. A. Maximenko, and P. W. Hacker (2007), YoMaHa'07: Velocity data assessed from trajectories of Argo floats at parking level and at the sea surface, *IPRC Technical Note*, *4*(2), 1–16.

Lemarié, F., J. Kurian, A. F. Shchepetkin, M. J. Molemaker, F. Colas, and J. C. McWilliams (2012), Are there inescapable issues prohibiting the use of terrain-following coordinates in climate models?, *Ocean Modelling*, *42*, 57–79.

Lorenz, E. N. (1955), Available potential energy and the maintenance of the general circulation, *Tellus*, *7*(2), 157–167.

Lozier, M. S. (1997), Evidence for large-scale eddy-driven gyres in the north atlantic, *Science*, *277*(5324), 361–364.

Lozier, M. S. (2012), Overturning in the North Atlantic, *Ann. Rev. Marine Sci.*, *4*, 291–315.

Lozier, M. S., S. F. Gary, and A. S. Bower (2013), Simulated pathways of the overflow waters in the North Atlantic: Subpolar to subtropical export, *Deep Sea Res. Part II: Topical Studies in Ocean.*, *85*, 147–153.

Lozier, M. S., S. Bacon, A. S. Bower, S. A. Cunningham, M. F. De Jong, L. De Steur, B. Deyoung, J. Fischer, S. F. Gary, B. J. Greenan, et al. (2017), Overturning in the subpolar north atlantic program: A new international ocean observing system, *Bulletin of the American Meteorological Society*, *98*(4), 737–752.

Lumpkin, R., A.-M. Treguier, and K. Speer (2002), Lagrangian eddy scales in the northern Atlantic Ocean, *J. Phys. Oceanogr*, *32*(9), 2425–2440.

Lutjeharms, J., and R. Van Ballegooyen (1988), The retroflection of the agulhas current, *Journal of Physical Oceanography*, *18*(11), 1570–1583.

Majda, A., and X. Wang (2006), *Nonlinear dynamics and statistical theories for basic geophysical flows*, Cambridge University Press.

Mann, C. (1967), The termination of the Gulf Stream and the beginning of the North Atlantic Current, *14*(3), 337–359.

Marchesiello, P., J. C. McWilliams, and A. Shchepetkin (2001), Open boundary conditions for long-term integration of regional oceanic models, *Ocean modelling*, *3*(1-2), 1–20.

Marchesiello, P., L. Debreu, and X. Couvelard (2009), Spurious diapycnal mixing in terrain-following coordinate models: The problem and a solution, *Ocean Modelling*, *26*(3-4), 156–169.

Marcus, P. S. (1990), Vortex dynamics in a shearing zonal flow, *Journal of Fluid Mechanics*, *215*, 393–430.

Martin, A. P., I. P. Wade, K. J. Richards, and K. J. Heywood (1998), The PRIME eddy, *Journal of Marine Research*, *56*(2), 439–462.

Mason, E., J. Molemaker, A. F. Shchepetkin, F. Colas, J. C. McWilliams, and P. Sangrà (2010), Procedures for offline grid nesting in regional ocean models, *Ocean Modelling*, *35*(1-2), 1–15.

Matsumoto, K. (2007), Radiocarbon-based circulation age of the world oceans, *Journal of Geophysical Research: Oceans*, *112*(C9).

McCoy, D., D. Bianchi, and A. Stewart (2020), Global Observations of Submesoscale Coherent Vortices in the Ocean, manuscript submitted for publication.

McDowell, S. E., and H. T. Rossby (1978), Mediterranean Water: an intense mesoscale eddy off the Bahamas, *Science*, *202*(4372), 1085–1087.

McWilliams, J. C. (1985), Submesoscale, coherent vortices in the ocean, *Rev. Geophys.*, *23*(2), 165–182.

McWilliams, J. C. (2006), *Fundamentals of geophysical fluid dynamics*, Cambridge University Press.

McWilliams, J. C. (2008), The nature and consequences of oceanic eddies, in *Ocean modeling in an eddying regime*, edited by M. W. Hecht and H. Hasumi, chap. 1, John Wiley and Sons.

McWilliams, J. C., and G. R. Flierl (1979), On the evolution of isolated, nonlinear vortices, *J. Phys. Oceanogr*, *9*(6), 1155–1182.

Mechoso, C. R. (1980), Baroclinic instability of flows along sloping boundaries, *J. Atmos. Sci.*, *37*(6), 1393–1399.

Meinen, C. (2001), Structure of the North Atlantic Current in stream-coordinates and the circulation in the Newfoundland Basin, *Deep Sea Res. Part I: Ocean. Res. Papers*, *48*(7), 1553–1580.

Meinen, C. S., S. Speich, R. C. Perez, S. Dong, A. R. Piola, S. L. Garzoli, M. O. Baringer, S. Gladyshev, and E. J. Campos (2013), Temporal variability of the meridional overturning circulation at 34.5 s: Results from two pilot boundary arrays in the south atlantic, *Journal of Geophysical Research: Oceans*, *118*(12), 6461–6478.

Merryfield, W. J. (1998), Effects of stratification on quasi-geostrophic inviscid equilibria, *Journal of Fluid Mechanics*, *354*, 345–356.

Merryfield, W. J., P. F. Cummins, and G. Holloway (2001), Equilibrium statistical mechanics of barotropic flow over finite topography, *Journal of physical oceanography*, *31*(7), 1880–1890.

Mertens, C., M. Rhein, M. Walter, C. W. Böning, E. Behrens, D. Kieke, R. Steinfeldt, and U. Stöber (2014), Circulation and transports in the Newfoundland Basin, western subpolar North Atlantic, *J. Geophys. Res: Oceans*, *119*(11), 7772–7793.

Molemaker, M. J., J. C. McWilliams, and W. K. Dewar (2015), Submesoscale instability and generation of mesoscale anticyclones near a separation of the California Undercurrent, *J. Phys. Oceanogr.*, *45*(3), 613–629.

Moler, C. B., and G. W. Stewart (1973), An algorithm for generalized matrix eigenvalue problems, *SIAM J. on Numer. Analysis*, *10*(2), 241–256.

Mysak, L. A., and F. Schott (1977), Evidence for baroclinic instability of the Norwegian Current, *J. Geophys. Res.*, *82*(15), 2087–2095.

Nøst, O. A., and P. E. Isachsen (2003), The large-scale time-mean ocean circulation in the Nordic Seas and Arctic Ocean estimated from simplified dynamics, *Journal of Marine Research*, *61*(2), 175–210.

Olson, D. B. (1991), Rings in the ocean, *Ann. Rev. of Earth and Plan. Sci.*, *19*, 283.

Ou, H. W., and W. P. De Ruijter (1986), Separation of an inertial boundary current from a curved coastline, *J. Phys. Oceanogr*, *16*(2), 280–289.

Owens, W. B., and N. G. Hogg (1980), Oceanic observations of stratified taylor columns near a bump, *Deep Sea Research Part A. Oceanographic Research Papers*, *27*(12), 1029–1045.

Paldor, N., and D. Nof (1990), Linear instability of an anticyclonic vortex in a two-layer ocean, *J. of Geophy. Res.: Oceans*, *95*(C10), 18,075–18,079.

Pasquero, C., A. Provenzale, and A. Babiano (2001), Parameterization of dispersion in two-dimensional turbulence, *Journal of Fluid Mechanics*, *439*, 279–303.

Pavlidis, T. (2012), *Algorithms for graphics and image processing*, Springer Science & Business Media.

Pedlosky, J. (1964), The stability of currents in the atmosphere and the ocean: Part I, *J. Atmos. Sci.*, *21*(2), 201–219.

Pedlosky, J. (1970), Flow in rotating stratified systems, *Notes on the 1970 Summer Study Program in GFD at WHOI*, pp. 1–68, https://darchive.mblwhoilibrary.org/handle/1912/3000.

Pedlosky, J. (1987), *Geophysical fluid dynamics*, Springer Science and Business Media.

Pedlosky, J. (2018), A note on interior pathways in the meridional overturning circulation, *J. Phys. Oceanogr*, *48*(3), 643–646.

Petrie, B., and J. Buckley (1996), Volume and freshwater transport of the labrador current in flemish pass, *J. Geophys. Res: Oceans*, *101*(C12), 28,335–28,342.

Phillips, N. A. (1951), A simple three-dimensional model for the study of large-scale extratropical flow patterns, *J. Meteor.*, *8*(6), 381–394.

Pichevin, T. (1998), Baroclinic instability in a three layer flow: a wave approach, *Dynam. Atmos. Ocean*, *28*(3), 179–204.

Pickart, R. S., and R. X. Huang (1995), Structure of an inertial deep western boundary current, *J. Marine Res.*, *53*(5), 739–770.

Pickart, R. S., N. G. Hogg, and W. M. Smethie Jr (1989), Determining the strength of the deep western boundary current using the chlorofluoromethane ratio, *Journal of Physical Oceanography*, *19*(7), 940–951.

Poulin, F. J., A. Stegner, M. Hernández-Arencibia, A. Marrero-Díaz, and P. Sangrà (2014), Steep shelf stabilization of the coastal Bransfield Current: Linear stability analysis, *J. Phys. Oceanogr.*, *44*(2), 714–732.

Pujol, M.-I., Y. Faugère, G. Taburet, S. Dupuy, C. Pelloquin, M. Ablain, and N. Picot (2016), DUACS DT2014: the new multi-mission altimeter data set reprocessed over 20 years, *Ocean Science*, *12*(5).

Raj, R. P., L. Chafik, J. E. Ø. Nilsen, T. Eldevik, and I. Halo (2015), The Lofoten Vortex of the Nordic Seas, *Deep Sea Res. Part I: Ocean. Res. Papers*, *96*, 1–14.

Rattan, S., P. G. Myers, A.-M. Treguier, S. Theetten, A. Biastoch, and C. Böning (2010), Towards an understanding of Labrador sea salinity drift in eddy-permitting simulations, *Ocean Modelling*, *35*(1-2), 77–88.

Rayleigh, L. (1880), On the stability, or instability, of certain fluid motions, *Proc. London Math. Soc.*, *11*, 57–70.

Read, J., and R. Pollard (2001), A long-lived eddy in the Iceland Basin 1998, *Journal of Geophysical Research: Oceans*, *106*(C6), 11,411–11,421.

Renault, L., M. J. Molemaker, J. C. McWilliams, A. F. Shchepetkin, F. Lemarié, D. Chelton, S. Illig, and A. Hall (2016a), Modulation of wind work by oceanic current interaction with the atmosphere, *Journal of Physical Oceanography*, *46*(6), 1685–1704.

Renault, L., M. J. Molemaker, J. Gula, S. Masson, and J. C. McWilliams (2016b), Control and stabilization of the gulf stream by oceanic current interaction with the atmosphere, *J. Phys. Oceanogr*, *46*(11), 3439–3453.

Renault, L., S. Masson, V. Oerder, S. Jullien, and F. Colas (2019), Disentangling the Mesoscale Ocean-Atmosphere Interactions, *Journal of Geophysical Research: Oceans*, *124*(3), 2164–2178.

Rhein, M., J. Fischer, W. M. Smethie, D. Smythe-Wright, R. F. Weiss, C. Mertens, D.-H. Min, U. Fleischmann, and A. Putzka (2002), Labrador Sea Water: Pathways, CFC inventory, and formation rates, *J. Phys. Oceanogr*, *32*(2), 648–665.

Rhein, M., D. Kieke, and R. Steinfeldt (2015), Advection of North Atlantic Deep Water from the Labrador Sea to the southern hemisphere, *Journal of Geophysical Research: Oceans*, *120*(4), 2471–2487.

Rhines, P. B., and W. R. Young (1982a), Homogenization of potential vorticity in planetary gyres, *Journal of Fluid Mechanics*, *122*, 347–367.

Rhines, P. B., and W. R. Young (1982b), Homogenization of potential vorticity in planetary gyres, *Journal of Fluid Mechanics*, *122*, 347–367.

Richards, C. G., and F. Straneo (2015), Observations of water mass transformation and eddies in the Lofoten Basin of the Nordic Seas, *Journal of Physical Oceanography*, *45*(6), 1735–1756.

Richardson, P. (1981), Anticyclonic eddies generated near the corner rise seamounts.

Riser, S. C., H. J. Freeland, D. Roemmich, S. Wijffels, A. Troisi, M. Belbéoch, D. Gilbert, J. Xu, S. Pouliquen, A. Thresher, et al. (2016), Fifteen years of ocean observations with the global Argo array, *Nature Climate Change*, *6*(2), 145.

Rossby, T. (1996), The North Atlantic Current and surrounding waters: At the crossroads, *Rev. Geophys.*, *34*(4), 463–481.

Rypina, I. I., L. J. Pratt, J. Pullen, J. Levin, and A. L. Gordon (2010), Chaotic advection in an archipelago, *Journal of Physical Oceanography*, *40*(9), 1988–2006.

Saha, S., S. Moorthi, H. Pan, X. Wu, J. Wang, S. Nadiga, et al. (2010), The NCEP climate forecast system reanalysis, *Bull. Amer. Meteor. Soc.*, *91*(8), 1015–1058.

Salmon, R. (1998), *Lectures on geophysical fluid dynamics*, Oxford University Press.

Salmon, R., G. Holloway, and M. C. Hendershott (1976), The equilibrium statistical mechanics of simple quasi-geostrophic models, *J. Fluid Mech.*, *75*(4), 691–703.

Schoonover, J., W. K. Dewar, N. Wienders, and B. Deremble (2017a), Local sensitivities of the gulf stream separation, *Journal of Physical Oceanography*, *47*(2), 353–373.

Schoonover, J., W. K. Dewar, N. Wienders, and B. Deremble (2017b), Local sensitivities of the gulf stream separation, *Journal of Physical Oceanography*, *47*(2), 353–373.

Schott, F. A., R. Zantopp, L. Stramma, M. Dengler, J. Fischer, and M. Wibaux (2004), Circulation and deep-water export at the western exit of the subpolar North Atlantic, *J. Phys. Oceanogr*, *34*(4), 817–843.

Shchepetkin, A. F. (1995), Interaction of Turbulent Barotropic Shallow-Water Flow With Topography, *IN THE OCEAN*, p. 225.

Shchepetkin, A. F., and J. C. McWilliams (2005), The regional oceanic modeling system (ROMS): a split-explicit, free-surface, topography-following-coordinate oceanic model, *Ocean modelling*, *9*(4), 347–404.

Shchepetkin, A. F., and J. C. McWilliams (2011), Accurate Boussinesq oceanic modeling with a practical,"Stiffened" Equation of State, *Ocean Modelling*, *38*(1-2), 41–70.

Shepherd, T. G., J. N. Koshyk, and K. Ngan (2000), On the nature of large-scale mixing in the stratosphere and mesosphere, *Journal of Geophysical Research: Atmospheres*, *105*(D10), 12,433–12,446.

Sherwin, T. J., M. O. Williams, W. R. Turrell, S. L. Hughes, and P. I. Miller (2006), A description and analysis of mesoscale variability in the färoe-shetland channel, *J. Geophys. Res. Oceans*, *111*(C3).

Smith, K. S. (2007), The geography of linear baroclinic instability in earth's oceans, *Journal of Marine Research*, *65*(5), 655–683.

Smith, P. C. (1976), Baroclinic instability in the Denmark Strait overflow, *J. Phys. Oceanogr.*, *6*(3), 355–371.

Smith, R. D. (1999), The primitive equations in the stochastic theory of adiabatic stratified turbulence, *J. Phys. Oceanogr.*, *29*(8), 1865–1880.

Søiland, H., L. Chafik, and T. Rossby (2016), On the long-term stability of the lofoten basin eddy, *Journal of Geophysical Research: Oceans*, *121*(7), 4438–4449.

Solodoch, A., A. L. Stewart, and J. C. McWilliams (2016), Baroclinic instability of axially symmetric flow over sloping bathymetry, *J. Fluid Mech.*, *799*, 265–296.

Solodoch, A., J. C. McWilliams, A. L. Stewart, J. Gula, and L. Renault (2020a), Why does the deep-western boundary current "leak" around flemish cap?, *Journal of Physical Oceanography*.

Solodoch, A., A. L. Stewart, and J. C. McWilliams (2020b), Formation of anticyclones above topographic depressions, in preparation.

Soufflet, Y., P. Marchesiello, F. Lemarié, J. Jouanno, X. Capet, L. Debreu, and R. Benshila (2016), On effective resolution in ocean models, *Ocean Modelling*, *98*, 36–50.

Spall, M. A. (2010), Non-local topographic influences on deep convection: An idealized model for the Nordic Seas, *Ocean Modell.*, *32*(1), 72–85.

Spence, P., O. A. Saenko, W. Sijp, and M. England (2012), The role of bottom pressure torques on the interior pathways of North Atlantic Deep Water, *J. Phys. Oceanogr*, *42*(1), 110–125.

Srokosz, M., M. Baringer, H. Bryden, S. Cunningham, T. Delworth, S. Lozier, J. Marotzke, and R. Sutton (2012), Past, present, and future changes in the Atlantic meridional overturning circulation, *Bull. Amer. Meteor. Soc.*, *93*(11), 1663–1676.

St-Laurent, P. (2018), Back of Envelope Ocean Model (BEOM), `www.nordet.net/beom.html`, accessed: 2019-12-25.

Stegmann, P. M., and F. Schwing (2007), Demographics of mesoscale eddies in the California Current, *Geophys. Res. Lett.*, *34*(14).

Stern, A., L. Nadeau, and D. Holland (2015), Instability and mixing of zonal jets along an idealized continental shelf break, *J. Phys. Oceanogr.*, *45*(9), 2315–2338.

Stewart, A. L., and P. J. Dellar (2016), An energy and potential enstrophy conserving numerical scheme for the multi-layer shallow water equations with complete coriolis force, *Journal of Computational Physics*, *313*, 99–120.

Stewart, A. L., P. J. Dellar, and E. R. Johnson (2011), Numerical simulation of wave propagation along a discontinuity in depth in a rotating annulus, *Computers & Fluids*, *46*, 442–447.

Stewart, A. L., P. J. Dellar, and E. R. Johnson (2014), Large-amplitude coastal shelf waves, in *Modeling Atmospheric and Oceanic Flows*, edited by T. von Larcher and P. D. Williams, pp. 229–253, Wiley, Hoboken, NJ, doi:doi:10.1002/9781118856024.ch12.

Stipa, T. (2004a), On the sensitivity of coastal quasigeostrophic edge wave interaction to bottom boundary characteristics: possible implications for eddy parameterizations, *arXiv preprint physics/0401119*.

Stipa, T. (2004b), Baroclinic adjustment in the Finnish coastal current, *Tellus A*, *56*(1), 79–87.

Stommel, H. (1948), The westward intensification of wind-driven ocean currents, *Eos, Transactions American Geophysical Union*, *29*(2), 202–206.

Stommel, H., and A. Arons (1959), On the abyssal circulation of the world ocean––I. Stationary planetary flow patterns on a sphere, *Deep Sea Res. (1953)*, *6*, 140–154.

Stommel, H., and A. B. Arons (1972), On the abyssal circulation of the world ocean—V. The influence of bottom slope on the broadening of inertial boundary currents, *19*(10), 707–718.

Takahashi, T., S. C. Sutherland, R. Wanninkhof, C. Sweeney, R. A. Feely, D. W. Chipman, B. Hales, G. Friederich, F. Chavez, C. Sabine, et al. (2009), Climatological mean and decadal change in surface ocean pco2, and net sea–air co2 flux over the global oceans, *Deep Sea Res. Part II: Topical Studies in Ocean.*, *56*(8-10), 554–577.

Talley, L., and M. McCartney (1982), Distribution and circulation of Labrador sea water, *J. Phys. Oceanogr*, *12*(11), 1189–1205.

Talley, L. D. (2011), *Descriptive physical oceanography: an introduction*, Academic press.

Trefethen, L. N., A. E. Trefethen, S. C. Reddy, and T. A. Driscoll (1993), Hydrodynamic stability without eigenvalues, *Science*, *261*(5121), 578–584.

Tréguier, A.-M., S. Theetten, E. P. Chassignet, T. Penduff, R. Smith, L. Talley, J. Beismann, and C. Böning (2005), The North Atlantic subpolar gyre in four high-resolution models, *J. Phys. Oceanogr*, *35*(5), 757–774.

Trenberth, K. E., and J. T. Fasullo (2017), Atlantic meridional heat transports computed from balancing Earth's energy locally, *Geophys. Res. Lett.*, *44*(4), 1919–1927.

Trodahl, M., and P. E. Isachsen (2018), Topographic influence on baroclinic instability and the mesoscale eddy field in the northern North Atlantic Ocean and the Nordic Seas, *Journal of Physical Oceanography*, *48*(11), 2593–2607.

Tulloch, R., and J. Marshall (2012), Exploring mechanisms of variability and predictability of Atlantic meridional overturning circulation in two coupled climate models, *Journal of Climate*, *25*(12), 4067–4080.

Tulloch, R., J. Marshall, C. Hill, and K. S. Smith (2011), Scales, growth rates, and spectral fluxes of baroclinic instability in the ocean, *Journal of Physical Oceanography*, *41*(6), 1057–1076.

Vallis, G. K. (2017), *Atmospheric and oceanic fluid dynamics*, Cambridge University Press.

Vallis, G. K., and M. E. Maltrud (1993), Generation of mean flows and jets on a beta plane and over topography, *Journal of physical oceanography*, *23*(7), 1346–1362.

Venaille, A. (2012), Bottom-trapped currents as statistical equilibrium states above topographic anomalies, *J. Fluid Mech.*, *699*, 500–510.

Volkov, D. L., A. A. Kubryakov, and R. Lumpkin (2015), Formation and variability of the lofoten basin vortex in a high-resolution ocean model, *Deep Sea Research Part I: Oceanographic Research Papers*, *105*, 142–157.

Wade, I. P., and K. J. Heywood (2001), Tracking the PRIME eddy using satellite altimetry, *Deep Sea Research Part II: Topical Studies in Oceanography*, *48*(4-5), 725–737.

Waugh, D. W., E. R. Abraham, and M. M. Bowen (2006), Spatial variations of stirring in the surface ocean: A case study of the Tasman Sea, *Journal of Physical Oceanography*, *36*(3), 526–542.

White, M., and C. Mohn (2004), Seamounts: a review of physical processes and their influence on the seamount ecosystem, *OASIS Report contract*, (38).

Whitehead, J. A., and A. Miller (1979), Laboratory simulation of the gyre in the alboran sea, *Journal of Geophysical Research: Oceans*, *84*(C7), 3733–3742.

Wilks, D. S. (2011), *Statistical methods in the atmospheric sciences*, vol. 100, Academic press.

Williams, P. D., P. L. Read, and T. W. N. Haine (2010), Testing the limits of quasi-geostrophic theory: application to observed laboratory flows outside the quasi-geostrophic regime, *J. Fluid Mech.*, *649*, 187–203.

Willis, J. K., and L.-L. Fu (2008), Combining altimeter and subsurface float data to estimate the time-averaged circulation in the upper ocean, *Journal of Geophysical Research: Oceans*, *113*(C12).

Wolfe, C. L., and C. Cenedese (2006), Laboratory experiments on eddy generation by a buoyant coastal current flowing over variable bathymetry, *Journal of Physical Oceanography*, *36*(3), 395–411.

Xu, X., P. B. Rhines, E. P. Chassignet, and W. J. Schmitz Jr (2015), Spreading of Denmark Strait Overflow Water in the western subpolar North Atlantic: insights from eddy-resolving simulations with a passive tracer, *J. Phys. Oceanogr.*, *45*(2015), 2913–2932.

Yashayaev, I., and J. W. Loder (2016), Recurrent replenishment of Labrador sea water and associated decadal-scale variability, *J. Geophys. Res: Oceans*, *121*(11), 8095–8114.

Young, W. R. (2012), An exact thickness-weighted average formulation of the Boussinesq equations, *J. Phys. Oceanogr*, *42*(5), 692–707.

Yu, L.-S., A. Bosse, I. Fer, K. A. Orvik, E. M. Bruvik, I. Hessevik, and K. Kvalsund (2017), The Lofoten B asin eddy: Three years of evolution as observed by Seagliders, *Journal of Geophysical Research: Oceans*, *122*(8), 6814–6834.

Zantopp, R., J. Fischer, M. Visbeck, and J. Karstensen (2017), From interannual to decadal: 17 years of boundary current transports at the exit of the Labrador Sea, *J. Geophys. Res: Oceans*, *122*(3), 1724–1748.

Zhao, J., A. Bower, J. Yang, X. Lin, and C. Zhou (2018), Structure and formation of anticyclonic eddies in the Iceland Basin, *Journal of Geophysical Research: Oceans*, *123*(8), 5341–5359.